Technical Physics, Vol. 46, No. 4, 2001, pp. 363–367. Translated from Zhurnal Tekhnicheskoĭ Fiziki, Vol. 71, No. 4, 2001, pp. 1–5.

Inhomogeneous Fluctuations in Liquids and Gases

S. O. Gladkov and I. V. Gladyshev

Moscow State Institute of Radio Engineering, Electronics, and Automation (Technical University), pr. Vernadskogo 86a, Moscow, 117454 Russia

Received January 25, 2000

Abstract—The coupled inhomogeneous density and temperature oscillations in liquids and gases are described with the help of dynamical equations of motion for fluctuations. It is proved that stationary points are asymptotically stable when the preset temperature distribution is inhomogeneous. It is shown that the temperature setting in a gas is a result of the competition between viscosity and heat conduction mechanisms. The phase trajectories in the T–ρ plane are constructed in the inhomogeneous case by numerically solving the derived equations. © *2001 MAIK "Nauka/Interperiodica".*

INTRODUCTION

A general approach to the description of the fluctuating behavior in time and space of any statistically independent parameters of physical subsystems was outlined in [1]. The mathematical model of fluctuation dynamics was described in a particular case of temperature T and density ρ fluctuations. It was shown that the fluctuations were strictly periodic with some characteristic period. The possible inhomogeneity of T and ρ was not taken into account.

Being a continuation of [1], this paper gives a description of temperature and density with an allowance for their inhomogeneous distributions.

THE APPROACH DESCRIPTION AND RESULTS

We start from the inhomogeneous equations of motion containing only the terms linear in δT and $\delta\rho$. According to [1], the following equations are valid for

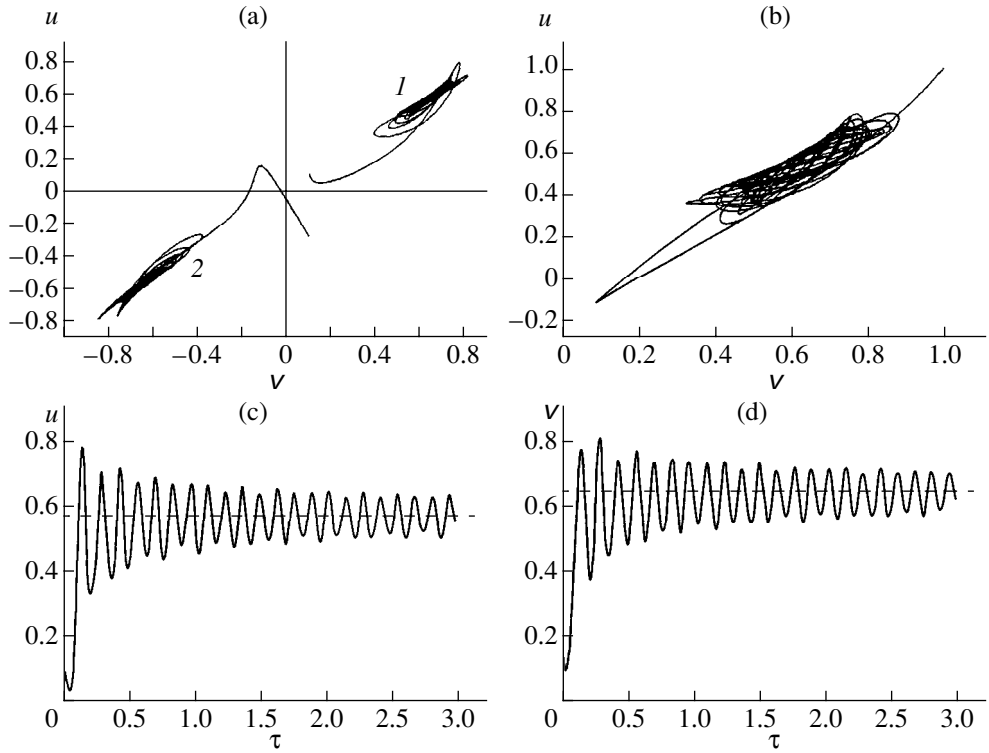

Fig. 1. The phase trajectories (a, b) for the initial distribution (11) with the following parameters: (a, *1*) $u(0) = v(0) = 0.1$; (a, *2*) $u(0) = -0.3$, $v(0) = 0.1$; (b) $u(0) = v(0) = 1$. The time dependences of (c) u and (d) v for the curve (a, *1*). The dashed lines in (c) and (d) mark the coordinates of the stable node at $c_v = 3/2$ [1].

1063-7842/01/4604-0363$21.00

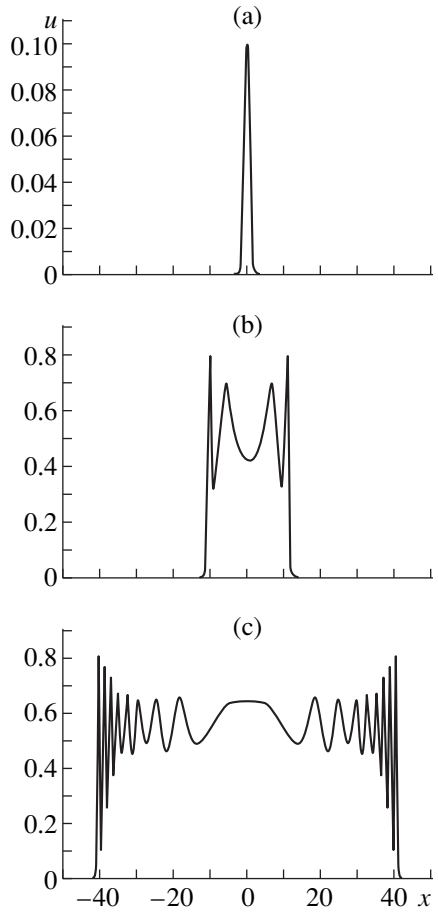

Fig. 2. The spatial distribution of fluctuations at various time moments: (a) τ_1, (b) τ_2, and (c) τ_3 ($\tau_1 < \tau_2 < \tau_3$). The initial distributions are the same as for the curve *1* in Fig. 1a.

the ideal gas

$$\frac{\partial u}{\partial \tau} = \nu t_0\left(\Delta u - \frac{\ddot{u}}{c_S^2}\right) - k_1 \Delta v - u + v + \Psi_1(u, v), \quad (1)$$

$$\frac{\partial v}{\partial \tau} = t_0\chi\left(\Delta v - \frac{\ddot{v}}{c_T^2}\right) - k_1 \Delta u - c_v v + u + \Psi_2(u, v), \quad (2)$$

where

$$u = \frac{\rho - \rho_0}{\rho_0}, \quad v = \frac{T - T_0}{T_0}, \quad (3)$$

ν is the kinematic viscosity, χ is the gas temperature conductivity, t_0 is some phenomenological relaxation time, k_1 is a constant, c_v is the isochoric heat capacity, c_T is the temperature spreading velocity, c_S is the sound speed in the gas, $\tau = t/t_0$ is the dimensionless time, and

$$\Psi_1(u, v) = \frac{1}{3}v^2 + u^2 + \frac{3}{4}u^2 v - u^3 - u^4 + 2u^3 v - u^5 - u^4 v, \quad (4)$$

$$\Psi_2(u, v) = \frac{2}{3}uv - 3c_v v^2 + \frac{1}{4}u^3 + \frac{1}{3}c_v v^3 - \frac{1}{4}c_v v^4 - \frac{1}{2}u^4 + \frac{1}{5}c_v v^5 - \frac{1}{5}u^5. \quad (4')$$

Concerning velocity c_T, it follows from Eq. (2) that at the times

$$\tau_1 \ll \delta\tau \ll \chi/c_T^2, \quad (5)$$

where τ_1 is a characteristic quantum time scale, specific temperature waves exist with the dispersion relation $\omega = c_T q$. As seen from Eq. (5), this spectrum is manifested when

$$\tau_1 \ll \delta\tau \ll \tau_2\left(\frac{v_T}{c_T}\right)^2, \quad (6)$$

where $v_T \sim \sqrt{T}$ is the average thermal velocity of molecules in the gas and τ_2 is the period of time between molecular collisions.

If $c_T \ll v_T$, region (6) is reasonable and the temperature waves may take place. Let us return to Eqs. (1) and (2). We are interested in the behavior of fluctuations at times

$$\delta t \gg \max\left\{\tau_2\left(\frac{v_T}{c_T}\right)^2, \tau_2'\left(\frac{v_T}{c_S}\right)^2\right\}, \quad (7)$$

where τ_2' is determined from the following gas-kinetic approximation

$$\nu \sim v_T^2 \tau_2'. \quad (8)$$

Equations (1) and (2) now take the form

$$\frac{\partial u}{\partial \tau} = \nu t_0 \Delta u - k_1 \Delta v - u + v + \Psi_1(u, v), \quad (9)$$

$$\frac{\partial v}{\partial \tau} = \chi t_0 \Delta v - k_1 \Delta u + c_v v + u + \Psi_2(u, v). \quad (10)$$

Omitting the terms proportional to k_1 and taking the initial distributions

$$v(0, x) = v(0)e^{-\frac{x^2}{2\sigma^2}}, \quad u(0, x) = u(0)e^{-\frac{x^2}{2\sigma^2}}, \quad (11)$$

where σ is a small width of the Gaussian distribution, we obtain the numerical solutions to Eqs. (9) and (10) shown in Figs. 1 and 2. Replacing one of the distributions (11) by a constant does not qualitatively change the solutions.

Taking into account the terms $k_1 \Delta v$ in Eq. (9) and $k_1 \Delta u$ in Eq. (10), and also when $k_1 < 0$, almost does not change the graphs in Figs. 1 and 2. If $k_1 > \nu t_0$ and χt_0, some changes occur in the spatial distribution of fluctuations.

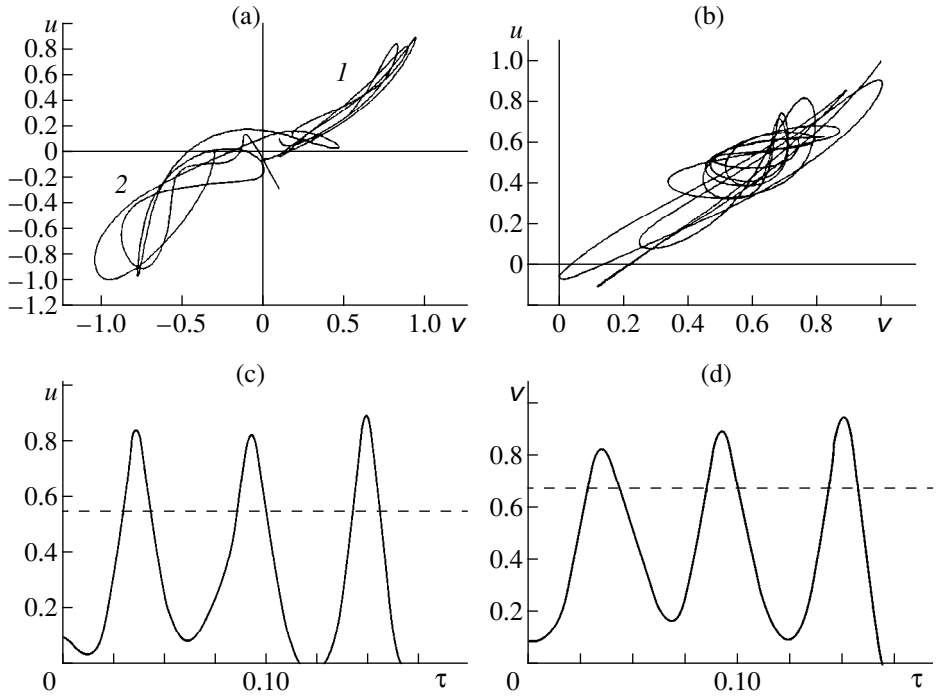

Fig. 3. The phase trajectories (a, b) for the initial distribution (12) with the following parameters: (a, *1*) $u(0) = v(0) = 0.1$; (a, *2*) $u(0) = -0.3$, $v(0) = 0.1$; (b) $u(0) = v(0) = 1$. The time dependences of (c) u and (d) v for the curve (a, *1*). The dashed lines in (c) and (d) mark the coordinates of the stable node at $c_v = 3/2$ [1].

When the initial distributions are more realistic, e.g., when

$$v(0, x) = \frac{v(0)}{3}\left\{e^{-\frac{(x+x_0)^2}{2\sigma^2}} + e^{-\frac{x^2}{2\sigma^2}} + e^{-\frac{(x-x_0)^2}{2\sigma^2}}\right\},$$
$$u(0, x) = \frac{u(0)}{3}\left\{e^{-\frac{(x+x_0)^2}{2\sigma^2}} + e^{-\frac{x^2}{2\sigma^2}} + e^{-\frac{(x-x_0)^2}{2\sigma^2}}\right\}, \quad (12)$$

functions $u(\tau)$ and $v(\tau)$ exhibit qualitatively different behavior if the peaks in the initial distributions are close to each other ($x_0 \approx 10\sigma$ or less). This is illustrated in Fig. 3 (see also the spatial distribution shown in Fig. 4). Increasing the number of the peaks in the initial distribution (12) up to five does not bring qualitative modifications. When $x_0 \ll 10\sigma$, both three and five peaks can be considered as independent from each other, as single perturbations with distributions like (11). A block scheme of the program numerically integrating Eqs. (9) and (10) is given in Fig. 5.

Let us solve analytically Eqs. (9) and (10) in the approximation linear with respect to u and v. Putting $k_1 = \Psi_1 = \Psi_2 = 0$, we obtain

$$\frac{\partial u}{\partial \tau} = \alpha\Delta u - u + v, \quad (13)$$

$$\frac{\partial v}{\partial \tau} = \beta\Delta v + c_v v + u, \quad (14)$$

where $\alpha = \nu t_0$ and $\beta = \chi t_0$. Finding u as the function of v from Eq. (14) and substituting the result into Eq. (13), we arrive at

$$\ddot{v} - (\alpha+\beta)\Delta\dot{v} - (c_v - 1)\dot{v} + \alpha\beta\Delta^2 v + (c_v\alpha - \beta)\Delta v - c_p v = 0, \quad (15)$$

where the dot means differentiating with respect to the dimensionless time τ and $c_p = c_v + 1$ is the isobaric heat capacity.

We solve Eq. (15) in the one-dimensional case, when $\Delta = \partial^2/\partial x^2$, by means of the Fourier transformation. For

$$v(x, \tau) = \int_{-\infty}^{\infty} v_p(\tau) e^{ipx} \frac{dp}{2\pi} \quad (16)$$

we derive from Eq. (15) the following equation

$$\ddot{v} + \gamma(p)\dot{v}_p + \Omega_p^2 v_p = 0, \quad (17)$$

where

$$\gamma(p) = (\alpha+\beta)p^2 + 1 - c_v,$$
$$\Omega_p^2 = \alpha\beta p^4 + (\beta - c_v\alpha)p^2 - c_p. \quad (18)$$

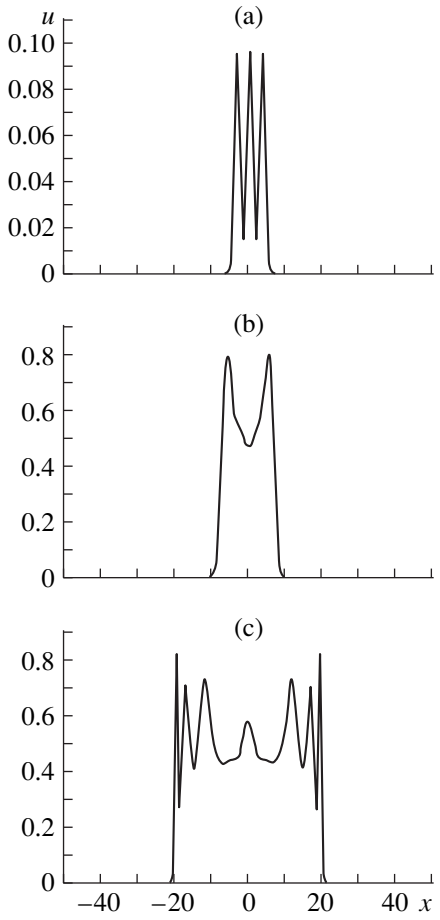

Fig. 4. The spatial distribution of fluctuations at various time moments: (a) τ_1, (b) τ_2, and (c) τ_3 ($\tau_1 < \tau_2 < \tau_3$). The initial distributions are the same as for the curve *1* in Fig. 3a.

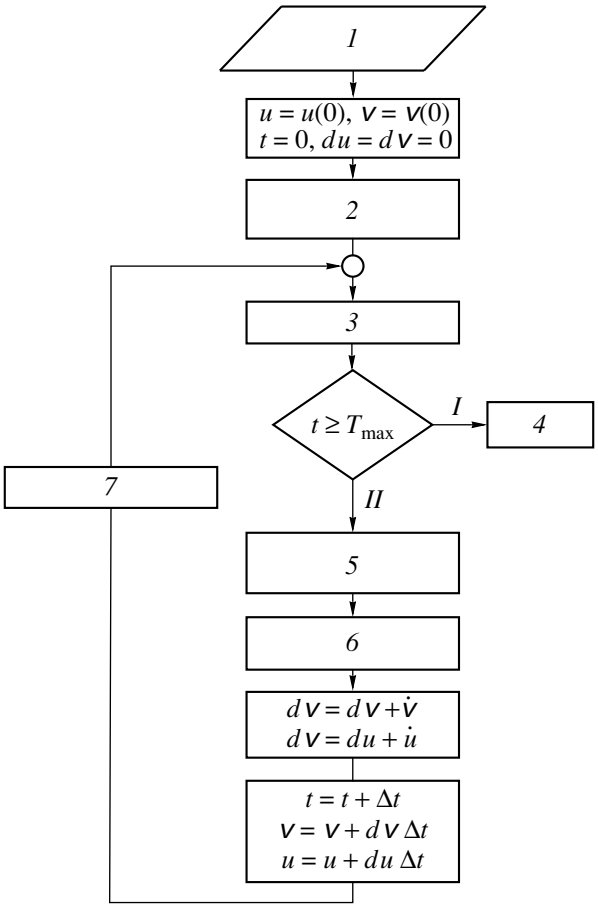

Fig. 5. The block scheme of the program calculating the phase trajectories: (*1*) initial data input, (*2*) calculation of the distribution function, (*3*) output of *u*, *v*, and *t* (*I* is logical yes), (*4*) stop (*II* is logical no), (*5*) the calculation of derivatives, (*6*) determination of $\dot{u}(u, v)$ and $\dot{v}(u, v)$, (*7*) calculation of changed distribution function.

Equation (17) has the following solution

$$v_p(\tau) = e^{-\gamma_p\frac{\tau}{2}}(C_1 e^{+\lambda\tau} + C_2 e^{-\lambda\tau}), \qquad (19)$$

where

$$\lambda = \sqrt{\frac{\gamma_p^2}{4} - \Omega_p^2}. \qquad (20)$$

After some transformations, Eq. (20) takes the form

$$\lambda = \frac{1}{2}\sqrt{(\alpha-\beta)^2 p^4 + 2p^2 c_p(\alpha-\beta) + c_p^2 + 4}. \qquad (21)$$

Finally, solution (16) is written as follows:

$$v(x, \tau) = \int_{-\infty}^{\infty} c(p, 0) e^{ipx - \gamma_p\frac{\tau}{2} - \lambda\tau}\frac{dp}{2\pi}. \qquad (22)$$

This solution is obtained by using Eq. (19) with $C_1 = 0$ and $C_2 = C(p, 0)$, where

$$C(p, 0) = \int_{-\infty}^{\infty} e^{-ipx} v(0, x)dx. \qquad (23)$$

The integral in expression (22) can be calculated with the help of the saddle point method. Let us consider the function

$$f(p) = ixp - \gamma_p\frac{\tau}{2} - \lambda\tau. \qquad (24)$$

Differentiating with respect to ρ and equating the result to zero, we have

$$f' = ix - p\tau(\alpha+\beta) - \frac{\tau p[(\alpha-\beta)^2 p^2 + (\alpha-\beta)c_p]}{2\lambda} = 0.$$

Assuming that time t_0 is large, we can write

$$\lambda \approx |\alpha - \beta| \frac{p^2}{2}.$$

Therefore, the equation $f' = 0$ leads to the following saddle point

$$\begin{aligned} p_0 &\approx \frac{ix}{2\alpha\tau} \quad \text{at} \quad \alpha > \beta, \\ p_0 &\approx \frac{ix}{2\beta\tau} \quad \text{at} \quad \alpha < \beta. \end{aligned} \tag{25}$$

With this p_0, the function $f(p)$ in Eq. (24) takes the following form:

$$\begin{aligned} f(p_0) &\approx -\frac{x^2}{4\alpha\tau} \quad \text{at} \quad \alpha > \beta, \\ f(p_0) &\approx -\frac{x^2}{4\beta\tau} \quad \text{at} \quad \alpha < \beta. \end{aligned} \tag{26}$$

The second derivative at the saddle point is as follows

$$f'' = -2\alpha\tau\left(1 + \frac{2\alpha\tau^2}{x^2} c_p\right). \tag{27}$$

Hence, when $\alpha > \beta$, Eq. (22) takes the form

$$v(x, t) \approx C(p_0) e^{-\frac{x^2}{4\nu t}} \sqrt{\frac{\pi}{2\nu t\left(1 + \frac{2\nu t^2 c_p}{t_0 x^2}\right)}}, \tag{28}$$

and for $\alpha < \beta$,

$$v(x, t) \approx C(p_0) e^{-\frac{x^2}{4\chi t}} \sqrt{\frac{\pi}{2\chi t\left(1 + \frac{2\chi t^2 c_p}{t_0 x^2}\right)}}. \tag{29}$$

The only difference of the resulting formulas (28) and (29) from the classical ones [2–4] is that their denominators contain the small terms proportional to the isobaric heat capacity c_p. When these terms are omitted, the classical result is obtained [2–4]. The table contains the values of χ and ν for substances of three types.

The kinematic viscosity and temperature conductivity of some substances under normal conditions

Substance	Water	Air	Mercury
Temperature conductivity χ, cm^2/s	0.00144	0.187	0.044
Kinematic viscosity ν, cm^2/s	0.01	0.15	0.0012

CONCLUSION

The above analytical and numerical analysis revealed the following results.

(i) In inhomogeneous liquids and gases, the system comes with time to an asymptotically stable stationary point.

(ii) In such media, where $\nabla\rho$ and ∇T exist, there are no fluctuating points. The parameters do not oscillate around the saddle point, as it is described in [1] for a homogeneous medium.

(iii) The viscosity strongly affects the way the temperature sets in a medium.

REFERENCES

1. S. O. Gladkov and I. V. Gladyshev, Zh. Tekh. Fiz. **71** (3), 1 (2001) [Tech. Phys. **46**, 273 (2001)].
2. H. S. Carslaw and J. C. Jaeger, *Conduction of Heat in Solids* (Clarendon Press, Oxford, 1959; Nauka, Moscow, 1964).
3. A. V. Lykov, *Theory of Heat Conduction* (Vysshaya Shkola, Moscow, 1967).
4. N. M. Belyaev and A. A. Ryadno, *Methods of Nonstationary Heat Conduction* (Vysshaya Shkola, Moscow, 1978).

Translated by V. Gursky

Technical Physics, Vol. 46, No. 4, 2001, pp. 368–374. Translated from Zhurnal Tekhnicheskoĭ Fiziki, Vol. 71, No. 4, 2001, pp. 6–12.

Hydrogen Atom in Quantum Mechanics and Quantization on Curved Surfaces

A. G. Chirkov and A. Ya. Berdnikov

St. Petersburg State Technical University,
ul. Politekhnicheskaya 29, St. Petersburg, 195251 Russia

Received June 20, 2000

Abstract—New quantization rules for classical systems are obtained using the Titchmarsh expansion. These rules generalize the conventional ones and are reduced to them when a transition to Cartesian coordinates exists. An equation generalizing the Schrödinger equation to arbitrary natural systems is found. The principle of minimal constraint (strong equivalence principle) makes it possible to extend this equation to any curved spaces. *© 2001 MAIK "Nauka/Interperiodica".*

In [1], Steklov formulates the basic tasks of mathematical physics as follows:

> After appropriate generalization, in terms of pure analysis, the physical problem of body cooling results in two problems of major importance: (A) the problem of integrating a linear differential equation with appropriate boundary conditions (finding eigenfunctions or fundamental functions as well as eigenvalues or characteristic values) and (B) the problem of expanding arbitrary functions into convergent series in terms of eigenfunctions.

In physical literature, most attention is customarily given to problem A, whereas problem B is not practically discussed. For instance, an explicit form of the expansion in terms of eigenfunctions for the problem of a hydrogen atom is presented only in [2, 3], although problem B is of no less importance than problem A for perturbation theory.

There exist three methods to solve problem B. The first is provided by the general spectral theory of linear self-adjoint operators in the Hilbert space (see, e.g., [4, 5]). The second is offered by methods of the theory of integral equations, the beginning of which was made by Weyl. Another (albeit rather close) approach to expansion theorems was proposed by Titchmarsh [6]. In this work, the expansions are proved on the basis of the residue theory and contour integration. Thus, this method makes it possible to avoid invoking both the theory of integral equations and the general theory of linear operators. The last fact is of particular importance, since physicists do not usually distinguish self-adjoint and symmetric operators. This simultaneously leads to two problems: first, the domain of an operator in the Hilbert space remains ambiguous that prevents using methods of the spectral theory; second, all functions, for which analytical operations involved in the operator expression make sense, are included in the domain of the operator irrespective of the fact whether these functions (and the result of applying the operator to them) are included in the Hilbert space [7]. A rigorous consideration of the latter case requires introducing a concept of the framed Hilbert space [8].

Besides that, the physics guides often state that each self-adjoint operator possesses a complete orthogonal system (basis set) of eigenvectors. This is the case for compact self-adjoint operators, but the Hamiltonian is never compact. Other general criteria for existence of the basis can hardly be formulated, however, the Hamiltonian sometimes has the basis (harmonic oscillator). This particular case is presumably the only interesting example in which the above-mentioned principle is valid; generally, operators have continuous spectrum as well. As a result of such intuitive operations, generally speaking, the expansion formula in the well-known problem of hydrogen atom [2, 3] turns out to be incorrect.

The Titchmarsh approach makes it possible to avoid all of the above-mentioned difficulties by developing an expansion in terms of normalized eigenfunctions using only the methods of mathematical analysis. Moreover, as it will be clear from what follows, this technique is quite accessible. Since the Titchmarsh method is poorly known, we present the main points of his theory that are needed for developing the expansion in the quantum-mechanical problem of hydrogen atom.

On the basis of these results, the new quantization rules for classical systems are obtained. These rules generalize the conventional ones and turn to them in the case when a transition to Cartesian coordinates exists.

The term "quantization" appeared in physical literature in the twentieth and from the very beginning has had two meanings. First, this is discretization of the range of a physical variable; second, the construction of the Hamiltonian $\hat{H}(\hat{p}, \hat{q}, t)$ from the *c*-number Hamiltonian function $H(p, q, t)$ for a classical mechanical sys-

1063-7842/01/4604-0368$21.00

tem, where $\hat{p}$ and $\hat{q}$ are the operators corresponding to classical canonical variables. In this paper, the term "quantization" is used in the latter meaning.

The traditional Weyl–Heisenberg quantization method is applied only to classical systems with a plane phase space and only in Cartesian coordinates [14]. In the general case, the quantization problem is nontrivial and ambiguous.

THE TITCHMARSH METHOD

Consider a function $y = y(x)$ satisfying the equation

$$\frac{d^2y}{dx^2} + \{\lambda - q(x)\}y = 0, \tag{1}$$

and some boundary conditions [6], where $q(x)$ is the given function of x that is defined on an interval (a, b).

In applications, the function $q(x)$ often has a singularity either at one or at both interval boundaries, or the interval extends to infinity either in one or in both directions. These are so-called singular problems.

Let us consider the case in which the interval is the real semiaxis $(0, \infty)$ and the function $q(x)$ is continuous in each finite interval. We assume that $\varphi(x) = \varphi(x, \lambda)$ and $\theta(x) = \theta(x, \lambda)$ are solutions of (1) with the Wronskian $W_x(\varphi, \theta) = W_0(\varphi, \theta) = 1$. Then, for arbitrary real λ, Eq. (1) has the solution

$$\psi(x, \lambda) = \theta(x, \lambda) + m(\lambda)\varphi(x, \lambda), \tag{2}$$

from $L^2(0, \infty)$. The function $m(\lambda)$ is referred to as the Weyl–Titchmarsh function, which is considered to have the following properties: $m(\lambda)$ is an analytic function of λ that is regular in the upper half-plane and $\mathrm{Im}\, m(\lambda) < 0$ [6]. In this case, if two linearly independent solutions $\varphi_1(x, \lambda)$ and $\varphi_2(x, \lambda)$ with the Wronskian $\omega(\lambda) = W[\varphi_1, \varphi_2] \neq 0$ are known, the required result is obtained by dividing by $\omega(\lambda)$. Let $f(y) \in L^2(0, \infty)$ and

$$\Phi(x, \lambda) = \psi(x, \lambda)\int_0^x \varphi(y, \lambda) f(y)dy + \varphi(x, \lambda)\int_x^\infty \psi(y, \lambda) f(y)dy, \tag{3}$$

where φ and ψ are the above-defined functions.

Then, for any x, the function $\Phi(x, \lambda)$ is analytic with respect to λ and is regular either at $\mathrm{Im}\, m(\lambda) > 0$ or $\mathrm{Im}\, m(\lambda) < 0$. In this case, when $\varphi_1(x, \lambda)$ and $\varphi_2(x, \lambda)$ with the Wronskian $\omega(\lambda) = W[\varphi_1, \varphi_2]$ are known, the corresponding expression for $\Phi(x, \lambda)$ has the form

$$\Phi(x, \lambda) = \frac{\varphi_2(x)}{\omega(\lambda)}\int_0^x \varphi_1(y) f(y)dy + \frac{\varphi_1(x)}{\omega(\lambda)}\int_x^\infty \varphi_2(y) f(y)dy. \tag{3a}$$

The function $\Phi(x, \lambda)$ is evidently expressed in terms of the Green function $G(x, y, \lambda)$

$$G(x, y, \lambda) = \begin{cases} \psi(x, \lambda)\varphi(y, \lambda), & y \le x \\ \varphi(x, \lambda)\psi(y, \lambda), & y > x \end{cases} \tag{4}$$

by the following relation:

$$\Phi(x, \lambda) = \int_0^\infty G(x, y, \lambda) f(y)dy. \tag{5}$$

The general form of the Titchmarsh expansion is given by

$$f(x) = \lim_{\substack{R \to \infty \\ \delta \to 0}} \left\{ -\frac{1}{i\pi}\int_{-R + i\delta}^{R + i\delta} \Phi(x, \lambda)d\lambda \right\}. \tag{6}$$

It can be proved [6] that

$$\lim_{\delta \to 0}\int_0^\lambda \{-\mathrm{Im}\, m(k + i\delta)\}dk = k(\lambda), \tag{7}$$

where $k(\lambda)$ is a nondecreasing function of λ.

In view of this fact, we formally obtain that at $R \longrightarrow \infty$ and $\delta \longrightarrow 0$

$$\mathrm{Im}\left[-\frac{1}{\pi}\int_{-R + i\delta}^{R + i\delta} \Phi(x, \lambda)d\lambda \right] \longrightarrow \frac{1}{\pi}\int_{-\infty}^{+\infty} \phi(x, \lambda)dk(\lambda) \times \int_0^\infty \varphi(y, \lambda) f(y)dy. \tag{8}$$

Particularly, this yields the fact that the expansion involves the Stieltjes integrals. Thus,

$$f(x) = \frac{1}{\pi}\int_{-\infty}^{+\infty} \varphi(x, \lambda)dk(\lambda)\int_0^\infty \varphi(y, \lambda) f(y)dy. \tag{9}$$

If one considers

$$g(\lambda) = \int_0^\infty \varphi(y, \lambda) f(y)dy, \tag{10}$$

formula (9) takes the form

$$f(x) = \frac{1}{\pi}\int_{-\infty}^{+\infty}\varphi(x,\lambda)g(\lambda)dk(\lambda). \quad (11)$$

Further,

$$\int_0^{\infty}\{f(x)\}^2dx = \frac{1}{\pi}\int_{-\infty}^{+\infty}\{g(\lambda)\}^2dk(\lambda). \quad (12)$$

This is the so-called Parseval equality. In the case of the interval $(0, \infty)$, the spectrum may be defined as the set of points λ forming the complement of the set of points in the neighborhood of which the function $k(\lambda)$ is constant. If $m(\lambda)$ is a meromorphic function, the spectrum coincides with the set of its poles (point spectrum). The interval where $k(\lambda)$ increases at each point belongs to continuous spectrum.

Let us consider a point spectrum, i.e., the only singularities of $m(\lambda)$ are the poles at $\lambda_0, \lambda_1, \ldots$ and $r_0, r_1, \ldots$ are the corresponding residues. Then, the functions

$$\psi_n(x) = \sqrt{r_n}\varphi(x,\lambda_n) \quad (13)$$

form the orthonormal system [6].

HYDROGEN ATOM

Consider

$$q(r) = \frac{l(l+1)}{r^2} - \frac{2}{r}, \quad 0 < r < \infty, \quad (14)$$

where l is a positive integer or zero.

The corresponding Eq. (1) has the form

$$\frac{d^2y}{dr^2} + \left\{\varepsilon + \frac{2}{r} - \frac{l(l+1)}{r^2}\right\}y = 0. \quad (15)$$

Here, r is the dimensionless variable that is equal to the ratio of corresponding dimensional variable to $a_0 = \hbar^2/mc^2$ and $\lambda = \varepsilon = 2E\hbar^2/mc^4$. Equation (15) results from the equation for the radial wave function $R(r)$ of the relative motion by the substitution $y = rR$. Putting $y = r^{-l}Y$ and $\varepsilon = s^2$, we arrive at the equation

$$Y'' - \frac{2l}{r}Y' + \left(s^2 + \frac{2}{r}\right)Y = 0. \quad (16)$$

Using the Laplace method [9] to find the solution, we obtain

$$\varphi_1(r,\varepsilon) = r^{-l}\oint_C (z+is)^{k-l-1}(z-is)^{-k-l-1}e^{rz}dz, \quad (17)$$

where C is the closed contour enclosing the points is and $-is$, $\arg(z+is)$ and $\arg(z-is)$ vary from $-\pi$ to π in tracing the contour, $k = i/s$, and

$$\varphi_2(x,\varepsilon) = r^{-l}\int_{-\infty}^{(is+)}(z+is)^{k-l-1}(z-is)^{-k-l-1}e^{rz}dz, \quad (18)$$

where the loop encloses the point is and does not contain $-is$. Here $\arg(z-is)$ varies from $-\pi$ to π and $\arg(z+is)$ varies from π to π for s from the first quadrant. According to Whittaker and Watson [9], we have

$$\varphi_2(r,\varepsilon) = \frac{2\pi i e^{i\pi k}}{\Gamma(k+l+1)}(2is)^{-l-1}W_{k-l-\frac{1}{2}}(-2isr). \quad (19)$$

Evaluating $\omega(\varepsilon) = r^{-2l}W[I_1, I_2]$, where I_1 and I_2 denote the integrals in (17) and (18), we obtain

$$\omega(\varepsilon) = \frac{-2\pi i(2is)^{-2l-1}(1-e^{2i\pi k})}{\Gamma(l-k+1)}\Gamma(-l-k). \quad (20)$$

Consider the function

$$\Phi(x,\varepsilon) = \frac{\varphi_2(r)}{\omega(\varepsilon)}\int_0^r\varphi_1(z)f(z)dz + \frac{\varphi_1(r)}{\omega(\varepsilon)}\int_r^{\infty}\varphi_2(z)f(z)dz. \quad (21)$$

This function has poles at the zeros of the function $\omega(\varepsilon)$, i.e., at the points

$$k_n = n_r + l + 1; \quad n_r = 0, 1, 2, \ldots \quad (22)$$

or

$$\varepsilon = \varepsilon_n = -\frac{1}{(n_r+l+1)^2} = -\frac{1}{n^2}, \quad (23)$$

where n_r is the radial quantum number and n is the principal quantum number.

Then,

$$\omega'(\varepsilon_n) = -\frac{8\pi^2(n_r)!}{(n_r+2l+1)!}\frac{(n_r+l+1)^{2l+4}}{2^{2l+3}}. \quad (24)$$

At $\varepsilon = \varepsilon_n$ we have

$$\varphi_1(r,\varepsilon_n) = \varphi_2(r,\varepsilon_n) = r^{l+1}e^{-\frac{r}{n}}\frac{2\pi i(n_r)!}{[(n+l)!]^2}L_{n+l}^{2l+1}\left(\frac{2r}{n}\right), \quad (25)$$

where L_p^m are the associated Legendre polynomials.

Therefore, the residue of $\Phi(x, \varepsilon)$ at $\varepsilon = \varepsilon_n$

$$\frac{2^{2l+2}(n_r)!}{[(n+1)!]^3 n^{2l+4}} r^{l+1} e^{-\frac{r}{n}} L_{n+l}^{2l+1}\left(\frac{2r}{n}\right) \times \int_0^\infty z^{l+1} e^{-\frac{z}{n}} L_{n+l}^{2l+1}\left(\frac{2z}{n}\right) f(z)\,dz. \tag{26}$$

The sum of such terms yields the part of the expansion which corresponds to negative points of the spectrum [6]. From (26), we find the orthonormal system of functions that is the basis for the expansion:

$$\psi_{nl}(r, \varepsilon_n) = \frac{2^{l+1}}{n^{l+2}} \frac{[(n_r)!]^{1/2}}{[(n+l)!]^{3/2}} \times r^{l+1} e^{-\frac{r}{n}} L_{n+l}^{2l+1}\left(\frac{2r}{n}\right) = rR_{nl}, \tag{27}$$

where R_{nl} are the radial functions of the discrete spectrum in the problem of hydrogen atom [2, 3].

Let us represent $\varphi_1(r, \varepsilon)$ in the form

$$\varphi_1(r, \varepsilon) = r^{-l} \int_{-\infty}^{(-is+)} (z+is)^{k-l-1}(z-is)^{-k-l-1} e^{rz}\,dz + r^{-l} \int_{-\infty}^{(is+)} (z+is)^{k-l-1}(z-is)^{-k-l-1} e^{rz}\,dz, \tag{28}$$

where in the first integral $\arg(z + is)$ varies from $-\pi$ to π and $\arg(z - is)$, from $-\pi$ to $-\pi$; in the second integral $\arg(z + is)$ varies from π to π and $\arg(z - is)$, from $-\pi$ to π. Hence, the second term in (28) coincides with $\varphi_2(x, \varepsilon)$.

It should be noted that at $\varepsilon = \varepsilon_n$, the first integral in (28) has no singularity and vanishes. Therefore, it is impossible to find the wave functions of a continuous spectrum by substituting the complex values of ε into the functions of discrete spectrum [2, 10]. Note that the normalization integral, e.g., in [10], is calculated for the total function (28). Increasing the args in the addend in (28) by π, we get

$$\varphi_1(r, \varepsilon) = \varphi_2(r, \varepsilon) + e^{2\pi i k} \varphi_2(r, \varepsilon) \tag{29}$$

in contrast to relation (25), where $\varphi_1(r, \varepsilon) = \varphi_2(r, \varepsilon)$ and, hence,

$$\omega(\varepsilon e^{2\pi i}) = -e^{-2\pi i k} \omega(\varepsilon). \tag{30}$$

Then, for positive real ε

$$\frac{\varphi_2(r, \varepsilon)}{\omega(\varepsilon)} - \frac{\varphi_2(r, \varepsilon e^{2\pi i})}{\omega(\varepsilon e^{2\pi i})} = \frac{\varphi_1(r, \varepsilon)}{\omega(\varepsilon)}. \tag{31}$$

Therefore,

$$\mathrm{Im}\Phi(x, \varepsilon) = \frac{\varphi_1(r, \varepsilon)}{2i\omega(\varepsilon)} \int_0^\infty \varphi_1(z, \varepsilon) f(z)\,dz, \tag{32}$$

where

$$i\omega(\varepsilon) = 2\pi(2s)^{-2l-1}\left(1 - e^{-\frac{2\pi}{s}}\right)\left[\prod_{m=1}^{l}(m^2 + 1/s^2)\right]^{-1}. \tag{32a}$$

Thus, the part of the expansion that corresponds to continuous spectrum is given by

$$\frac{1}{4\pi^2} \int_0^\infty \frac{\prod_{m=1}^{l}(m^2 + 1/s^2)(2s)^{2l+1}}{[1 - \exp(-2\pi/s)]s} \varphi_1(r, s^2)\,ds^2 \times \int_0^\infty \varphi_1(z, s^2) f(z)\,dz. \tag{33}$$

From (33) it follows that normalized eigenfunctions, which are the basis for the expansion, have the form

$$\psi_l(r, s^2) = r \frac{\sqrt{2}}{[1 - \exp(-2\pi/s)]^{1/2}} \times \prod_{m=1}^{l}(m^2 + 1/s^2)^{1/2} (2|s|r)^l e^{isr} \times F(-i/s + l + 1;\ 2l + 2;\ -2isr), \tag{34}$$

where $F(\alpha, \beta, \gamma)$ is the confluent hypergeometric function.

The function (34) differs from the radial wave functions of continuous spectrum in the problem of hydrogen atom [10] by a factor of r.

Finally, the expansion for a function $f(r) \in L^2([0, \infty); dr)$ has the form

$$f(r) = \sum_{n=0}^{\infty} a_{nl} \psi_{nl}(r, \varepsilon) + \int_0^\infty a_l(s^2) \psi_l(r, s^2)\,ds^2 \tag{35}$$

and the coefficients are given by

$$a_{nl} = \int_0^\infty f(r) \overline{\psi_{nl}}(r, \varepsilon)\,dr, \qquad a_l(s^2) = \int_0^\infty f(r) \overline{\psi_l}(r, s^2)\,dr, \tag{36}$$

where the bar denotes complex conjugation.

In the same way one may find [6] that the expansion for a function $g(\vartheta, \varphi) \in L^2(S^2; d\vartheta; d\varphi)$, where ϑ and φ are the angular coordinates on the sphere surface, has the form

$$g(\vartheta, \varphi) = \sum_{l=0}^{\infty} \sum_{m=-l}^{+l} b_{lm} \Theta_{lm}(\vartheta, \varphi), \tag{37}$$

$$\Theta_{lm}(\vartheta, \varphi) = \sqrt{\sin\vartheta}\, Y_{lm}(\vartheta, \varphi), \tag{38}$$

where $Y_{lm}(\vartheta, \varphi)$ are the spherical harmonics [11] and the coefficients b_{lm} are given by

$$b_{lm} = \int_0^{\pi} \int_0^{2\pi} g(\vartheta, \varphi) \overline{\Theta_{lm}}(\vartheta, \varphi) d\vartheta d\varphi. \tag{39}$$

The function Θ_{lm} differs from the traditionally used by the factor $\sqrt{\sin\vartheta}$. The conventional expansion has the form (see, e.g., [3, p. 42])

$$F(r, \vartheta, \varphi) = \sum_{l, m} Y_{lm}(\vartheta, \varphi) \times \left\{ \sum_n C_{nlm} R_{nl}(r) + \int_0^{\infty} C_{slm} R_{sl}(r) ds^2 \right\}, \tag{40}$$

where the coefficients of the expansion are given by the formulas

$$C_{nlm} = \int_0^{\infty} r^2 dr \int_0^{\pi} \int_0^{2\pi} F(r, \vartheta, \varphi) R_{nl}(r) Y^*_{lm}(\vartheta, \varphi) \sin\vartheta d\vartheta d\varphi,$$
$$C_{slm} = \int_0^{\infty} r^2 dr \int_0^{\pi} \int_0^{2\pi} F(r, \vartheta, \varphi) R_{sl}(r) Y^*_{lm}(\vartheta, \varphi) \sin\vartheta d\vartheta d\varphi. \tag{41}$$

An evident difference between the Titchmarsh and Bethe–Salpeter expansions lies in the fact that in the former one the Jacobian of the transform is shared symmetrically between the expansion functions, whereas in the latter case it is involved as a whole only in the expression for the coefficients. Actually, the expansions (40) and (41) result from the Titchmarsh expansion if one takes into account that its functions form complete orthonormal system in the space $L^2([0, \infty); dr) \otimes L^2(S^2; d\vartheta, d\varphi)$ and the standard functions, in $L^2(R^3; dxdydz) = L^2(R^3; r^2 \sin\vartheta dr d\vartheta d\varphi)$. In its turn, this difference leads to the fact that the solution of the Srödinger equation $\psi(r, \vartheta, \varphi)$ in the spherical coordinates does not have the meaning of the probability density, whereas the Titchmarsh functions have, since, e.g., the radial-coordinate distribution $w(r) = r^2 R_{nl}^2 = \psi_{nl}^2$. The last fact is the trivial consequence of the general theorems of the probability theory about the convertion of the probability density to curvilinear coordinates [12].

QUANTIZATION OF NATURAL SYSTEMS

The quantization problem is to construct the Hamiltonian $\hat{H}(\hat{p}, \hat{q}, t)$ on the basis of *c*-number Hamiltonian function of a classical problem, which is assumed to be given. This procedure is nontrivial and ambiguous especially in curvilinear and generalized coordinates, since there are a number of ways to choose the form of the operator $\hat{p}$ and the sequence of the operators $\hat{q}$ and $\hat{p}$ in $\hat{H}(\hat{p}, \hat{q}, t)$ [13, 14].

Let us consider a natural mechanical system, namely, the triple (M, T, V), where M is a smooth manifold (position space), T is the Riemann metric on M (positive-definite quadratic form, kinetic energy), and V is a smooth function on M (potential of force field) [15]. The motion of such a system is smooth mappings $\hat{q}: R^1 \longrightarrow M$ that are the extremals of the action functional with the Lagrangian function $L = T - V$. In the local coordinates the Lagrangian function is given by

$$L = \frac{1}{2} g_{ik} \dot{q}^i \dot{q}^k - V(q), \tag{42}$$

so that the Hamiltonian function corresponding to (42) is equal to

$$H = \frac{1}{2} g^{ik} \pi_i \pi_k + V(q), \tag{43}$$

where $\pi_i = g_{ik} \dot{q}^k$ is the generalized momentum.

The local coordinates q^i and π_i are canonical on the cotangent bundle T^*M of the smooth manifold M. In the case of nontrivial values $g_{ik} \neq \delta_{ik}$, the traditional quantization procedure becomes essentially ambiguous. However, the above-stated results allow making this procedure quite certain. Indeed, the conventional method to solve quantum problems in curvilinear coordinates is as follows. First, the quantization of the classical system is performed in Cartesian coordinates. As a result, the kinetic energy $T = (p_x^2 + p_y^2 + p_z^2)/2m$ (in the Srödinger coordinate representation) is associated with the operator $\hat{T} = -\hbar^2 \Delta/2m$ is the Laplace–Beltrami operator, which is defined on the tangent bundle of the smooth manifold M), and then, the conversion to the curvilinear coordinates q is performed. As it has been noted in the previous section, the resulting wave function $\psi(q) = \psi(x(q))$ (x is the set of Cartesian coordinates) is not the probability amplitude and, hence, does not describe any physical states.

Allowing for the Titchmarsh expansion, one can straightforwardly derive the equation for the probability amplitude $\tilde{\psi}(\dot{q})$ on the basis of the above-stated procedure. It is clear that the Titchmarsh functions $\tilde{\psi}(q)$ and $\psi(q)$ are related to each other by equation

$\tilde{\psi}(q) = g^{1/4}\psi(x(q))$, where $g = \det|g_{ik}|$. In doing so, we arrive at the equation for $\tilde{\psi}(q)$

$$\left[\left(g^{-1/4}\frac{\partial}{\partial q^i}g^{1/4}\right)g^{ik}\left(g^{1/4}\frac{\partial}{\partial q^k}g^{-1/4}\right)\tilde{\psi} + \frac{2m}{\hbar^2}[E - V(q)]\right]\tilde{\psi} = 0 \quad (44)$$

or

$$\tilde{\Delta}\tilde{\psi}(q) + \frac{2m}{\hbar^2}[E - V(q)]\tilde{\psi}(q) = 0, \quad (45)$$

where $\tilde{\Delta} = g^{1/4}\Delta g^{-1/4}$.

The symmetry (self-adjointness) of the operator $\tilde{\Delta}$ with respect to the scalar product $(\tilde{\varphi}, \tilde{\psi}) = \int \bar{\tilde{\psi}}(q)\tilde{\psi}(q)dq$ (the bar denotes complex conjugation and $dq = dq^1 \ldots dq^n$) is evident from the equation sequence $(\tilde{\Delta}\tilde{\varphi}, \tilde{\psi}) = (\Delta\varphi, \psi) = (\varphi, \Delta\psi) = (\tilde{\varphi}, \tilde{\Delta}\tilde{\psi})$. Let us introduce the operators of generalized-momentum projections

$$\hat{\pi}_i = -i\hbar g^{-1/4}\frac{\partial}{\partial q^i}g^{1/4},$$

satisfying the commutation relations $[\hat{\pi}_l, q^i] = -i\hbar\delta^i_l$ and $[\pi_i, \pi_k] = 0$. In this case the adjoint operator

$$\hat{\pi}^*_i = +i\hbar g^{+1/4}\frac{\partial}{\partial q^i}g^{-1/4},$$

so that the kinetic-energy operator $T = -\hbar^2\pi\pi^*/2m$.

The commutation relations $[\hat{\pi}_l, q^i] = -i\hbar\delta^i_l$, $[\pi_i, \pi_k] = 0$, and $[q^i, q^k] = 0$ are algebraically identical to the customary Heisenberg commutation relations. However, the operators $\hat{\pi}_i$ and q^k define the representation that is unitarily nonequivalent to the Schrödinger representation. The Neumann–Stone unicity theorems [16] are invalid in this case, since the operators $\hat{\pi}_i$ are not symmetric.

The generalized momentum operator corresponding to the radial coordinate (radial momentum operator) has the form $\hat{\pi}_r = \partial/\partial r + (n - 1)/2r$, where n is the dimension of the manifold M with the domain of definition $D(\hat{\pi}_r) = \{y \in L^2((0, \infty), dr); (\psi' + (n - 1)/2r) \in L^2((0, \infty), dr)\}$. This result coincides with relation (7.8.2) in [17], where the form of the radial momentum operator is postulated. It is of interest that only for $n = 3$ does the squared radial momentum operator coincide with the r-dependent term in the Laplace–Beltrami operator multiplied by $(-\hbar^2)$.

Equation (45) involves opportunities for generalizations. Indeed, from the standpoint of the theory of manifolds even the plane space is by no means simple, i.e., it has much more rich structure compared to the ordinary differentiable manifold, since the affine connection is defined on it. In the Cartesian coordinate system this connection does not manifest itself, since the Cristoffel symbols are equal to zero. However, if the physical laws are formulated in plane space in term of curvilinear coordinates, the connection becomes observable. The Cristoffel symbols rather than Riemann tensor appear in most of laws represented in such a way. Hence, the equations have the same form irrespective of the fact whether the manifold is plane or curved. Thus, it is natural to assume that the form of the Schrödinger equation (45) for the curved manifolds in which there are no global Cartesian coordinates system, is the same as in the curvilinear coordinates in plane manifold. This postulate is an analog of the principle of minimal constraint in the general relativity [18].

Moreover, using the methods developed by Goncharov (see, e.g., [19, 20]), it is possible to generalize Eq. (45) to manifolds with nontrivial topology.

The problem of quantization of natural systems (quantization of a classical system defined on a curved configurational space) was announced even in the first Schrödinger paper, however, the solution was represented only in Cartesian coordinates.

A wide discussion of quantum theory on the Riemann manifolds in mathematical papers began as soon as the modern quantum mechanics was developed [21, 22]. The expression for the generalized integral found in this paper coincides with those obtained in the WKB approximation in [23]. The exact Schrödinger operator has the form $-\hbar^2/2m(\Delta - \alpha R)$, where Δ is the Laplace–Beltrami operator, R is the scalar curvature, and $\alpha = 1/3$. The value of the constant α essentially depends on the chosen quantization procedure: in the Liu–Qian method [24] $\alpha = 1/8$; Underhill [25] found $\alpha = 1/2$; and in the approach of geometric quantization [26], $\alpha = 1/6$. Woodhouse [27], Wu [28], and Emmrich [29] obtained a value of $\alpha = 0$.

All of the mentioned Schrödinger operators in the plane space in curvilinear coordinates are reduced to the Laplace–Beltrami operator ($R = 0$). At the same time, as it is clear from the Titchmarsh results and Eq. (44), in this case there is nonzero correction to the Laplacian, which turns to zero only in Cartesian coordinate system. Note that, unlike this paper, where Eq. (44) has been simply derived from the physical meaning of the wave function as a probability amplitude, all of the above-mentioned papers are purely mathematical and rather complicated.

REFERENCES

1. V. A. Steklov, *Fundamental Problems of Mathematical Physics* (Nauka, Moscow, 1983).

2. H. A. Bethe and E. E. Salpeter, *Quantum Mechanics of One- and Two-Electron Atoms* (Academic, New York, 1957; Fizmatgiz, Moscow, 1960).
3. V. A. Fock, *The Principles of Quantum Mechanics* (Nauka, Moscow, 1976; Mir, Moscow, 1978).
4. N. Dunford and J. T. Schwartz, *Linear Operators* (Interscience, New York, 1963; Mir, Moscow, 1966), Vol. 2.
5. T. Kato, *Perturbation Theory for Linear Operators* (Springer-Verlag, Berlin, 1966; Mir, Moscow, 1972).
6. E. C. Titchmarsh, *Eigenfunction Expansions Associated with Second-Order Differential Equations* (Clarendon, Oxford, 1946; Inostrannaya Literatura, Moscow, 1960), Vol. 1.
7. V. V. Batygin and A. V. Bukhvalov, *Probabalistic Principles of Quantum Mechanics. Hilbert Space as State Space* (Leningr. Politekh. Inst. im. M.I. Kalinina, Leningrad, 1982).
8. F. A. Berezin and M. A. Shubin, *The Schrödinger Equation* (Mosk. Gos. Univ., Moscow, 1983; Kluwer, Dordrecht, 1991).
9. E. T. Whittaker and G. N. Watson, *A Course of Modern Analysis* (Cambridge Univ. Press, Cambridge, 1952; Fizmatgiz, Moscow, 1963), Vol. 2.
10. L. D. Landau and E. M. Lifshitz, *Course of Theoretical Physics*, Vol. 3: *Quantum Mechanics: Non-Relativistic Theory* (Fizmatgiz, Moscow, 1963; Pergamon, New York, 1977).
11. N. N. Lebedev, *Special Functions and Their Applicatiors* (Fizmatgiz, Moscow, 1963; Prentice Hall, Englewood Cliffs, 1965).
12. W. Feller, *An Introduction to Probability Theory and Its Applications* (Wiley, New York, 1971; Mir, Moscow, 1985), Vol. 2.
13. G. G. Emch, *Algebraic Methods in Statistical Mechanics and Quantum Field Theory* (Wiley, New York, 1972; Mir, Moscow, 1976).
14. F. A. Berezin, Izv. Akad. Nauk SSSR, Ser. Mat. **38** (5), 1116 (1974).
15. V. V. Kozlov, *Symmetry, Topology, and Resonance in Quantum Mechanics* (Udmurts. Gos. Univ., 1995).
16. N. Hurt, *Geometric Quantization in Action* (Reidel, Dordrecht, 1983; Mir, Moscow, 1985).
17. R. D. Richtmyer, *Principles of Advanced Mathematical Physics* (Springer-Verlag, New York, 1978; Mir, Moscow, 1982), Vol. 2.
18. B. F. Schutz, *Geometrical Methods of Mathematical Physics* (Cambridge Univ. Press, Cambridge, 1980; Mir, Moscow, 1984).
19. Yu. Goncharov, Mod. Phys. Lett. A **9** (34), 3175 (1994).
20. Yu. Goncharov, Phys. Lett. B **398**, 32 (1997).
21. J. S. Dokew, *Functional Integration and Its Application*, Ed. by A. M. Arthur (Clarendon, Oxford, 1974), pp. 34–52.
22. N. P. Landsman, *Mathematical Topics between Classical and Quantum Mechanics* (Springer-Verlag, New York, 1998).
23. N. P. Landsman, J. Geom. Phys. **12** (2), 93 (1993).
24. Z.-J. Liu and M. Qian, Trans. Am. Math. Soc. **331**, 321 (1992).
25. J. Underhill, J. Math. Phys. **19**, 1932 (1978).
26. J. Smatyki, *Geometric Quantization and Quantum Mechanics* (Springer-Verlag, Berlin, 1980).
27. N. M. J. Woodhouse, *Geometric Quantization* (Clarendon, Oxford, 1992).
28. Y. Wu, J. Math. Phys. **39**, 867 (1998).
29. C. Emmrich, Commun. Math. Phys. **151**, 515 (1993).

Translated by M. Fofanov

Technical Physics, Vol. 46, No. 4, 2001, pp. 375–385. Translated from Zhurnal Tekhnicheskoĭ Fiziki, Vol. 71, No. 4, 2001, pp. 13–22.

ATOMS, SPECTRA, RADIATION

Elastic Scattering of Slow Electrons by Calcium Atoms into an Angular Range Depending on the Collision Energy

E. Yu. Remeta, O. B. Shpenik, and Yu. Yu. Bilak

Institute of Electronic Physics, National Academy of Sciences of Ukraine, Uzhgorod, 88000 Ukraine

e-mail: remeta@iep.uzhgorod.ua

Received March 2, 2000; in final form, July 17, 2000

Abstract—The use of trochoidal and hypocycloidal spectrometers that are applied in modern experimental techniques for studying processes of electron scattering by atoms, ions, and surfaces is considered in some detail. The angular range of the collection of scattered electrons is determined by the operation mode of the spectrometer and depends on the collision energy. To analyze the structure of the measured energy dependence $S(E)$, an analytical formalism reflecting both resonance and nonresonance features of low-energy scattering was used. A theoretical analysis of elastic scattering of slow (to 2 eV) electrons by Ca atoms permitted the interpretation of the observed structure of $S(E)$ as a manifestation of the ^2D shape resonance. A comparison of the theoretical values of the $S(E)$ function with the total and differential scattering cross sections was performed. © *2001 MAIK "Nauka/Interperiodica".*

INTRODUCTION

Of special interest in electron–atom collisions is the range of low energies, at which resonances can arise. However, there are certain difficulties in studying scattering of slow electrons (to 5 eV), such as those related to the divergence of the electron beam under the effect of the space charge or the dependence of the transmission of the analyzer on the energy of scattered electrons. These difficulties can partially be eliminated by using a longitudinal uniform magnetic field and a trochoidal electron spectrometer (TES) and almost fully eliminated by the use of a spectrometer modification that was called hypocycloidal.

A hypocycloidal electron spectrometer (HES) makes it possible to measure the energy dependence $S(E)$ of electron scattering into an angular range that depends on the energy E. This function reflects various features of a concrete experimental setup, regimes of its operation, and the information on the processes of collisions themselves. Therefore, it is very important to study its analytic form, for this permits one to separate the dynamic features of scattering (related to phases) from kinematic ones (related to angles).

For the first time, the $S(E)$ function was measured in [1, 2] and numerically calculated in [2–4] for the case of elastic scattering of slow electrons by Ca atoms. However, neither its analytic form nor its behavior as determined by its constituent parts have been studied in detail in [2–4].

In recent years, the spectrometers of the new type (TES and HES) are also used for experiments on the elastic backscattering of electrons by ions [5–7] and by thin films [8–10] (see also the review [11]); therefore, the analysis of the $S(E)$ function is of great importance. The main problem in the theoretical description of electron–atom scattering at low energies is the allowance for the polarizability of the electron shells of the atoms of the target, i.e., taking into account the distortion of the atomic potential under the effect of an incident electron. At low energies, when only a few channels are operative, a sufficiently correct allowance is only possible in terms of the method of strong coupling of various channels. However, in many cases it is difficult to do this in terms of this method or its modifications even at low energies. The second possibility of taking into account the polarizability is based on the optical-potential approximation (see [3, 4] and references therein). However the direct calculation of the optical potential is as difficult as the exact solution of the scattering problem. Therefore, various approximate methods (e.g., theory of perturbation in electron–electron interaction) or phenomenological models are employed to determine optical potential. In recent years, there appeared numerous works on the calculation of electron–atom collisions using a model optical potential, in which both complex and real potentials were used [3, 4]. An important part of a model optical potential is the polarization potential. For alkaline-earth elements, its role is large, since the polarizability of these atoms is relatively large ($\alpha \sim 70$–270 au).

The scattering of low-energy electrons by Ca atoms has been considered in a number of theoretical works. Fabrikant [12] used the method of strong coupling of two and three states (4^1S–4^1P–4^3P) and obtained an energy $E_1^r \approx 1.76$ eV for the ^2P resonance. McCurdy *et al.* [13] used the self-consistent field method for calculating the energies E_l^r and widths Γ_l of the ^2P and ^2D

1063-7842/01/4604-0375$21.00

shape resonances and obtained $E_1^r = 0.225$ eV ($\Gamma_1 = 0.162$ eV) and $E_2^r = 2.28$ eV ($\Gamma_2 = 0.335$ eV).

Amus'ya *et al.* [14, 15] calculated the energy dependence of the integrated cross section of elastic electron scattering by Ca atoms in a range of $E < 4$ eV in terms of the random-phase approximation with exchange. They obtained two cross-section maxima, which were caused by *p* and *d* waves (they were interpreted as shape resonances). Their parameters are as follows: $E_1^r = 0.27$ eV ($\Gamma_1 = 0.14$ eV) and $E_2^r = 1.25$ eV ($\Gamma_2 = 0.78$ eV). However, the first maximum was not observed in experiment in [16]. In terms of the same approximation, Gribakin *et al.* [17] investigated the elastic electron scattering by Ca, Sr, and Ba atoms. In [3, 4], it was shown that scattering occurred through the ^2D shape resonance. The parameters of this resonance are $E_2^r = 1.44$ eV ($\Gamma_2 = 1.4$ eV) for Ca, 0.87 eV (0.88 eV) for Sr, and 0.21 eV (0.03 eV) for Ba.

Kelemen *et al.* [18, 19] used a complex energy-dependent optical potential to describe the elastic and inelastic scattering of electrons by Be, Mg, Ca, and Sr atoms at energies 0–40 eV. In low-energy scattering, *P* and *D* shape resonances were obtained. The existence of a *P* shape resonance in electron–calcium elastic scattering was also predicted earlier [20]. It is these *P* resonances that were identified with the low-energy features revealed in experimentally measured cross sections [16, 21, 22].

However, in both experimental [23] and theoretical [24] works, the existence of a stable negative ion Ca^- in the $4s^24p^2P$ state was revealed. Later, the existence of stable negative ions Sr^-, Ba^-, Ra^-, and Yb^- was predicted (see [3, 4, 17] and references therein). Experimental results [25] confirmed the existence of negative ions Sr^-, Ba^-, and Yb^-. The investigation of the structure of these ions showed the important role of the (monopole, dipole, and quadrupole) polarizability of the atomic shell upon the capture of an electron. The polarizability effects are also important upon low-energy scattering of electrons by these atoms; this results in the formation of only ^2D shape resonance, which is possible due to the existence of negative ions in ns^2np^2P states [3, 4].

Thus, along with the traditional theoretical calculations and experiments concerning scattering, a new technique based on the use of hypocycloidal spectrometers was introduced into the practice of investigations of the interaction of slow electrons with atoms, ions, and surfaces. The energy dependences that are measured in these experiments differ from the familiar concepts such as the total and differential cross sections. It is of great importance to theoretically consider these dependences, calculate and study their constituents (direct and interference, resonance and nonresonance contributions) as well as of the role of possible inelastic processes. Therefore, the aim of this work was the development and application of an analytical formalism for analyzing the $S(E)$ function measured in experiments on the elastic scattering of slow electrons by atoms using a hypocycloidal electron spectrometer.

BRIEF DESCRIPTION OF A HYPOCYCLOIDAL ELECTRON SPECTROMETER

In this section, we consider the main constructive features of a hypocycloidal electron spectrometer, modes of its operation, and its application to experiments on low-energy electron scattering. The trochoidal electron monochromator was first developed by Stamatovich and Schultz [26] and later used for studying resonances in molecules, inert gases, and atoms of Group II metals [16]. A setup with a trochoidal electron spectrometer was used in [27–29] and modernized and modified in [1, 2, 30].

In a trochoidal electron monochromator, a combined effect of crossed magnetic and electric fields is used for the selection of electrons in velocities. In the region where these fields act simultaneously, the electrons drift along equipotential surfaces of the transverse electric field. The exit diaphragm of the analyzer, whose orifice is shifted relative to the entrance orifice, discriminates particles with a definite longitudinal component of velocity; this effect is used to determine the energy distribution of electrons. Because of the effect of the fringing field of the condenser (in a trochoidal electron monochromator, a condenser with flat plates is used), the displacement of an electron at the exit from the monochromator depends on the inlet coordinate of the electron in the region of drift. This derates the separation and decreases the coefficient of transmission of the analyzer [27].

In connection with the above-said, attempts were made to find configurations of fields such that ensure a minimum deviation of the beam profile from the cyclic one at the exit from the region of the crossed fields. Calculations of electron trajectories show that this condition is satisfied by the field of a cylindrical condenser consisting of two coaxial cylinders whose radii meet certain conditions [30]. Thus, a nonuniform electric field of a cylindrical condenser whose axis is parallel to the magnetic field should be employed.

A hypocycloidal electron monochromator, in comparison with the trochoidal electron monochromator, has a better resolution at the same exiting current, and its use as an electron analyzer permits one to obtain a transmission coefficient close to 100%.

Like the trochoidal electron spectrometer, the hypocycloidal electron spectrometer consists of a hypocycloidal electron monochromator and analyzer separated by a collision chamber. The scheme of a spectrometer is shown in Fig. 1 along with the distribution of potentials at its electrodes. Electrons emitted by an oxide cathode *K* enter the region of drift of the monochroma-

tor between the diaphragms A_2 and A_3 through the entrance slit of electrode A_1. The transverse electric fields in the selector and analyzer are produced by cylindrical condensers B_1, B_2, and B_3, B_4, respectively, to which a potential difference is applied. Electrons, being accelerated into the collision chamber A_4 to an energy E_{in}, intersect there with the atomic beam and then enter the drift region of the analyzer between the diaphragms A_5 and A_6. An auxiliary electrode A_7, along with a Faraday cylinder Π_1, serves to detect the primary beam of electrons and reduce the background of reflected electrons. The scattered electrons are deviated into the exit slit of the analyzer and are detected by a multichannel electron photomultiplier. The spectrometer is placed in a uniform magnetic field produced by a pair of Helmholtz coils [30].

In the drift region of the analyzer, the electrons are deviated at a distance D [29]

$$D = \frac{E_r}{B} L \left(\frac{2e}{m}\right)^{1/2} [W_r \cos\Theta - (E_{in} - eU_A)]^{1/2}, \quad (1)$$

where E_r and B are the strengths of the electric and magnetic fields, L is the length of the analyzer, Θ is the scattering angle, $W_r = E_{in} - E_n$, E_n is the energy lost by electrons for excitation, and U_A is the potential of the analyzer.

Hence, in the case of elastic scattering ($W_r = E_{in}$), the scattering angle is equal to

$$\Theta = \arcsin\sqrt{\frac{eU_A - K/D^2}{E_{in}}}, \quad K = \frac{E_r}{B} L \left(\frac{2e}{m}\right)^{-\frac{1}{2}}. \quad (2)$$

Take also into account that if the analyzer has an exit window of width $\Delta D = D_2 - D_1$, then an electron will pass into the outlet of the analyzer if it is scattered into an angular range $\Delta\Theta = \Theta_1(D_2) - \Theta_2(D_1)$ and it is this circumstance that determines the experimental constants $\bar{a}$ and b. In order to investigate the backscattering of electrons by metal ions and thin films, all the components of the HES are used in the same form as in the case of scattering by atoms. However, the mutual arrangement of the analyzer (B_3, B_4) and the collision chamber (A_4) is different in this case [9].

The spectrometer can operate in the regimes of energy dependence of elastically or inelastically scattered electrons, constant residual energy, inelastically scattered electrons, or incident-electron-energy loss. In the regime of energy dependence [1–4], the potential of the analyzer U_A relative to the cathode was maintained constant and the energy of incident electrons E_{in} was varied. An analysis of the transmission function of the analyzer performed as in the case of the threshold spectrum shows that it achieves the maximum magnitude at such an excess over the threshold of the process studied, at which the potential of the collision chamber equal to E_{in} is close to the potential of the analyzer U_A.

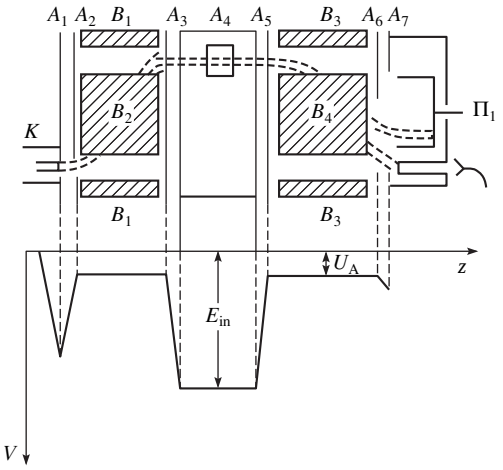

Fig. 1. Schematic of a hypocycloidal electron spectrometer and the distribution of potentials on its electrodes.

With increasing energy, the angular acceptance is sharply shifted to the region of smaller angles and the optical efficiency falls sharply.

The current of elastically scattered electrons within the angular range $\Theta_1 - \Theta_2$ is expressed by the following formula (below, the electron energy will be designated merely E):

$$i_p = i_0 N d S(E), \quad S(E) = \int_{\Theta_1}^{\Theta_2} \frac{d\sigma}{d\Omega} d\Omega, \quad (3)$$

where i_0 is the incident-electron current, N is the concentration of target atoms, d characterizes the spatial dimensions of the collision region, and $d\sigma/d\Omega$ is the differential scattering cross section.

For the case of a pointlike introduction of the electron beam into the collision region, the angular acceptance of the analyzer $\Theta_1 - \Theta_2$ depends on the electron energy as follows:

$$\Theta_1 = \arcsin\sqrt{\frac{\bar{a}}{E}}, \quad \Theta_2 = \arcsin\sqrt{\frac{b}{E}}. \quad (4)$$

The constants $\bar{a}$ and b can be obtained from the experimental conditions (see Eqs. (1), (2)): $\bar{a}$ = 0.482 eV, b = 0.508 eV [1, 2], which corresponds to U_A = 0.55 V. Note that in the case of the limiting scattering angles ($\Theta_1 = 0$, $\Theta_2 = \pi$), the value of $S(E)$ coincides with the total scattering cross section $\sigma(E)$.

Figure 2 displays the experimental function $S(E)$ (curve *1*) [1, 2] of the elastic scattering of electrons by Ca atoms and the angles given by Eq. (4) (curves *7*, *8*). Its rise at $E \le 0.5$ eV is due to the sharp change in the energy dependence of the transmission function of the analyzer, and its falloff toward 2.0 eV represents a threshold feature, which is due to the existence of the 4*p* state of Ca atoms. As is seen, the angular acceptance

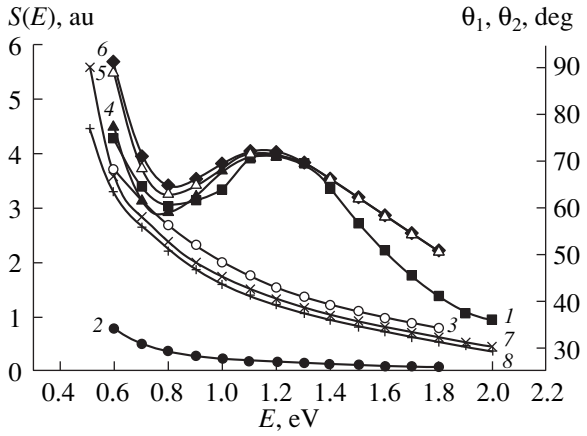

Fig. 2. Energy dependence of elastic scattering of electrons by Ca atoms and the angular acceptance: (*1*) experimental $S(E)$ curve; (*2*)–(*6*) theoretical $S_k(E)$ functions for k = 1–5, respectively (k is the number of partial waves that are taken into account); and (*7*) and (*8*) the angular dependences $\Theta_2(E)$ and $\Theta_1(E)$, respectively.

of the analyzer in this region changes from 76.9°–90° at E = 0.508 eV to 28.5°–29.5° at E = 1.8 eV.

THEORETICAL ANALYSIS OF KINEMATIC AND DYNAMIC FEATURES OF ELASTIC SCATTERING OF SLOW ELECTRONS

1. General Formalism

Using the partial-wave expansion in amplitudes [31] and its connection with the differential cross section, we obtain from Eq. (3) the following expression for the $S(E)$ function through the direct (S_d) and interference (S_i) contributions:

$$S(E) = S_d(E) + S_i(E) = \sum_l \sigma_{el,l}(E)Q_{ll}(E)$$

$$+ \frac{\pi}{E}\sum_{l,l'>l}\sqrt{(2l+1)(2l'+1)}[\eta_l \sin 2\bar{\delta}_l \eta_{l'} \sin 2\bar{\delta}_{l'} \quad (5)$$

$$+ (1-\eta_l \cos 2\bar{\delta}_l)(1-\eta_{l'}\cos 2\bar{\delta}_{l'})]Q_{ll'}(E).$$

Here, $\bar{\delta}_l$ is the real part; η_l is related to the imaginary part $\eta_l(E) = \exp(-2\bar{\eta}_l(E))$ of the partial phase of scattering $\delta_l(E) = \bar{\delta}_l(E) + i\bar{\eta}_l(E)$ of the electron in the field of optical potential; $\sigma_{el,l}(E)$ is the partial cross section of the elastic scattering of electrons

$$\sigma_{el}(E) = \sum_l \sigma_{el,l}(E) = \frac{2\pi}{k^2}\sum_l (2l+1)[1-\eta_l \cos 2\bar{\delta}_l]$$

$$-\frac{\pi}{k^2}\sum_l (2l+1)[1-\eta_l^2] \quad (6)$$

$$\equiv \sum_l \sigma_{t,l} - \sum_l \sigma_{r,l} = \sigma_t - \sigma_r,$$

$k^2 = 2E$ (in au); and $\sigma_t(\sigma_{t,l})$ and $\sigma_r(\sigma_{r,l})$ are the total (partial) cross sections of the total scattering and reaction, respectively.

The functions $Q_{l,l'}(E)$ in Eq. (5) are related to Legendre polynomials $P_l(x)$ (see Appendix):

$$Q_{l,l'}(E) = \frac{\sqrt{(2l+1)(2l'+1)}}{2}\int_{x_1}^{x_2} dx P_l(x)P_{l'}(x), \quad (7)$$

$$x_1 = \cos\Theta_2(E), \quad x_2 = \cos\Theta_1(E).$$

In the case of real partial phases $\delta_l(E)$ (for energies below the threshold for inelastic processes), Eq. (5) goes into

$$S(E) = S_d(E) + S_i(E) = \sum_l \sigma_l(E)Q_{ll'}(E)$$

$$+ \frac{4\pi}{E}\sum_{l'\neq l, l'>l}\sqrt{(2l+1)(2l'+1)} \quad (8)$$

$$\times \sin\bar{\delta}_l \sin\bar{\delta}_{l'}\cos[\bar{\delta}_l(E) - \bar{\delta}_{l'}(E)]Q_{ll'}(E).$$

Here, $\sigma_l(E)$ is the partial cross section of elastic scattering. To obtain estimates (which are given below), it is expedient to use formula (8) in the approximate form (with the $S_i(E)$ term expressed through partial cross sections):

$$S(E) = S_d(E) + S_i(E) = \sum_l \sigma_l(E)Q_{ll'}(E) + 2\sum_l \sqrt{\sigma_l}(E) \quad (9)$$

$$\times \sum_{l'\neq l, l'>l}\sqrt{\sigma_{l'}(E)}\cos[\delta_l(E) - \delta_{l'}(E)]Q_{ll'}(E).$$

Thus, a hypocycloidal electron spectrometer can be considered as a device that discriminates the role of various partial waves upon the interaction of electrons with atoms and ions.

2. Nonresonance Low-Energy Electron Scattering

For the nonresonance low-energy scattering of electrons by a potential with an asymptotics $-\alpha/2r^4$ (α is the dipole static polarizability of atoms), the partial phases $\delta_l(E)$ can be written as follows [31]:

$$k\cot\delta_0 k = -\frac{1}{a} + \frac{\pi\alpha}{3a^2}k + \frac{2\alpha}{3a}k^2 ln\left(\frac{\alpha k^2}{16}\right) + O(k^2), \quad (10)$$

$$k^2\cot\delta_l(k) = \frac{8(l-1/2)(l+1/2)(l+3/2)}{\pi\alpha}.$$

Here, a is the scattering length. At small k, restricting ourselves to two waves ($l = 0, 1$) and small order in k (for $l = 0$), we have

$$\cot\delta_0(k) = -\frac{1}{ka} + \frac{\pi\alpha}{3a^2}, \quad \cot\delta_1(k) = \frac{15}{\pi\alpha k^2}, \quad (11)$$

hence,

$$\sigma_0 = \frac{4\pi a^2}{1 + a^2k^2 + \dfrac{\pi^2\alpha^2k^2}{9a^2} - \dfrac{2\pi\alpha k}{3a}}, \qquad \sigma_1 = \frac{12\pi^3\alpha^2k^2}{225 + \pi^2\alpha^2k^4}. \quad (12)$$

Substituting Eqs. (11) and (12) into Eq. (9), we obtain for $S(E)$ at small energies (expressions for Q_{00}, Q_{11}, and Q_{01} are given in the Appendix)

$$S(E) = \frac{6\pi a^3}{3a - 2\pi\alpha\sqrt{2E}}\frac{\sqrt{E-\bar a} - \sqrt{E-b}}{\sqrt{E}} + \frac{4\pi^3\alpha^2}{75\sqrt{E}}[(E-\bar a)^{3/2} - (E-b)^{3/2}] + \frac{2\pi^2\alpha a\sqrt{2E}}{5E}\frac{(\pi\alpha\sqrt{2E} - 3a)}{(3a - 2\pi\alpha\sqrt{2E})}(b - \bar a). \quad (13)$$

If $\bar a$ and b in Eq. (4) are such that the energy of the Ramsauer minimum is $E_0 \geq b$, then we have for the vicinity of E_0

$$S(E) = \frac{\pi^2\alpha^2}{3}\left\{\frac{(E-E_0)^2}{3E\sqrt{E}}(\sqrt{E-\bar a} - \sqrt{E-b}) + \frac{4}{25}\frac{(E-\bar a)^{3/2} - (E-b)^{3/2}}{\sqrt{E}}\right\} + \frac{\pi^3\alpha^2}{3}\left\{\frac{2}{5}(b-\bar a)\frac{E-E_0}{E}\cos\left[\frac{3a^2}{2\pi\alpha} - \frac{7}{15}\pi\alpha E\right]\right\}. \quad (14)$$

For the electron energy E_0 (i.e., at $E = E_0 \geq b$), we obtain from Eq. (14)

$$S(E_0) = \frac{\pi^3\alpha^2}{3}\frac{4}{25}\frac{(E_0-\bar a)^{3/2} - (E_0-b)^{3/2}}{\sqrt{E_0}}. \quad (15)$$

We see that $S(E_0)$ has a maximum at $E_0 = b$. This can be used to find the scattering length or the polarizability from the equality [31]

$$b = \frac{1}{2}\left(\frac{3a}{\pi\alpha}\right)^2. \quad (16)$$

A comparison of Eqs. (14) and (15) shows that, for given $\bar a$ and b, the function $S(E)$ has a minimum at E_0 (analogous to the minimum in the total cross section) and increases at $E > E_0$.

3. Resonance Scattering of Electrons

Let us consider the case where there exists a resonance in a certain partial wave. In this case, the partial scattering phase in the resonance energy range has the form [31]

$$\delta_l(E) = \delta_l^0 + \delta_l^r(E), \quad (17)$$

where δ_l^0 is the nonresonance (background) part of the phase shift and $\delta_l^r(E)$ is the resonance phase shift due to resonance at an energy E_l^r with a width Γ_l

$$\delta_l^r(E) = \arctan\left[\frac{\Gamma_l/2}{E_l^r - E}\right]. \quad (18)$$

The resonance partial cross section has the form

$$\sigma_l(E) = \frac{4\pi}{k^2}(2l+1)\sin^2\delta_l^0\frac{(q_l + \varepsilon_l)^2}{1 + \varepsilon_l^2}, \quad (19)$$

where the reduced width and the parameter of the shape resonance (index of the line profile) are

$$\varepsilon_l = -\cot\delta_l^r(E), \quad q_l = -\cot\delta_l^0, \quad (20)$$

respectively. Expressions (17)–(20) for the resonance energy range should be used in Eqs. (8) and (9). Let there be a resonance in the nth partial wave. Then, separating terms with the characteristics of this wave in (9), we obtain the following expression for $S(E)$ through the resonance (R) and nonresonance (NR) parts

$$S(E) = S_R(E) + S_{NR}(E) = \sigma_n(E)Q_{nn}(E) + 2\sqrt{\sigma_n}\sum_{l'\neq n}\sqrt{\sigma_{l'}(E)}Q_{nl'}(E)\cos[\delta_n(E) - \delta_{l'}(E)] + \sum_{l\neq n}\sigma_l(E)Q_{ll}(E) + 2\sum_{l\neq n,\, l'\neq l}\sum_{l'\neq n,\, l'>l}\sqrt{\sigma_l(E)\sigma_{l'}(E)} \times Q_{ll'}(E)\cos[\delta_l(E) - \delta_{l'}(E)], \quad (21)$$

where, in turn, these parts are separated into direct (d) and interference (i) contributions

$$S_R(E) = S_{Rd}(E) + S_{Ri}(E), \qquad S_{NR}(E) = S_{NRd}(E) + S_{NRi}(E). \quad (22)$$

For example, at $l = 0$–3 and resonance in the d wave ($n = 2$), the resonance part has the form

$$S_R(E) = \sigma_2 Q_{22} + \frac{2\sqrt{\sigma_2}}{\sqrt{1+\varepsilon_2^2}}[\sqrt{\sigma_0}Q_{02}(\varepsilon_2\cos\delta_{20}^0 + \sin\delta_{20}^0) + \sqrt{\sigma_1}Q_{12}(\varepsilon_2\cos\delta_{21}^0 + \sin\delta_{21}^0) + \sqrt{\sigma_3}Q_{23}(\varepsilon_2\cos\delta_{23}^0 + \sin\delta_{23}^0)], \quad (23)$$

where $\delta_{2j}^0 = \delta_2^0 - \delta_j$.

At $E \ll E_2^r$, $\varepsilon_2 \approx -E_2^r/(\Gamma_2/2)$, and $\Gamma_2 \ll 1$, we have

$$S_R(E) = \sigma_2 Q_{22} - 2\sqrt{\varepsilon_2}\{\sqrt{\sigma_0}Q_{02}\cos\delta_{20}^0 - \sqrt{\sigma_1}Q_{12}\cos\delta_{21}^0 + \sqrt{\sigma_3}Q_{23}\cos\delta_{23}^0\}. \quad (24)$$

For $E \gg E_2^r$, $\varepsilon_2 \approx E/(\Gamma_2/2)$, and $\Gamma_2 \ll 1$, we obtain

$$S_R(E) = \sigma_2 Q_{22} + 2\sqrt{\varepsilon_2}\{\sqrt{\sigma_0}Q_{02}\cos\delta_{20}^0 + \sqrt{\sigma_1}Q_{12}\cos\delta_{21}^0 + \sqrt{\sigma_3}Q_{23}\cos\delta_{23}^0\}. \quad (25)$$

In Eqs. (24) and (25),

$$\sigma_2 = \frac{5\times 4\pi}{k^2}\sin^2\delta_2^0.$$

In the resonance, $E = E_2^r$, $\varepsilon_2 = 0$,

$$\sigma_2 = \frac{5\times 4\pi}{k^2}\cos^2\delta_2^0$$

and

$$S_R(E) = \sigma_2 Q_{22} + 2\sqrt{\sigma_2}[\sqrt{\sigma_0}Q_{02}\sin\delta_{20}^0 + \sqrt{\sigma_1}Q_{12}\sin\delta_{21}^0 + \sqrt{\sigma_3}Q_{23}\sin\delta_{23}^0]. \quad (26)$$

If Γ_l is not small, then $\varepsilon_l = (E - E_l^r)/(\Gamma_l/2)$ in the resonance region and, e.g., for $l = 2$, we have

$$S_R(E) = \sigma_2 Q_{22} + 2\sqrt{\sigma_2}\frac{\Gamma_2/2}{\sqrt{\Gamma_2^2/4 + (E-E_2^r)^2}} \times\left[\sqrt{\sigma_0}Q_{02}\left(\frac{E-E_2^r}{\Gamma_2/2}\cos\delta_{20}^0 + \sin\delta_{20}^0\right) + \sqrt{\sigma_1}Q_{12}\left(\frac{E-E_2^r}{\Gamma_2/2}\cos\delta_{21}^0 + \sin\delta_{21}^0\right) + \sqrt{\sigma_3}Q_{23}\left(\frac{E-E_2^r}{\Gamma_2/2}\cos\delta_{23}^0 + \sin\delta_{23}^0\right)\right]. \quad (27)$$

Thus, we can conclude that resonance leads to irregular behavior of the function $S_R(E)$ (and, consequently, of $S(E)$) in the resonance region. If the background phase is $\delta_l^0 \in (0, \pi/2)$, then $q_l = -\cot\delta_l^0 \le 0$ and $\varepsilon_l \ge 0$ (at $E \ge E_l^r$) or $\varepsilon_l \le 0$ (at $E \le E_l^r$). The quantity $q_l + \varepsilon_l$ is negative at $E < E_l^r$, can have an arbitrary sign or equal zero at $E > E_l^r$, and depends on the relationship between $|q_l|$ and $|\varepsilon_l|$. It is of interest to find the energy at which $q_l + \varepsilon_l = 0$. This means that $|q_l| = |\varepsilon_l|$ and, thus,

$$\cot\delta_l^0 = \frac{E - E_l^r}{\Gamma_l/2}.$$

Considering δ_l^0 to be constant, we obtain for the resonance region that the partial cross section is $\sigma_l = 0$ at $E_{l\min} = \frac{\Gamma_l}{2}\cot\delta_l^0 + E_l^r$. Therefore, the magnitude of σ_l increases at $E < E_{l\min}$, reaches a maximum

$$\frac{4\pi}{k^2}(2l+1)\cos^2\delta_l^0$$

at $E = E_l^r$, and then decreases to zero at $E_{l\min}$, whereas the small increase in $\delta_l(E)$ at $E < E_{l\min}$ is described by the formula

$$\frac{4\pi}{k^2}(2l+1)\sin^2\delta_l^0.$$

The case where $\delta_l^0 \in (\pi/2, \pi)$ is considered analogously (here, we obtain that $E_{l\min} < E_l^r$). In the resonance region, $S_R(E)$ can be estimated from Eq. (27). At $E = E_{l\min}$, we have $S_R = 0$ and, then, $S(E) = S_{NR}$. At $E_{l\min} > E_l^r$, i.e., in the region of the monotonically decreasing $Q_{ij}(E)$, we obtain $Q_{ij}(E_{l\min}) < Q_{ij}(E_l^r)$ and $S_{NR}(E_{l\min}) < S(E_l^r)$. A similar relationship will also be fulfilled at $E_{l\min} < E_l^r$ although in this case $Q_{ij}(E_{l\min}) > Q_{ij}(E_l^r)$, but $S_{NR}(E_{l\min}) < S(E_l^r)$. Therefore, the function $S(E)$ possibly reaches a minimum at $E_{l\min}$, since the resonance cross section is zero, while at E_l^r it will be maximum. In the absence of resonances, $S(E)$ will be monotonically dependent on the energy in the range of the monotonic behavior of $Q_{ij}(E)$. Note that at $E < E_l^r$, the functions $Q_{ij}(E)$ can have singularities in their behavior (zeros and extrema, see the Appendix); therefore, we should take into account this behavior of $Q_{ij}(E)$ and its effect on $S(E)$. Thus, the singularities in the behavior of $S(E)$ originate from both the existence of resonances in some waves and the singularities in the behavior of the $Q_{ij}(E)$ functions.

In the beginning of the energy scale ($E = b$), the magnitude of $S(b)$ in experiments of this type will have finite values, as follows from the boundedness of

$Q_{ij}(E)$. With increasing energy, the $Q_{ll'}(E)$ functions fall off up to zero; therefore, $S(E)$ also drops.

If the background phase $\delta_l^0(E)$ is small, which is the case upon the elastic scattering of slow electrons by the atoms of alkaline-earth elements [3, 4], it follows from Eq. (19) that σ_l has the Breit–Wigner form:

$$\sigma_l(E) = \frac{4\pi}{k^2}(2l+1)\frac{\Gamma_l^2/4}{(E-E_l^r)^2+\Gamma_l^2/4} = \frac{4\pi}{k^2}(2l+1)\frac{1}{1+\varepsilon_l^2}. \quad (28)$$

At $E = E_l^r$, the partial cross section reaches the unitary bound

$$\sigma_{l\max} = \frac{4\pi}{k^2}(2l+1).$$

At $E \ll E_l^r$, the cross section has a finite magnitude

$$\sigma_l(E) = \frac{4\pi}{k^2}(2l+1)\frac{\Gamma_l^2/4}{(E_l^r)^2+\Gamma_l^2/4} < \sigma_{l\max}.$$

At $E \gg E_l^r$, we have $\varepsilon_l = 2E/\Gamma_l$, and the cross section decreases with increasing energy E. Such a behavior of σ_l affects the behavior of $S_R(E)$. For example, for d resonance at $E = E_2^r$ and $\varepsilon_2 = 0$, we have from Eq. (23) that

$$S_R(E_2^r) = \sigma_{2\max}Q_{22} + 2\sqrt{\sigma_{2\max}}[\sqrt{\sigma_0}Q_{02}\sin\delta_{20}^0 + \sqrt{\sigma_1}Q_{12}\sin\delta_{21}^0 + \sqrt{\sigma_3}Q_{23}\sin\delta_{23}^0]. \quad (29)$$

At $E \ll E_2^r$, we have $\varepsilon_2 = 2E_2^r/\Gamma$, and formula (24) is valid. At $E \gg E_2^r$, the function $S_R(E)$, just as $\sigma_2(E)$ and $Q_{ij}(E)$, falls off with increasing energy. The function $S_R(E)$ in Eq. (29) depends on the behavior of the functions $Q_{22,\,02,\,12,\,23}$ in the energy range considered. At large energies, both S_R and S_{NR} are known to decrease to zero. Thus, we can separate the irregularities in the behavior of the function $S(E) = S_{NR}(E) + S_R(E)$ generated due to the existence of resonance in a certain wave (dynamic singularities in $S_R(E)$) from those caused by the energy-dependent behavior of the functions $Q_{ij}(E)$ (kinematic singularities in both $S_{NR}(E)$ and $S_R(E)$).

ELASTIC SCATTERING OF SLOW ELECTRONS BY CALCIUM ATOMS

The above formalism was applied to theoretically calculate the $S(E)$ function and its parts for the case of the elastic scattering of slow electrons by Ca atoms. The values of the parameters $\bar{a}$ and b correspond to the technique used in one of our experiments performed on a hypocycloidal electron spectrometer [2, 29] and its theoretical interpretation performed both numerically [2–4] and analytically [32–34].

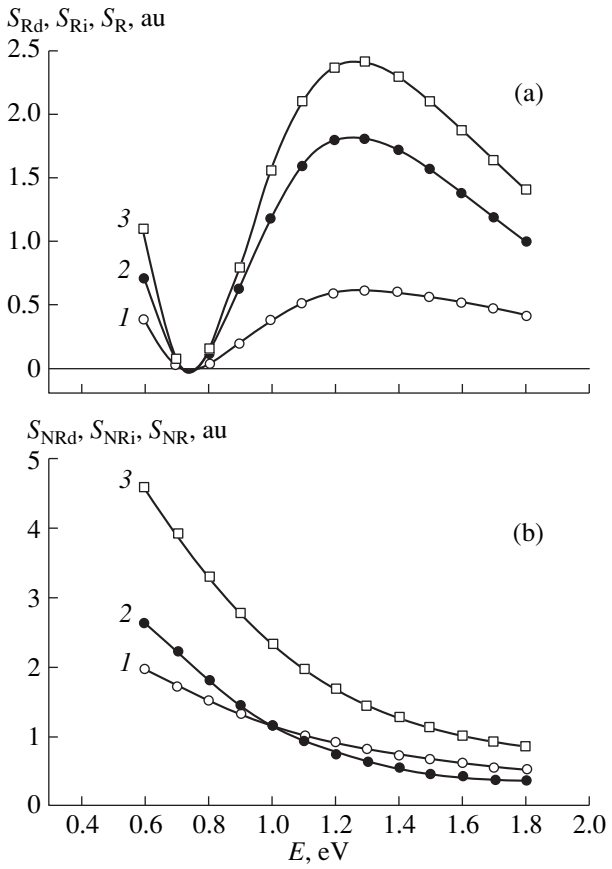

Fig. 3. (a) Resonance (S_R) and (b) nonresonance (S_{NR}) parts of the $S(E)$ function: (*1*) direct components (S_{Rd} in (a) and S_{NRd} in (b)); (*2*) interference components (S_{Ri} in (a) and S_{NRi} in (b)); and (*3*) total functions (S_R in (a) and S_{NR} in (b)).

The partial (l = 0–4) phases were found from the phase equation with an optical potential in which the polarization potential took into account the dipole (α_d = 148.86 au) and quadrupole (α_q = 335.9 au) polarizabilities; in addition, we used a local exchange potential (see [3, 4] and the references therein). The adjustable parameter r_q = 5.94 au in the polarization potential was found from the requirement for the existence of a stable ion Ca^- with an electron configuration $4s^24p^2P^0$ with an electron-affinity energy $E_A = -0.043 \pm 0.007$ eV. The calculation of phases showed the presence of a ^2D shape resonance (l = 2) with the following parameters: the energy E_2^r = 0.87 eV and the width Γ_2 = 0.98 eV. The phase of the d wave passes through the value $\pi/2$ and, on the whole, changes by π while going from low to high energies [3, 4, 31]. The Ramsauer–Townsend minimum in $\sigma_0(E)$ lies near the scattering threshold at an energy of 0.012 eV and cannot affect $S(E)$.

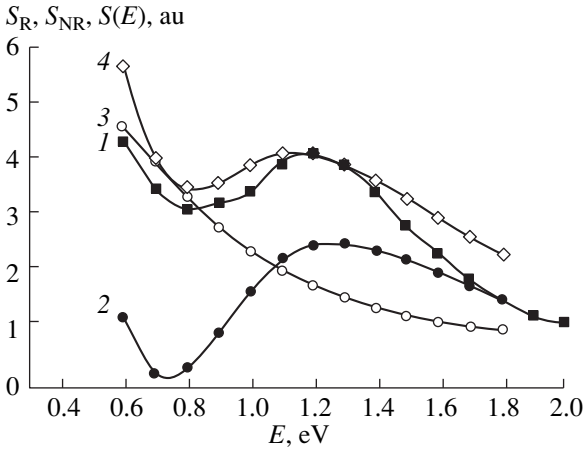

Fig. 4. Energy dependences of the elastic scattering of electrons by calcium atoms: (*1*) experimental $S(E)$ curve; (*2*)–(*4*) theoretical curves; (*2*) resonance function S_R; (*3*) nonresonance function S_{NR}; and (*4*) total function $S(E)$.

In order to reveal the dependence of the $S(E)$ function on the number of partial waves k that are taken into account, we calculated functions $S_k(E)$. In Fig. 2, they are given along with the experimental curve. It is seen that the S_1 (s wave) and S_2 (s and p waves) functions reveal a monotonic behavior, whereas beginning from S_3 (s, p, and d waves), the S_k functions have a minimum ($E \approx 0.8$ eV) and a maximum ($E \approx 1.2$ eV). Note that beginning from the allowance for the d wave, there is not only a qualitative but also a quantitative agreement with the experimental curve normalized to S_5 at E = 1.3 eV.

The magnitudes of the direct $S_d(E)$, interference $S_i(E)$, and total $S(E)$ functions (see Eq. (5)) depending on the number of partial waves are demonstrated in the table. It can be seen that the interference terms are relatively large, especially for small energies corresponding to large angles Θ_1 and $\Theta_2 \sim 64°$–$67°$. Both the interference and direct contributions exhibit nonmonotonic behavior (they have minima at 0.8 and 0.9 eV and maxima at 1.2 and 1.1 eV, respectively, beginning from the allowance for the d wave).

Owing to resonance, we can represent the $S(E)$ function in the form (21) and (22), i.e., single out the resonance (contribution of the d wave) and the nonresonance parts of $S(E)$ and divide these parts into direct and interference components. These functions are shown in Fig. 3; it is seen that the resonance parts and components (Fig. 3a) exhibit a nonmonotonic behavior (a minimum $S_R(E) \approx 0$ at $E \approx 0.75$ eV and a maximum at $E \approx 1.2$–1.4 eV), whereas the nonresonance parts change monotonically (Fig. 3b). Note the intersection of the direct and interference nonresonance terms at $E \approx 1$ eV.

A comparison of the $S_R(E)$ and $S_{NR}(E)$ functions and the total and experimental $S(E)$ functions is displayed in Fig. 4; it is seen that it is the S_R component that determines (due to its nonmonotonic behavior) the total behavior of the $S(E)$ function; this qualitatively agrees with the experiment. As to the behavior of S_R, S_{Rd}, and S_{Ri} (see also Fig. 3a), we can note that when going from 0.7 to 0.8 eV, the angles Θ_1 and Θ_2 pass through a value of 54.7° when the Legendre polynomial $P_2(\cos\Theta)$ is zero and the functions $Q_{i2}(E)$ are small.

Figure 5 illustrates the behavior of the total ($\sigma(E)$) and differential ($d\sigma/d\Theta$) cross sections (calculated using five partial waves) in comparison with the theoretical and experimental functions $S(E)$. The differential cross section was estimated for an average angle

Direct S_{dk}, interference S_{ik} and total S_k (k = 1–5 is the number of included partial waves) functions (in arb. units) of elastic scattering by Ca atoms

E, eV	l = 0	l = 0, 1			l = 0, 1, 2			l = 0, 1, 2, 3			l = 0, 1, 2, 3, 4		
	S_1	S_{d2}	S_{i2}	S_2	S_{d3}	S_{i3}	S_3	S_{d4}	S_{i4}	S_4	S_{d5}	S_{i5}	S_5
0.60	0.79	1.88	1.85	3.72	2.25	2.24	4.48	2.31	3.18	5.49	2.32	3.35	5.67
0.70	0.50	1.65	1.50	3.15	1.67	1.47	3.14	1.72	2.00	3.72	1.73	2.25	3.97
0.80	0.36	1.45	1.25	2.70	1.49	1.43	2.92	1.52	1.71	3.23	1.53	1.89	3.42
0.90	0.28	1.28	1.05	2.33	1.47	1.76	3.23	1.48	1.91	3.40	1.49	2.02	3.52
1.00	0.22	1.13	0.89	2.02	1.50	2.16	3.66	1.51	2.24	3.75	1.52	2.32	3.83
1.10	0.18	1.00	0.77	1.77	1.51	2.41	3.92	1.51	2.47	3.98	1.52	2.52	4.04
1.20	0.15	0.89	0.66	1.55	1.47	2.47	3.94	1.47	2.51	3.98	1.48	2.55	4.03
1.30	0.13	0.79	0.58	1.37	1.40	2.38	3.78	1.40	2.40	3.80	1.40	2.44	3.84
1.40	0.11	0.71	0.51	1.22	1.30	2.20	3.50	1.30	2.21	3.51	1.30	2.24	3.54
1.50	0.10	0.64	0.45	1.09	1.19	1.99	3.18	1.20	1.99	3.18	1.20	2.00	3.20
1.60	0.08	0.58	0.40	0.97	1.08	1.76	2.84	1.09	1.75	2.85	1.09	1.76	2.86
1.70	0.07	0.52	0.35	0.88	0.98	1.54	2.52	0.99	1.53	2.52	0.99	1.53	2.53
1.80	0.06	0.47	0.32	0.79	0.88	1.34	2.22	0.90	1.32	2.22	0.90	1.32	2.22

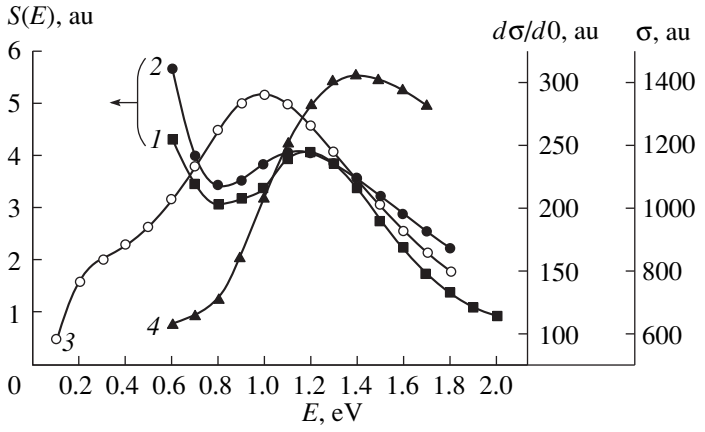

Fig. 5. Energy dependences and the total and differential cross sections of elastic scattering: (*1*) experimental $S(E)$ dependence; (*2*) theoretical $S(E)$ dependence; (*3*) total cross section $\sigma(E)$; and (*4*) differential cross section $d\sigma/d\Theta$.

$\Theta(E) = [\Theta_1(E) + \Theta_2(E)]/2$. As was said above, the $S(E)$ function exhibits features of both the total and differential cross sections, which is confirmed by the figure. Under the experimental conditions used in [1, 2] and for the features characteristic of the resonance interaction of slow electrons with Ca atoms, the $S(E)$ function is closer to the distorted (in the region of the maximum) total cross section. This can be seen from the figure: the shape of the $S(E)$ curve qualitatively coincides with the behavior of the total cross section at energies above 1.3 eV, while in the region of the minimum $S(E)$ the differential cross section also is minimum. This feature is a manifestation of the above-mentioned passage of the angles through the value equal to 54.7°. It is also interesting that the minimum in $S(E)$ is almost coincident with the maximum of the total cross section $\sigma(E)$, although is slightly (by 0.2 eV) shifted toward the range of smaller energies.

The calculations performed showed that the features observed in the experimental $S(E)$ function are determined by the ^2D shape resonance. This resonance manifests itself both in the direct and interference parts of this function.

CONCLUSION

This paper gives a brief qualitative review of experimental techniques (with intersecting electron and atomic beams) with the use of a trochoidal electron spectrometer and its modification, a hypocycloidal electron spectrometer, which are applicable for the investigation of the process of the elastic scattering of slow electrons by atoms.

For the interpretation of experiments on the elastic scattering of slow electrons by atoms into an angular range depending on the electron energy, which is determined by the various regimes of operation of the (trochoidal or hypocycloidal) electron spectrometer, we developed a general analytical formalism. In the case of electron scattering into the angular range $\Theta_1(E) - \Theta_2(E)$ given by Eqs. (4), this formalism permitted us to analyze the nonresonance and resonance (shape resonance) scattering of slow electrons by an atom, when the kinematic features of scattering (which are connected with the scattering angles through specially introduced functions $Q_{ij}(E)$) can be separated from dynamic features (linked with phases, partial cross sections, and optical potential).

A detailed theoretical analysis of the elastic scattering of slow electrons (performed on the basis of five partial waves) by a Ca atom under experimental conditions used in [1, 2] showed that the nonmonotonic behavior of the $S(E)$ energy dependence is due to the existence of a ^2D shape resonance, which manifests itself in both the direct and interference parts of $S(E)$. This analysis indicates not only qualitative but even good quantitative agreement with experiment. The minimum of $S(E)$ lies in the region of the resonance, and the angular range $\Theta_1(E) - \Theta_2(E)$ contains the angle 54.7° (at $E \approx 0.72$–0.76 eV). The position of the minimum (0.8 eV) of the measured and calculated $S(E)$ function is close to the position of the maximum (1.0 eV) of the total cross section of elastic scattering, which is also a consequence of the presence of a resonance in the *d* wave. The behavior of the $S(E)$ function is partly similar to the energy dependence of the total and differential cross sections.

Generalizing what was said above, we may conclude that the use of the trochoidal and hypocycloidal electron spectra in scattering experiments permits one to reveal the resonance character of the interaction of electrons with atoms.

ACKNOWLEDGMENTS

We are grateful to A.N. Zavilopulo, N.I. Romanyuk, and V.I. Kelemen for fruitful discussions of the results of this work. The work was supported in part by the

Foundation for Basic Research of the Ukrainian Ministry of Science (project no. F41675-97).

APPENDIX

For the first five partial waves (l = 0–4), we can obtain the following general expressions for the $Q_{ij}(E)$ functions (see Eq. (7)):

$$Q_{00} = \frac{x_2 - x_1}{2}, \quad Q_{11} = \frac{x_2^3 - x_1^3}{2}, \quad Q_{01} = \frac{\sqrt{3}(x_2^2 - x_1^2)}{4},$$

$$Q_{22} = \frac{1}{8}[9(x_2^5 - x_1^5) - 10(x_2^3 - x_1^3) + 5(x_2 - x_1)],$$

$$Q_{33} = \frac{1}{8}[25(x_2^7 - x_1^7) - 42(x_2^5 - x_1^5) + 21(x_2^3 - x_1^3)],$$

$$Q_{44} = \frac{1}{128}[1225(x_2^9 - x_1^9) - 2700(x_2^7 - x_1^7) + 1998(x_2^5 - x_1^5) - 540(x_2^3 - x_1^3) + 81(x_2 - x_1)],$$

$$Q_{02} = \frac{\sqrt{5}}{4}[x_2^3 - x_1^3 - (x_2 - x_1)],$$

$$Q_{03} = \frac{\sqrt{7}}{16}[5(x_2^4 - x_1^4) - 6(x_2^2 - x_1^2)],$$

$$Q_{04} = \frac{3}{16}[7(x_2^5 - x_1^5) - 10(x_2^3 - x_1^3) + 3(x_2 - x_1)],$$

$$Q_{12} = \frac{\sqrt{15}}{16}[3(x_2^4 - x_1^4) - 2(x_2^2 - x_1^2)],$$

$$Q_{13} = \frac{\sqrt{21}}{36}[9(x_2^5 - x_1^5) - 11(x_2^3 - x_1^3)],$$

$$Q_{14} = \frac{\sqrt{3}}{32}[35(x_2^6 - x_1^6) - 45(x_2^4 - x_1^4) + 9(x_2^2 - x_1^2)],$$

$$Q_{23} = \frac{\sqrt{35}}{16}[5(x_2^6 - x_1^6) - 7(x_2^4 - x_1^4) + 3(x_2^2 - x_1^2)],$$

$$Q_{24} = \frac{3\sqrt{5}}{32}[15(x_2^7 - x_1^7) - 25(x_2^5 - x_1^5) + 13(x_2^3 - x_1^3) - 3(x_2 - x_1)],$$

$$Q_{34} = \frac{\sqrt{7}}{256}[15(x_2^8 - x_1^8) - 1020(x_2^6 - x_1^6) + 630(x_2^4 - x_1^4) - 108(x_2^2 - x_1^2)],$$

where, under the conditions used in [1, 2, 29] for the angles given by Eq. (4), we have $x_1 = (1 - b/E)^{1/2}$, and $x_2 = (1 - \bar{a}/E)^{1/2}$.

REFERENCES

1. N. I. Romanyuk, F. F. Papp, J. A. Mandy, *et al.*, in *Proceedings of the 17th International Conference on Physics of Electron and Atom Collision (ICPEAC), Brisben, Australia, 1991*, p. 145.
2. N. I. Romanyuk, O. B. Shpenik, F. F. Papp, *et al.*, Ukr. Fiz. Zh. **37** (11), 1639 (1992).
3. V. I. Kelemen, E. Yu. Remeta, and E. P. Sabad, in *Physics of Electron and Atom Collision* (FTI, Leningrad, 1991), No. 12, p. 152.
4. V. I. Kelemen, E. Yu. Remeta, and E. P. Sabad, J. Phys. B **28**, 1527 (1995).
5. I. V. Chernyshova, A. I. Imre, J. E. Kontros, *et al.*, in *Proceedings of the 20th International Conference on Physics of Electron and Atom Collision (ICPEAC), Vienna, 1997*, p. MO156.
6. I. V. Chernyshova, J. E. Kontros, and O. B. Shpenik, in *Proceedings of the 21st International Conference on Physics of Electron and Atom Collision (ICPEAC), Sindai, Japan, 1999*, p. 403.
7. E. Yu. Remeta, Yu. Yu. Bilak, and L. L. Shimon in *Proceedings of the 21st International Conference on Physics of Electron and Atom Collision (ICPEAC), Sindai, Japan, 1999*, p. 404.
8. O. B. Shpenik, N. M. Erdevdy, and T. Yu. Popik, Zh. Tekh. Fiz. **67** (5), 103 (1997) [Tech. Phys. **42**, 550 (1997)].
9. O. B. Shpenik, N. M. Erdevdy, N. I. Romanyuk, *et al.*, Prib. Tekh. Éksp., No. 1, 109 (1998).
10. M. M. Erdevdy, O. B. Shpenik, V. M. Feyer, *et al.*, in *Proceedings of the 21st International Conference on Physics of Electron and Atom Collision (ICPEAC), Sindai, Japan, 1999*, p. 720.
11. I. P. Zapesochnyĭ and O. B. Shpenik, Ukr. Fiz. Zh. **43** (11), 1363 (1998).
12. I. I. Fabrikant, *Atomic Processes* [in Russian] (Zinatne, Riga, 1975), p. 80.
13. W. C. McCurdy, J. C. Laderdale, and R. S. Mowrey, J. Chem. Phys. **75**, 1835 (1981).
14. M. Ya. Amus'ya, V. A. Sosnivker, N. A. Cherepkov, *et al.*, Zh. Tekh. Fiz. **55**, 2304 (1985) [Sov. Phys. Tech. Phys. **30**, 1369 (1985)].
15. M. Ya. Amus'ya, V. A. Sosnivker, N. A. Cherepkov, *et al.*, Preprint No. 863, FTI im. A.F. Ioffe, AN SSSR (Ioffe Physicotechnical Institute, Academy of Sciences of USSR, Leningrad, 1983).
16. N. I. Romanyuk, O. B. Shpenik, and I. P. Zapesochnyĭ, Pis'ma Zh. Éksp. Teor. Fiz. **32** (7), 472 (1980) [JETP Lett. **32**, 452 (1980)].
17. G. F. Gribakin, V. K. Ivanov, and M. Yu. Kuchiev, in *Physics of Electron and Atom Collision* (FTI, Leningrad, 1991), No. 12, p. 77.
18. V. I. Kelemen, E. Yu. Remeta, and E. P. Sabad, in *Proceedings of the 16th International Conference on Physics of Electon and Atom Collision (ICPEAC), New York, 1989*, p. 868.
19. V. I. Kelemen, E. Yu. Remeta, and E. P. Sabad, Zh. Tekh. Fiz. **61** (2), 46 (1991) [Sov. Phys. Tech. Phys. **36**, 150 (1991)].
20. H. A. Kurtz and K. D. Jordan, J. Phys. B **14**, 4361 (1981).

21. A. R. Johnston, G. A. Gallup, and P. D. Burrow, Phys. Rev. A **40**, 4770 (1989).

22. S. N. Kazakov and O. V. Khristoforov, Opt. Spektrosk. **54**, 750 (1983) [Opt. Spectrosc. **54**, 443 (1983)].

23. D. G. Pegg, R. N. Thompson, and G. D. Alton, Phys. Rev. Lett. **59** (20), 2267 (1987).

24. C. Froese Fischer, J. B. Lagowsky, and S. H. Vosko, Phys. Rev. Lett. **59** (20), 2263 (1987).

25. A. E. Litherland, L. R. Kilius, M. A. Gaewan, *et al.*, J. Phys. B **24**, L233 (1991).

26. A. Stamatovic and G. J. Schultz, Rev. Sci. Instrum. **41**, 423 (1970).

27. N. I. Romanyuk, Candidate's Dissertation (Leningrad State University, Leningrad, 1981).

28. A. R. Johnston and P. D. Burrow, J. Electron Spectrosc. Relat. Phenom. **25**, 119 (1982).

29. N. I. Romanyuk, F. F. Papp, I. V. Chernyshova, *et al.*, in *Physics of Electron and Atom Collision* (FTI, St. Petersburg, 1991), Vol. 12, p. 174.

30. N. I. Romanyuk and O. B. Shpenik, Meas. Sci. Technol. **5**, 238 (1994).

31. P. G. Burke, *Potential Scattering in Atomic Physics* (Plenum, New York, 1977).

32. Yu. Yu. Bilak and E. Yu. Remeta, *Naukovi Pratsi IEF'96, Uzhgorod, 1996*, p. 244.

33. E. Yu. Remeta and Yu. Yu. Bilak, in *Proceedings of the 2nd Photon and Electron Collision with Atoms and Moleculs (PECAM), Belfast, 1996*, p. 35.

34. E. Yu. Remeta, Yu. Yu. Bilak, and L. L. Shimon, in *Proceedings of the 20th International Conference on Physics of Electron and Atom Collision (ICPEAC), Vienna, 1997*, p. TH013.

Translated by S. Gorin

Technical Physics, Vol. 46, No. 4, 2001, pp. 386–390. Translated from Zhurnal Tekhnicheskoĭ Fiziki, Vol. 71, No. 4, 2001, pp. 23–27.

The Electromagnetic Field in the Plasma Jet of a Microwave Plasmatron

A. Ya. Kirichenko, A. P. Motornenko, A. F. Rusanov, O. A. Suvorova, and V. M. Yakovenko

Usikov Institute of Radiophysics and Electronics, National Academy of Sciences of Ukraine, Kharkov, 61085 Ukraine
e-mail: shig@ire.kharkov.ua

Received May 12, 2000

Abstract—A coaxial microwave plasmatron operating at a frequency of 10 GHz is investigated. The microwave field distribution in the plasma jet of the plasmatron is studied using a vibrating string as a small perturbation source. The phase structure of the microwave field inside the plasma is found to differ from that on the outer side of the plasma jet boundary. A slow surface electromagnetic wave propagating along the plasma jet is observed. *© 2001 MAIK "Nauka/Interperiodica".*

INTRODUCTION

Sources of a dense low-temperature plasma (plasmatrons) are widely used in physical experiments and engineering. In these devices, a cold working gas is blown through the discharge region. In the 1970s, it was shown that a cw 3-cm-wavelength microwave source could be used to produce a steady-state flow of a strongly nonequilibrium cold plasma at atmospheric pressure [1, 2]. The electrodynamic structure of such a plasmatron is a coaxial-to-waveguide junction. The working gas (argon) is introduced into the plasmatron through a hollow inner conductor of the coaxial line. A laminar plasma jet is a continuation of the inner conductor. The spectral and electric parameters of the plasma jet in various modes of plasmatron operation were studied in [1, 2]. In those papers, it was shown that at a magnetron wavelength of 3 cm and a power of up to 10 W, a laminar flow of high-brightness microwave discharge plasma is formed by the free outflow of argon into atmospheric air at a rate of 0.2–0.6 l/min. The plasma jet diameter is less than 1 mm, and the jet length attains 10 mm. The plasma electron temperature is $\sim 10^4$ K, the gas temperature at the plasma jet axis is 600–1000 K, and the plasma electron density is higher than 10^{14} cm^{-3}. In view of the unique parameters of such a plasmatron, it was suggested to use it as a light source for spectral analysis and as a plasma gas heater for the automated soldering of multilayer printed circuit boards. It should be noted that nonequilibrium steady-state plasma sources still attract great interest (see, e.g., [3, 4]).

The authors of [1, 2] believe that plasma is produced due to the high electric field strength in the jet. However, the data on the structure of electromagnetic fields in the microwave plasmatron under consideration are still lacking. This is explained, first of all, by the fact that the diameter of the plasma jet is significantly smaller than the wavelength of the electromagnetic field producing the discharge. The longitudinal size of the plasma jet is significantly smaller than this wavelength, whereas the transverse size of the jet is one and one-half orders of magnitude smaller than the wavelength. An additional difficulty is that the discharge is produced in free air, in which case there are only few methods for studying microwave fields. We note that the electrical plasma parameters in a microwave plasmatron under consideration meet the conditions for the propagation of a surface electromagnetic wave. The unique parameters of the plasma jet are expected to be caused by a slow surface wave propagating in a plasmatron.

The goal of this study is to investigate the microwave field parameters both inside and outside the plasma jet and examine the possibility of the existence of an intense surface electromagnetic wave propagating along the plasma jet.

SURFACE WAVE FEATURES IN A SMALL-RADIUS PLASMA CYLINDER

Surface electromagnetic waves play an important role in various electromagnetic processes in bounded plasmas. The propagation of these waves was studied in detail, e.g., in [5, 6]. In those papers, the waveguide properties of a bounded cold isotropic plasma were also studied. Several specific cases in which the dispersion relations could be solved analytically were thoroughly investigated. An analysis of the dispersion relation of a microwave plasmatron plasma jet, which has a shape of a finite-length cylinder and is characterized by certain specific parameters, requires applying numerical methods.

We consider an infinitely long plasma cylinder of radius a (with permittivity ε_1) surrounded by air

1063-7842/01/4604-0386$21.00

($\varepsilon_2 = 1$). We assume the plasma to be cold and uniform and take into account particle collisions. The propagation of a surface electromagnetic wave in such a structure can be described by the following dispersion relation [5]:

$$\left[1 - \frac{\omega_p^2}{\omega(\omega + i\nu)}\right]\frac{\chi_2 I_1(\chi_1 a)}{\chi_1 I_0(\chi_1 a)}\frac{K_0(\chi_2 a)}{K_1(\chi_2 a)} + 1 = 0, \quad (1)$$

where $\omega_p = \sqrt{4\pi e^2 N_e/m}$ is the plasma frequency; ω is the circular frequency of the surface electromagnetic wave; $\chi_\alpha = \sqrt{q_z^2 - k_\alpha^2}$; $k_\alpha^2 = \varepsilon_\alpha \omega^2/c^2$; $\alpha = 1, 2$ (the z-axis is directed along the plasma cylinder); q_z is the longitudinal wavenumber; $I_0(\chi_1 a)$ and $I_1(\chi_1 a)$ are the modified Bessel functions of the first kind; $K_0(\chi_2 a)$ and $K_1(\chi_2 a)$ are the modified Bessel functions of the second kind; ν is the effective collision frequency; N_e is the plasma electron density; e and m are the electron charge and mass, respectively; and c is the speed of light in vacuum.

The phase velocity of the electromagnetic wave is

$$v = \omega/\mathrm{Re}\, q_z. \quad (2)$$

Figure 1 shows the normalized phase velocity of the electromagnetic wave v/c as a function of ω_p^2/ω^2. The curves are obtained by numerically solving Eq. (1) for plasma cylinders with $a/\lambda = 0.01$ (solid curves) and 3 (dashed curves) (where $\lambda = 2\pi c/\omega$). The wave phase velocities are calculated for $\nu/\omega = 0$ (no collisions; curves *1*, *1*'), 2×10^{-1} (curves *2*, *2*'), and 1 (curves *3*, *3*').

It is seen that for both plasma cylinders, the condition for the propagation of a surface electromagnetic wave in the absence of collisions ($\nu/\omega = 0$) corresponds to the well known inequality

$$\omega^2 \le \omega_p^2/2. \quad (3)$$

For a thin plasma cylinder (curve *1*), the wave phase velocity is considerably less than for a wide plasma cylinder (curve *1*'). Under actual plasma conditions ($\nu/\omega \neq 0$), collisions substantially hinder the excitation of a slow surface electromagnetic wave in a wide plasma cylinder (curves *2*', *3*'). This case is an analogue to a semibounded plasma in plane geometry. At $\nu/\omega = 1$ for this cylinder (curve *3*'), the wave phase velocity is close to the speed of light at all values of ω_p^2/ω^2 for which surface waves exist.

In contrast, for a thin plasma cylinder at the same values of ν/ω (curves *2* and *3*), the surface wave is slowed within a wide range of ω_p^2/ω^2. Even at $\nu/\omega = 1$, the normalized phase velocity can be as low as $v/c \approx 0.1$.

For a surface electromagnetic wave in a thin cylinder and $\omega_p^2/\omega^2 = 80$–300, the relative skin depth is $D/a \approx 1$–0.3 and the normalized attenuation length is $l/\lambda \approx 0.1$–1. Therefore, for medium values of ω_p^2/ω^2 within this range, the skin layer in a thin plasma cylinder can be ignored and the wave propagation can be examined on a short plasma segment of length $L \le \lambda/2$. This conclusion is consistent with the results of many experiments with microwave plasmas.

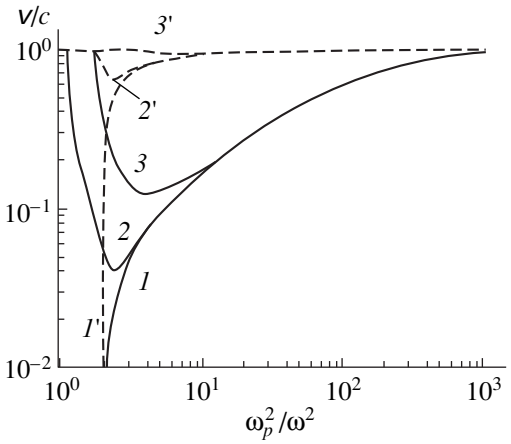

Fig. 1. Calculated dependences of the normalized electromagnetic wave phase velocity v/c on the ratio ω_p^2/ω^2 for $\nu/\omega = (1, 1')\ 0, (2, 2')\ 2 \times 10^{-1}$, and $(3, 3')\ 1$.

EXPERIMENTAL TECHNIQUE

The design of a microwave plasmatron under consideration and its power supply circuit are described in detail in [1, 2]. To measure the microwave fields in the plasmatron jet, a directional coupler was introduced in the microwave waveguide connecting the magnetron with the plasma source. The coupler recorded both the reference and information signals. For comparison, a metal conductor was substituted for the plasma jet and the fields excited along the conductor were studied. The electric component of the microwave field in free space near the nozzle (both inside and outside the plasma jet) was examined by perturbing the field with a small test body. A steel string 0.3 mm in diameter and 180 mm in length was used for this purpose. String vibrations were excited using an electromagnet supplied from an audio frequency oscillator. The same signal was used to synchronize the horizontal sweep of an oscilloscope. The oscilloscope was used to record the signal from a detector placed in the metering arm of the directional coupler. The reference signal from the plasmatron nozzle outlet was applied to this arm of the coupler. The amplitude and phase of this signal were constant. The signal reflected by the vibrating string was also applied to the metering arm of the directional coupler. Parameters of this signal depended on the electric field to be measured.

The amplitude of the signal reflected from a test body and recorded by the receiver is proportional to the strength of the microwave electric field at the site of the test body. The reference signal applied to the detector was summed with the signal from the test body with allowance for the phase difference between these signals. Therefore, the video signal on the oscilloscope screen indicated not only the change in the field strength amplitude along the test body trajectory, but also a possible change in phase. Thus, the amplitude–phase structure of the field under study was observed on the oscilloscope screen. The amplitude of vibrations of the metal string was up to 10 mm. The microwave signal reflected from the test body was amplitude modulated at the string vibration frequency. This signal was viewed on the oscilloscope screen, while the reference signal was cut off by a transfer capacitance at the oscilloscope input. The metering circuit used for field measurements in the near field of emitters in free space is described in more detail in [7].

RESULTS AND DISCUSSION

A plasma jet generated in the plasmatron under study had the shape of a slightly tapered cylinder with a diameter of 0.5–0.8 mm (depending on the power supply mode). The plasma jet length depended on the microwave power of the generator and the argon flow rate. In our experiments, the plasma jet length attained 3–8 mm.

Microwave measurements showed that the major fraction of the power supplied to the discharge (more than 90%) was expended on generating and maintaining the discharge. Only a small fraction of the supplied power (less than 2–3%) was emitted into free space by the plasma antenna, and 7–8% of the supplied power was reflected from the plasmatron nozzle back to the magnetron. When the plasma jet was replaced with a copper wire of the same length, the power emitted into free space increased by two orders of magnitude, provided that the power supplied from the magnetron remained almost unchanged. This fact confirms the conclusion that the major fraction of power is absorbed in the plasma jet. The dependence of the emitted power on the emitter length was almost the same for both the plasma jet under conditions of a stable discharge and a metal wire simulating the plasma jet.

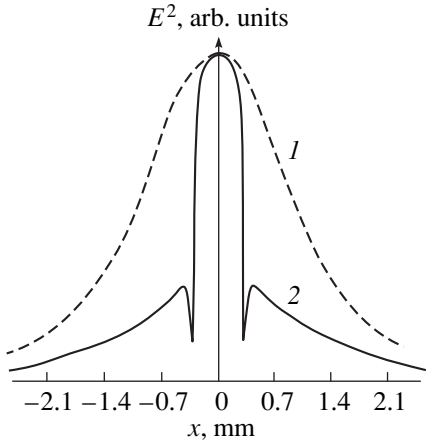

Fig. 2. Electric field profile (*1*) in the absence and (*2*) in the presence of a discharge.

In the absence of a microwave discharge and metal antenna, the electromagnetic field virtually did not extend beyond the plasmatron nozzle (the electromagnetic field outside the nozzle could be detected only within a distance comparable to the diameter of the outer nozzle electrode). Figure 2 shows the profile of the electric field squared (E^2) across the plasma jet at a distance z = 0.5 mm from the nozzle (curve *1*). After igniting a microwave discharge, a sharp increase in the electromagnetic field was observed both near the nozzle and at a considerable distance from the nozzle outlet. The transverse profile of the electric field squared in the presence of a microwave discharge with diameter of 0.7 mm at a distance z = 3 mm is also shown in Fig. 2 (curve *2*). It should be noted that the amplification of curve *1* is 25 times greater than that for curve *2*. We also note that a jump in the electric field was observed at the point where the test body emerged from the plasma.

The amplitude–phase structure of the microwave field in several cross sections of the plasma jet are shown in Fig. 3. A plasma jet length of L = 5 mm was obtained at the magnetron power P = 7 W and argon flow rate V = 0.6 l/min. As is seen from Fig. 3, the field phase at the beginning of the plasma jet differs by 180° from that at the end of the jet. In all cross sections, the field inside the plasma jet is far greater than the field on the outer side of the plasma boundary. A jump in the field strength was universally observed at the plasma boundary. A slight asymmetry of the field profile at the plasma jet boundary at the beginning of the jet is caused by a slightly asymmetric arrangement of the inner electrode of the coaxial line. The field profile asymmetry disappears as the distance from the plasmatron nozzle increases. In all experiments, the maximum value of the field in the discharge was attained near the nozzle. The phase of the maximum field coincided with the phase of the reference signal.

These specific features manifest themselves most clearly when measuring the field distribution along the plasma jet axis. Figure 4 shows the amplitude–phase structure of the microwave field along the plasma jet axis (curves *1*), the longitudinal profile of the maximum field value on the outer side of the plasma boundary (curves *2*), and the amplitude–phase structure of the field along a copper wire substituted for the plasma jet (curves *3*). The curves shown in Fig. 4a were obtained for a plasma jet and metal wire 3 mm in length and an argon flow rate of 0.05 l/min. The curves shown in Fig. 4b were obtained for a plasma jet and metal wire 7 mm in length and an argon flow rate of 0.7 l/min. In both cases, the generator power was P = 8 W.

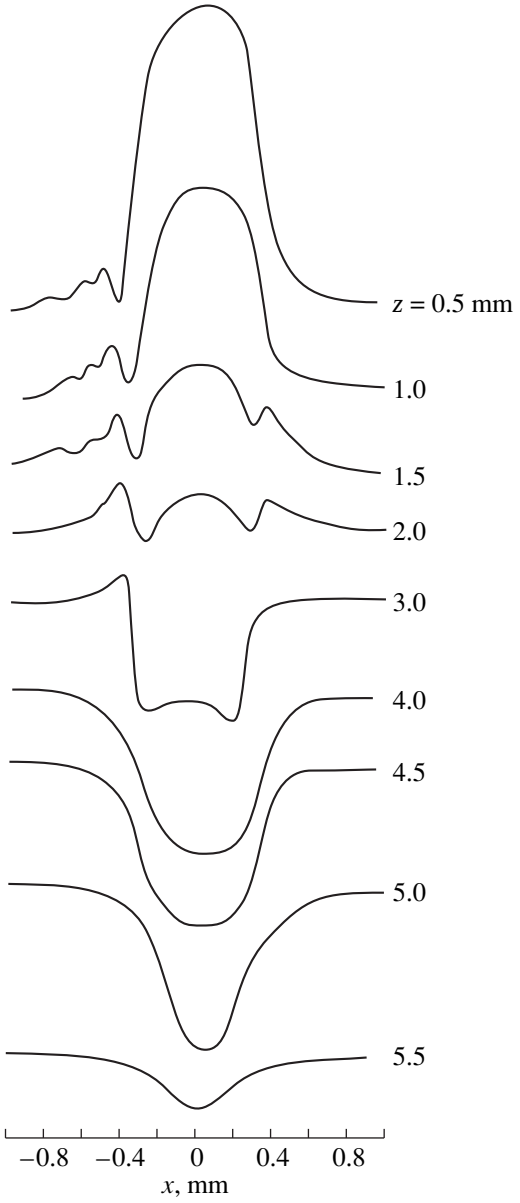

Fig. 3. Electric field profile in several cross sections of the plasma jet for P = 7 W, V = 0.6 l/min, and L = 5 mm.

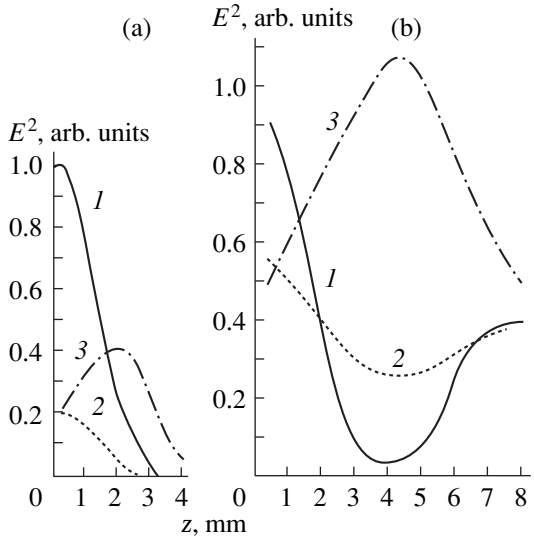

Fig. 4. Amplitude–phase structure of the electromagnetic field for (a) the plasma jet length L = 3 mm and argon flow rate V = 0.05 l/min and (b) L = 7 mm and V = 0.7 l/min.

The amplitude–phase structure of the field measured in experiments with a plasma jet differ both quantitatively and qualitatively from those obtained in experiments with a metal wire of the same length. The field strength near the surface of the metal wire can be either greater or less than the field strength inside the plasma jet, depending on the jet length. The field on the outer side of the plasma boundary is always much smaller than that on the surface of a metal wire or inside the plasma. This is because the microwave energy is mainly concentrated in the plasma and is spent on maintaining the plasma flow.

The difference in the phase structures of the fields should also be taken into account. For a metal wire with a very low resistivity, the wave reflected from the free end of the wire affects strongly the field distribution. The field phase near the nozzle outlet (z = 0) depends strongly on the wire length L (Figs. 4, curves *3*). It should be noted that the amplitude–phase measurements of the field distribution along a copper wire that was longer than the wavelength of the electromagnetic field in vacuum allowed us to reliably determine the wavelength and phase shift of the excited field near the nozzle outlet for various wire lengths.

On the other hand, the electromagnetic field in the plasma was maximum near the nozzle independent of the power supply mode and the plasma jet length. This fact indicates that the reflected wave is absent and the microwave power losses in the plasma are significant (i.e., the plasma jet is well matched with the microwave waveguide).

It was suggested in the literature (see, e.g., [8]) that variations in the microwave field outside the plasma flow reflect the structure of the microwave field inside the flow. Our experiments demonstrate that this is not universally true.

The measurement of the standing wave distribution along a metal wire simulating the plasma jet allowed us to determine the wavelength of the propagating wave (λ = 31 mm). It is seen in Fig. 4a that the wavelength inside the plasma is approximately half as long as the wavelength of the wave propagating along a metal wire. Therefore, the phase velocity of the wave in the plasma jet is approximately half as high as the phase velocity of the wave propagating along a metal wire. The latter may be a surface electromagnetic wave propagating along the plasma jet with the electron density far exceeding the critical value (in our case, $N_e = 1.2 \times 10^{12}$ cm^{-3}). It is seen in Fig. 1 that, for the charged par-

ticle density in the plasmatron jet $N_e = 10^{14}$–4×10^{14} cm^{-3} [2] and $\nu \approx \omega$, the normalized phase velocity v/c of the surface electromagnetic wave falls within a range from 0.5 to 0.7. Taking into account that the model under consideration (a uniform plasma cylinder with a sharp boundary) is rather rough, these results can be regarded as agreeing well with the experimental data.

CONCLUSION

Our study has shown that a vibrating string can be used to measure the microwave field in a plasmatron jet. This method allows one to determine the specific features of the microwave field distribution both inside and outside the plasma jet.

The phase structure of the microwave field inside the plasma is found to differ from the phase structure of the field on the outer side of the plasma jet boundary. Our experiments confirm that the major fraction of electromagnetic energy is absorbed by the plasma jet. A high-amplitude slow surface electromagnetic wave propagating along the plasma jet is observed. It is reasonable to suggest that this surface wave is the cause of the unique geometric and electric parameters of the plasmatron jet.

REFERENCES

1. S. P. Martynyuk, A. P. Motornenko, and A. Ya. Usikov, Dokl. Akad. Nauk Ukr. SSR, Ser. A: Fiz.-Mat. Tekh. Nauki, No. 8, 734 (1975).
2. S. P. Martynyuk and A. P. Motornenko, Dokl. Akad. Nauk Ukr. SSR, Ser. A: Fiz.-Mat. Tekh. Nauki, No. 2, 161 (1978).
3. A. N. Didenko, E. A. Vinogradov, G. A. Lyakhov, *et al.*, Dokl. Akad. Nauk **344**, 182 (1995) [Phys. Dokl. **40**, 452 (1995)].
4. A. N. Kozlov, G. A. Lyakhov, I. V. Pavlov, *et al.*, Pis'ma Zh. Tekh. Fiz. **25** (13), 27 (1999) [Tech. Phys. Lett. **25**, 517 (1999)].
5. A. N. Kondratenko, *Surface and Body Waves in Bounded Plasma* (Énergoatomizdat, Moscow, 1985).
6. W. Shuman, Z. Naturforsch. A **5** (4), 181 (1950).
7. A. Ya. Kirichenko and O. A. Suvorova, in *Proceedings of the 3rd International Symposium "Physics and Engineering of Millimeter and Submillimeter Waves," Kharkov, 1998*, Vol. 2, p. 742.
8. S. Miyake, S. Takeuchi, and Y. Arata, Jpn. J. Appl. Phys. **13**, 296 (1974).

Translated by K. Chamorovskiĭ

Technical Physics, Vol. 46, No. 4, 2001, pp. 391–399. Translated from Zhurnal Tekhnicheskoĭ Fiziki, Vol. 71, No. 4, 2001, pp. 28–35.

Relaxation of the Electron Temperature in an Inert-Gas Afterglow Plasma at Elevated Pressures

N. A. Gorbunov, N. B. Kolokolov, and F. E. Latyshev

Institute of Physics, St. Petersburg State University, St. Petersburg, 198904 Russia

e-mail: gorbunov@paloma.spbu.ru

Received March 29, 2000; in final form, June 28, 2000

Abstract—The relaxation of the electron temperature T_e in helium and neon afterglow at elevated pressures is studied theoretically and experimentally. It is shown that the processes in which fast electrons are produced are accompanied by the heating of thermal electrons. The high-energy part of the electron energy distribution function is studied in the intermediate regime (between the local and nonlocal regimes) of its formation. It is shown that, in this case, the calculated effective energy transferred from the fast electrons to the thermal electrons depends substantially on the wall potential of the discharge tube. Comparison of these calculations with experiments testifies to the reliability of the probe technique for measuring T_e in an afterglow at elevated pressures.

INTRODUCTION

In recent years, much attention has been paid to studies of plasmas that are characterized by active processes leading to the generation of fast electrons. Among such processes are chemoionization reactions

$$A^* + A^* \longrightarrow \begin{cases} A^+ + A + \mathbf{e} \\ A_2^+ + \mathbf{e} \end{cases} \quad (1)$$

and collisions of the second kind between the excited atoms and slow electrons,

$$A^* + e \longrightarrow A + \mathbf{e}. \quad (2)$$

Here, A^* and A are the atoms in the excited and ground states, respectively; A^+ and A_2^+ are the atomic and molecular ions; and **e** is the fast electron (with energy much higher than the mean energy of the bulk electrons) that is produced in reactions (1) or (2). Although various excited states may be involved in reactions (1) and (2), the main attention in studying an electric-discharge afterglow plasma is paid to the elements that have metastable states (inert gases, mercury, etc.). This choice is motivated by the fact that, because of the relatively high density of metastable particles in the plasma, the active reactions (1) and (2) with the participation of these particles may substantially affect the optical and electron-kinetic characteristics of the plasma.

Reactions (1) and (2) and their role in the formation of the electron energy distribution function (EEDF) in inert-gas afterglow plasmas have thoroughly been studied at low pressures, in which case diffusion toward the wall of the gas-discharge tube plays a decisive role in the balance of excited and charged particles ($pR \le 1$ torr cm, where p is the neutral gas pressure and R is the radius of the gas-discharge tube). The results of these studies are generalized in [1]. The EEDF was experimentally measured using the conventional Langmuir probe technique modified for time-resolved measurements. It was revealed that the electron energy distribution is formed in the nonlocal regime; i.e., the EEDF at a given point is determined by the plasma parameters throughout the entire discharge [2, 3]. It was shown that, under these conditions, the EEDF consists of two characteristic components and, for its theoretical description, can be represented as the sum

$$f(\varepsilon) = f_{es}(\varepsilon) + f_{ef}(\varepsilon), \quad (3)$$

where $f_{es}(\varepsilon)$ is the EEDF of the bulk electrons, which obey the Maxwellian distribution, because of the dominant role of electron–electron collisions in the thermal energy range; and $f_{ef}(\varepsilon)$ is the EEDF of the nonequilibrium fast electrons produced in reactions (1) or (2).

It was shown that the high-energy part of the EEDF affects the electron temperature T_e of the bulk electrons, the processes of step excitation, and the diffusion of charged particles. The average energy of fast electrons $\bar{\varepsilon}_{ef}$ may be on the order of the energy with which they are produced ($\bar{\varepsilon}_{ef} \sim 10$ eV). The heating of thermal electrons by fast electrons depends substantially on both the degree of ionization in the plasma and the rates of diffusion of charge particles toward the wall. In this case, the value of T_e can be several times higher than the temperature of heavy particles.

The influence of reactions (1) and (2) on the afterglow at elevated pressures is not as well studied. The reason is that, to date, there have been no reliable experimental methods for measuring the EEDF at such pressures. As the parameter pR increases, the regime of

EEDF formation changes. The role of diffusion decreases in comparison with the processes occurring in the plasma volume. When theoretically describing the electron energy distribution, one can use the local model, which significantly simplifies the analysis. On the other hand, as the gas pressure increases, the role of various plasmochemical processes occurring in the plasma volume (the conversion of atomic ions and excited atoms into molecular ions and excited molecules, dissociative recombination, etc.) increases. These processes, in turn, affect the temperature T_e and must be incorporated in the theoretical analysis.

In an inert-gas afterglow plasma, conditions can arise such that the high-energy part of the EEDF is formed in the nonlocal regime, whereas for the low-energy electrons, the criterion of the local EEDF formation is satisfied. However, studies devoted to the peculiarities of the electron energy balance under conditions when the nonlocal regime of the EEDF formation changes to the local regime are still lacking.

In this paper, we analyze the influence of the reactions in which fast electrons are produced on the relaxation of the electron temperature in an afterglow plasma in the intermediate regime (between the nonlocal and local regimes) of EEDF formation. The relevant studies were conducted in helium and neon. First, the problem of the relaxation of the electron temperature is important for applications, because these gases are frequently used as buffer media in high-power gas lasers [4]. The mechanism for creating the inversion in those devices depends substantially on charged-particle recombination, which, in turn, depends strongly on the temperature of bulk electrons. Second, afterglow discharges are often used to study various elementary processes (recombination, collisions of electrons with excited atoms, etc.) occurring in a plasma [5]. For the most part, in the literature, estimates for the heating of thermal electrons by fast electrons are only presented. For this reason, the problem of constructing a simplified model of the EEDF formation such that T_e can be determined from the energy balance equation [6] is important. Here, we present the results of the comparison of the experimental values of T_e and the measured distribution of fast electrons with theoretical predictions for the intermediate case between the nonlocal and local regimes of EEDF formation, which is the most difficult for analysis.

Until now, the measurements of T_e at elevated pressures were performed using microwave techniques, which only provide information about the volume-averaged plasma parameters. This is a rather complicated technical problem [5]. In [7], the probe technique was developed for EEDF measurements in a helium afterglow at elevated pressures (20 and 40 torr). Under these conditions, the probe could not be used as a conventional Langmuir probe (because, in this case, $a \gg \lambda$, where a is the probe radius and $\lambda(\varepsilon)$ is the electron mean free path) and the experimental procedure was based on the measurements of $f(eV) \sim i'/V$ (the EEDF was proportional to the first derivative of the probe current i' with respect to the probe potential relative to the plasma V). It was shown that, in the thermal energy range, the EEDF was Maxwellian. It was also found that, the value of T_e was higher than the atom temperature T_a at times $t \leq 500$ μs after switching off the discharge. However, the problem of the mechanism for heating thermal electrons was not addressed and systematic measurements of T_e were not performed. For this reason, one of the aims of this paper is to assess the reliability of the T_e measurements from the first derivative of the probe current in an afterglow discharge at elevated pressures by comparing them with the results of calculations.

EXPERIMENTAL SETUP

Experiments were carried out in a cylindrical glass tube with an inner radius of $R = 0.6$ cm and a length of $L = 22$ cm. A repetitive electric discharge in the tube was produced with a pulsed power source. The EEDF and the electric field inside the tube were measured by movable electric probes of radius $a = 0.045$ mm and length $l = 2.5$ mm. The electric circuit for the measurements of the *I–V* characteristic is described in detail in [8]. Under these experimental conditions, the probe radius was on the order of or larger than the electron mean free path $\lambda(\varepsilon)$. Therefore, to measure the EEDF in the thermal energy range, we used the method proposed in [9] and developed in [7] for non-Langmuir probes at $a \gg \lambda(\varepsilon)$, which makes it possible to determine the EEDF from the first derivative of the probe current. The electron temperature was deduced from the experimental dependences of $\ln(i'/V)$ on V. To avoid the systematic error of this method in determining T_e at $a \sim \lambda(\varepsilon)$, as well as in measuring the high-energy part of the EEDF from the second derivative of the *I–V* characteristic of the probe, we introduced corrections to the electron current following from the general probe theory [7].

Measurements of the density of excited atoms at the discharge-tube axis were performed using the absorption technique. We used a cell branch in which a low-current RF discharge was ignited as the probing light source. The presence of this discharge had no influence on the plasma parameters in the main tube. Optical signals were recorded with a gated photon-counting detector.

The electron density was determined from the plasma conductivity. For this purpose, an additional voltage pulse was applied at a certain instant during the afterglow in order to produce a weak longitudinal electric field [10].

To study the reactions involving metastable helium and neon atoms, it is necessary to satisfy stringent requirements of the concentration of impurity gases. The electron produced in the Penning reaction with the participation of metastable atoms and impurities may have an uncontrollable influence on the plasma proper-

ties. For this influence to be neglected, the impurity density must be lower than the density of excited atoms ($\sim 10^{11}$ cm^{-3}). With this purpose, before spectrally pure inert gases were injected into the cell, they were additionally cleaned and passed through activated carbon cooled to cryogenic temperatures. To maintain the high purity of inert gases in the discharge tube, getter electrodes were used.

ANALYSIS OF THE PROCESSES AFFECTING THE RELAXATION OF THE ELECTRON TEMPERATURE

To specify the problem, all subsequent estimates are made for the typical regimes under study: the gas pressure is $p = 20$ torr and the electron density n_e in the afterglow varies from 2.3×10^{12} to 2×10^{11} cm^{-3} for helium and from 2×10^{11} to 10^9 cm^{-3} for neon.

Analysis showed that, among the processes leading to the energy loss of thermal electrons, we may neglect diffusion cooling and electron–ion collisions, whereas elastic electron–atom collisions play a decisive role. The time behavior of T_e was determined from the energy balance equation which, under conditions of interest, takes the form

$$\frac{3}{2}\frac{dT_e}{dt} = -\delta\langle\nu_{ea}(T_e)\rangle(T_e - T_a) + \sum_k\left(N_k\sum_{n\neq k}\Delta E_{kn}\beta_{kn}(T_e)\right) + \frac{1}{N_e}\sum_i \varepsilon_{ef} I_i, \quad (4)$$

where $\delta = 2m/M$ is the fraction of energy transferred from electrons to atoms in elastic collisions; m and M are the electron and atom masses, respectively; $\langle\nu_{ea}(T_e)\rangle$ is the frequency of elastic electron–ion collisions averaged over the Maxwellian distribution; T_a is the neutral gas temperature; the second term on the right-hand side of Eq. (4) describes the change in the electron energy after the transition of an atom from kth state (with energy E_k and population N_k) to the nth state (with energy E_n); $\beta_{kn}(T_e)$ is the rate constant of the transition $k \longrightarrow n$; $\Delta E_n = E_n - E_k$ is the energy gap between the levels; the last term on the right-hand side of Eq. (4) describes the heating of thermal electrons by fast electrons; and I_i and ε_{ef} are the production rate and effective energy of the fast electrons, respectively.

Let us consider each term in more detail. For a helium afterglow, the rate constants of elementary processes were taken from [5] (unless otherwise specified). To calculate $\langle\nu_{ea}(T_e)\rangle$, we used the data on the cross sections for elastic electron–atom collisions from [11]. The estimate of gas heating shows that, under our conditions, when the mean value of the current during the discharge is $I_d \sim 1.5$ mA, the difference between the gas temperatures at the axis and on the wall is 4 K. For this reason, we neglected variations in the gas temperature in the afterglow and assumed $T_a = 300$ K.

Among inelastic collisions with thermal electrons, we analyzed the processes with the participation of excited atoms and atomic and molecular ions. According to the bottleneck approximation [12], the change in the energy H_{rec} due to impact–radiative recombination (summed over the upper levels) has the form

$$H_{\text{rec}} = E_R\alpha_{\text{rec}}(T_e)n_e N^+, \quad (5)$$

where E_R is the energy of the level separating the energy spectrum of an atom into the regions in which collisional or radiative kinetics is dominant, $\alpha_{\text{rec}}(T_e)$ is the three-body recombination coefficient, and N^+ is the density of positive atomic ions.

The impact processes are dominant above E_R, whereas the radiative quenching of excited states is dominant below E_R. The value E_R was calculated by the formulas of a modified diffusion model [12]. The above process is of importance in the early phase ($t < 100$ μs) of a helium afterglow. The density of He^+ ions was calculated from the corresponding balance equation taking into account the ion loss due to three-body recombination, ambipolar diffusion and conversion into molecular ions, and the ion production in chemoionization reactions.

In neon, the decrease in the charged-particle density is determined by dissociative recombination from the ground vibrational state of Ne_2^+ molecular ions. Estimates of the increase in T_e due to the loss of low-energy electrons in this reaction show that this process can be neglected in comparison with heating by fast electrons.

Under the conditions of interest, the molecular ions are produced in highly excited vibrational states whose energy differs from the dissociation energy D_i by the value $\sim T_a$ due to either the conversion of atomic ions (the characteristic conversion time is $\tau_c \sim 40$ μs) or reaction (1). The relaxation of the vibrationally excited states occurs in collisions with both atoms and electrons. The question of the rate of vibrational relaxation of molecular helium or neon ions in their collisions with the parent gas atoms still remains open [13, 14]. Thus, in [13], the vibrational relaxation constant is estimated to be $k_a^{1,0} < 10^{-14}$ cm^3/s (the transition $v = 1 \longrightarrow v = 0$) for helium and $k_a^{1,0} = 5 \times 10^{-15}$ cm^2/s for neon. In [14], it is believed that these processes proceed more rapidly ($k_a^{1,0} \approx 10^{-13}$ cm^3/s). The value of the relaxation constant of vibrationally excited He_2^+ ions by electron impact at $T_e \sim 300$ K is equal to $k_e^{1,0} \approx 10^{-7}$ cm^3/s [15], whereas the corresponding constant for neon is $k_e^{1,0} \approx 1.3 \times 10^{-7}$ cm^3/s [13]. Calculations show that, in the early phase of a helium afterglow ($t < 50$ μs), the relaxation of vibrationally excited molecular ions is determined by their collisions with electrons and contributes nearly 10% to the total heating of thermal electrons.

Varying the value of the atom-impact relaxation rate constants within the range $k_a^{1,0} = 10^{-14}$–10^{-13} cm^3/s slightly affects the relaxation of T_e at times $t > 50$ μs. For a neon afterglow, the dominant process is the atom-impact relaxation of molecular ions. For the degree of ionization of a neon plasma under our experimental conditions, the processes with the participation of molecular ions can be neglected in the energy balance equation.

Analysis show that, among the deexcitation processes, the mixing of metastable He(2^1S) and He(2^3S) states ($\Delta E = 0.8$ eV) may contribute appreciably in T_e (nearly 5–10%) in the early phase ($t < 50$ μs) of a helium afterglow. For a neon plasma, excitation from the lower metastable state Ne($^3P_2$) $\longrightarrow$ Ne($^3P_1$) plays a significant role. The constant of this process is equal to $\beta_{21} = 1.25 \times 10^{-7}\exp(-\Delta E_{21}/T_e)$, where $\Delta E_{21} = 0.052$ eV [16, 17].

An inert-gas afterglow at intermediate and high pressures is characterized by a relatively high density of metastable atoms and, for helium, by a high density of atoms and $He_2(a^3\Sigma_u^+)$ molecules. The fast electrons are produced at a rate of $I_{11} = \beta_e N_i n_e$ in collisions of the second kind and at a rate of $I_{ch} = \sum_{ik}\beta_{ik} N_i N_k$ in chemoionization reactions, where N_i and N_k are the metastable particle densities and β_e and β_{ik} are the constants for collisions of the second kind and for chemoionization, respectively. The energy spectrum width for the fast electrons produced in reaction (2) is equal to $\sim T_e$, and that for the fast electrons produced reaction (1) is on the order of 1 eV, which is substantially lower than the initial electron energy value. Consequently, when theoretically analyzing the high-energy part of the EEDF, we may assume that, under our conditions, the sources of fast electrons are monoenergetic. In this case, the effective energy contributed by the fast electrons with the initial energy ε' to the system of slow electrons is equal to [18]

$$\varepsilon_{ef} = \int_0^{\varepsilon'} \frac{\nu_{ee}}{\nu_{ee} + \delta\nu_{ea}} \exp\left(-\int_\varepsilon^{\varepsilon'} \frac{d\varepsilon}{\varepsilon k(\varepsilon)}\right) d\varepsilon, \qquad (6)$$

where $\nu_{ee}(\varepsilon)$ and $\nu_{ea}(\varepsilon)$ are the frequencies of the electron–electron and elastic electron–atom collisions,

$$k(\varepsilon) = (\nu^* + \nu_{ee} + \delta\nu_{ea})\tau_{df}. \qquad (7)$$

Here, ν^* is the frequency of inelastic collisions, $\tau_{df}(\varepsilon) = \Lambda^2/D_e(\varepsilon)$ is the time of free electron diffusion toward the tube wall, Λ is the diffusion length, and $D_e(\varepsilon) = 2\varepsilon/3\nu_{ea}(\varepsilon)$ is the electron diffusion coefficient.

In our calculations, we assumed that the initial energy of fast electrons produced in reaction (1) is equal to ε' = 14.6 eV for helium and ε' = 11.7 eV for neon; in reaction (2), these energies are ε' = 19.8 and 16.6 eV, respectively.

For a helium afterglow, calculations yield $k(\varepsilon') \approx 3$ and $\nu_{ee}(\varepsilon') < \delta\nu_{ea}(\varepsilon')$. The values of $k(\varepsilon)$ increase at $\varepsilon < \varepsilon'$. This allows us to conclude that $f_{ef}(\varepsilon)$ in this regime is formed locally ($k \gg 1$) and the exponent in the integrand of expression (6) for calculating ε_{ef} can be set to be unity. In the local model, the effective energy is determined by the initial energy of fast electrons and the degree of ionization of the gas and is independent of the rate of free diffusion of electrons toward the tube wall. For a helium afterglow, the effective energy is in the range $4 < \varepsilon_{ef} < 12$ eV, depending on the afterglow phase.

The main source of fast electrons in a neon afterglow is chemoionization reactions. Estimates show that $k(\varepsilon') \approx 0.3$ and $k(1\text{ eV}) \approx 0.3$–5. Thus, under these conditions, we have an intermediate case between the local and nonlocal regimes of the formation of $f_{ef}(\varepsilon)$. Calculation of the effective energy with the use of expression (6) yields values in the range $0.015 < \varepsilon_{ef} < 0.25$ eV, depending on the neon afterglow phase. This indicates that most of the fast electrons are lost on the wall of the discharge tube. Calculation of ε_{ef} according to the local model gives values higher by a factor of 20–80. Such a substantial difference is related to the fact that, in the local model, only the relaxation of the energy of fast electrons in the volume, which leads to electron or gas heating, is taken into account.

The question of the character of electron diffusion is important for describing nonlocal features of the EEDF. The fast electrons move toward the tube wall in the regime of free diffusion only when their kinetic energy exceeds the wall potential $e\varphi_w$. If their kinetic energy is less than $e\varphi_w$, they cannot reach the wall and the time of their free diffusion is formally infinite. In this case, when calculating ε_{ef} from expression (6), we divide the integration interval into two subintervals: $0 < \varepsilon \le e\varphi_w$, in which the local model is valid ($k(\varepsilon) \longrightarrow \infty$), and $e\varphi_w \le \varepsilon \le \varepsilon'$, in which expression (6) can be used with $k(\varepsilon)$ defined by formula (7). Therefore, in order to calculate the effective energy, it is necessary to know the wall potential, which is a priori unknown.

The problem of the wall potential under afterglow conditions with allowance for the fast-electron sources was considered in [19–21]. The quantity φ_w is the sum of the ambipolar and wall potential drops (φ_{es} and φ_{eh}) and is determined from the condition that the electron and ion fluxes (Γ_e and Γ_i) toward the wall are equal to each other. The flux Γ_e consists of the fluxes of thermal and fast electrons (Γ_{es} and Γ_{ef}). For the nonlocal case ($k(\varepsilon') \ll 1$), we may assume that all the fast electrons escape onto the wall. Thus, their influence may be estimated using the parameter $P = \Gamma_{ef}/\Gamma_i \approx \bar{I}\,\tau_{da}/\bar{n}_e$, where $\bar{I}$ and $\bar{n}_e$ are the radius-averaged source of fast electrons and the average electron density, respectively;

$\tau_{da} = \Lambda^2/D_a$ is the ambipolar diffusion time; $D_a = D_i(1 + T_e/T_i)$ is the ambipolar diffusion coefficient; and D_i is the ion diffusion coefficient. For $P \ll 1$, the fast electrons contribute insignificantly to the total electron flux toward the wall and the value of φ_w is determined by thermal electrons and is equal to ~(6–10)T_e. For $P > 1$, in order for the electron and ion fluxes toward the wall to neutralize each other, φ_{eh} should increase to such high values that a fraction of fast electrons is locked in the volume and a continuous EEDF is formed. Previously, the regime with a potential jump near the wall was observed in a xenon afterglow plasma at low pressures ($k(\varepsilon') \ll 1$) [20] at times $t > 200$ μs after the end of the current pulse.

From the above estimate of the parameter P, it follows that, at elevated pressures, when $k(\varepsilon') \le 1$ and the ambipolar diffusion rate is reduced, the probability of the occurrence of the regime with a potential jump increases. In fact, calculations show that, in a neon afterglow, as early as 50 μs after the end of the current pulse, we have $P \approx 10$ and, consequently, the regime with a potential jump near the wall is realized. To experimentally verify the regime of the formation of $f_{ef}(\varepsilon)$, we measured the high-energy part of the EEDF at the axis and compared it with that calculated by formula [20]

$$f_{ef}(\varepsilon) = \frac{\bar{I}_{ch}(\varepsilon_2')}{\varepsilon^{3/2}(\bar{\nu}_{ee} + \delta\nu_{ea})}\exp\left(-\int_{\varepsilon}^{\varepsilon_2'}\frac{d\varepsilon}{\varepsilon k(\varepsilon)}\right), \qquad (8)$$

where $\bar{\nu}_{ee}$ and $\bar{I}_{ch}(\varepsilon_2')$ are the averaged (over the cross section of the tube) electron–electron collision frequency and the averaged rate of production of fast electrons in chemoionization reactions with the initial energy $\varepsilon_2' = 11.7$ eV, respectively.

To determine φ_w, we use the fact that Γ_i is equal to Γ_{ef}. The ambipolar ion flux per unit length of the tube is determined by the radial profile of the density of slow electrons $n_e(r)$ and is equal to

$$\Gamma_i = 2\pi R D_a \left.\frac{\partial n_i(r)}{\partial r}\right|_{r=R}. \qquad (9)$$

In calculations, we took into account the deflection of the $n_i(r)$ profile from the Bessel distribution $J_0(\mu r/R)$ [22], where $\mu = 2.4$ is the first root of the zero-order Bessel function. This deflection is caused by the intense dissociative recombination of electrons and Ne_2^+ molecular ions. In the initial afterglow phase ($t \le 100$ μs), the recombination rate at the tube axis was 10–20 times higher than the decay rate of the main diffusion mode. The profile formed due to recombination decreases less slowly in the center of the tube and drops more rapidly at the periphery as compared to the main diffusion mode. In our case, such a profile increases the flux toward the wall in comparison with the purely diffusive distribution by a factor of up to 1.5 [22].

Since the dominant mechanism for the loss of fast electrons is related to diffusion toward the tube wall, their distribution was assumed to be close to $J_0(\mu r/R)$ when calculating Γ_{ef}. Note that, although the distribution function at $\varepsilon > e\varphi_w$ is nonlocal, we use the kinetic energy as its argument, which, in the case of an afterglow plasma under consideration, almost coincides with the total energy, because of the small value of the radial ambipolar field. The latter is determined by the temperature of slow electrons and is on the order of kT_e/e, which is substantially less than ε_2'/e. In agreement with formula (8), the flux Γ_{ef} is determined by the averaged (over $f_{ef}(\varepsilon)$) rate at which fast electrons escape from the plasma volume [20]:

$$\Gamma_{ef} = 2\pi R J_1(\mu)\int_{e\varphi_w}^{\varepsilon_2'} D_e(\varepsilon) f_{ef}(\varepsilon)\sqrt{\varepsilon}\,d\varepsilon, \qquad (10)$$

where $J_1(2.4) = 0.52$.

This expression is the upper estimate and may exceed the actual value by 30–40%. The reasons are, first, that we neglect the difference between the total and kinetic energies (due to slowing down the electrons by the ambipolar field) and second, that the source of fast electrons is located near the axis and the radial distribution of fast electrons can be narrower than $J_0(\mu r/R)$, which increases the diffusion time. However, the previous measurements of the radial dependence under consideration [20, 21] confirm that the value $\mu = 2.4$ used by us is a close approximate.

Figure 1 shows the results of measurements of $f_{ef}(\varepsilon)$ in a neon afterglow at the tube axis at $\tau = 100$ μs. The EEDF was determined from the second derivative of the probe current, because the solution of model problems showed [7] that this method ensured a smaller error in comparison with the first-derivative method. However, the method used yields underestimated (by a factor of 2–3 at low energies) values of the EEDF in comparison with the actual EEDF. Here, we also present the results of two calculations of the EEDF that were made with different values of φ_w. In the first case (curve *2*), $\varphi_w = \varphi_{es} = 5T_e \approx 0.3$ eV. In this case, a depletion of the EEDF in the range $0.5 \le \varepsilon \le 11$ eV due to electron diffusion toward the wall is observed in the relaxation stage. In the second case (curve *3*), the value of φ_w was determined by solving the set of equations for T_e together with the equality $\Gamma_{ef} = \Gamma_i$, which gave $\varphi_w = 9.5$ eV. In this case, most of the fast electrons are locked in the volume by the wall potential jump and the number of fast electrons increases substantially. Comparison shows that calculations with allowance for the wall potential jump correlate with the measured high-energy part of the EEDF. Under the assumption that the

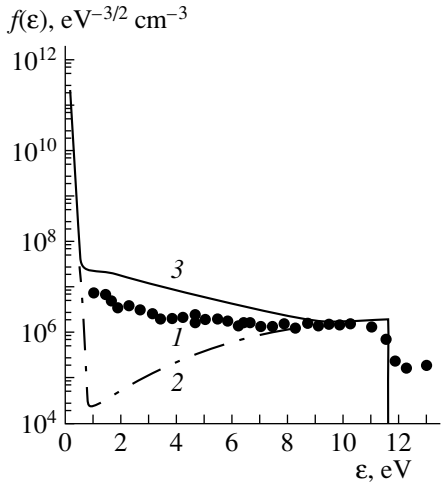

Fig. 1. EEDF in a neon afterglow: (*1*) experimental result and the results of calculations for the wall potential φ_w = (*2*) 0.3 and (*3*) 9.5 eV.

wall potential is determined by the flux Γ_{es} (curve *2*), the calculated EEDF has a qualitatively different form, which confirms that, under these conditions, the regime with a wall potential jump is realized.

RESULTS FROM STUDIES OF ELECTRON TEMPERATURE RELAXATION IN HELIUM AND NEON AFTERGLOWS

For a helium afterglow, Eq. (4) together with the balance equations for the density of $He_2(a^3\Sigma_u^+)$ metastable molecules, atomic ions, molecular ions in the ground He_2^+ and vibrationally excited He_2^{+*} states, supplemented with the plasma quasineutrality condition $n_e = [He^+] + [He_2^+] + [He_2^{+*}]$ and the measured values of the metastable-atom densities, form a closed set for calculating T_e. Numerical calculations were performed for the tube axis. The initial electron density was deduced from the plasma conductivity at the end of the discharge pulse. Since the dominant mechanism for the charged-particles loss in the active discharge phase is ambipolar diffusion, the radial electron distribution is close to $J_0(\mu r/R)$. For a pulsed current of I_d = 90 mA, we have $n_e(0) = 2.3 \times 10^{12}$ cm^{-3}. Estimates show that, by the end of the active discharge phase, the molecular-ion density is about 20% of n_e. The initial value of $[He_2^{+*}]$ is determined by the decay of these molecules in the active discharge phase. Under our experimental conditions, $[He_2^{+*}]$ decreases by nearly one-half during the current pulse. Note that varying the initial conditions for $[He_2^{+*}]$, $[He_2^+]$, or $[He_2(a^3\Sigma_u^+)]$ by 50% has little effect on the relaxation of T_e at times $t \geq 30$ μs.

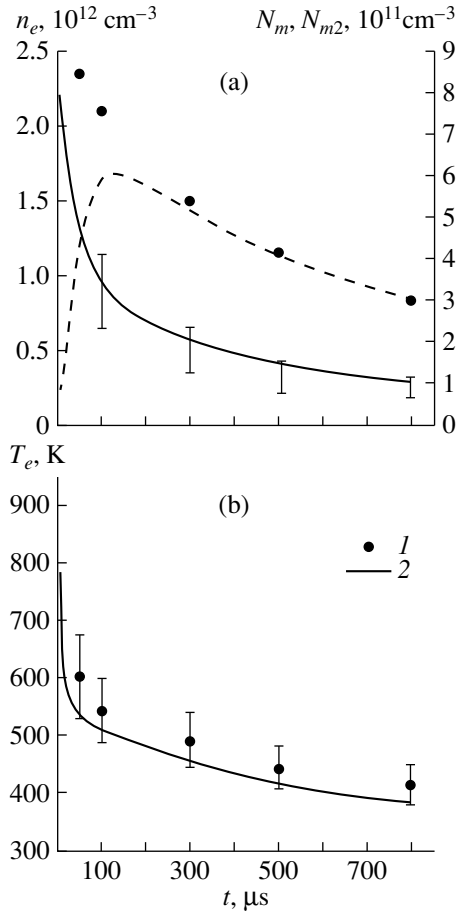

Fig. 2. Plasma parameters in a helium afterglow: (a) densities of the excited and charged particles (the circles show the measured values of $[He(2^3S)]$, the dashed line shows the results of calculations of $[He_2(a^3\Sigma_u^+)]$, and the solid line shows the results of calculations of n_e at the axis; the measured values of the electron density are also shown), and (b) the electron temperature (the circles and the solid line correspond to the experiment and calculations, respectively).

Figure 2a shows the results of calculations of $n_e(t)$ and $[He_2(a^3\Sigma_u^+)(t)]$; for comparison, the experimental values of the electron density at the axis $n_e(0, t)$ are also shown. Since we determine the density $\bar{n}_e(t)$ averaged over the cross section from the plasma conductivity, the density values at the axis $n_e(0, t)$ fall into the range from $\bar{n}_e(t)/0.43$ to $\bar{n}_e(t)/0.8$ shown by bars. As is seen in the figure, the results of calculations of $n_e(t)$ in the initial afterglow phase agree with the experimental values obtained, assuming that the electron density profile is determined by recombination, which correlates with the above estimates. In the later afterglow phase, $n_e(t)$ coincides with the values calculated assuming a Bessel

distribution of charged particles, which is reached for a time $\tau_{da} \sim 10^3$ μs. Hence, the fact that the theoretical description of the relaxation of charged particles agrees well with the experimental results allows us to conclude that the model used is correct.

Figure 2b shows the results of calculations and experimental measurements of T_e. The temperature T_e was determined from the first derivative of the probe current. It is seen from the figure that, in the time interval under study ($t \le 10^3$ μs), T_e is substantially higher than T_a. Since the characteristic time of T_e relaxation due to elastic collisions is estimated as $[\delta\langle\nu_{ea}(T_e)\rangle]^{-1} < 0.5$ μs, the observed difference can be attributed to heating by fast electrons. An analysis shows that, in our case, thermal electrons are mainly heated due to impacts of the second kind with atoms and molecules in metastable states. The theoretical results agree with the experiment.

The accuracy of the experimental measurements of T_e was tested by special measurements in a non-self-sustained discharge. For this purpose, at $t = 400$ μs, a weak electric field was created in the afterglow by applying an additional voltage pulse. In this case, T_e is mainly determined by the value of the electric field E. Figure 3 compares the measured value of T_e with the calculated dependence $T_e(E/p)$. Calculations carried out with allowance for heating by the electric field differs from the experiment by 8%. If additional heating by fast electrons is taken into consideration, then the calculations and experiment coincide within an error of about 4%. This confirms the reliability of the probe method used to determine T_e at elevated pressures.

For a neon afterglow, the measured electron densities and the densities of the atoms in the most populated excited states N^* are shown in Fig. 4a. Since all necessary values of n_e and N^* are known from the experiment and the relaxation time is equal to $[\delta\langle\nu_{ea}(T_e)\rangle]^{-1} \sim 3$ μs, the temperature T_e and the fluxes of charged particles onto the wall were calculated using the quasistatic approximation ($dT_e/dt = 0$).

The temperature T_e was determined from the first derivative of the EEDF. The cross section for elastic collisions for neon in the thermal energy range is five times smaller than that for helium. For this reason, according to the solution of model problems [7], this method leads to an underestimate of T_e by 10% under our experimental conditions ($a \sim \lambda(\varepsilon)$). The obtained results were corrected for this systematical error. As seen from the measurement results presented in Fig. 4b, the difference between T_e and T_a in the early afterglow phase ($t \le 100$ μs) can attain 200 K.

In the thermal energy range, where the electron distribution is Maxwellian, the energy relaxation rate is determined by $\delta\nu_{ea}$ and by the rate ν^* at which the excited states are mixed. Estimates yield the value $k(0.1) \sim (0.3–1)$. In the energy range corresponding to the nonequilibrium formation of the EEDF ($T_e \ll \varepsilon \le \varepsilon'$), the efficiency of energy transfer in the mixing processes decreases with energy as $\Delta E_{21}/\varepsilon$ and $k(\varepsilon)$ is determined by $\delta\nu_{ea}$ and ν_{ee}. Hence, in neon, an intermediate regime (between the local and nonlocal regimes) of the EEDF formation is realized. The high-energy part of the EEDF is mainly formed in the nonlocal regime. In the region where thermal electrons are concentrated in the initial afterglow phase, the local regime of EEDF formation takes place.

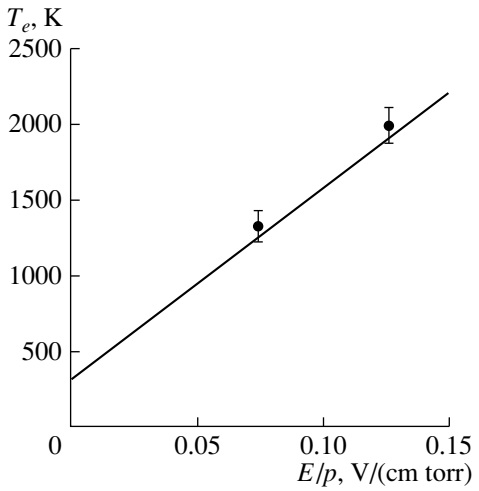

Fig. 3. Electron temperature in a non-self-sustained discharge in helium: the circles and the solid line correspond to the experiment and calculations, respectively.

When calculating T_e, we compared the limiting cases of the local and nonlocal models. The comparison showed a significant difference in the calculated effective energies for the local (ε_l) and nonlocal (ε_{nl}) models. Thus, for $t = 50$ μs, we have $\varepsilon_l = 4.2$ eV and $\varepsilon_{nl} = 0.26$ eV; the difference is more than one order of magnitude. As time increases, this difference increases even more and, at $t = 500$ μs, reaches almost two orders of magnitude: $\varepsilon_l = 1.3$ eV and $\varepsilon_{nl} = 0.015$ eV. This difference significantly affects the calculated T_e values. Calculations by the local model, according to which we used ε_l and the values of n_e and N^* at the axis, give a temperature difference $T_e - T_a$ that is several times greater than the experimental value in the initial afterglow phase (Fig. 4b, ▲). In contrast, calculations by the nonlocal model without allowance for the wall potential jump, according to which we used ε_{nl} and the radius-averaged values of n_e and N^*, cannot explain the experimentally observed difference between T_e and T_a (Fig. 4b, ●).

As was mentioned above, under these conditions, the regime with a potential jump of $\varphi_w \sim 9–10$ eV near the wall takes place. This circumstance substantially increases the value of the effective energy calculated by the nonlocal model. The results of calculations of T_e by

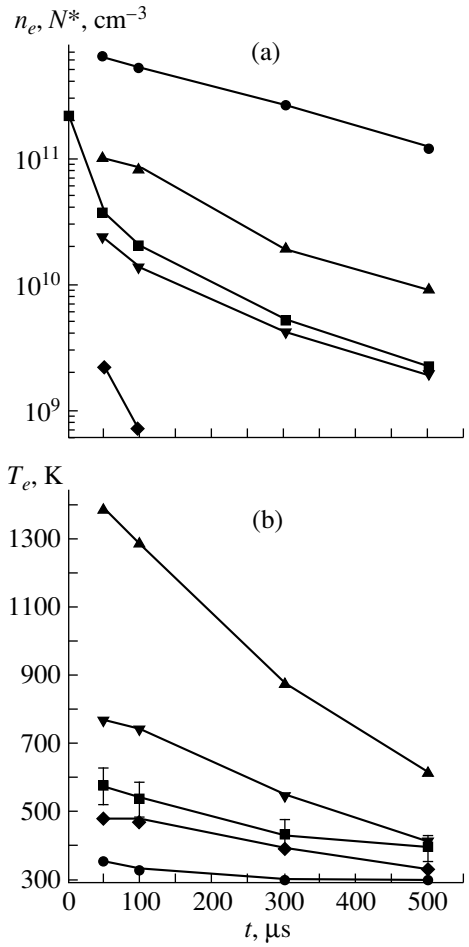

Fig. 4. Plasma parameters in a neon afterglow. (a) The measured densities of the excited and charged particles: (■) n_e, (●) [Ne($^3P_2$)], (▲) [Ne($^3P_1$)], (▼) [Ne($^3P_0$)], and (◆) [Ne($^1P_1$)]; (b) the electron temperature: the experimental results (■) and the temperature T_e at the tube axis calculated by (▲) the local model and (●), (◆), (▼) the nonlocal model for φ_w = (●) 0.3, (◆) 9.5 eV (the value of n_e at the axis is used), and (▼) 9.5 eV (the radius-averaged value of n_e is used).

solving the set of equations for T_e together with the equation for determining φ_w are presented in Fig. 4b (◆ and ▼). In one case (◆), we used the value of n_e at the axis, which corresponded to the local regime in the formation of the energy distribution of thermal electrons. In the second case (▼), we used the radius-averaged value of n_e, which corresponded to the nonlocal regime of formation of the energy distribution of thermal electrons in the later afterglow phase. The corridor between these curves corresponds to an uncertainty in the results of calculations in this intermediate regime of EEDF formation. As is seen, the experimental values lie inside this corridor between the calculated values of T_e. In order to calculate the temperature more accurately, it is necessary to know the radial dependences of the ambipolar potential and the densities of excited atoms and electrons.

CONCLUSION

It is shown that, at elevated pressures, the processes in which fast electrons are produced substantially affect the rate of electron temperature relaxation. The relaxation time is much longer than the characteristic time of electron energy loss due to elastic collisions with atoms. It is found that the wall potential has a strong effect on the electron temperature in the intermediate regime (between the local and nonlocal regimes) of EEDF formation. The increase in the probability of the appearance of a potential jump near the wall at elevated pressures is related to the fact that the ion ambipolar flux toward the wall decreases as compared to that in a low-pressure plasma.

ACKNOWLEDGMENTS

This work was supported in part by the Russian Foundation for Basic Research, project no. 00-02-17662.

REFERENCES

1. N. B. Kolokolov, A. A. Kudrjavtsev, and A. B. Blagoev, Phys. Scr. **50**, 371 (1994).
2. L. D. Tsendin and Yu. B. Golubovskiĭ, Zh. Tekh. Fiz. **47**, 1839 (1977) [Sov. Phys. Tech. Phys. **22**, 1066 (1977)].
3. N. B. Kolokolov, A. A. Kudryavtsev, and V. A. Romanenko, Zh. Tekh. Fiz. **56**, 1737 (1986) [Sov. Phys. Tech. Phys. **31**, 1033 (1986)].
4. L. I. Gudzenko and S. I. Yakovlenko, *Plasma Lasers* (Atomizdat, Moscow, 1978).
5. R. Deloche, R. Monchicourt, M. Cheret, *et al.*, Phys. Rev. A **13**, 1140 (1976).
6. R. R. Arslanbekov and A. A. Kudryavtsev, Phys. Rev. E **58**, 6539 (1998).
7. N. A. Gorbunov, N. B. Kolokolov, and A. A. Kudryavtsev, Fiz. Plazmy **15**, 1513 (1989) [Sov. J. Plasma Phys. **15**, 881 (1989)].
8. N. A. Gorbunov, N. B. Kolokolov, and A. A. Kudryavtsev, Zh. Tekh. Fiz. **58**, 1817 (1988) [Sov. Phys. Tech. Phys. **33**, 1104 (1988)].
9. Yu. B. Golubovskiĭ, V. M. Zakharova, V. N. Pasunkin, and L. D. Tsendin, Fiz. Plazmy **7**, 620 (1981) [Sov. J. Plasma Phys. **7**, 340 (1981)].
10. G. N. Gerasimov, R. I. Lyagushchenko, and G. P. Startsev, Opt. Spektrosk. **30**, 606 (1971).
11. L. G. H. Huxley and R. W. Crompton, *The Diffusion and Drift of Electrons in Gases* (Wiley, New York, 1974; Mir, Moscow, 1977).
12. L. M. Biberman, V. S. Vorob'ev, and I. T. Yakubov, *Kinetics of Nonequilibrium Low-Temperature Plasmas* (Nauka, Moscow, 1982; Consultants Bureau, New York, 1987).
13. V. A. Ivanov, in *Plasma Chemistry*, Ed. by B. M. Smirnov (Énergoatomiztat, Moscow, 1987), Vol. 13, p. 74.

14. G. V. Karachevtsev and V. L. Tal'roze, in *Plasma Chemistry*, Ed. by B. M. Smirnov (Énergoatomiztat, Moscow, 1987), Vol. 14, p. 255.

15. A. A. Bol'shakov and Yu. É. Skoblo, Opt. Spektrosk. **68**, 1248 (1990) [Opt. Spectrosc. **68**, 732 (1990)].

16. N. Pilosof and A. Blagoev, J. Phys. B **21**, 639 (1988).

17. V. A. Ivanov, Opt. Spektrosk. **84**, 709 (1998) [Opt. Spectrosc. **84**, 635 (1998)].

18. A. B. Blagoev, Yu. M. Kagan, N. B. Kolokolov, and R. I. Lyagushchenko, Zh. Tekh. Fiz. **44**, 339 (1974) [Sov. Phys. Tech. Phys. **19**, 215 (1974)].

19. V. I. Demidov and N. B. Kolokolov, Zh. Tekh. Fiz. **50**, 564 (1980) [Sov. Phys. Tech. Phys. **25**, 338 (1980)].

20. V. I. Demidov, N. B. Kolokolov, and O. G. Toronov, Fiz. Plazmy **12**, 702 (1986) [Sov. J. Plasma Phys. **12**, 402 (1986)].

21. N. B. Kolokolov, A. A. Kudryavtsev, and V. A. Romanenko, Zh. Tekh. Fiz. **58**, 2098 (1988) [Sov. Phys. Tech. Phys. **33**, 1274 (1988)].

22. E. P. Gray and D. E. Kerr, Ann. Phys. **17**, 276 (1962).

Translated by N. Larionova

Technical Physics, Vol. 46, No. 4, 2001, pp. 400–403. Translated from Zhurnal Tekhnicheskoĭ Fiziki, Vol. 71, No. 4, 2001, pp. 36–39.

Dispersion Relation for the Lowest Mode of the Ion-Acoustic Instability in a High-Current Ion Laser

V. I. Donin, V. A. Ivanov, and D. V. Yakovin

Institute of Automation and Electrometry, Siberian Division, Russian Academy of Sciences, pr. Acad. Koptyuga 1, Novosibirsk, 630090 Russia

e-mail: donin@iae.nsk.su

Received May 22, 2000

Abstract—The lowest frequency mode of the ion-acoustic instability in a high-current low-pressure wall-confined discharge, which serves as an active medium of cw ion gas lasers, is studied experimentally. The dispersion relation for this mode is obtained using the spectral correlation analysis of spontaneous plasma emission. The dependences obtained are compared with the available theoretical models of ion-acoustic instability in low-pressure discharges. © *2001 MAIK "Nauka/Interperiodica".*

INTRODUCTION

In a nonisothermal plasma of a high-current low-pressure discharge in a cylindrical tube, along with high-frequency ion-acoustic oscillations at frequencies $\omega \lesssim \Omega_i$ (where Ω_i is the ion plasma frequency), low-frequency oscillations at frequencies $\omega \lesssim 10^{-2}\Omega_i$ can also be excited [1–7]. According to [7], these oscillations are excited by the longitudinal discharge current. The threshold current for this instability depends on the gas pressure, discharge diameter, and gas density distribution along the discharge. Increase in the current above the threshold value may result in the destruction of the discharge tube wall [3] and other undesirable effects, such as the limitation on the output power of a cw ion laser [6].

The low-frequency spectra of argon plasma oscillations in discharge tubes 5–30 mm in diameter consist of separate narrow peaks within the range $0.1 \lesssim f \lesssim 2$ MHz (where $f = \omega/2\pi$). The number of peaks increases as the current increases above the threshold value. The results of [7, 8] indicate that the observed frequencies are the lower normal modes of long-wavelength ion-acoustic oscillations in a wall-confined plasma. However, the dispersion relation for these oscillations, which is of importance for understanding and identifying them, was not measured. In this study, which is a continuation of [7, 8], we investigate the frequency and wave-vector spectra of the lowest oscillation mode. The dispersion relation for this mode is determined using the spectral correlation analysis of spontaneous emission from two plasma regions spatially separated along the discharge axis. An important feature of our experimental scheme is the absence of any frequency filters limiting the correlator passband.

EXPERIMENTAL SETUP AND RESULTS

A diagram of the experimental facility for measuring the dispersion relation for plasma oscillations is shown in Fig. 1. Argon plasma is produced by a continuous high-current discharge in a 1-m-long tube with a 16-mm-diameter channel. The tube with a cold arc cathode, which incorporates a self-heated refractory bush, consists of aluminum sections covered with an oxide film and cooled with water [6]. To withdraw plasma emission, two sections of the discharge tube have 4×16-mm slit windows oriented perpendicularly to the discharge axis. These sections are placed near the cathode, where the oscillations are most intense (Fig. 2a). The distance between the windows is 15 cm. For a filling argon pressure of 0.2–0.4 torr (the discharge pressure is much lower, particularly in the cathode region), the threshold discharge current is $I = 300$–400 A. The discharge plasma parameters were as fol-

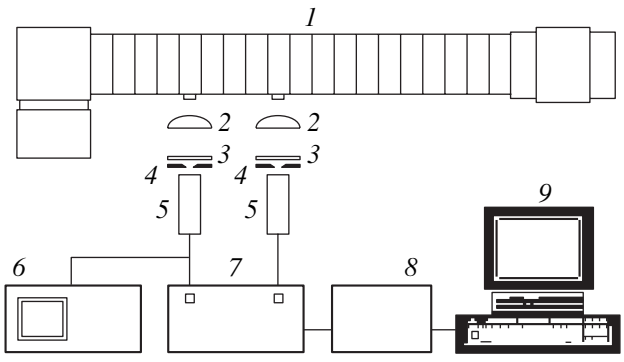

Fig. 1. Schematic of the experimental facility for measuring the spectral and dispersion parameters of oscillations in a high-current plasma: (*1*) discharge tube, (*2*) lenses, (*3*) light filters, (*4*) diaphragms, (*5*) photomultipliers, (*6*) spectrum analyzer, (*7*) correlator, (*8*) analog-to-digital converter, and (*9*) PC.

1063-7842/01/4604-0400$21.00 © 2001 MAIK "Nauka/Interperiodica"

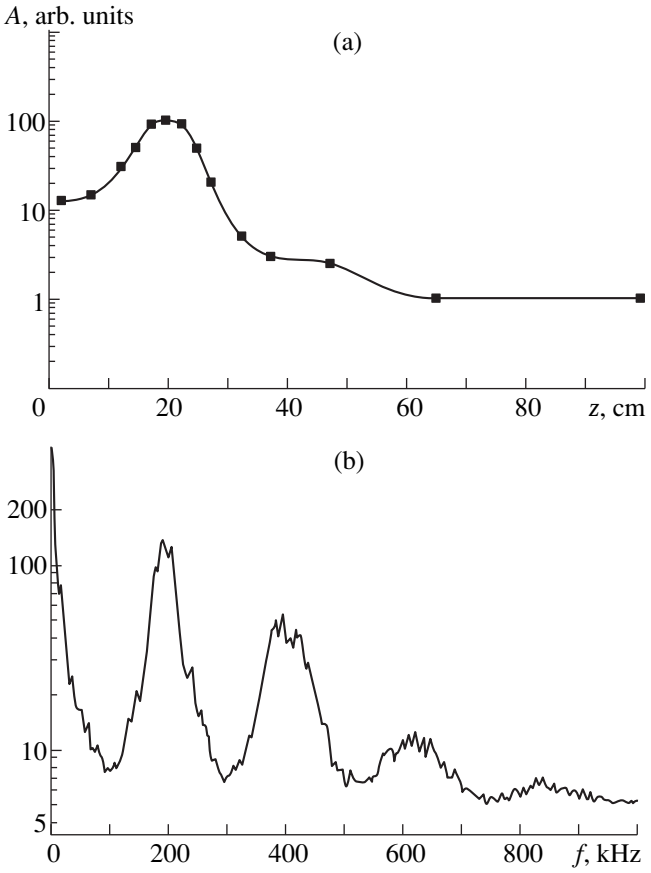

Fig. 2. (a) Profile of the oscillation amplitude A along the discharge axis and (b) the spectrum of low-frequency oscillations.

lows [6]: the electron density was $n_e \simeq 10^{14}$ cm^{-3}, the electron temperature was $T_e \simeq 5$ eV, and the ion temperature was $T_i \simeq 2$ eV. The plasma contained ≃10% doubly-charged ions at the discharge axis.

A typical spectrum of the developed oscillations in an argon plasma is shown in Fig. 2b. Under our experimental conditions (see below), the spectrum consisted of no more than two peaks; i.e., the measurements were carried out near the threshold. Due to the spatial mode structure of oscillations [8], it was possible to adjust the optical tract to select the lowest mode with a frequency of 205 kHz and bandwidth of ≃80 kHz. Spontaneous plasma emission was collected by lenses with focal lengths of 8 mm and, after passing through 1-mm-diameter diaphragms and blue-green light filters, was recorded by two photomultipliers, which operated in a photon-counting mode. The signals from the photomultipliers were fed to the spectrum analyzer with a frequency bandwidth of 0.01–110 MHz and to a high-speed correlator. The correlator with a maximum clock rate of 160 MHz [9] measured the autocorrelation and cross-correlation functions of the electric signals from two windows. The sampling time was $\tau_0 = 0.5$–1.0 μs.

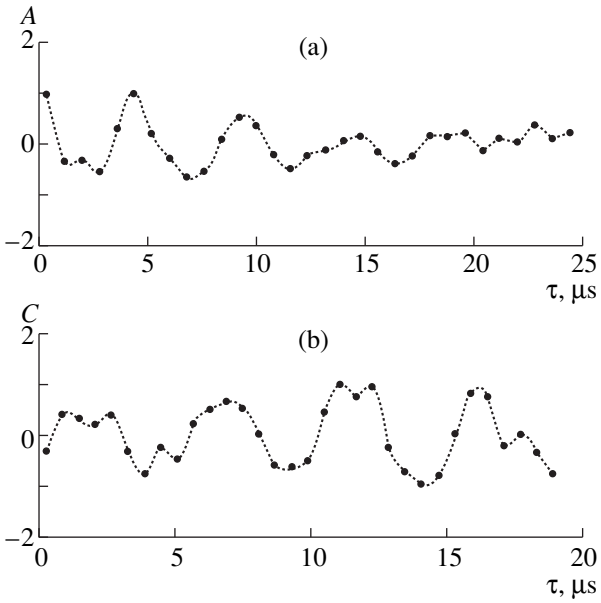

Fig. 3. (a) Autocorrelation and (b) cross-correlation functions of plasma oscillations; τ_0 = (a) 0.8 and (b) 0.6 μs.

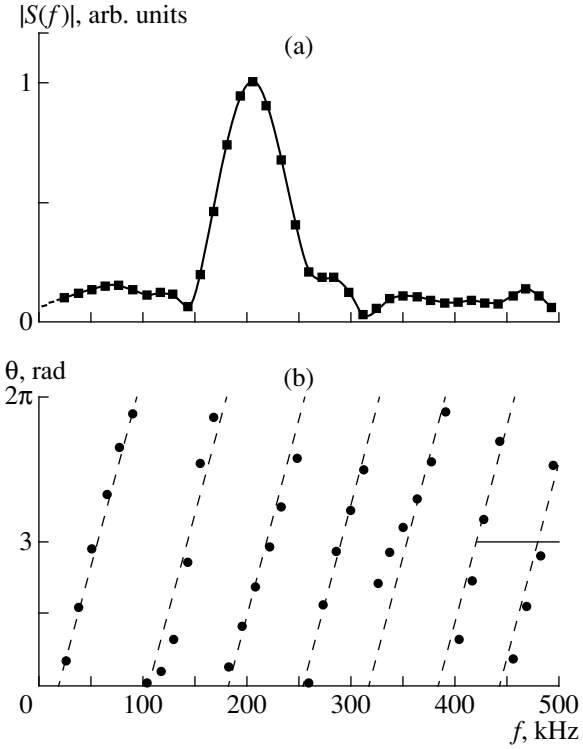

Fig. 4. (a) Modulus and (b) phase angle of the cross-spectral density $S(f)$.

The analyzer output data were recorded by an analog-to-digital converter with a response time no longer than 30 μs and a personal computer.

The recorded emission consists mainly of blue-green lines of the excited argon ions with the density n_i^*. When

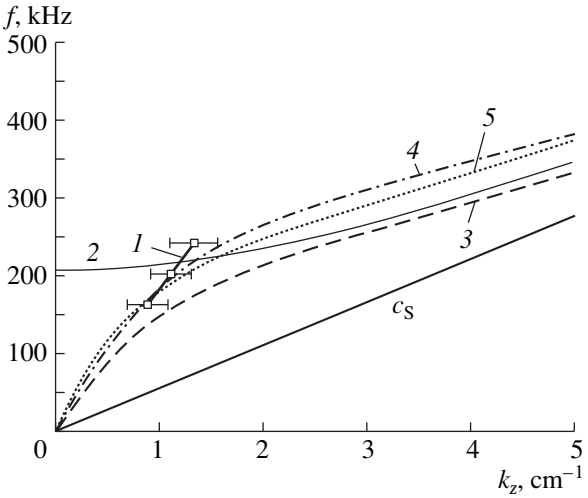

Fig. 5. Oscillation frequency f vs. k_z; (*1*) our experimental results; the closest calculated dependences (the mode numbers are designated as in the sources): (*2*) mode (1,1) [8], (*3*) mode (0,1) [12], (*4*) mode (1,2) [12], and (*5*) mode (0,1) [13].

the excess over the threshold current is not large, the density of ions in the ground state contains a small oscillating term, $n_i(t) = n_i + \tilde{n}_i(t)$, where n_i is a constant term. Under our experimental conditions, we have $n_i^*(t) \sim n_i(t)$, at least for frequencies in the range $f < \beta_i$ (where β_i is the ionization rate) [6]. The oscillation cross-correlation function measured at the points z' and $z' + d$ at the discharge axis ($z > 0$) is

$$C(\tau) = n_i^2 + \lim_{T\to\infty}\frac{1}{T}\int_0^T \tilde{n}_i(\tau, z')\tilde{n}_i(t+\tau, z'+d)dt, \quad (1)$$

where τ is the delay time and T is the averaging time.

Figure 3 presents the normalized autocorrelation and cross-correlation functions measured at the discharge current $I = 380$ A. The shift $\Delta\tau \simeq 12$ μs between the maxima of the autocorrelation and cross-correlation functions indicates that the oscillation propagates along the discharge from the cathode to the anode. The group velocity of oscillations, which was estimated from the shift of the maximum as $d/\Delta\tau$ for different values of I and τ_0, appeared to be $(1.23 \pm 0.25) \times 10^6$ cm/s.

The dispersion relation for the oscillations was determined from the measured correlation functions using spectral analysis [10]. According to the Wiener–Khinchin theorem, the correlation function is related to the spectral density of a stationary random process by the Fourier transformation. The cross-spectral density $S(\omega)$ for the two local processes $\tilde{n}_i(t, z')$ and $\tilde{n}_i(t, z' + d)$ is defined as the Fourier transform of expression (1). The dependence $\tilde{n}_i(t, z)$ can be represented by a wave packet propagating along the discharge axis

$$\tilde{n}_i(t, z) = \int_0^\infty N(\omega)\exp[ik_z(\omega)z - i\omega t]d\omega, \quad (2)$$

where $N(\omega)$ is a slowly varying real function and $k_z(\omega)$ is the longitudinal component of the wave vector **k** as a function of frequency.

The phase angle $\theta(\omega)$ of the complex function $S(\omega)$ (Fig. 4) is related to the delay time corresponding to the propagation of the wave packet from z' to $z' + d$. The local dispersion relation for expression (2) is $k_z(\omega) = \theta(\omega)/d$, where $\theta(\omega)$ is determined from the experiment. The dispersion relation for the lowest oscillation mode obtained from the statistical analysis of experimental data is shown in Fig. 5. The phase velocity is equal to $(1.15 \pm 0.15) \times 10^6$ cm/s, which is much higher than the ion-acoustic velocity $c_s = \sqrt{T_e/M_i} = 3.46 \times 10^5$ cm/s (where M_i is the ion mass) in the plasma under study. Under our conditions, taking into account T_i can increase c_s by a factor of no more than 1.5. The group velocity was estimated as $d\omega/dk = (1.25 \pm 0.28) \times 10^6$ cm/s. The measurements of the spatial radial structure of oscillations [11] showed that, under these conditions, $k_z \simeq |\mathbf{k}| = 2\pi/\lambda$ (where λ is the oscillation wavelength).

DISCUSSION OF THE RESULTS

The dispersion relations for ion-acoustic waves in a bounded low-pressure plasma were first derived in [12], in which the lowest order radial and azimuthal modes were found in the hydrodynamic approximation with allowance for the ion loss at the wall. Later, in [13], the dispersion relations were modified, taking into account volumetric particle collisions, particle drift, and the influence of the external longitudinal magnetic field. At low frequencies, the results obtained in [12] and [13] differ insignificantly (Fig. 5). However, they fail to describe the appearance of the lowest boundary frequencies observed in the experiment. The approximate model [8] explain the existence of these frequencies. The limitation on the lowest frequency also follows from the consideration of a plasma waveguide [14, 15].

AKNOWLEDGMENTS

We are grateful to O.E. Trofimov for fruitful discussions.

REFERENCES

1. A. A. Zaĭtsev and B. N. Shvilkin, Dokl. Akad. Nauk SSSR **172**, 565 (1967) [Sov. Phys. Dokl. **12**, 68 (1967)].
2. F. W. Crawford, Phys. Rev. Lett. **6**, 663 (1961).

3. V. I. Donin, Zh. Éksp. Teor. Fiz. **62**, 1648 (1972) [Sov. Phys. JETP **35**, 858 (1972)].
4. N. P. Gadetskiĭ, Yu. V. Tkach, A. V. Sidel'nikova, and V. P. Zeĭdlits, Ukr. Fiz. Zh. **19**, 931 (1974).
5. H. R. Lüthi and W. Seelig, J. Appl. Phys. **48**, 4922 (1977).
6. V. I. Donin, *High-Power Ion Gas Lasers* (Nauka, Novosibirsk, 1991).
7. G. N. Alferov, V. I. Donin, G. I. Smirnov, and D. A. Shapiro, Kvantovaya Élektron. (Moscow) **6**, 13 (1981) [Sov. J. Quantum Electron. **11**, 5 (1981)].
8. V. I. Donin, D. A. Shapiro, D. V. Yakovin, and A. S. Yatsenko, Zh. Tekh. Fiz. **58**, 80 (1988) [Sov. Phys. Tech. Phys. **33**, 46 (1988)].
9. G. I. Ersh and D. V. Yakovin, Avtometriya, No. 2, 85 (1985) [Optoelectr. Instrum. Data Processing, No. 2, 91 (1985)].
10. J. S. Bendat and A. G. Piersol, *Engineering Applications of Correlation and Spectral Analysis* (Wiley, New York, 1980; Mir, Moscow, 1983).
11. V. I. Donin, V. A. Ivanov, and D. V. Yakovin, Preprint No. 486, IAÉ SO RAN (Institute of Automation and Electrometry, Siberian Division, Russian Academy of Sciences, Novosibirsk, 2000).
12. L. C. Woods, J. Fluid Mech. **23**, 315 (1965).
13. H. N. Ewald, F. W. Crawford, and S. A. Self, Phys. Fluids **12**, 303 (1969).
14. B. Anderson and P. Weissglas, Phys. Fluids **9**, 271 (1966).
15. A. N. Kondratenko, *Plasma Waveguides* (Énergoatomizdat, Moscow, 1976).

Translated by N. Ustinovskiĭ

Technical Physics, Vol. 46, No. 4, 2001, pp. 404–410. Translated from Zhurnal Tekhnicheskoĭ Fiziki, Vol. 71, No. 4, 2001, pp. 40–46.

Evolution of the Density Profiles and Flows of Charged Particles during the Diffusive Decay of an Electronegative Gas Plasma

E. A. Bogdanov*, A. A. Kudryavtsev, and L. D. Tsendin*****

** St. Petersburg State Mining Institute (Technical University), Vtoraya liniya 21, St. Petersburg, 199026 Russia*

*** St. Petersburg State University, St. Petersburg, 198904 Russia*

**** St. Petersburg State Technical University, ul. Politekhnicheskaya 29, St. Petersburg, 195251 Russia*

Received August 28, 2000

Abstract—Different scenarios of the spatiotemporal evolution of the parameters of the diffusive decay of a pulsed electronegative gas plasma in the absence of plasma chemical processes are studied. It is shown that nonlinear diffusion in a plasma with negative ions occurs in several stages. The rate of electron density decay increases with time and, in the beginning of the second stage, almost all the electrons escape from the discharge volume. On the other hand, the ion density profile is smoothed out due to ion–ion ambipolar diffusion and the flow of negative ions toward the wall is absent in the first stage of decay. In the second stage, the main diffusion mode is first established and then the ion–ion (electronless) plasma decays exponentially with a characteristic time determined by ion–ion ambipolar diffusion. © *2001 MAIK "Nauka/Interperiodica".*

The evolution of inhomogeneities of the electron and ion densities in a multicomponent plasma is described by nonlinear equations [1]. Therefore, attempts to reduce the problem to the determination of a set of effective coefficients of ambipolar diffusion for every charged component (as is usually done in the case of a simple plasma) may lead to fundamental errors [1]. It was shown in [1, 2] that the spreading of inhomogeneities in a multicomponent plasma may occur in several stages and is accompanied by the formation of propagating jumps of the ion density. In the simplest case in which no current flows through the system, the mechanism for this phenomenon in electronegative gases is as follows [1–3]. In view of plasma quasineutrality, the most mobile particles (i.e., electrons) must be confined in a plasma and an ambipolar charge-separation field arises, which is determined by the electron temperature T_e and the electron density gradient. In a gas-discharge plasma, T_e is considerably higher than the ion temperature ($T \ll T_e$); hence, the field components of the ion flows substantially exceed the diffusion components and the negative ions are drawn into the discharge volume by the field. As a result, the plasma is divided into regions with different ion compositions and highly inhomogeneous spatial distributions of charged particle densities are formed over the discharge cross section [3]. Under steady-state conditions, the external region (region 1) of an electron–ion plasma is composed of electrons and positive ions ($n_p \sim n_e \gg n_n$), while almost all the negative ions ($n_n \sim n_p > n_e$) are concentrated in the internal region (region 0). The presence of two regions with different spatial distributions and charged particle compositions results in the decay of electronegative gas plasma in two stages (electron–ion and ion–ion stages). In addition, the transition to an ion–ion plasma occurs with a sharpening [4]; i.e., almost all electrons escape from the discharge volume within a finite amount of time.

Since plasma decay in the presence of negative ions is of great practical importance [5–8], it deserves detailed investigation. In this paper, we consider the spatiotemporal evolution of the densities and flows of charged particles during diffusive decay in an electronegative gas plasma in the absence of bulk plasma chemical processes. Such a situation is typical of low-pressure plasmas, in which plasma decay is mainly governed by diffusion. The fact that the rates of many important plasma chemical processes depend strongly on T_e and these processes stop during the afterglow also support this model.

In the case of plane-parallel cold absorbing walls located at $x = \pm L$, the set of equations describing the plasma evolution after switching off the discharge has the form [1, 2]

$$\frac{\partial n_j}{\partial t} = -\frac{\partial}{\partial x}\Gamma_j = \frac{\partial}{\partial x}\left(D_j\frac{\partial n_j}{\partial x} \pm b_j n_j E\right). \qquad (1)$$

Here, Γ is the particle flux; subscripts $j = e$, n, and p refer to electrons and negative and positive ions, respectively; and D and b are the diffusion and mobility coefficients.

The self-consistent (ambipolar) field has the form

$$E = (D_p n_p' - D_n n_n' - D_e n_e')/(b_p n_p + b_n n_n + b_e n_e). \quad (2)$$

Here, the prime stands for the spatial derivative. At the center ($x = 0$), the derivatives are zero (symmetry conditions). The boundary conditions at the wall ($x = L$) in

a plasma with negative ions require more detailed consideration, because the drift component of the flow may be higher than the diffusion component and may have the opposite sign (unlike for positive ions). For this reason, zero boundary conditions for the densities,

$$n_j(L, t) = 0, \quad j = e, n, p, \tag{3}$$

which are usually used when considering the diffusive decay of an ordinary (two-component) plasma, may result in negative values of $\Gamma_n(L, t)$ (the flow is directed from the wall), because field (2) under conditions (3) tends to infinity as $x \longrightarrow L$ and the drift flux of negative ions $b_n n_n(x, t)E$ does not vanish as $x \longrightarrow L$. This is equivalent to the presence of negative ion emission at the wall and can result in the nonphysical growth of the total number of negative ions. This can be easily ascertained by considering the model profiles $n_j(x, t) = \tilde{n}_j(t)\cos(\pi x/(2L))$ for each particle species [9]. These profiles meet the symmetry conditions at the center and the zero conditions at the wall and reduce set (1) to a set of ordinary first-order differential equations for unknown functions $\tilde{n}_j(t)$. If $\tilde{n}_e \simeq \tilde{n}_n$, $b_e \gg b_n \simeq b_p$, and $D_e \gg D_n \simeq D_p$, then calculating the right-hand sides of the set of equations obtained, we can see that $d\tilde{n}_n/dt > 0$ and the integral density of negative ions grows with time. The boundary conditions of the form

$$\Gamma_j(L, t) = C_0 n_j(L, t), \quad j = e, n, p \tag{4}$$

do not have the above drawbacks. They automatically meet the quasineutrality condition and provide both the nonnegative flux of each component and vanishingly small values of $n_j(L, t)$ at high positive values of the constant C_0. Although in the limit $C_0 \longrightarrow \infty$, conditions (4) transform into conditions (3), the above example shows that conditions (3) cannot generally be used. They are degenerate in the sense that the sign of C_0 may be either positive or negative when transiting from conditions (4) to conditions (3). However, a negative flux results in the nonphysical growth of the density of negative ions due to their emission from the walls. If the fluxes of all the components are not negative when using boundary conditions (3), the solutions to set (1) with conditions (3) and (4) coincide. The higher C_0, the higher accuracy of the coincidence. Therefore, in practice, conditions (4) were used only when conditions (3) resulted in solutions with high negative fluxes $\Gamma_n(L, t)$.

The calculated density profiles of a steady-state low-pressure discharge plasma were used as initial conditions. In this case, both the electrons and negative ions obey the Boltzmann distribution in region 0; i.e., the flux Γ_n in the central region can be set at zero. A flat electron profile appears at low pressures [1] when the efficiency of transport processes in the active phase is much higher than that of plasmochemical processes (ionization, attachment, detachment, etc.). In this case, the rate of electron transport is $T_e T_i$ times higher than

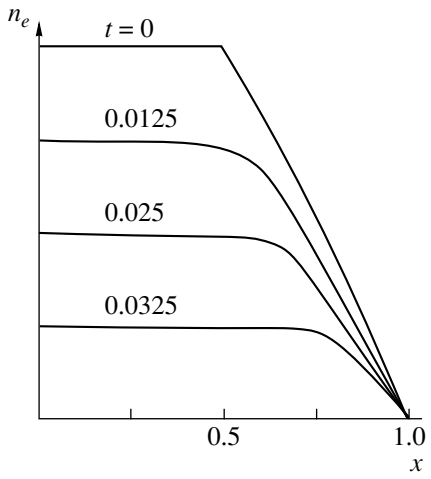

Fig. 1. Evolution of the electron density profile during plasma decay at a high electron temperature ($k = 33$). Here and in the other figures, the ratio of the initial densities is $n_{n0}/n_{e0} = 6$.

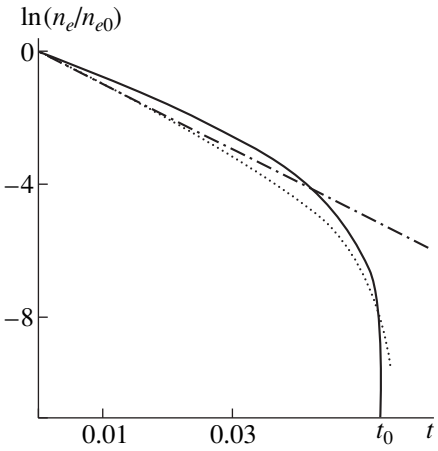

Fig. 2. Time dependence of the central electron density $n_{e0}(t)$ (solid line) and calculations by formula (7) (dotted line) and formula (6) with $x_0(\tau)$ obtained from numerical simulations (dash-dot line).

that of the ion transport, which results in a flat n_e profile in the central region. As the pressure decreases further (we will consider the pressure range that is of greatest practical interest nowadays), ion diffusion comes into play. In this case, negative ions are trapped and the diffusion coefficient of positive ions is equal to $2D_p$. It follows that the initial profile of negative ions is parabolic and the initial profile of electrons is flat [3]. In this case, even a small addition of electrons to the flat n_e profile is sufficient for the Boltzmann potential for electrons to be established. In essence, the potential is determined by the Boltzmann equilibrium for negative ions, while the Boltzmann equilibrium for electrons determines only a small inessential addition to the flat n_e profile.

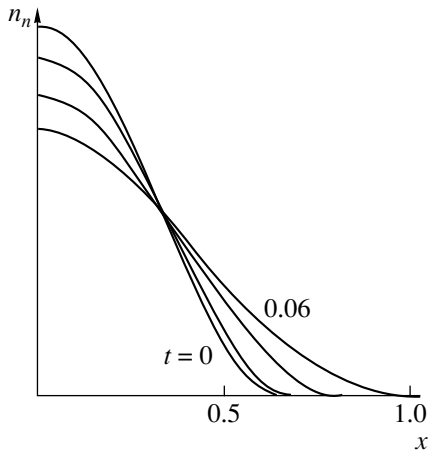

Fig. 3. Evolution of the negative ion density profile for k = 33. Here and in the other figures, the time intervals between the curves are constant.

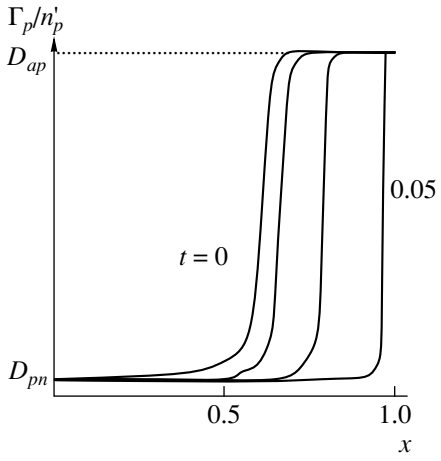

Fig. 4. Profile of the effective diffusion coefficient of positive ions (k = 33).

The typical initial distribution that was used in calculations is shown in Figs. 1 and 3.

The time during which T_e relaxes after switching off the external energy source is known to be much less than the plasma decay time (see, e.g., [10]). On the other hand, the steady-state value of T_e may be much higher than the gas temperature [1]. Therefore, we have considered both moderate ($k \sim 1$) and large ($k \gg 1$) values of the parameter $k = T_e/T$.

The results of calculations show that the density profiles evolve in different ways depending on the value of k and the ratio of the ion mobilities $g = b_p/b_n$. In the simplest case $k \gg 1$, the electron temperature remains high even after switching off the discharge. In practice, this can be achieved when the power supply is not switched off completely. The typical results of calculations for k = 33 and the mobility ratios $g = 1/\sqrt{2}$ and b_e/b_n = 250 are shown in Figs. 1–5. In the figures, the coordinates are in units of L and time is in units of $\tau_n = L^2/D_n$, which is the characteristic time of free diffusion of negative ions.

A specific feature of the decay mode at large k is that the electron density profile in region 0 remains almost flat (as in the active phase). As is seen from Fig. 1, in the course of evolution, only the width x_0 of this region increases; i.e., the ion profile broadens and an unneutralized outflow of negative ions ($\Gamma_n(t) > 0$) appears. This flow violates the initial Boltzmann distribution of negative ions so that, in this case (unlike a steady-state discharge), the ion density profiles cannot be determined from this distribution. However, since $b_e \gg b_n$, electric field (2) still has the form $E = T_e n'_e n_e$ (determined by the Boltzmann equilibrium for electrons) until $n_e b_e > n_n b_n + n_p b_p$, which is valid for the first stage of decay. Then, from the condition $\Gamma_n(t) > 0$, the inequality $|n'_e| < |n'_n| n_e/(kn_n)$ follows, which results in the almost flat electron profile $n_n > n_e$ at large k and $n_e \simeq n_{e0}$.

The change in the central electron density $n_{e0}(t)$ at $k \gg 1$ is shown in Fig. 2. It is seen that over a relatively long time, density decreases exponentially and then drops abruptly at a certain instant t_0. The reason for this almost exactly exponential dependence, which is hardly expected for the solution of a rather complicated set of nonlinear equations (1), is as follows. For a flat electron density profile, the rate $\partial n_e/\partial t$ does not depend on the coordinate at $x < x_0$. Hence, the linear dependence of the electron flux Γ_e on the coordinate follows from balance equation (1) [11]. At the same time, in the external region ($x > x_0$), where ordinary electron–ion ambipolar diffusion with the coefficient $D_{ap} = (k+1)D_p$ takes place, the $n_e(x)$ profile is close to linear. As a result, the electron density n_{e0} (Fig. 2) satisfies the equation

$$\Gamma_e(x_0) = \frac{\partial n_{e0}}{\partial t} x_0 = -D_{ap} n_{e0}/(L - x_0). \qquad (5)$$

From here, it follows that

$$n_e(t) = n_{e0} \exp\left[-D_{ap} \int_0^t \frac{d\tau}{x_0(\tau)(L - x_0(\tau))}\right], \qquad (6)$$

where $x_0(\tau)$ is the current position of the boundary between regions 0 and 1. As x_0 varies over a wide range, the product $x_0(\tau)(1 - x_0(\tau))$ in the denominator of the integrand in Eq. (6) changes only slightly. Hence, the integral itself, which is less sensitive to variations in this product, can be approximated by $4/L^2$ for $0.1 < x_0 < 0.9$. Substituting this value in Eq. (6), we obtain that the

dependence $n_e(t)$ has an extended initial exponential part

$$n_e(t) \approx n_{e0}\exp\left(-4\frac{1}{\tau_{ap}}\right), \quad (7)$$

shown by a dotted line in Fig. 2 (here, $\tau_{ap} = L^2/D_{ap}$ is the characteristic time of electron–ion ambipolar diffusion). As the distance from the wall decreases ($x_0 > 0.9$), the denominator in Eq. (6) increases drastically, the decay starts to sharpen, and almost all of the electrons leave the discharge volume at a certain time t_0 (Fig. 2). Substituting the values obtained from the numerically solving set (1) into Eq. (6), we obtain the dependence shown by the dash-dot line in Fig. 2. The time t_0 corresponds to the disappearing of the external region ($x_0 \longrightarrow 1$). Ambipolar field (2) in this external sheath, which consists of only electrons and positive ions, always has the form $E = T_e n_e'/n_e$. For $k > 1$, the field traps the negative ions in the discharge volume, thus preventing them from escaping to the walls [1]. At $t < t_0$ (the first stage of decay of an electron–ion plasma), this sheath provides a peculiar surface tension for negative ions and the density profiles evolve at the almost constant total number of negative ions $\langle n_n\rangle = \langle n_{n0}\rangle$. It should be emphasized that the absence of a negative ion flux toward the wall in the first stage of decay is a distinguishing feature of the afterglow in a plasma with negative ions. At $t < t_0$, only electrons and positive ions arrive at the walls, their fluxes being equal to each other (Fig. 9). Hence, attempts to characterize the escape of charged particles by introducing effective diffusion coefficients of the plasma components (the same over the entire discharge volume) seem to be worthless. For example, such a coefficient for negative ions would be equal to zero at $t < t_0$.

As the boundary $x_0(t)$ shifts toward the wall, the main parts of the ion density profiles ($x < x_0(t)$), where the ion density is higher than the electron density, broaden (Fig. 3). In region 0, where $n_n(x, t)$, $n_p(x, t) > n_e(x, t)$, these parts of the profiles evolve due to ion–ion ambipolar diffusion with the coefficient $D_{pn} = 2D_pD_n/(D_p + D_n) = 2g/(1 + g)$ (Fig. 4). Hence, the sign of the ambipolar field in region 0 (unlike the active stage of discharge and region 1, where the ambipolar field is always directed outward) depends on the mobility ratio g between the positive and negative ions. If $g < 1$, the field is directed outward; i.e., it decelerates electrons as it does in the external region. For $g > 1$, which corresponds to more mobile positive ions, the ion–ion ambipolar field is directed inward; i.e., it is opposite to the field in region 1. As was shown above, at $k \gg 1$, the electron profile is almost flat. In this case, if $g < 1$, then the electron profile in region 0 is slightly convex. For $g > 1$, the electron profile in region 0 is slightly concave. At moderate electron temperatures ($k \sim 1$), these features are more pronounced (see below).

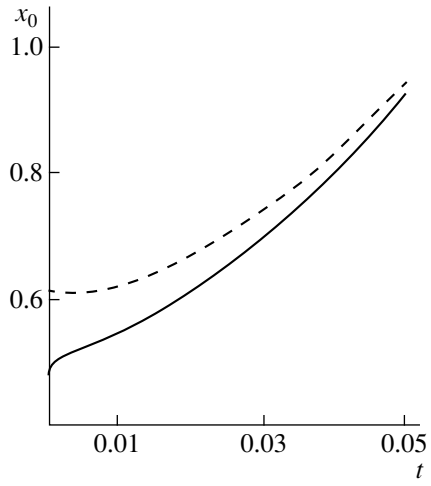

Fig. 5. Time dependences of the boundary coordinate $x_0(t)$ determined from the positions of the point where the electron and negative ion densities are equal to each other (solid line) and the point where one type of diffusion changes sharply to another (see Fig. 4) (dashed line).

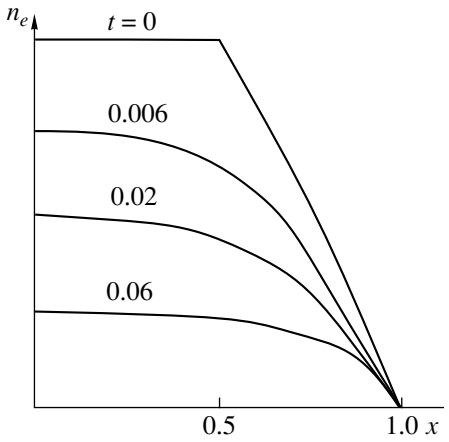

Fig. 6. Evolution of the electron density profile at a low electron temperature ($k = 3$).

When describing diffusion analytically with the help of moving boundaries, we obtain rather cumbersome expressions that are difficult to analyze (see, e.g., [12]). This process can be approximately described by a simple self-similar solution for heat propagation in an infinite media [12]

$$n_n(x, t) = (1/(2\sqrt{\pi D_{pn}t})) \times \int_{-x_{00}}^{x_{00}} n_{n0}(\xi)\{\exp[-(x-\xi)^2/(4D_{pn}t)]\}d\xi. \quad (8)$$

This solution describes the evolution of the central part of the profile $n_n(x, t)$ well. However, it is violated near the point $x_0(t)$ where the negative ion density is low, $n_n(x, t) \ll n_n(0, t)$. At the same time, evolution in

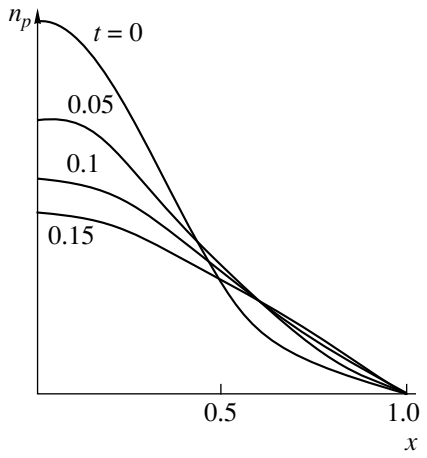

Fig. 7. Evolution of the positive ion density profile during decay for $k = 3$.

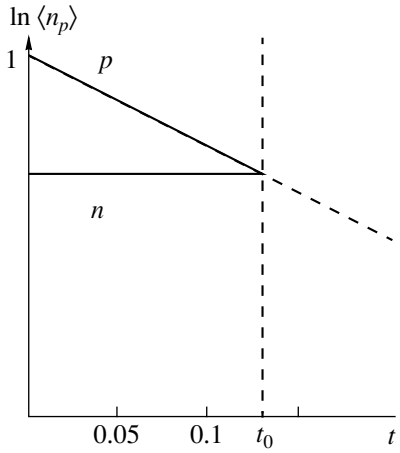

Fig. 8. Time dependences of the integral densities of electrons and positive and negative ions for $k = 3$ (solid lines). The dashed line shows the calculations by formula (9).

region ($x > x_0(t)$), where negative ions are almost absent, is governed by ordinary electron–ion ambipolar diffusion with the coefficient $D_{ap} = (k + 1)D_p$. Note that, for $k \gg 1$, the boundary between regions 0 and 1 is sharp (Fig. 4).

To determine the sharpening time t_0, i.e., the time during which the electrons rapidly escape from the discharge volume (Fig. 2), it is necessary to know the position of the boundary as a function of time, $x_0(t)$. In [11], the motion of this boundary was interpreted as the propagation of the ion density front. Simulations [11] showed that this front often propagates at a constant velocity. However, in Fig. 4, this motion is evidently nonuniform. The dependences $x_0(t)$ for this case are shown in Fig. 5. The dependences were obtained two different ways: from the positions of the point where the electron and negative ion densities are equal to each other and the point where one type of diffusion changes abruptly to another (Fig. 4). It is seen that the above example does not confirm the conclusion drawn in [11] because, according to our results, the time dependence $x_0(t)$ is closer to quadratic than to linear. Special simulations in which k varied over a wide range showed that the interval within which the dependence $x_0(t)$ was almost linear appeared only when k decreased to 3–5. The duration of this interval depends on both the initial density ratio n_{n0}/n_{e0} and the initial position of the boundary $x_{00} = x_0(0)$. We have found no universal dependence describing the change of the boundary position $x_0(t)$. In the case at hand, in our opinion, there is little sense in interpreting the change in $x_0(t)$ as a sharp front propagation by analogy with the results of [2].

A rapid decrease in the electron temperature to low values (i.e., the case of small temperature ratios, $k \sim 1$–5) is more typical of a decaying plasma. Since the initial electron profile is bent at the boundary between regions 0 and 1, the smoothing of this sharp bend is the most rapid process in such regimes. In this case, if negative ions are more mobile (i.e., $g \leq 1$), then, as is seen from Fig. 6, the initially flat profile $n_e(x)$ rapidly becomes cosine and similar to the $n_p(x)$ profile (Fig. 7). As above, the electron density decreases rapidly with time and the broadening of the main parts of the ion density profiles proceeds at the constant total number of negative ions, $\langle n_n \rangle = \langle n_{n0} \rangle$. For small k, the decay of the integral density of positive ions $\langle n_p \rangle$ in the first stage is described by the usual exponential law (Fig. 8)

$$\langle n_p \rangle(t) = \langle n_p \rangle_0 \exp(-t/\tau_{ap}) \tag{9}$$

with a time constant

$$\tau_{ap} = 4\langle x_0 \rangle^2/(\pi^2 D_{ap}), \tag{10}$$

which is determined by ambipolar electron–ion diffusion. Since the width of the main part of the ion profile $x_0(t)$ changes during decay, τ_{ap} is determined by a certain averaged diffusion length $\langle x_0 \rangle$ that varies within the range $x_{00} \leq \langle x_0 \rangle \leq L$. For the time dependence $\langle n_e \rangle(t) = \langle n_p \rangle(t) - \langle n_{n0} \rangle$, it follows from Eq. (9) that the n_e decay sharpens and the electrons disappear at the instant

$$t_0 \approx \frac{1}{\tau_{ap}} \ln \frac{\langle n_{n0} \rangle}{\langle n_{p0} \rangle}, \tag{11}$$

which agrees with the results obtained in [4]. When the initial thickness x_{00} of region 0 is not small, we can take $\langle x_0 \rangle = L$, as in [4]. In the opposite case (for narrow initial profiles), we can take the averaged value $\langle x_0 \rangle = (x_{00} + L)/2$ as the estimate of $\langle x_0 \rangle$ in Eq. (10).

At $t > t_0$ (ion–ion decay stage), when the electrons and, accordingly, the external sheath (region 1) are absent, negative ions can escape to the walls. In this case, plasma decay is governed by ion–ion ambipolar diffusion toward the stationary boundaries (walls) with the coefficient $D_{pn} = 2D_pD_n/(D_p + D_n)$ and the solution has a standard form. Since, by the time t_0, the ion pro-

files are not cosine yet, the main diffusion mode is established in a time of $\sim t_{pn} = 4L^2/\pi^2 D_{pn}$. Then an ordinary decay at the main diffusion mode occurs,

$$n_n = n_p \sim \exp(-t/t_{pn}). \quad (12)$$

The time dependence of the negative ion flux toward the wall is shown in Fig. 9. It is seen that, at $t < t_0$, we have $\Gamma_n(L, t) = 0$, while at $t > t_0$, the main diffusion mode is established and the plasma decays according to the exponential law (12).

As was mentioned above, for $g > 1$, the ambipolar field in region 0 is directed outward; i.e., it decelerates positive ions and carries negative ions and electrons away to the walls. It is well known that in a quasineutral plasma, the electron flow caused by the density gradient is always balanced by the drift flow in the self-consistent ambipolar field (due to the high electron mobility, these flows are almost equal in magnitude and opposite in direction). Hence, for $g > 1$, the electron density in region 0 should increase (rather than decrease, as usual) from the center to the periphery. Since the densities of all the charged particles in region 1 always decrease toward the wall, a nonmonotonic profile of the electron density is formed there. As was mentioned above, for $k \gg 1$, this effect is feebly marked; however, at moderate electron temperatures, the situation changes drastically. Figure 10 shows the calculated evolution of the electron profile (analogous to those presented in Figs. 1 and 6) for $g = 10$. It is seen that, during the decay of a plasma with less mobile negative ions, a pronounced nonmonotonic electron density profile is formed; i.e., we meet a phenomenon that has no analogy in a simple plasma. The evolution of the profile of ambipolar field over the discharge cross section is shown in Fig. 11, which additionally illustrates this phenomenon. It is seen that the field is also nonmonotonic and changes its sign when crossing the boundary between regions 0 and 1.

Spatiotemporal behavior of the positive and negative ions at $g > 1$ is similar to that considered above. In the first stage, the electron density decreases rapidly with time. The broadening of the main parts of the ion density profiles proceed at the constant total number of negative ions, $\langle n_n \rangle = \langle n_{n0} \rangle$. In this stage, the change in the integral density of the positive ions $\langle n_p \rangle$ is described by exponential law (9) and expressions (10) and (11) are valid.

The above analysis has shown that two stages can be distinguished in the spatiotemporal evolution of the charged particle densities during the diffusive decay of an electronegative gas plasma [1–4].

1. In the first stage, the ambipolar field produced by the electrons locks the negative ions in a plasma, while an ion flow toward the walls is almost absent. In this stage, the ion profiles only broaden due to ion–ion ambipolar diffusion, which accelerates the less mobile ion component. Since, in this case, the value and sign of the ambipolar field are determined by the ions, the

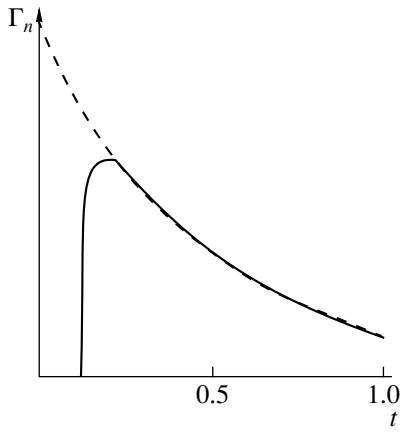

Fig. 9. Time dependence of the negative ion flux onto the wall (solid line) and calculations for the main diffusion mode (dashed line).

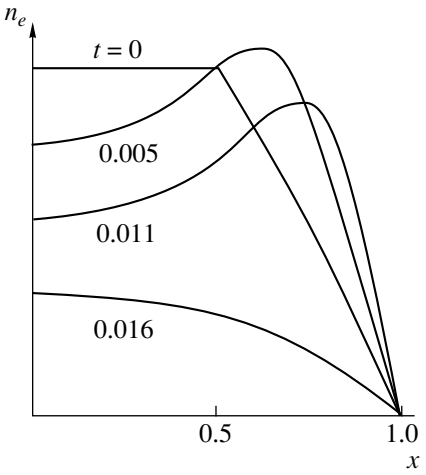

Fig. 10. Evolution of the density profiles of electrons and less mobile negative ions ($g = 10$) during decay at a low electron temperature ($k = 3$).

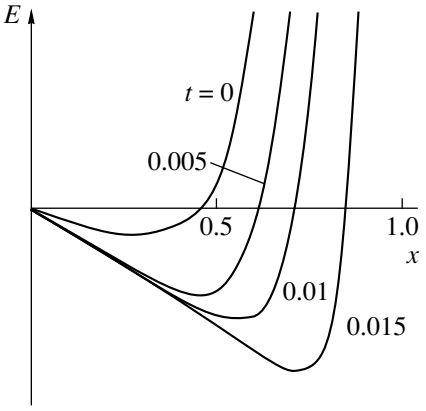

Fig. 11. Evolution of the profile of the ambipolar field over the discharge cross section for less mobile negative ions ($g = 10$).

electron profile changes drastically during decay. If the mobility of negative ions is lower than that of positive ions, then the ambipolar field accelerates electrons and a nonmonotonic electron profile is formed in order to sustain plasma quasineutrality. Such an electron profile cannot in principal be formed during diffusion in an ordinary plasma. In this stage, the number of electrons and positive ions decreases and the transition to an ion–ion (electronless) plasma occurs with sharpening; i.e., almost all the electrons escape from the volume in a finite time.

2. In the second stage (ion–ion decay), electrons are almost absent and the ions leave the plasma due to ion–ion ambipolar diffusion toward the wall, where they are neutralized. First, the main diffusion mode is established. Then, the ion densities decay by an exponential law with a characteristic time determined by ion–ion ambipolar diffusion.

Therefore, an analysis of the evolution of the plasma parameters in an electronegative gas afterglow has confirmed the model proposed in [1–4], which predicts the sharpening of the electron density decay and the formation of an ion–ion plasma in the second stage of decay.

ACKNOWLEDGMENTS

This work was supported by the Russian Foundation for Basic Research, projects nos. 98-02-17778 and 98-02-16000.

REFERENCES

1. A. V. Rozhanskiĭ and L. D. Tsendin, *Collision Transport in a Partially Ionized Plasma* (Énergoatomizdat, Moscow, 1988).
2. I. D. Kaganovich and L. D. Tsendin, Fiz. Plazmy **19**, 1229 (1993) [Plasma Phys. Rep. **19**, 645 (1993)].
3. L. D. Tsendin, Zh. Tekh. Fiz. **59** (1), 21 (1989) [Sov. Phys. Tech. Phys. **34**, 11 (1989)].
4. S. A. Gutsev, A. A. Kudryavtsev, and V. A. Romanenko, Zh. Tekh. Fiz. **65** (11), 77 (1995) [Tech. Phys. **40**, 1131 (1995)].
5. M. B. Hopkins, M. Bacal, and W. G. Graham, J. Appl. Phys. **70**, 2009 (1991).
6. S. Samukawa and H. Ohtake, J. Vac. Sci. Technol. A **14**, 3049 (1996).
7. T. H. Ahn, K. Nakamura, and S. Sugai, Plasma Sources Sci. Technol. **5**, 139 (1996).
8. M. A. Lieberman and S. Ashida, Plasma Sources Sci. Technol. **5**, 145 (1996).
9. M. V. Konyukov, Zh. Éksp. Teor. Fiz. **34**, 908 (1958) [Sov. Phys. JETP **7**, 629 (1958)].
10. L. M. Biberman, V. S. Vorob'ev, and I. T. Yakubov, *Kinetics of Nonequilibrium Low-Temperature Plasmas* (Nauka, Moscow, 1982; Consultants Bureau, New York, 1987).
11. I. D. Kaganovich, D. J. Economou, B. N. Ramamurthi, and V. Midha, Phys. Rev. Lett. **84**, 1918 (2000).
12. É. M. Kartashev, *Analytical Methods in the Theory of Heat Conduction of Solids* (Vysshaya Shkola, Moscow, 1985).

Translated by M. Astrov

Technical Physics, Vol. 46, No. 4, 2001, pp. 411–416. Translated from Zhurnal Tekhnicheskoĭ Fiziki, Vol. 71, No. 4, 2001, pp. 47–52.

SOLID-STATE ELECTRONICS

Study of the Structural Perfection and Distribution/Redistribution of Silicon in Epitaxial GaAs Films Grown by Molecular Beam Epitaxy on (100), (111)A, and (111)B Substrates

G. B. Galiev*, V. G. Mokerov*, V. V. Saraĭkin*, Yu. V. Slepnev*, G. I. Shagimuratov*, R. M. Imamov, and É. M. Pashaev****

** Institute of Radio Engineering and Electronics, Russian Academy of Sciences, Mokhovaya ul. 11, Moscow, 103907 Russia*

*** Shubnikov Institute of Crystallography, Russian Academy of Sciences, Leninskiĭ pr. 59, Moscow, 113333 Russia*

Received March 21, 2000

Abstract—Silicon distribution before and after thermal annealing in thin doped GaAs layers grown by molecular beam epitaxy on (100)-, (111)A-, (111)B-oriented substrates is studied by X-ray diffraction and SIMS. The surface morphology of the epitaxial films inside and outside an ion etch crater that arises during SIMS measurements is studied by atomic force microscopy. Distinctions in the surface relief inside the crater for different orientations have been revealed. Observed differences in the doping profiles are explained by features of the surface relief developing in the course of ion etching in SIMS measurements and by enhanced Si diffusion via growth defects. © *2001 MAIK "Nauka/Interperiodica".*

INTRODUCTION

Until now, silicon has remained the principal material for doping III–V epitaxial films (EF) grown by molecular beam epitaxy (MBE). Depending on growth conditions and the substrate orientation, it can, as an amphoteric impurity, occupy sites in the gallium sublattice (Si_{Ga}) or in the arsenic sublattice (Si_{As}). In the case of growth of gallium arsenide, the (100) substrate silicon occupies sites mostly in the gallium sublattice producing *n*-type EF. On substrates with (111)A orientation, depending on the growth conditions, that is, on the substrate temperature and the ratio γ of the flows of arsenic and gallium ($\gamma = P_{As}/P_{Ga}$, where P_{As} and P_{Ga} are the partial pressures of arsenic and gallium, respectively in the growth zone) both compensated and *n*- or *p*-doped EF can be obtained [1–5]. However, the structural perfection of these epitaxial films varies widely [6].

The abruptness of the interface between the substrate and the epitaxial layer and distribution of impurities in EF are of great importance in fabrication of the devices. While the behavior of silicon in the gallium sublattice Si_{Ga} of GaAs(100) in the course of growth and thermal annealing has been studied in detail [7–13], there is practically no data for EFs of silicon-doped GaAs grown on the substrates with (111)A and (111)B orientations.

The aim of the present work is to study the structural perfection of the GaAs EFs grown on (100)-, (111)A-, and (111)B-oriented substrates and the silicon distribution of these EFs during growth and after thermal annealing.

EXPERIMENTAL

The structures for this study were grown by MBE on the semi-insulating (100)-, (111)A-, and (111)B-oriented substrates at $\gamma = 28$ and a growth temperature $T_G = 600°C$. EFs grown on (111)A and (111)B substrates at this value of γ are close to compensation and have mirrorlike surfaces [3], because Si atoms occupy both As and Ga sites in the GaAs lattice. The samples were grown on the three substrates in different orientations under one process in order to provide identical technological conditions. The substrates were glued with indium to a molybdenum sample holder. After growing a buffer layer of thickness ~0.5 μm, three silicon-doped layers ~320 Å thick were grown separated by undoped 640 Å-thick layers. The thickness of the uppermost undoped layer (cap layer) was 1280 Å. The structure of the samples under study is shown schematically in Fig. 1. The temperature of the silicon source during growth of the doped layers was set at such a value as to obtain the concentration of the condition electrons of $n_e \cong 10^{18}$ cm^{-3} GaAs(100) EF.

The study of the EF crystal structure was carried out in an automatic X-ray spectrometer having a double-crystal dispersionless scheme with high-perfection Ge crystals in the reflecting positions (400) and (111) as crystal monochromators and using Cu$K_{\alpha 1}$ radiation. The sizes of the output slits of the monochromator and

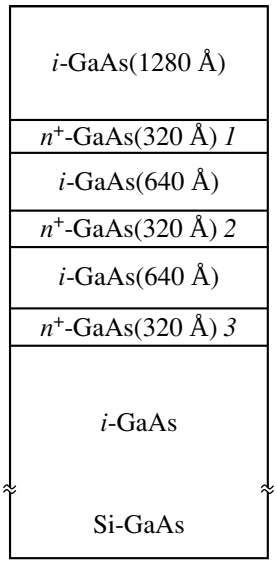

Fig. 1. Schematic cross section of the samples under study. *1–3*-silicon-doped regions.

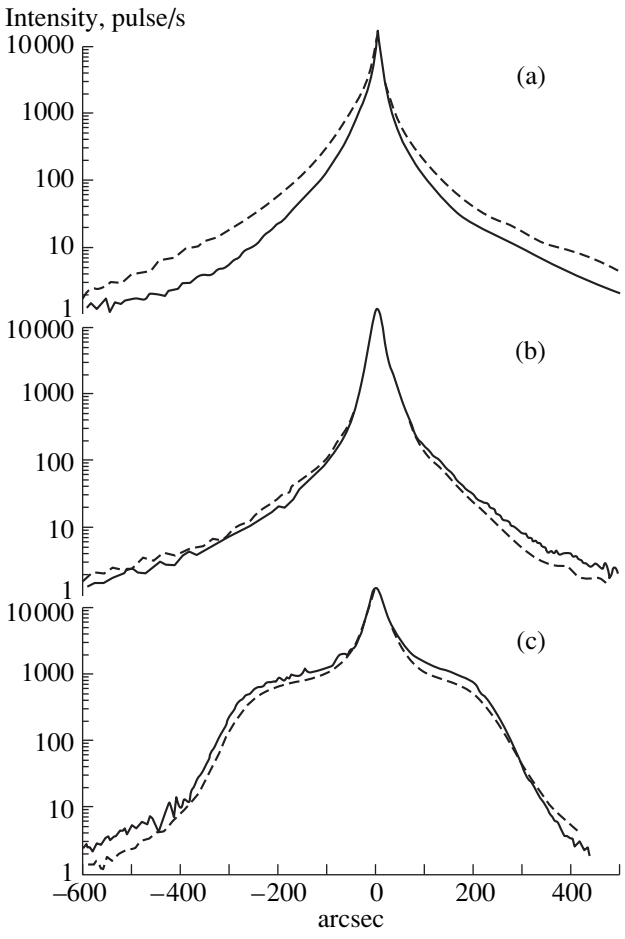

Fig. 2. The diffraction rocking curves of the epitaxial films grown on the substrates with the orientations (100) (a), (111)A (b), (111)B (c). Solid curves are DRC before annealing; dashed curves are DRC after annealing.

the input slit of the scintillation detector were 0.2 × 0.5 mm and 1 × 2 mm, respectively. The measurements were carried out over an angle range $\Theta \sim 1100''$ in steps of 5″ outside the region of strong diffraction maxima and 0.5″ in the region of the GaAs substrate peak. The acquisition time at a point was 60 s. The intensity variation of the incident radiation over the time of measurement did not exceed 1.5%. The intrinsic noise of the detector did not exceed 0.2 pulse/s. The reproducibility of the results in repeat measurements was no worse than 3%.

The depth profiles of the silicon concentration $N_{Si}(x)$ were measured using a CAMECA IMS-4F secondary ion mass spectrometer. As the primary beam, O_2^+ oxygen ions of energy E_p = 5 keV were used. The scanned area was 250 × 250 μm and secondary silicon ions were collected from the central part of the scanned area 60 × 60 μm in size with a mass resolution of 5000. The measurements of the sample surface roughness inside and outside the crater after ion etching with SIMS were carried out in an (AFM) P7-SPMLS-MDT atomic force microscope (manufactured by HT-MDT) in a temping mode regime. The scanning area was ~10000 × 10000 nm. The subsequent sample annealing for the study of the Si redistribution was carried out in the growth chamber of the MBE setup in the arsenic flow at a temperature of T_a = 750°C for 1 h and at an arsenic pressure of $P_{As} \cong 10^{-5}$ torr.

RESULTS AND DISCUSSION

The measured diffraction rocking curves (DRC) for all samples under study are presented in Fig. 2 before and after annealing at T_a = 750°C for 1 h. As seen in Fig. 2a, the sample grown on the GaAs(100) substrate after annealing has a lower DRC peak halfwidth (W) (15″ before annealing to 13″ after annealing) and the decay of the DRC tails is observed. This indicates that annealing improves the EF crystal structure [7].

A somewhat different situation is observed for EFs grown on GaAs(111)A substrates. As seen from Fig. 2b, DRC is not significantly different in this case. The DRC halfwidths are 24″ before and 28″ after the annealing.

A situation quite different from the (100) and (111)A orientations is found for the case of the (111)B orientation. As seen in Fig. 2c, the DRC for the EF on the (111)B substrate looks distinctly different. Beside the main peak with $W \approx 33''$, wide tails of large intensity are observed on each side of the peak in the angle range from ±100″ to ±300″. These features of the DRC can be related both to the X-ray scattering by lattice imperfections and to the possible formation of an additional coherent region. Thus, the experimental data on the structural perfection of the samples under study demonstrate the strong dependence of these properties on the orientation of the substrate.

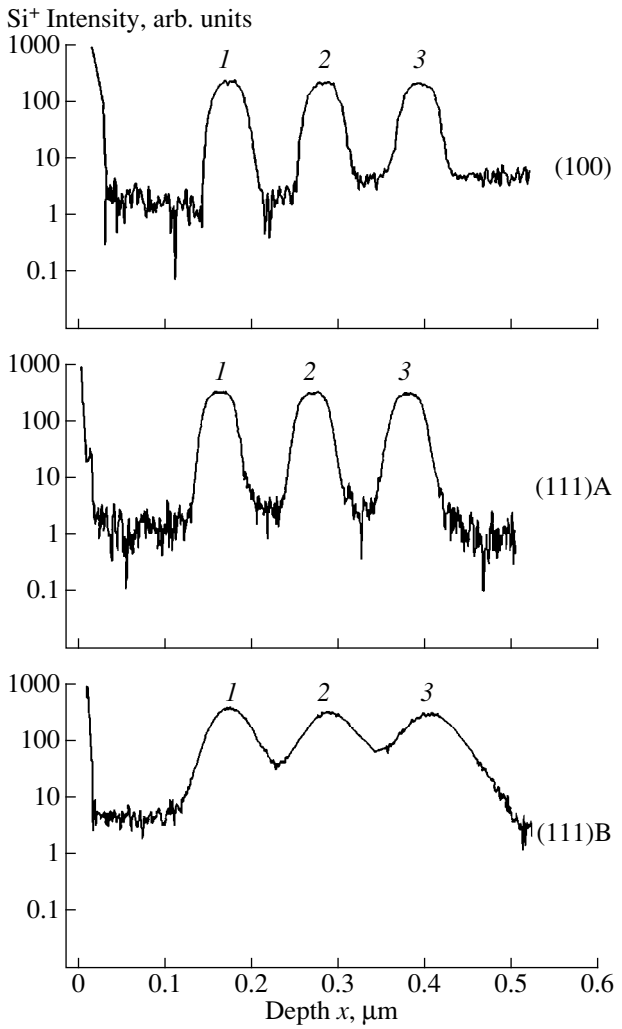

Fig. 3. Profiles of silicon distribution over the depth $N_{Si}(x)$ obtained by SIMS for the samples grown on (100)-, (111)A-, and (111)B-oriented substrates before annealing.

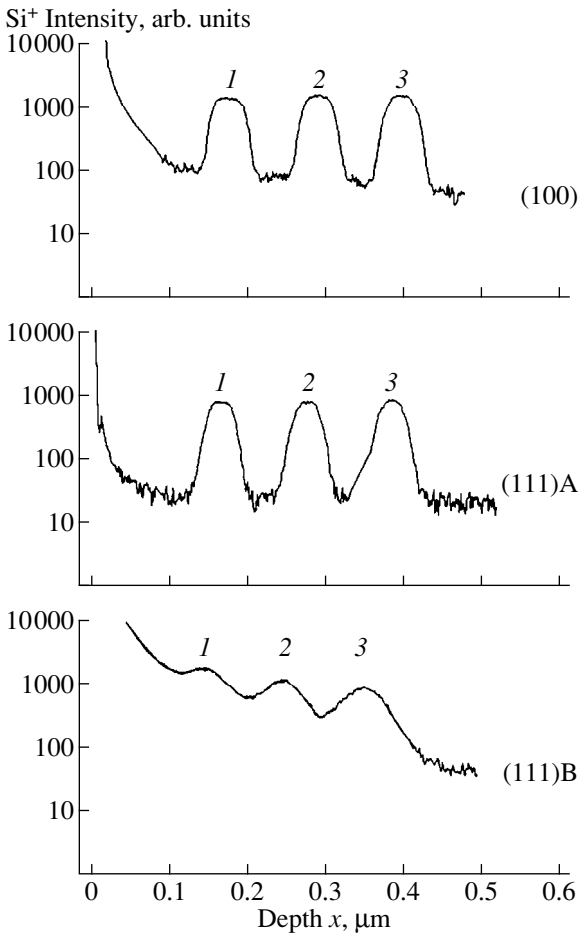

Fig. 4. The same as in Fig. 3 after annealing.

Consider now the measurement results of the silicon content $N_{Si}(x)$ for the samples discussed above before (Fig. 3) and after (Fig. 4) annealing. The silicon doped-layers are denoted by numbers *1–3* beginning from the surface. It is seen that in the near-surface region the silicon content is high and, in annealed samples, this region is larger and the Si content is higher. The modifications of the $N_{Si}(x)$ curves for different orientations are different. Before annealing, $N_{Si}(1) \geq N_{Si}(2) \geq N_{Si}(3)$ for all three samples, which is characteristic of the doping profile measured by SIMS. It is related to the peculiarities of the techniques, in particular, to the so-called mixing effect [12–14]. (Hereafter, $N_{Si}(1)$, $N_{Si}(2)$, $N_{Si}(3)$ are the maximum silicon concentrations in the doped regions *1–3*, respectively, according to Fig. 1). As seen in Fig. 4, the situation is different for the annealed samples, namely, $N_{Si}(1) < N_{Si}(2) < N_{Si}(3)$ for (100) and (111)A orientations and $N_{Si}(1) > N_{Si}(2) > N_{Si}(3)$ for (111)B orientation.

In Table 1, values of the full width at half maximum (FWHM) for the peaks in the $N_{Si}(x)$ curves (Figs. 3 and 4) are given for the as-grown and annealed samples. The FWHM values of the corresponding doped layers (according to Fig. 1) before annealing are denoted as $\Delta_{00}(1, 2, 3)$, $\Delta_{0A}(1, 2, 3)$, and $\Delta_{0B}(1, 2, 3)$; and after the annealing, as $\Delta_{a0}(1, 2, 3)$, $\Delta_{aA}(1, 2, 3)$, and $\Delta_{aB}(1, 2, 3)$ for the orientations (100), (111)A, and (111)B, respectively. These data show that, for the orientations (100) and (111)B, relationships between the FWHM values for the peaks *1–3* before annealing are $\Delta_{00}(1) < \Delta_{00}(2) < \Delta_{00}(3)$ and $\Delta_{0B}(1) < \Delta_{0B}(2) < \Delta_{0B}(3)$ and for the (111)A orientation $\Delta_{0A}(1) \approx \Delta_{0A}(2) \approx \Delta_{0A}(3)$. It should be noted as well that for the (111)B orientation FWHM values are essentially larger than for the (100) and (111)A orientations.

Consider the (100) and (111)B orientations before annealing. Broader doping profiles of the layers *2* and *3* compared with layer *1* (the increase of Δ) in this instance can be explained by, the mixing effect that occurs in the SIMS method and/or by the surface relief development in the course of ion etching. Besides, the broadening of the deeper layers of the doping profiles,

Table 1

Layer no.	Orientation								
	(100)			(111)A			(111)B		
	1	2	3	1	2	3	1	2	3
Designations of the FWHM (before annealing)	$\Delta_{00}(1)$	$\Delta_{00}(2)$	$\Delta_{00}(3)$	$\Delta_{0A}(1)$	$\Delta_{0A}(2)$	$\Delta_{0A}(3)$	$\Delta_{0B}(1)$	$\Delta_{0B}(2)$	$\Delta_{0B}(3)$
FWHM values in Å (before annealing)	350	364	376	350	350	350	475	575	650
Designations of the FWHM (after annealing at T = 750°C)	$\Delta_{a0}(1)$	$\Delta_{a0}(2)$	$\Delta_{a0}(3)$	$\Delta_{aA}(1)$	$\Delta_{aA}(2)$	$\Delta_{aA}(3)$	$\Delta_{aB}(1)$	$\Delta_{aB}(2)$	$\Delta_{aB}(3)$
FWHM values in Å (after annealing at T = 750°C)	440	440	420	374	385	385	–	–	660

Table 2

	Orientation					
	(100)		(111)A		(111)B	
	outside the crater	inside the crater	outside the crater	inside the crater	outside the crater	inside the crater
R_{max}, nm	20	27	23	140	139	160
R_{mean}, nm	4.9	10.79	7.8	58	79	74
R_a, nm	0.9	3.47	1.7	30	14	17
R_q, nm	1.29	4.3	2.27	36	19	21

$\Delta(2)$ and $\Delta(3)$, can be the result of Si diffusion during growth since layers *2* and *3* are exposed to $T = T_G$ for longer than layer *1*. Similar results were obtained in [12] for the δ-doped layers. However, in our case, annealing the grown structures at T_a = 750°C for 60 min caused no significant broadening of the profiles. Therefore, the variations of Δ in the unannealed samples for the (100) and (111)B orientations are most likely related to the development of surface relief during $N_{Si}(x)$ measurements by SIMS. Table 2 gives the parameters R_{max}, R_{mean}, R_a, and R_q obtained from AFM measurements (R_{max} is the maximal deviation from the mean value, R_{mean} is the mean value, R_a is the surface roughness, and R_q is the root-mean-square deviation).

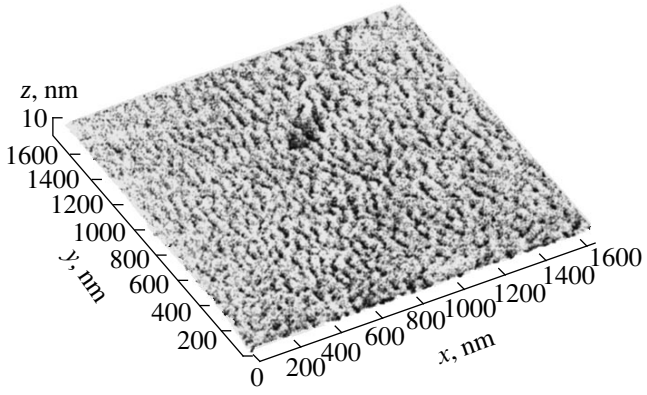

Fig. 5. The initial surface of the epitaxial layer imaged by atomic-force microscopy. The sample is grown on a (100)-oriented substrate.

Note the considerable difference of FWHM values for the (100) and the (111)B; in particular, $\Delta_{00} < \Delta_{0B}$ for all layers (Table 1). Comparison of the data for these samples (Tables 1 and 2) suggests that the difference in the FWHM values is most likely related to both the initial roughness and the surface relief development in the course of ion etching. For the (100) orientation, $R_a \cong 0.9$; and for the (111)B, $R_a \cong 14$. In addition, as mentioned above, the DRC data for the (111)B orientation (Fig. 2) are essentially different from the data for the (100) and (111)B orientations. Apparently, these growth conditions are not optimum for the (111)B orientation. Since DRCs characterize the structural perfection of EFs, it can be supposed that the EFs grown on the (111)B-oriented substrates are highly imperfect and the silicon distribution is strongly smeared even before annealing.

In distinction to the (100) and (111)B orientations, the FWHM values before annealing are essentially constant (Table 1) in the (111)A orientation, although variations of R_{max}, R_a, R_q inside crater are considerably larger compared with data for the (100) orientation. This result can be explained by different surface relief developments for different orientations in the course of ion etching in SIMS measurements. In Figs. 5 and 6, the surfaces outside (Fig. 5) and inside (Fig. 6) the ion etch crater samples with (100) and (111)A orientations acquired by the atomic-force microscopy. Since there is no cardinal difference between images of the surfaces outside the crater for the three samples under study, only one image is presented here. As seen in Fig. 6, the surface relief for the (111)A orientation after ion etch-

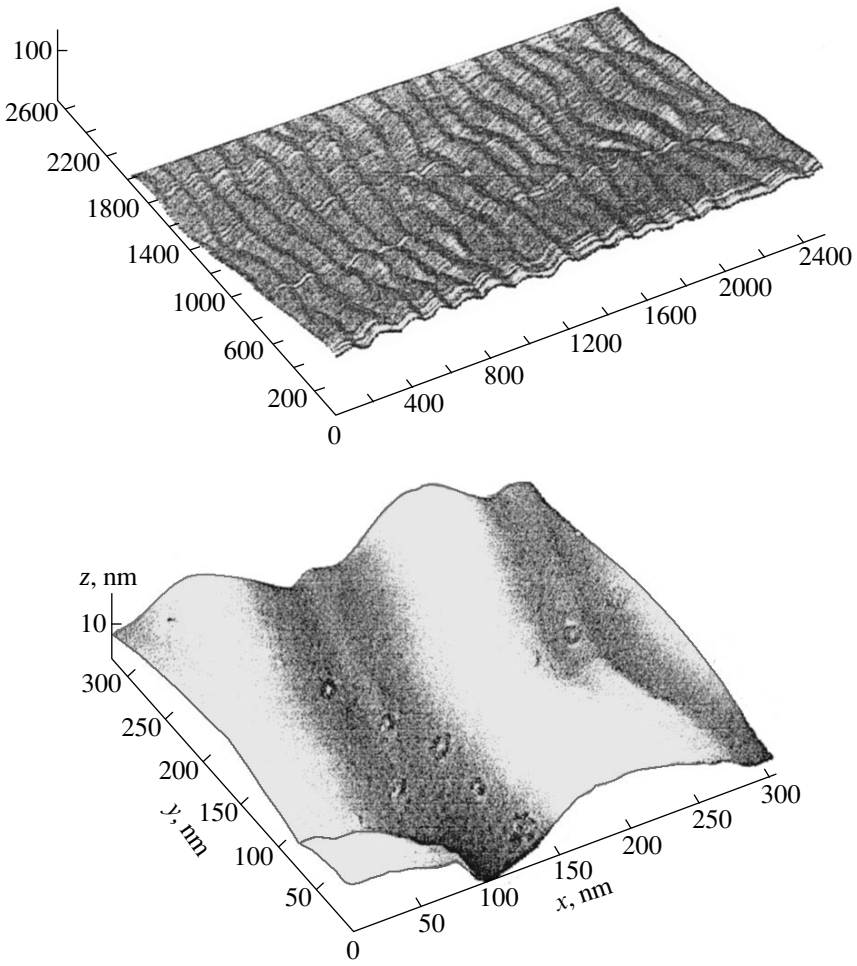

Fig. 6. The surface inside the ion etch crater imaged by atomic-force microscopy. The sample is grown on the (111)A-oriented substrate. At the bottom is an enlarged view of the ion-etched surface.

ing has a periodic structure of alternating ridges and hollows with a swing of ~120 Å. Note that for the (100) and (111)B orientations, this surface relief is not observed after ion etching.

A similar relief of the GaAs surface in the ion etch crater produced in SIMS measurements, also in the (111)A orientation, was observed in [15] and called ripples. The authors studied in detail the conditions for emergence, the parameters of the ripple-type irregularities and their variations with the energy and angle of incidence of the primary ion beam (O_2^-).

Like in [15], ripples were observed in the crater only on (111)A samples. Since the angle of incidence and the energy of the primary beam were the same in our SIMS measurements, the occurrence of ripples is probably related to specific features of the interaction of the primary ion beam with the GaAs(111)A surface. Apparently, the yield of Si ions in the SIMS analysis in this case is averaged over the width (amplitude) of the ripples (~120 Å in our study), which weakens the dependence of the broadening of the profiles on depth.

Consider the data for the samples after annealing. As seen in Fig. 4, in addition to the changing shape of the $N_{Si}(x)$ curves, annealing affects the FWHM values. In particular, for the (100) orientation, variations of the FWHM values for the silicon-doped regions *1–3* before and after the annealing are as high as $\Delta_{a0}(1) - \Delta_{00}(1) \cong$ 90 Å, whereas for the (111)A orientation, these variations are insignificant and comprise $\Delta_{aA}(3) - \Delta_{0A}(3) \cong$ 30 Å. The increase of FWHM for the (100) orientation can be explained by Si diffusion during annealing, and the observed minor increase of the FWHM value for the (111)A orientation can be explained by both diffusion and, as already noted above, by ripple-type irregularities emerging during SIMS measurements, as well as by the details of the exit of the secondary ions from such a surface. For the sample with the (111)B orientation, the FWHM variation after the annealing could not be determined (except peak *3*), because of the significant modification of the $N_{Si}(x)$ curves. As seen in Fig. 4, the Si redistribution in this case is substantial. Apparently, in this case enhanced Si diffusion occurs via defects. Both AFM and X-ray diffraction data show

that the EFs on the (111)B substrates are the most imperfect; this the Si distribution profiles should be considerably smeared in this case.

Finally, consider the variation of $N_{Si}(x)$ in the near-surface region. The presence of background silicon in the thin near-surface region for the silicon-doped deep GaAs epitaxial layers was observed in many studies [8, 11, 12]. In some studies, this region is not considered at all, but the authors of [11] consider that the high Si content in the initially undoped region does not really mean high silicon concentration at the GaAs lattice sites and rather comes from Si inclusions at the growth defects, which was observed by the authors under microscope. In our case, these inclusions were clearly seen during SIMS analysis in the ion image regime as fluorescent spots in the analyzed region. The substantial withdrawal of silicon to the surface after annealing for the sample grown on the (111)B-oriented substrate can be explained by enhanced Si diffusion via growth defects, because this surface is the most imperfect under the given growth conditions.

CONCLUSIONS

Thus, from the results of the performed study, the following conclusions can be made.

The structural perfection and the surface roughness of epitaxial films grown on (100)-, (111)A-, and (111)B-oriented substrates at the same γ value is different. In particular, at $\gamma = 28$, the structural perfection is highest for the (100) orientation and lowest for the (111)B orientation ($W_{(100)} < W_{(111)B}$, $R_a(100) \ll R_a(111)B$).

In the surface study by AFM, it has been found that during ion etching in SIMS measurements, the relief of the GaAs surface with the (111)A orientation, in contrast to the (100) and (111)B orientations, develops in the form of ripple-type irregularities. It is shown that such a peculiarity of the relief development can deteriorate the depth resolution of the SIMS method, particularly in measurements of the impurity distribution profile in thin and ultrathin layers.

The observed increase of the silicon content in the near-surface region in annealed samples, in our opinion, is related to enhanced Si diffusion via defects.

ACKNOWLEDGMENTS

The authors are grateful to V.K. Nevolin for his help with AFM measurements and useful discussions.

The study was supported by the Ministry of Sciences and Technology of the Russian Federation (Grant nos. 98-3009 and 99-2044).

REFERENCES

1. W. I. Wang, E. E. Mendez, T. S. Kuan, and L. Esaki, Appl. Phys. Lett. **47**, 826 (1985).
2. F. Piazza, L. Pavesi, M. Henin, and D. Johnston, Semicond. Sci. Technol. **7**, 1504 (1992).
3. V. G. Mokerov, G. B. Galiev, Yu. V. Slepnev, and Yu. V. Khabarov, Fiz. Tekh. Poluprovodn. (St. Petersburg) **32**, 1320 (1998) [Semiconductors **32**, 1175 (1998)].
4. Y. Okano, H. Seto, H. Katahama, *et al.*, Jpn. J. Appl. Phys. **28** (2), L151 (1989).
5. Y. Kadoya, A. Sato, and H. Kano, J. Cryst. Growth **111**, 280 (1991).
6. G. B. Galiev, V. G. Mokerov, Yu. V. Slepnev, *et al.*, Zh. Tekh. Fiz. **69** (7), 68 (1999) [Tech. Phys. **44**, 801 (1999)].
7. G. B. Galiev, R. M. Imamov, B. K. Medvedev, *et al.*, Fiz. Tekh. Poluprovodn. (St. Petersburg) **31** (10), 1168 (1997) [Semiconductors **31**, 1003 (1997)].
8. Ph. Jansen, M. Meuris, M. van Rossum, and G. Borghs, J. Appl. Phys. **68**, 3766 (1990).
9. E. F. Schubert, J. B. Stark, T. H. Chiu, and B. Tell, Appl. Phys. Lett. **53**, 293 (1988).
10. K. H. Lee, D. A. Stevenson, and M. D. Deal, J. Appl. Phys. **68**, 4008 (1990).
11. L. Paves, N. H. Ky, J. D. Ganiere, *et al.*, J. Appl. Phys. **71**, 2225 (1992).
12. R. B. Beall, J. B. Clegg, and J. J. Harris, Semicond. Sci. Technol. **3**, 612 (1988).
13. A.-M. Lanzillotto, M. Santos, and M. Shayegan, Appl. Phys. Lett. **55**, 1445 (1989).
14. Mark E. Greiner and J. F. Gibbons, Appl. Phys. Lett. **44**, 750 (1984).
15. A. Ishitani, A. Karen, Y. Nakagawa, *et al.*, in *Proceedings of the 8th Conference on Semiconducting and Insulating Materials, SIMS-VIII* (International Congress Centre RAI, Amsterdam, 1991), p. 315.

Translated by V. Lebedev

Technical Physics, Vol. 46, No. 4, 2001, pp. 417–421. Translated from Zhurnal Tekhnicheskoĭ Fiziki, Vol. 71, No. 4, 2001, pp. 53–57.

SOLID-STATE ELECTRONICS

Mass Transfer in Non-Steady-State Hydride Epitaxy of $Si_{1-x}Ge_x$/Si Structures

L. K. Orlov, S. V. Ivin, A. V. Potapov, and N. L. Ivina

Institute of Physics of Microstructures, Russian Academy of Sciences, Nizhni Novgorod, 603600 Russia

e-mail: orlov@ipm.sci-nnov.ru

Received May 12, 2000

Abstract—Numerical simulation of the non-steady-state kinetics for the solid solutions MBE-grown from silane and germane with vapor sources was carried out. The smearing of the germanium distribution at the interfaces in the $Si_{1-x}Ge_x$/Si structures was studied both in the absence of the atomic fluxes in the reactor and in their presence (the "hot-wire" method). It is shown that the use of an additional hot source enhances the growth. Moreover, at gas pressures exceeding 10^{-3} torr (provided that the gas flow remains molecular) and at growth temperatures $T_{gr} < 600$°C, such conditions can minimize the width of the transition regions at the interfaces. *© 2001 MAIK "Nauka/Interperiodica".*

INTRODUCTION

In the last decade, the extensive study of silicon- and germanium-based heteroepitaxial structures has advanced to their application in the active elements of various semiconductor devices. Large-scale production of the device-grade heterostructures needs more feasible normal- and low-pressure vapor-phase epitaxial techniques, which use Si and Ge hydrides and hydrochlorides [1, 2]. The vapor-phase epitaxial methods produce the highly uniform large-area films and offer higher throughput, since several substrates simultaneously can be placed in the growth chamber. Moreover, film growth in the rarefied hydrogen environment stabilizes the film properties. Finally, a reduction of the Si and Ge surface diffusion rate due to surface bond saturation by hydride decomposition products lowers the breakdown probability for two-dimensional growth, thus providing good interface planarity in strained nanostructures. The application of this technique for the growth of complex semiconductor structures, however, has been retarded by extremely low growth rates at reduced process temperatures and by difficulties in obtaining abrupt (within a monolayer) interfaces required to form subnanometer heterostructures.

To tackle the first problem, it has been suggested to use both molecular and atomic fluxes of the material in vapor-source MBE equipment. The atomic fluxes can be formed by using an additional heated element (a tungsten wire [3–5] or a sublimating silicon bar [6, 7]) placed in the reactor. The effect of the additional atomic fluxes on the rate of atom incorporation into a growing $Si_{1-x}Ge_x$ layer in the hot-wire method of vapor-phase MBE was analyzed in [8, 9]. The aim of this study was to see how the additional hot source in the reactor affects mixing of the alloy composition at the interfaces of the Si/$Si_{1-x}Ge_x$ structure and, by correlating the profiles of the structures grown under different conditions, to find optimal regimes for obtaining strained heterostructures with extremely abrupt interfaces.

To do this, we numerically solved a system of kinetic equations that relate the concentrations Θ_i of the Ge, Si, and H atoms and SiH_3 and GeH_3 molecules adsorbed by the growing surface to the atomic and molecular flows coming to the substrate. Earlier [8–13], we considered the kinetics of hydride decomposition at the surface of an epitaxial film and its effect on the steady-state growth of $Si_{1-x}Ge_x$ layers. Therefore, the form of the equations used will be excluded from consideration. Note only that the validity of the kinetic equations and the surface chemical reactions has been checked by contrasting calculations with the steady-state characteristics of the real growth process. This allowed us to derive the hydride molecule decomposition times required for subsequent simulation [8, 9].

NUMERICAL SIMULATION OF THE NON-STEADY-STATE GROWTH KINETICS AND ANALYSIS OF THE TRANSITION REGIONS

Hydride pyrolysis and the formation of the transition regions at the interfaces will be studied as follows. Consider the growth of a $Si_{1-x}Ge_x$ layer in a vapor-source MBE reactor where an extremely sharp pulse (of width $t_1 - t_0$) of germane molecules is imposed on a steady silane flow. The applicability of such a model is based on the possibility of instantaneous flow switching in the modern reactors. However, the component distribution in the growing $Si_{1-x}Ge_x$ layer is almost always far from rectangular (Fig. 1). The simulation of the component distribution was carried out for two

1063-7842/01/4604-0417$21.00

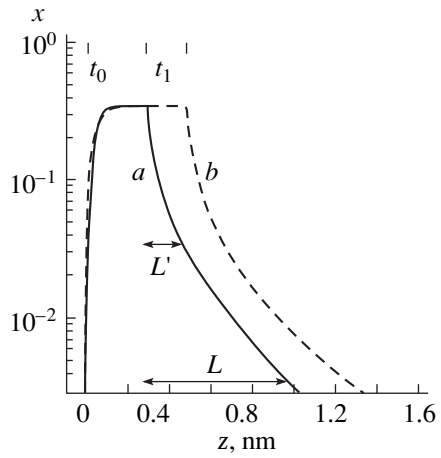

Fig. 1. Germanium distribution in the $Si_{0.65}Ge_{0.35}$ layer of the $Si/Si_{0.65}Ge_{0.35}/Si$ heterostructure when a pulse (of width $t_0 - t_1$) of germane molecules is switched on. $P_{GeH_4} = 1 \times 10^{-5}$ torr, g = (*a*) 0 and (*b*) 0.037, $P_{SiH_4} = 3.45 \times 10^{-5}$ torr, $T_{gr} = 500°C$, $x = 0.35$, and $k = 1$.

cases: (1) atomic flows in the system are absent ($g = 0$) and (2) atomic flows in the reactor are significant (the hot-wire technique) ($g \neq 0$). Hereafter, the process parameter values are taken close to those most frequently used in the experiment: $T_{gr} = 500°C$, $x = 0.35$, $k = r_{Ge}/r_{Si} = 1$, $P_{GeH_4} = 1 \times 10^{-5}$ torr, and $P_{SiH_4} = 3.45 \times 10^{-5}$ torr. Here, T_{gr} is the substrate temperature, $r_{Ge(Si)}$ are the rate constants for crystallization of Ge(Si) atoms adsorbed by the surface, and $P_{GeH_4(SiH_4)}$ are the hydride partial pressures in the reactor. In the general case, the r values depend on the surface coverage by hydride decomposition products, which was included in the calculations. The characteristic values of r_{Si} for different growth temperatures and gas pressures are presented in [8].

The introduction of an additional hot source (Fig. 1, dashed curve) does not change the composition of the alloy but markedly increases the growth rate and alters the thickness of individual layers of the heterostructure compared with the case $g = 0$ (solid curve). As follows from Fig. 1, the germanium distribution in the structure is highly asymmetric. This is presumably due to the different roles played by mechanisms involved in the formation of the transition regions at the interfaces. We exclude from consideration the segregation effects, caused particularly by the difference in the coefficients of incorporation of silicon and germanium atoms into a growing layer. The segregation becomes of great importance at higher growth temperatures. At the lower boundary of the layer ($t \geq t_0$), the interface smearing is determined by the rate of germanium accumulation on the surface of the growing film. Near the upper boundary ($t \geq t_1$), the smearing is determined by relaxation processes related to the finite rate of hydride pyrolysis on the surface and to the finite rate of atom incorporation into the growing layer.

From time dependences of the surface concentrations of GeH_3 and SiH_3 hydride radicals and Si, Ge, and H atoms, as well as of the film growth rate (Figs. 2a–2f), one can gain a better understanding of the processes occurring on the growing surface at the instant the germane pulse is applied to the reactor. In this study, we do not consider specific paths of molecule decomposition on the film surface. All the intermediate chemical reactions with the formation of $Si(Ge)H_2$ and Si(Ge)H radicals were combined into the overall reaction characterized by the effective times of complete $Si(Ge)H_3$ decomposition. These times were evaluated [8, 9] using steady-state dependences of the growing layer composition and the growth rate on basic epitaxy parameters. Figure 2 shows that, with the appearance of germane molecules in the reactor, the concentration of both GeH_3 molecules (Fig. 2c) and germanium atoms (Fig. 2a) on the surface of the growing film abruptly increases, while the surface concentrations of the other components sharply drops (Figs. 2b, 2d, and 2e). In particular, germanium atoms on the silicon surface considerably reduce its coverage by hydrogen (Fig. 2e), since the energy of hydrogen desorption from Ge is lower than from Si [1, 8]. The difference between the hydride decomposition rates and the hydrogen desorption rate, as well as between the Si–Si and Si–Ge bond energies [E_{bond}(Si–Si) > E_{bond}(Si–Ge)], explains the nonmonotonic behavior of the surface concentration of Si adatoms and of the growth rate at the instants the germane molecular flow is switched on and off. The extremely low surface coverage by SiH_3 molecules during the $Si_{1-x}Ge_x$ growth stems from the fact approximately order of magnitude larger decomposition rate compare with GeH_3.

Below, we will consider the transition processes only near the upper boundary of the layer. Let the width of the diffusion smearing of the profile at the interface be L' at a level of $0.1x$ and L at a level of $0.01x$. Typical dependences of these values on the germane pressure in the reactor for $g = 0$ and $g = 0.037$ are shown in Fig. 3b (the corresponding values of the silane pressure can be determined from curve *1* in Fig. 3a). For the parameter values chosen and in a rather wide range of the gas pressures at $g = 0$, the value of L' is equal to 2 Å and L is about 7–9 Å. The solid solution growth rate therewith remains very small (of the order of one angstrom per minute, solid curve *2* in Fig. 3a), although it seems that just such rates may be more suitable for the growth of, for instance, Si_1Ge_1 heterostructures where the quality of individual monolayers within the unit cell is the key issue. However, extremely low growth rates make this method impractical for growing the structures under industrial conditions.

The way out without going to higher growth temperatures and higher hydride pressures is to use the hot-

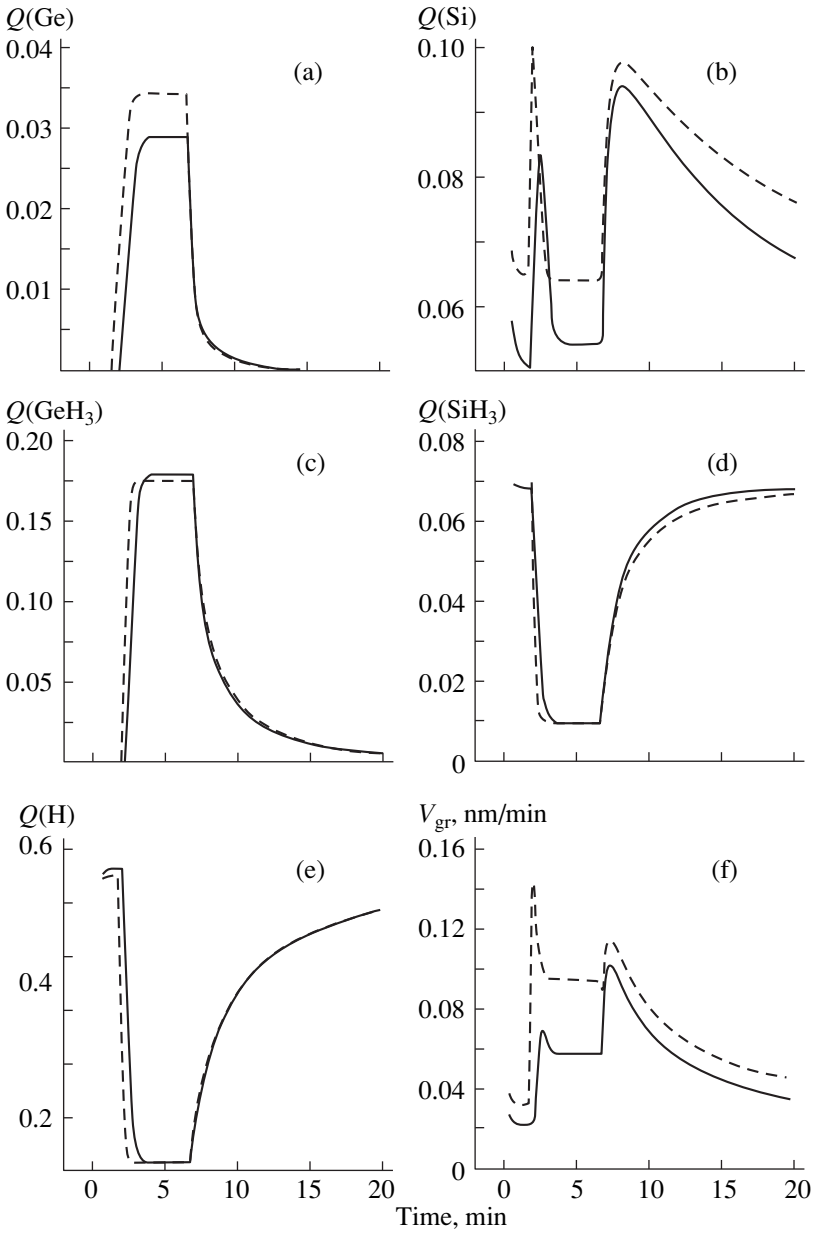

Fig. 2. Time dependences of the $Si_{0.65}Ge_{0.35}$ growth rate and the surface concentrations Q at T_{gr} = 500°C, k = 1, P_{SiH_4} = 3.45 × 10^{-5} torr, and P_{GeH_4} = 1 × 10^{-5} torr; g = 0 (solid curves) and 0.037 (dashed curves).

wire method (dashed curve *2* in Fig. 3a), that is, to combine molecular and atomic flows in the reactor (dashed curve *2* in Fig. 3b). With this method, the growth rate can easily be increased several times, while the smearing of the composition profile also grows. In the most common range of pressures (0.1–1 mtorr), the smearing is as large as 10–20 Å (dashed curve *2* in Fig. 3b) even though the germanium distribution in the $Si_{1-x}Ge_x$ layer may become more abrupt at the initial portion of germanium concentration decay (dashed curve *1* in Fig. 3b). Calculations show that the interface is the most abrupt ($L \approx 1$ Å) at sufficiently high pressures and high growth rates, where the atomic beams from the hot source make a major contribution to the growth. In this case, the process becomes akin to traditional MBE with solid sources of Si and Ge.

In Fig. 4b, L is plotted against the efficiency g of the hot source for two gas pressures in the reactor. At the higher pressure (solid curve), the atomic fluxes from the hot wire dominate in the growth process, while, at the lower pressure (dashed curve), the molecular fluxes prevail and the growth process is controlled mainly by hydride pyrolysis on the substrate. For better understanding of the different behavior of curves *1* and *2* in

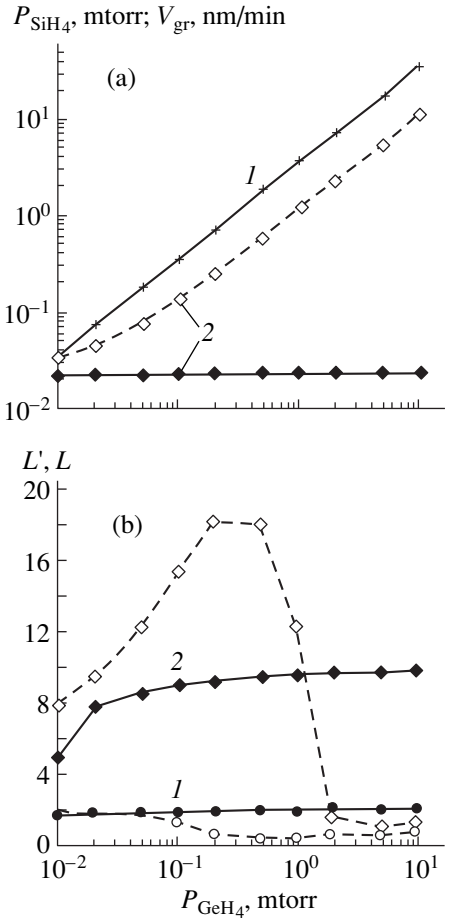

Fig. 3. (a) Dependences of the (*1*) silane pressure in the reactor and (*2*) $Si_{0.65}Ge_{0.35}$ growth rate on the germane pressure; (b) characteristic values (*1*) *L*' and (*2*) *L* of component mixing at the upper interface vs. germane pressure at $x = 0.35$, $T_{gr} = 500°C$, and $k = 1$; $g = 0$ (solid curves) and 0.037 (dashed curves).

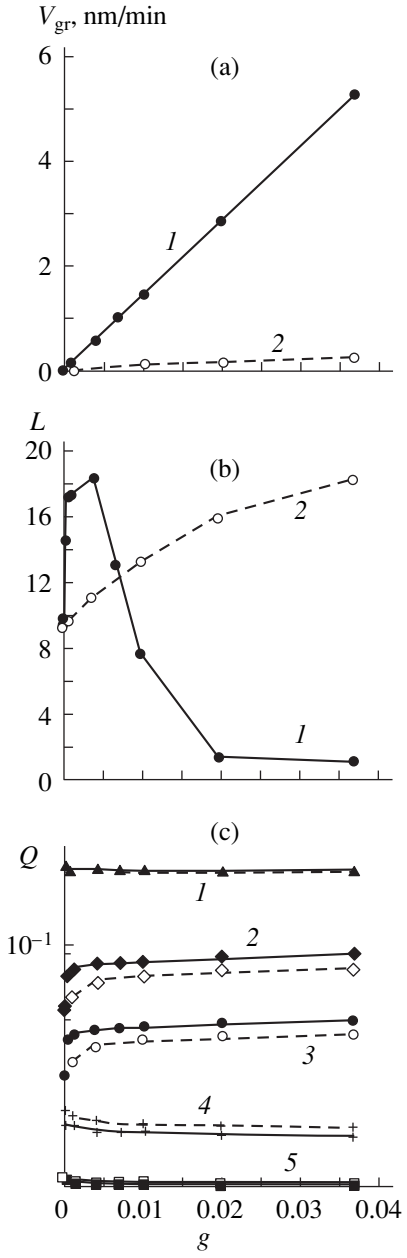

Fig. 4. (a) Growth rates, (b) upper interface smearing, and (c) surface concentrations *Q* of the atoms and molecules as functions of the hot source efficiency *g*. $x = 0.35$, $T_{gr} = 500°C$, and $k = 1$; $P_{GeH_4(SiH_4)} = 5 \times 10^{-3}(1.72 \times 10^{-2})$ (solid curves) and $2 \times 10^{-4}(6.9 \times 10^{-4})$ torr (dashed curves). (*1*) GeH_3, (*2*) Si, (*3*) Ge, (*4*) H, and (*5*) SiH_3.

Fig. 4b, Fig. 4c shows the corresponding dependences of the surface concentrations of the atoms and molecules on the hot source efficiency. As *g* increases, all the surface components rapidly saturate and the main reason for the different behavior of the curves in Fig. 4b is the competition between different mass transfer mechanisms (growth from atomic or molecular fluxes). The initial increase of curve *1* and the increase of curve *2* in the whole range of *g* are related to a monotonic rise in the growth rate when the molecular-beam growth mechanism is essential (Fig. 4a). The subsequent sharp decrease in the *L* value, followed by an approach to the steady-state value of the diffusion interface smearing (within 1–2 Å) (curve *1* in Fig. 4b), is related to a change in the mass transfer mechanism. In this range of *g*, the atomic fluxes of Si and Ge from the hot source are of primary importance in the growth process.

In closing, let us to discuss characteristic dependences of the transition layer width *L*' on the growth temperature and gas pressure in the reactor (Fig. 5). The *L*' values considerably diverge in the presence and absence of the hot source in the reactor. The *L*' value increases with an increase in the gas pressure (and, hence, in the growth rate). If the decomposition times for molecules adsorbed on the film surface are the same, the transition region is the thicker, the higher is V_{gr}. For the same reason, the interfaces become diffuse when the additional hot element is applied. Exceptions

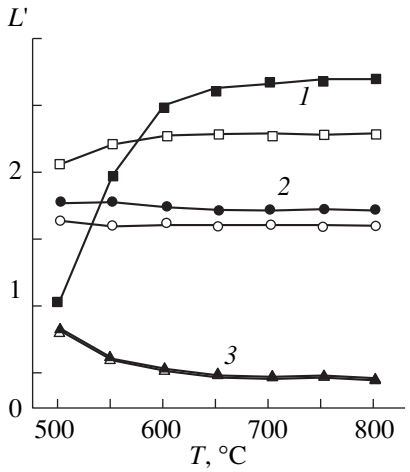

Fig. 5. L' as a function of the growth temperature. $P_{SiH_4}/P_{GeH_4} = 5$; P_{SiH_4} = (*1*) 1×10^{-3}, (*2*) 1×10^{-4}, and (*3*) 1×10^{-5} torr. Open symbols, $g = 0$; closed circles, $g = 0.1$ (hot-wire method).

are the case of extremely low gas pressures (Fig. 5, curves *3*), where the atomic fluxes from the hot source are insignificant, and the case of high gas pressures and growth temperatures $T_{gr} < 600$°C (Fig. 5, curves *1*). It is clear that the transition region at the interfaces may become very thin only in the latter case, where low growth temperatures ($T_{gr} < 600$°C) and atomic fluxes from the "hot wire" ($g \neq 0$) control the formation of the solid solution layer.

CONCLUSION

Note basic reasons that specify the component profile smearing at the interfaces when the process parameters are changed. One is a decrease in the lifetime of molecules adsorbed on the surface with increasing substrate temperature. Another is associated with a change in the roles of the atomic and molecular fluxes in mass transfer toward the growing surface. At high pressures, the latter has a more profound effect on the transition layer width. The hot-wire method increases the growth rate (provided that the flow of gases remains molecular). At gas pressures exceeding 10^{-3} torr and at growth temperatures below 600°C, it may be optimal for the minimization of the transition regions near the interfaces.

ACKNOWLEDGMENTS

The work was supported by the program "Universities of Russia" (grant no. 992849) and by the INTAS (grant no. 96-0580).

REFERENCES

1. D. W. Greve, Mater. Sci. Eng. B **18**, 22 (1993).
2. L. T. Vinh, V. Aubry-Fortuna, Y. Zheng, *et al.*, Thin Solid Films **294**, 59 (1997).
3. J. Thiesen, E. Iwaniczko, K. M. Jones, *et al.*, Appl. Phys. Lett. **75**, 992 (1999).
4. P. Brogueira, J. P. Conde, S. Arekat, and V. Chu, J. Appl. Phys. **78**, 3776 (1995).
5. R. Chelly, J. Werckmann, T. Angot, *et al.*, Thin Solid Films **294**, 84 (1997).
6. L. K. Orlov, V. A. Tolomasov, A. V. Potapov, *et al.*, in *Proceedings of the 9th Conference on Semiconducting and Insulating Materials, SIMC-IX*, Ed. by C. Fontaine (IEEE, New York, 1996), p. 215.
7. V. A. Tolomasov, L. K. Orlov, A. V. Potapov, *et al.*, Kristallografiya **43**, 535 (1998) [Crystallogr. Rep. **43**, 493 (1998)].
8. A. V. Potapov, A. V. Orlov, and C. V. Ivin, Thin Solid Films **336**, 191 (1998).
9. L. K. Orlov, A. V. Potapov, and S. V. Ivin, Zh. Tekh. Fiz. **70** (6), 102 (2000) [Tech. Phys. **45**, 770 (2000)].
10. L. K. Orlov, A. V. Potapov, and S. V. Ivin, in *Proceedings of the 3rd International Conference "Single Crystal Growth, Strength Problems, and Heat Mass Transfer," Obninsk, 1999*, p. 78.
11. L. K. Orlov, A. V. Potapov, and S. V. Ivin, Solid State Phenom. **69–70**, 221 (1999).
12. L. K. Orlov, A. V. Potapov, R. A. Rubtsova, and N. L. Orlova, Izv. Akad. Nauk **53**, 267 (1999).
13. L. K. Orlov, V. A. Tolomasov, A. V. Potapov, and V. I. Vdovin, Izv. Vyssh. Uchebn. Zaved., Mater. Élektron. Tekh., No. 2, 30 (1998).

Translated by M. Lebedev

Technical Physics, Vol. 46, No. 4, 2001, pp. 422–426. Translated from Zhurnal Tekhnicheskoĭ Fiziki, Vol. 71, No. 4, 2001, pp. 58–62.

Domain Dynamics in a Gunn Diode Inserted in a Resistive Circuit

S. I. Domrachev and A. A. Kuznetsov

Chernyshevsky State University, ul. Astrakhanskaya 83, Saratov, 410026 Russia

e-mail: KuznecovAA@info.sgu.ru

Received October 13, 1999; in final form July 25, 2000

Abstract—Temporal parameters of the current pulses generated by a Gunn diode operating in domain mode in relation to the supply voltage and load resistance are numerically simulated. The results of the numerical and analytical studies are compared. The validity range of the analytical formulas is ascertained in detail. In the context of the considered model, the minimum pulse duration and the time of domain formation are obtained at zero load and for a supply voltage exceeding the critical value by a factor of 1.25. © *2001 MAIK "Nauka/Interperiodica".*

INTRODUCTION

A number of attractive features of electrical current short pulses generated by a Gunn diode make it promising for application in high-speed electronic and optoelectronic devices [1–4]. For example, a Gunn diode enables one to obtain high amplitude ultrashort pulses of current (tens of amperes) with a duration ranging between tens and hundreds of picoseconds at a low-resistance load.

From practical point of view, it is important to know the dependences of the amplitude, the shape and the temporal characteristics of the pulses on the load (in external circuit) and supply voltage, as well as the operating conditions that yield the minimum duration of the pulses generated. There are numerous studies concerning Gunn diode transients. The most detailed analysis of the domain dynamics were carried out in [2, 5, 6], and a brief overview of the previous results related to this problem was presented in [7]. However, these studies are not free of drawbacks and are subject to refinement. By way of example, in the often sited publications [5, 6], the transient time of domain formation is specified as the time of settling of a steady-state voltage at a domain, whereas the time of establishment of a steady-state current through the sample is practically important. For the supply voltage considerably exceeding the Gunn effect threshold, the latter time can be considerably shorter than the former due to the saturation of the current at a high domain voltage. An additional point to clarify is the validity range of analytical formulas derived in [2, 5] for the time of domain formation in relation to the load resistance and the supply voltage.

In this paper, we report the results of studying the temporal parameters of pulses: the total width τ_w, the rise time τ_r, the decay time τ_d in the steady-oscillation mode, and the time of establishment of a steady-state current τ_s in the single-pulse mode in relation to the supply voltage and the resistive load. All the calculations are accomplished for a Gunn diode model with parameters representing those of an actual diode. The supply voltage and the load vary in the ranges corresponding to the absence of impact ionization in an actual sample.

MODEL REPRESENTATION AND CALCULATION TECHNIQUE

We numerically simulated the dynamics of charge and current in *n*-GaAs samples with the following parameters: length $l = 100$ μm, $\mu_0 = 0.8$ m^2/(V s), $D = 200$ cm^2/s, $V_s = 0.85 \times 10^5$ m/s, and $E_0 = 4 \times 10^5$ V/m. The set of phenomenological parameters given above corresponds to the diode characteristics used in [3]. The calculations were made in terms of the local-field one-dimensional model [4] including the equation for the total electric current

$$\varepsilon\varepsilon_{00}\left(\frac{\partial E}{\partial t} + V(E)\frac{\partial E}{\partial x} - D\frac{\partial^2 E}{\partial x^2}\right) + q\left(V(E)n_0(x) - D\frac{dn_0}{dx}\right) = J(t), \quad (1)$$

where $n_0(x) = n_d f(x)$ stands for the equilibrium concentration of electrons, D is the diffusion coefficient, and ε is the permittivity. The equation for the external circuit is

$$J(t) = \frac{U_0 - \int_0^L E(x,t)dx}{SR_n}, \quad (2)$$

1063-7842/01/4604-0422$21.00

where S is the area of the sample, U_0 is the supply voltage, and R_n is the load resistance.

The field dependence of the electron velocity (velocity–field characteristic) is approximated by the well-known expression [8]

$$V(E) = \frac{\mu_0 E + V_s (E/E_0)^4}{1 + (E/E_0)^4}, \quad (3)$$

where E_0 is a normalizing field, V_s is the saturation rate, U_0 is the supply voltage, and μ_0 is the weak-field mobility.

Strictly speaking, the local field model that treats the electron velocity as an instantaneous function of field is not adequate for the analysis of transients lasting for tens of picoseconds. However, its application to the case under consideration is justified by the fact that we are interested in the relative variations in the pulse durations with the load resistance and the supply voltage rather than in the absolute duration of pulses. For the same reason, the model of the sample (Fig. 1) does not account for contact inhomogeneities and the boundary conditions are given by

$$\frac{\partial E}{\partial x}(0) = \frac{\partial E}{\partial x}(L) = 0, \quad (4)$$

$$E(x, 0) = \frac{U_t}{L}, \quad (5)$$

where U_t denotes the threshold voltage of the Gunn effect and L is the length of the sample.

The domain formation was initiated by a stepwise, change (amounting to about 10%) in the equilibrium concentration of the near-cathode electrons, the so-called "notching." Variation of the notch depth within the 5–10% range affected only slightly on the results of calculations. Moreover, the calculated duration of pulses is very close to that experimentally observed [3]. It is convenient to search for a numerical solution of Eqs. (1) and (2) in terms of the dimensionless variables: $X = x/l_0$, $T = t/\tau_0$, $V_1 = V/V_0$, and $E_1 = E/E_0$, where the unit velocity $V_0 = \mu_0 E_0$, the unit time $\tau_0 = (\varepsilon\varepsilon_0)/(qn_d\mu_0)$, and the unit length $l_0 = V_0\tau_0$. On rearrangement, the system of Eqs. (1) and (2) becomes

$$\frac{\partial E}{\partial T} = -V_1 \frac{\partial E_1}{\partial X} + c\frac{\partial^2 E_1}{\partial X^2} - fV_1 + J_1 + c\frac{df}{dX}, \quad (6)$$

$$J_1 = \frac{R_0}{R_n}\left(\frac{U}{E_0 L} - \frac{1}{X_{\max}}\int_0^{X_{\max}} E_1 dX\right), \quad (7)$$

where $X_{\max}$ is the dimensionless diode length, $f = (n(x))/n_d$ is the diode doping profile, $c = (D\tau)/l_0^2$ is the dimensionless diffusion-length squared, $R_0 = L/(en_0\mu_0 S)$ is the low field resistance of the sample, and $J_1 = J/(qn_0V_0)$ is the normalized current density.

The system in question was approximated with an absolutely stable and conservative implicit difference scheme obtained by an integro-interpolation technique [9, 10]. For a grid $x = ih$, $t - j\tau$, we have

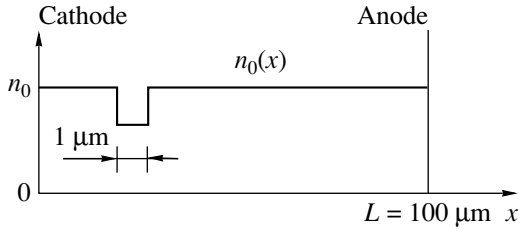

Fig. 1. Doping profile in the Gunn diode.

$$\frac{E_i^{j+1} - E_i^j}{\tau} = -\frac{(E_{i+1} - E_{i-1})^{j+1} V_i^{j+1}}{2h} + c\frac{(E_{i+1} - 2E_i + E_{i-1})^{j+1}}{h^2} - f_i V_i^{j+1} + J_1^j + c\frac{(f_{i+1} - f_{i-1})}{2h}. \quad (8)$$

In order to find the field E_i^{j+1} at the $(j + 1)$th time layer, the system of nonlinear difference Eqs. (8) is reduced to the following iterative scheme (s is the number of iteration):

$$A_i^s E_{i-1}^{s+1} - C_i^s E_i^{s+1} + B_i^s E_{i+1}^{s+1} = -F_i^s. \quad (9)$$

Here, A, B, and C coefficients are determined from (8) and can be written as

$$A_i^s = \frac{c\tau}{h^2} + \frac{\tau}{2h}V_i(E_i^s), \quad B_i^s = \frac{c\tau}{h^2} - \frac{\tau}{2h}V_i(E_i^s),$$

$$C_i^s = 1 + \frac{2c\tau}{h},$$

$$F_i^s = E_i^j + \tau\left(J_1^j + \frac{c}{2h}[f_{i+1} - f_{i-1}] - f_i V(E_i^s)\right).$$

The system of linear Eqs. (9) is solved for E_i^{s+1} by the sweep method [10] with the boundary and initial conditions (4) and (5), respectively. We assume that, at zero iteration step, E_i^s is equal to E_i^j and after two iterations, E_i^{j+1} is equal to E_i^{s+1}. The mesh width was chosen from conditions for ensuring computation convergence, reasonable calculation time, and amounts $\tau = 0.2$ and $h = 0.5$.

RESULTS AND DISCUSSION

Steady-State Self-Oscillation Mode

The duration of the domain pulse of current versus the notch amplitude for different resistive loads is shown in Fig. 2. It is evident that the notch amplitude

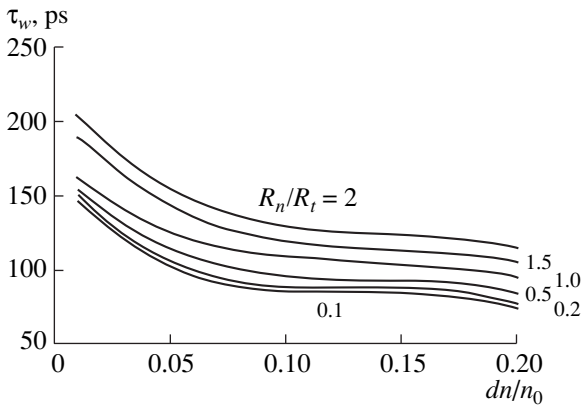

Fig. 2. Pulse duration in the steady-state self-oscillation mode versus the depth of a notch in the doping profile for different resistive loads U given by (10); $m = 1$.

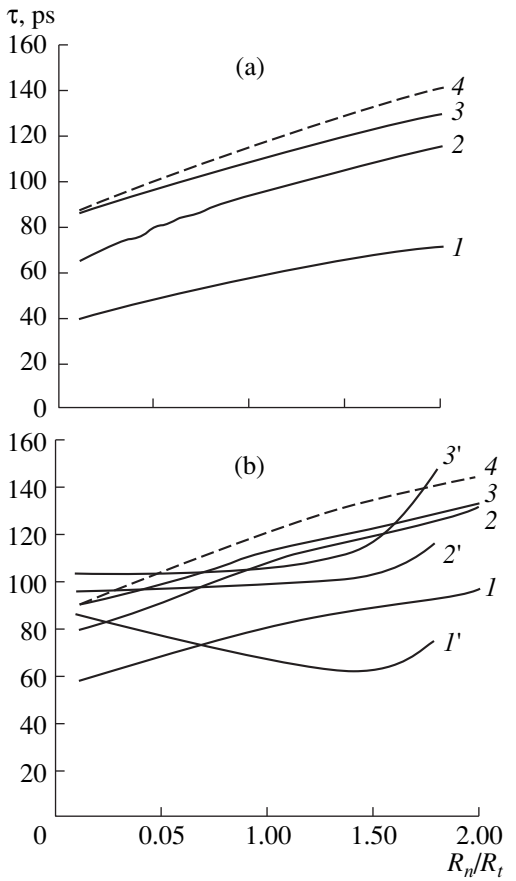

Fig. 3. Temporal parameters of pulse versus the resistive load R_n and voltage given by (10) (a) for $m = 1$ and (*1*) τ_d, (*2*) τ_r, (*3*) τ_w, and (*4*) $\tau_w = \tau_{0w}(1 + R_n/R_t)^{1/2}$; (b) for $m = 1.5$ (curves *1–4*) and constant supply voltage $U = 2.5U_t$: (*1*') τ_d, (*2*') τ_r, and (*3*') τ_w.

optimal for our calculation amounts approximately to 10%, which corresponds to the flat portion of the curves. The influence of the load resistance was studied with the bias voltage maintained at the threshold level (or larger than the threshold by a given factor of m); i.e., we have

$$U = mU_t\left(1 + \frac{R_n}{R_t}\right), \tag{10}$$

where

$$R_t = \frac{E_t L}{en_0 V(E_t) S}$$

is the resistance of the sample at the threshold voltage $E_t = U_t/L$.

The temporal parameters of the current pulse in the steady-state self-oscillation mode (for the second and subsequent domain cycles) versus the resistive load are shown in Figs. 3a and 3b for $m = 1$ and 1.5, respectively. In addition, for the sake of comparison, we also show the results of analytical approximation [4]:

$$\tau_w = \tau_{0w}\sqrt{\left(1 + \frac{R_n}{R_0}\right)}$$

fitted to numerical curve *3* at $R_n = 0$. Here, τ_{0w} stands for the pulse width at $R_n = 0$.

The pulse temporal parameters against the load resistance R_n at constant supply voltage $U = 2.5U_t$ are plotted in Fig. 3b. It can be seen that, at constant voltage maintained at a threshold (or by a factor of m larger), all the parameters increase steadily with load. This follows from an increase in the domain charging discharging time constant proportional to the domain capacity and the load resistance [2]. The monotonic character of the curves in this case is attributed to the fact that, whatever R_n is, the conditions for domain formation are the same, specifically, when the sample voltage equals mU_t. Therefore, the initial capacitance of the domains remains constant. A comparison of Figs. 3a and 3b shows that the analytical and numerical curves coincide at the threshold voltage and that further increase in the diode voltage draws them apart. At constant supply voltage (Fig. 3b), the temporal parameters of the pulse generally exhibit a weak dependence on the low-resistance load but rise steeply for greater R_n. The latter phenomenon is due to the load–diode voltage redistribution, resulting in the drop of the diode bias below the threshold and the cessation of generation.

The temporal parameters of pulses in relation to the supply voltage in the steady-state self-oscillation mode for $R_n = 0.01R_t$ and $R_n = 0.5R_t$ are shown in Figs. 4a and 4b, respectively. In the latter case, the rise and decay times increase steadily with voltage, while the total pulse width first decreases somewhat and then increases steadily. When analyzing the transient process, it is important to bear in mind that the build-up conditions for the first and the following domains are different. In particular, the first domain emerges in homogeneous samples (within the model assumed), while every successive domain is affected by the pre-

ceding one. The larger the bias voltage, the more pronounced the influence of a preceding domain; i.e., for most of the oscillation period, two domains coexist. As was mentioned in [6], the domain outgoing into the anode serves as a resistive load for the dipole layer under formation. This resistive load increases with the bias voltage, thus extending both the decay time and the total pulse width.

Evolution of current pulses was simulated for various supply voltages (Fig. 5). It is evident that the current-pulse shape depends on the law of the voltage build-up. The curves shown in Fig. 5a correspond to voltage increasing exponentially with time constant at 50 ps; Fig. 5b corresponds to a stepwise increase in the voltage.

Single-Pulse Mode

As was mentioned above, it is convenient to characterize the Gunn diode transients using the time of establishing the steady-state current τ_s. Let us define it as the time period lasting from switching on the power supply up to the moment when the diode current exceeds saturation by 0.1 of the difference between the threshold and saturation currents. For all calculations, a stepwise rise of the supply voltage is assumed. The transient time τ_s calculated as a function of the load resistance is plotted in Fig. 4c, with $m = 1$. The time of domain formation analytically estimated by expression (4.7.28) given in [2] and the formula from [4], which is mentioned above, is also shown for comparison. These two curves indicate that there is good agreement between the numerical and analytical results, especially for the large notch values. The last feature follows from the fact that expression (4.7.28) in [2] was derived disregarding the low-signal stage of the domain growth.

The time of the current transient as a function of the supply voltage for $R_n = 0.01R_t$ is presented in Fig. 4a. The corresponding analytical estimation (4.7.28) [2] is also shown. It can be seen that, at high voltages, the analytical curve does not even qualitatively agree with the numerical one; the latter predicts an increase in all the characteristic temporal parameters of pulse with voltage for both the first and the successive domains. Therefore, the analytical expression from [2] for the time constant of domain formation is valid only at low diode voltage, since this expression is based on the assumption of $V(E_r) = \mu_0 E_r$ which is valid only for the residual field E_r below the threshold. In this connection, we should note the that the interpretation [6] of the analytically predicted acceleration of the domain formation with voltage in [2, 5] is generally incorrect. This interpretation is based on the assumption that at high voltages, the domain capacitance is charged with a larger current; hence, the domain has an increased capacitance for a shorter time. The above consideration is inappropriate since it does not account for a high-field leveling-off of the carrier velocity. The acceleration of the domain formation with voltage manifests itself only in a decrease in the decay time τ_c from the threshold to the saturation value (Fig. 5b). In this case, the assumption $V(E_r) = \mu_0 E_r$ is correct and the analytical formula for the voltage dependence of the pulse decay time is qualitatively adequate (Fig. 4a). Quantitative discrepancies stem, firstly, from the saturation of current (analytically, it is the time of voltage settling that is considered) and, secondly, from the fact that the domain acquires basically different shape in a strong

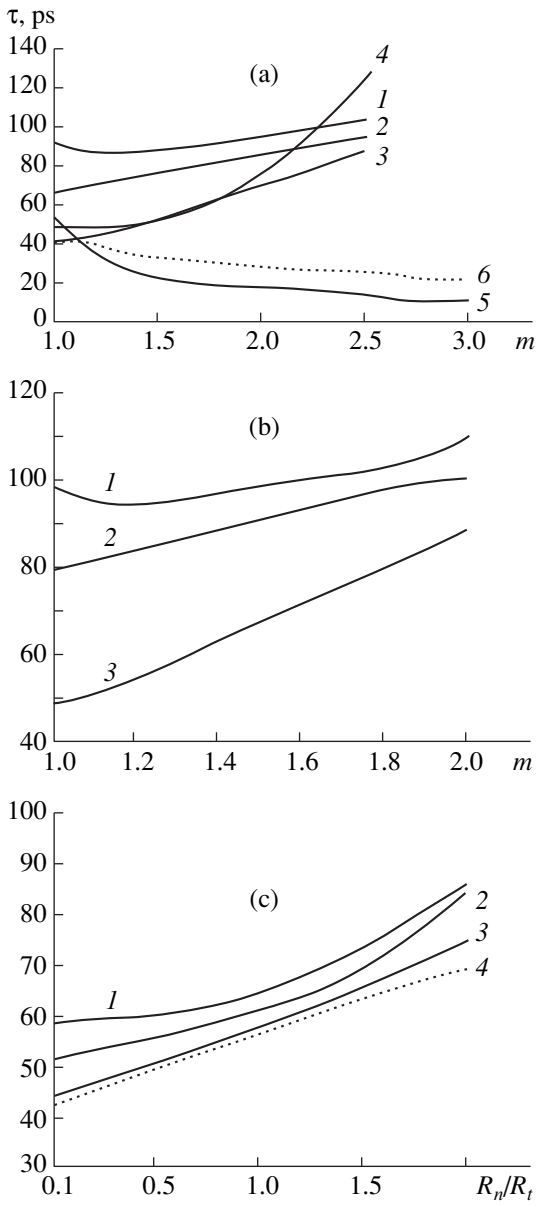

Fig. 4. Temporal parameters of pulse versus the supply voltage for different resistances of (a) $R_n = 0.01R_t$ and (b) $0.5R_t$: (*1*) τ_w, (*2*) τ_r, (*3*) τ_d, (*4*) τ_s, (*5*) τ_c, and (*6*) analytically estimated time of domain formation; (c) transient time versus load resistance at $m = 1$ for depth of the doping notch dn/n_0: (*1*) 0.02, (*2*) 0.1, and (*3*) 0.4; (*4*) corresponds to analytically estimated time of domain formation.

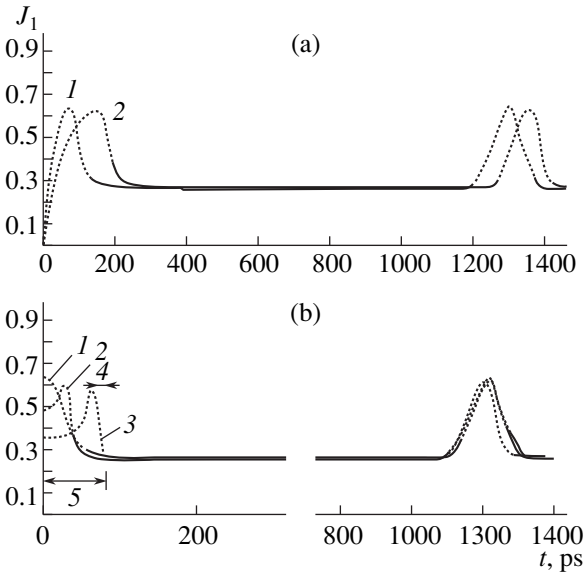

Fig. 5. Shape of diode current pulses resulting from supply voltage with different rise times: (a) exponential rise with time constant 50 ps for m: (*1*) 1 and (*2*) 1.5; (b) stepwise rise for m: (*1*) 1, (*2*) 1.5, and (*3*) 2; (*4*) τ_c, (*5*) τ_s.

field during the formation of the transient rather than a steady-state domain; the latter circumstance is disregarded in analytical treatment for simplicity.

From the above discussion, it is easy to explain qualitatively the shape of the current pulse during the domain formation transient and also the dependence of the transient time on the supply voltage. When slightly above the threshold, the supply voltage validates the assumptions made in analytical theory [5] and the theory is applicable. At higher voltages, the domain formation can be divided into two stages. In the first stage, the field in the sample is above the threshold and the diode current is small. During domain formation, the outside domain field decreases and the diode current increases (Fig. 5b). As a result of the leveling off of the velocity–field characteristic, the difference in electron velocities inside and outside the domain decreases with the voltage (Fig. 5b). In the second stage, when the diode current and the residual field E_r in the diode drop below the threshold, theory [5] is valid and the decay time of current decreases with voltage due to a decrease in the domain capacitance. For comparatively low supply voltages, a decrease in the domain capacitance prevails, while at higher voltages, an increase in the rise time due to the carrier velocity saturation is dominant. Therefore, the time of formation is shortest when these two effects are counterbalanced.

CONCLUSION

The dynamics of a dipole domain in a Gunn diode connected to a resistive load is studied. The calculation shows that, for a constant voltage maintained at the threshold level, the duration of current pulses steadily grows with the load and can be approximated as

$$\tau_w = \tau_{0w}\sqrt{\left(1 + \frac{R_n}{R_0}\right)},$$

where τ_{0w} is the pulse duration for $R_n = 0$.

For a constant supply voltage, the parameters of a pulse vary with the load resistance only slightly; however, as R_n/R_t increases above 1.5, the pulse duration increases, and then up to break down of oscillations. In the general case, voltage dependences of the temporal parameters of pulse are nonmonotonic. As voltage increases, the pulse duration first slightly decreases, attains a minimum at $U/U_t = 1.25$, and then begins to increase. The analytical estimation of the time of domain formation proved to be correct only for fields close to the threshold value. In contrast to analytical predictions, neither the domain formation time nor the transient time of the current decrease with voltage; rather, both of them increase. Only the decay time of current decreases with voltage: it decreases from the threshold to the saturation value. Our calculation indicates that the minimum transient time (within the model assumed) is attained at the supply voltage exceeding the threshold by a factor of 1.25 and with zero load resistance. The results obtained hold much promise for the design of high-power Gunn generators of picosecond pulses.

REFERENCES

1. S. A. Kostylev, V. V. Goncharov, I. I. Sokolovskiĭ, and A. V. Chelyadin, *Semiconductors with Bulk Negative Conduction in Microwave Fields: Electron Processes and Functional Possibilities* (Naukova Dumka, Kiev, 1987).
2. M. Shur, *GaAs Devices and Circuits* (Plenum, New York, 1987; Mir, Moscow, 1991).
3. S. I. Domrachev, S. A. Alaverdyan, and V. N. Skorokhodov, Zh. Tekh. Fiz. **69** (5), 74 (1999) [Tech. Phys. **44**, 544 (1999)].
4. M. E. Levinshtein, Yu. K. Pozhela, and M. S. Shur, *Gunn Effect* (Sov. Radio, Moscow, 1975).
5. M. S. Shur, Fiz. Tekh. Poluprovodn. (Leningrad) **7** (6), 1178 (1973) [Sov. Phys. Semicond. **7**, 791 (1973)].
6. M. E. Levinshtein and G. S. Simin, Fiz. Tekh. Poluprovodn. (Leningrad) **13** (5), 903 (1979) [Sov. Phys. Semicond. **13**, 529 (1979)].
7. G. S. Simin, Fiz. Tekh. Poluprovodn. (Leningrad) **8** (5), 1028 (1974) [Sov. Phys. Semicond. **8**, 669 (1974)].
8. H. Thim, J. Appl. Phys. **39** (8), 3897 (1968).
9. V. I. Nayanov, S. K. Potapov, and M. A. Safonova, Élektron. Tekh., Ser. 1: Élektron. SVCh **5**, 28 (1983).
10. A. N. Tikhonov and A. A. Samarskii, *Equations of Mathematical Physics* (Nauka, Moscow, 1972; Pergamon, Oxford, 1964).

Translated by A. Sidorova

Technical Physics, Vol. 46, No. 4, 2001, pp. 427–430. Translated from Zhurnal Tekhnicheskoĭ Fiziki, Vol. 71, No. 4, 2001, pp. 63–67.

OPTICS, QUANTUM ELECTRONICS

Dynamic Range of Materials for the Magneto-Optic Imaging of Magnetic Fields

V. I. Butrim, V. G. Vishnevskiĭ, and S. V. Dubinko

Domen Design Bureau, Tauria National University, Simferopol, 95001 Ukraine

e-mail: domain@home.cris.net

Received February 21, 2000; in final form, September 1, 2000

Abstract—The range of rearrangement of the natural domain structure of epitaxial garnet ferrite films in magnetic fields produced by conventional recording magnetic media was calculated using numerical methods. Maximum and minimum periods of the recording medium signalograms that could be imaged using the film domain rearrangement were obtained as functions of the recording medium and film parameters. © *2001 MAIK "Nauka/Interperiodica".*

Magneto-optic methods of information processing have many applications. This makes the problem of studying the behavior of the domain structure (DS) of epitaxial garnet ferrite films (EGFF) in spatially nonuniform magnetic fields fairly topical. Domain structure rearrangement in magnetic fields produced by conventional recording magnetic media (RMM) is of special interest. The period of nonuniformity of these fields is comparable with the natural period of the domain structure of EGFF, whereas the field amplitude does not exceed the field of collapse of the natural DS. Rearrangement of DS can be implemented by changing the natural DS period [1–3] or by domain width modulation [4, 5].

Calculations of the statistical parameters and conditions for stability of strip DS induced by a spatially nonuniform field of RMM were performed in [1–3]. However, only thick EGFF were studied in these papers. The natural period d_0 of narrow stripe domains formed in such EGFF is smaller than the film thickness h. Such films can be used to image signalograms with large stray fields. Topographizing of signalograms from weakly magnetized RMM should be performed using thin films even though the total Faraday rotation is decreased, because the amplitude of the stray field of the periodic signal decays exponentially upon increasing the spatial frequency and distance to RMM. However, if the film thickness is less than the characteristic length λ of EGFF material, the natural DS period becomes approximately equal to the film thickness. In this case, the results obtained in [1, 2] are invalid. Thus, it seems reasonable that the imaging of signalograms with small stray fields should be performed using thin films with the DS period much larger than the film thickness. The calculations given below are valid for any value of $x_0 = d_0/h$.

In the approximation of high uniaxial anisotropy (quality factor $Q \gg 1$), a natural strip or labyrinth DS with linear domain boundaries (DB) is formed in the film. The magnetization vector is parallel to the DB plane. The exchange energy and the energy of anisotropy can be included in the DB energy. Let the consideration be restricted to the case of one-to-one correspondence. In this case, the period of the DS induced by the RMM field is exactly the same as the signalogram period [1], and the sinusoidal instability effects are absent (i.e., the DB are linear). Development of sinusoidal instability of the DB results in the formation of a DS combining uniformly magnetized areas with labyrinth patterns. In a sense, this case meets the conditions for analog representation of the signalogram field by the domain width modulation [5].

Let us consider a two-layer system consisting of an RMM and an indicator EGFF separated from one another by a gap a. The recording medium is the source of a spatially nonuniform magnetic field. Assuming that the residual magnetization distribution in the RMM with longitudinal magnetization is described by the harmonic function with a period d, the system energy density can be written in a conventional form [1]

$$W(x, \nu) = \frac{4\pi M_s^2}{1 + k + a_0}\left[\frac{2\lambda_0}{x} + \frac{2}{\pi^3}xF(x) - \frac{\nu}{\pi^3}xG(x)\right], \quad (1)$$

where $\lambda_0 = \lambda/h$, $k = t/h$, $a_0 = a/h$, $x = p/h$, $\nu = (\pi/4)(M_t/M_s)$; t and M_t are the thickness and the residual magnetization of RMM, respectively; p and M_s are the induced DS period (equal to the RMM field period) and the EGFF saturation magnetization, respectively. Func-

1063-7842/01/4604-0427$21.00

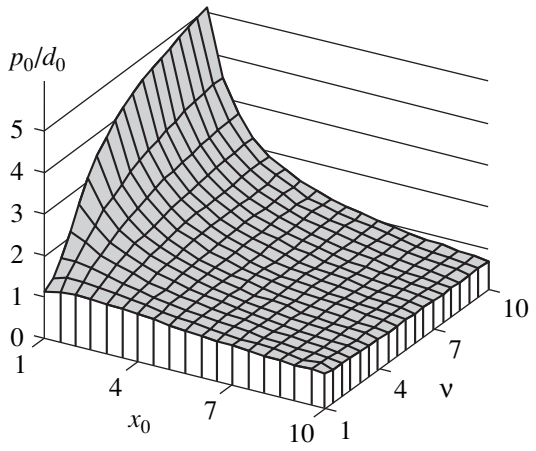

Fig. 1. Equilibrium period of the induced DS normalized to the natural period d_0 as a function of x_0 and ν.

tions $F(x)$ and $G(x)$ are determined as follows:

$$F(x) = \sum_{n=1}^{\infty} \frac{1}{n^3}[1 - \exp(-2\pi n/x)], \quad n = 1, 3, 5, \ldots;$$
$$G(x) = \exp(-2\pi a_0/x) \times [1 - \exp(-2\pi/x)][1 - \exp(-2\pi k/x)]. \quad (2)$$

The first two terms in Eq. (1) are the DB energy density and the magnetostatic energy density, respectively. The last term describes the interaction between EGFF and RMM.

The equilibrium period p_0 of the induced DS of EGFF is subject to the condition for minimum W and should satisfy the following equation ($q = p_0/h$)

$$qF(q) - 2\pi Q(q) - \pi\nu\left[G(q)\left(a_0 + \frac{q}{2\pi}\right) - R(q)\right] - \frac{\pi^3\lambda_0}{q} = 0, \quad (3)$$

where

$$Q(q) = \sum_{n=1}^{\infty} \frac{1}{n_2}\exp\left(-\frac{2\pi n}{q}\right), \quad n = 1, 3, 5, \ldots;$$
$$R(q) = \exp\left(-\frac{2\pi a_0}{q}\right)\left[k\exp\left(-\frac{2\pi k}{q}\right)\left(1 - \exp\left(-\frac{2\pi}{q}\right)\right) + \exp\left(-\frac{2\pi}{q}\right)\left(1 - \exp\left(-\frac{2\pi k}{q}\right)\right)\right]. \quad (4)$$

Parameter λ_0 involved in Eq. (3) can be expressed in terms of the natural period d_0 of EGFF DS. If $\nu = 0$, we obtain from Eq. (3) that ($x_0 = d_0/h$)

$$\pi^3\lambda_0 = x_0[x_0F(x_0) - 2\pi Q(x_0)], \quad (5)$$

from which it follows, in particular, that the natural DS period in thin films ($\pi\lambda_0 > 1$) is of the order of thickness h [1]:

$$x_0 = \exp(\pi\lambda_0 - c), \quad c = 1.3.$$

Thus, Eqs. (3) and (5) determine the equilibrium period of the induced DS of EGFF as a function of the natural DS period and the system parameters ν, l, and a_0. In the least understood range $p_0/h > 1$ and $x_0 > 1$, this equation can be solved numerically. The dependence of p_0/d_0 on x_0 and ν for $k = 1$ and $a_0 = 0.2$ is shown in Fig. 1. It can be seen that p_0 significantly exceeds d_0 at large values of ν and is virtually independent of x_0.

Analysis of Eq. (1) shows that the energy branch of the EGFF–RMM system is below the energy branch of the separate EGFF. Therefore, there is a range of parameters x and ν (k and a_0 being fixed) within which

$$W(x, \nu) \le W(x_0, \nu = 0), \quad (6)$$

so that the induced DS rather than natural DS is energy-optimal within this range.

Expression (6) can be regarded as the amplitude–frequency characteristic of the system, because it relates the frequency characteristics of EGFF (x_0) and RMM (x) to their amplitude characteristics (ν). Solving this inequality for x, we obtain the limits of rearrangement of the induced DS of EGFF exposed to the RMM field as a function of x_0 and ν:

$$\left[F(x) - \frac{\nu}{2}G(x)\right]x^2 - \left[x_0F(x_0) + \pi^3\frac{\lambda_0}{x_0}\right]x - \pi^3\lambda_0 = 0. \quad (7)$$

This equation has two roots corresponding to the minimum (p_{min}) and maximum (p_{max}) periods of RMM signalograms that can be imaged using the EGFF DS rearrangement. A stable strip structure representing the spatial distribution of the field should exist within this range of periods.

The results of the numerical solution of Eq. (7) are shown in Fig. 2. It can be seen that the induced DS rearrangement range is extended with increasing amplitude of the RMM stray field, provided that the EGFF magnetization is constant. As seen from Fig. 2, the range of periods significantly larger than the natural DS period (i.e., low spatial frequency range) is included in the rearrangement range. The properties of the film also affect the rearrangement range. The imaging range is extended with increasing x_0. It should be noted that p_{min} depends on x_0, ν, and k much differently than p_{max}. The period p_{min} is a monotonically decreasing function of both x_0 and ν and depends only slightly on k, whereas p_{max} is virtually independent of the EGFF properties (x_0) and depends on k and ν in the following manner: $p_{max} \cong \alpha(k)\nu$, where $\alpha(k)$ is a monotonically increasing function of k.

On solving Eq. (7) for ν, we obtain the amplitude sensitivity threshold ν_{min} for EGFF:

$$\nu_{min} = \frac{2}{xG(x)}\left[\pi^3\lambda_0\left(\frac{1}{x}-\frac{1}{x_0}\right) + xF(x) - x_0F(x_0)\right]. \quad (8)$$

Within the range $1 < x_0 < 10$, Eq. (8) can be approximated as $\nu_{min} \cong 0.35(\gamma - 1)$, where $\gamma = x/x_0 > 1$. If the EGFF DS period is equal to the RMM field period, $\gamma = 1$ and $\nu_{min} = 0$. Thus, the condition (6) for the occurrence of the induced DS can be recast as:

$$p_{min} < p < p_{max}, \quad \nu > \nu_{min}. \quad (9)$$

The spatial frequency characteristics of EGFF used as transducers in imaging devices were determined experimentally using special reference signalograms stored on magnetic tape. The signalograms consisted of a series of sinusoidally magnetized areas (signal packages modulated onto the harmonic carrier). The spatial frequency of all packages constituting the given signalogram was constant, whereas the residual magnetization of a package was half as high as that of the preceding package. Such signalograms were recorded using a high-frequency bias-current pulse series modulated in amplitude such that the amplitude of each subsequent pulse was half as high as that of the preceding pulse (Fig. 3). The package-shaping device provided an 11-bit record of signal amplitude, discrete frequency adjustment, high-frequency bias-current optimization, and nonlinear distortion monitoring. Tapes with various magnetic coatings (including two-layer tapes) were used for recording. Reference standards of nonuniform magnetic fields with spatial frequencies falling within a range of 1000 to 5 mm^{-1} inclusive were obtained. Maximum residual magnetization of the obtained standards did not exceed 0.7 of the RMM saturation magnetization.

Signal package imaging was based on the Faraday effect in reflected polarized light. Packages meeting condition (9) were distinctly seen against the background of the natural DS of EGFF as strip domains with a period equal to the signalogram period. Packages that did not meet condition (9) could not rearrange DS and, therefore, could not be observed. The number N of observed packages is related to ν_{min} by the equation

$$2^N = \nu_{max}/\nu_{min}, \quad (10)$$

where ν_{max} corresponds to the package with the maximum residual magnetization (this value is constant for a given EGFF–RMM system).

As follows from Eq. (10), N increases with decreasing γ and reaches its maximum for $\gamma \longrightarrow 1$. This is illustrated in Fig. 4, in which a film segment with an induced magnetization jump (natural period) in the RMM field is shown (signal was recorded as shown in Fig. 3). In the region A, $\gamma = 1.2$ and the number of observed packages $N = 5$, whereas in the region B, $\gamma = 0.5$ and $N = 2$. The dynamic range of the natural DS rearrangement also depends on N:

$$D = 20\log 2^N. \quad (11)$$

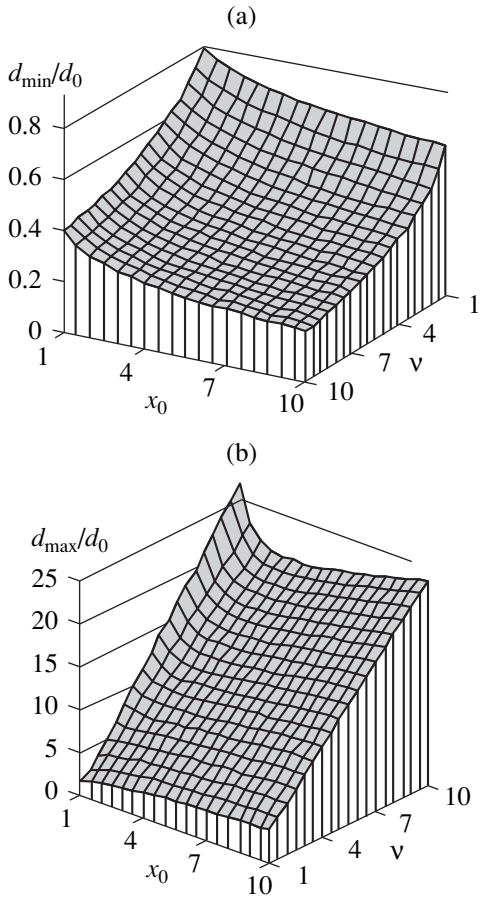

Fig. 2. (a) Minimum and (b) maximum periods of the induced DS normalized to the natural period of the film d_0 as a function of x_0 and ν.

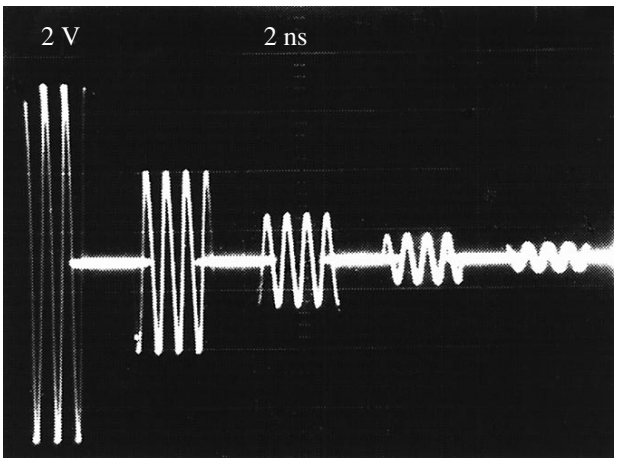

Fig. 3. Signal package recording signal oscillogram.

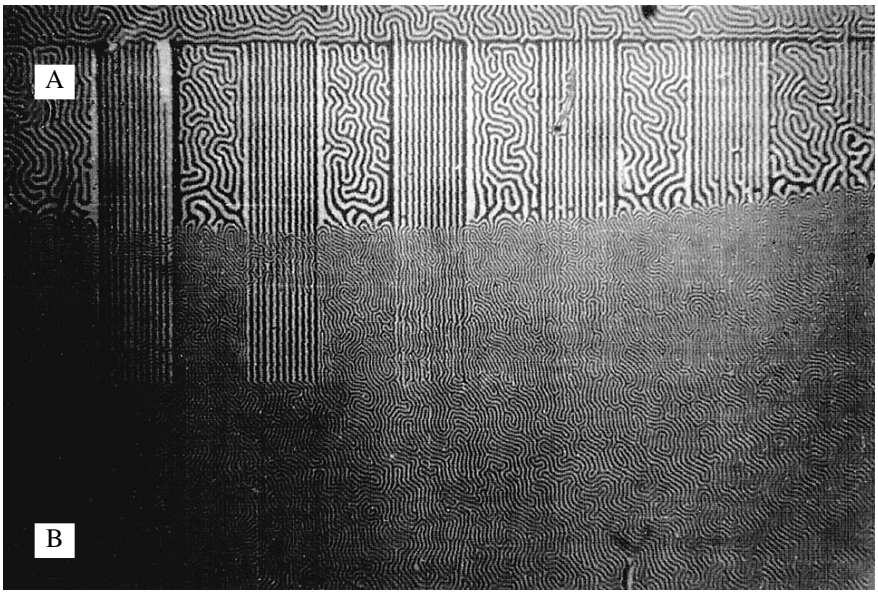

Fig. 4. Control signalogram imaging using EGFF with a local gradient of saturation magnetization. In region *A*, magnetization is less than in region *B*. The spatial period is 50 μm.

The dependence of D on x for given x_0 and ν_{max} is shown in Fig. 5. As seen from Fig. 5, there is a singularity in D for $\gamma \longrightarrow 1$. The dynamic range of EGFF was evaluated by calculating the number N of packages discerned during imaging. In the region A of the film (Fig. 4) the dynamic range D was 24 dB; in the region B, 18 dB. The majority of EGFF with perpendicular anisotropy used in imaging devices have a dynamic range D of approximately 30–35 dB. A decrease in the dynamic range is observed at high spatial frequencies, which correlates well with the calculations made above.

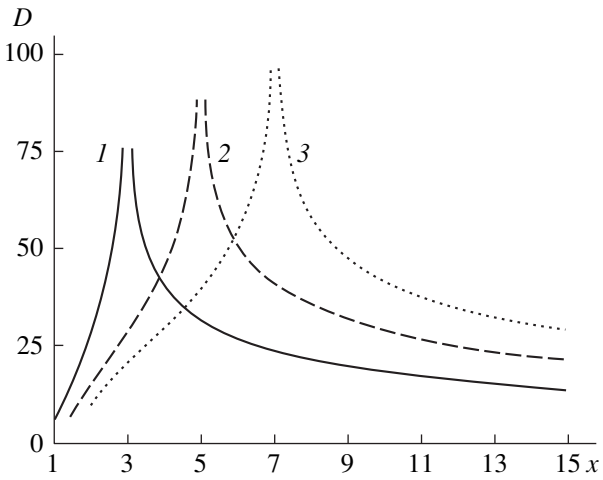

Fig. 5. Dependence of the dynamic range D on x: $\nu_{max} = 7$; $x_0 =$ (*1*) 3, (*2*) 5, and (*3*) 7.

Thus, the analysis of magnetostatic interactions in the system EGFF–RMM showed that (a) the dynamic range D is maximum for $\gamma \longrightarrow 1$, the sensitivity is also maximum for $\gamma \longrightarrow 1$ ($\nu_{min} \longrightarrow 0$), (b) the induced DS rearrangement range depends mainly on the ratio between the tape and film magnetizations, (c) it is expedient to use films with the period d_0 far exceeding the film thickness h for imaging high-spatial-frequency signalograms, and (d) imaging of large spatial periods requires the parameter k of EGFF to be increased.

REFERENCES

1. S. V. Gerus, F. V. Lisovskiĭ, and E. G. Mansvetova, Mikroélektronika **10** (6), 506 (1981).
2. S. Neubert, J. Lehureau, J. Colineau, and J. Castera, IEEE Trans. Magn. **23** (3), 1919 (1987).
3. N. F. Kubrakov, Tr. Inst. Obshch. Fiz. Akad. Nauk SSSR **35**, 136 (1992).
4. S. A. Gladkiĭ, I. I. Davidenko, É. P. Didyk, *et al.*, Ukr. Fiz. Zh. **36** (1), 103 (1991).
5. V. V. Volik, I. I. Davidenko, V. F. Kovalenko, and S. N. Lyakhimets, Mikroélektronika **25** (6), 467 (1996).

Translated by K. Chamorovskiĭ

Technical Physics, Vol. 46, No. 4, 2001, pp. 431–437. Translated from Zhurnal Tekhnicheskoĭ Fiziki, Vol. 71, No. 4, 2001, pp. 68–75.

Recombination Population of Highly Excited CO_2 States in a Shock-Heated Jet

A. V. Eremin, V. S. Ziborov, and V. V. Shumova

Institute of High Temperatures Scientific Association (IVTAN), Russian Academy of Sciences, Izhorskaya ul. 13/19, Moscow, 127412 Russia

Received March 31, 2000

Abstract—The spectral distribution of nonequilibrium emission from electron bands of partially dissociated CO_2 in a supersonic jet was studied. A detailed model of kinetic and energy-exchange processes in a vibrationally nonequilibrium recombining CO_2 flow is elaborated. Within this model, the basic kinetic equation for the distribution of CO_2 excited state populations was solved in a ladder approximation. It is shown that inverse population for the $^3B_2 \longrightarrow X^1\Sigma$ transition ($\lambda = 400$ nm) is a possibility. The effect of mixture and flow parameters on the population inversion for electron vibrational transitions in CO_2 was analyzed. © *2001 MAIK "Nauka/Interperiodica".*

INTRODUCTION

The development of new high-intensity radiation sources, such as high-power gas lasers, necessitates advanced techniques for simulating nonequilibrium processes in a high-temperature gas and in a plasma. Of special interest are supersonic jets of a high-temperature gas, where a variety of complex nonequilibrium phenomena may occur. Among these are the quenching of internal degrees of freedom and recombination of dissociated components. Gas-dynamic vibrational transition lasers and recombination electron vibrational transition lasers are well-known applications of these effects [1, 2]. While the kinetics of vibrational states has been studied thoroughly, recombination population of excited electron states calls for in-depth analysis.

Gas-dynamic recombination lasers (GDRLs) utilize thermal pumping. Like other visible-light lasers, their basic advantage is the simplicity of producing the inverted medium. The working medium in GDRLs is created as follows. In a supersonic jet of dissociated molecular gases, partial freezing of the vibrational and electron degrees of freedom of the particles takes place. Even for slight recombination and low radiation cooling of several levels, this effect disturbs the equilibrium distributions of the molecules and causes nonequilibrium emission from dissociated gas jets. Under certain conditions, inverse population for electron vibrational transitions may be observed.

The possibility of creating a GDRL was first studied in [3]. Later, early versions of these devices were implemented [4–7]. A theoretical model of a CO_2 GDRL was suggested in [8, 9]. However, reliable data for mechanisms and rates of kinetic processes that lead to inversion in lasing media containing molecular gases were lacking. Up to now, this has retarded the fabrication of visible-light GDRLs.

The most complete information on energy exchange in a jet of a recombining gas is gained from a solution to the basic kinetic equation (BKE) for the populations of all microscopic states in a given molecular system. The ladder approach to solving the BKE for systems of multiatomic molecules is known [10, 11], which was extended in [12, 13] and applied to describe energy exchange in recombining CO_2 jets [14]. In this work, the ladder approach is used to describe recombination emission from supersonic jets of high-enthalpy gases. We applied it to see whether population inversion for electron vibrational transitions in CO_2 is possible under supersonic flow conditions. Also, we tried to develop a model of kinetic and energy-exchange processes in a recombination CO_2 laser. Finally, our goal was to estimate the effect of the most crucial factors (mixture and flow parameters) on the population inversion for CO_2 electron vibrational transitions. The basis for our study was experimental data for the spectral distribution of nonequilibrium emission from supersonic jets of dissociated CO_2.

EXPERIMENT

Our experimental setup combines a shock tube 50 mm in diameter and a 45-mm-wide two-dimensional (planar) chamber (for details, see [15]). We studied shock-heated (T_0 = 3000–4500 K) jets of a 20% CO_2 + 80% Ar mixture under a slowing-down pressure P_0 varying from 0.4 to 3.5 MPa. The jets were expanded through a planar sonic nozzle of half-width $h_* = 1$ mm into a vacuum chamber kept at 10^3–10^4 Pa. Experimental conditions were such that the degree of CO_2 dissociation (30 to 50% before the nozzle inlet) was frozen in the supersonic jet, so that the concentration distribution for the mixture components was

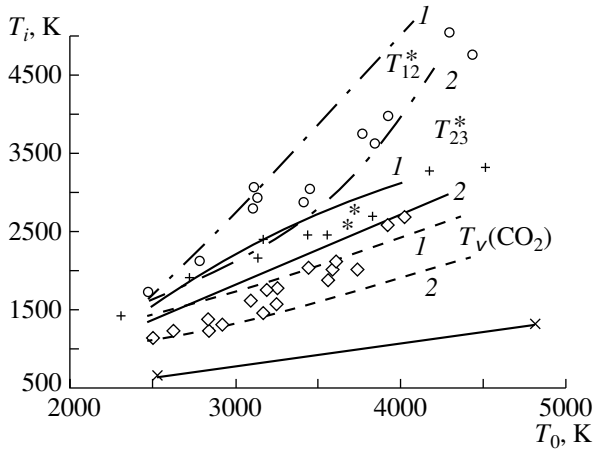

Fig. 1. Vibrational temperatures T_{12}, T_{23}, and T_V vs. slowing-down temperature T_0. T_{12} refers to levels with energies of 7.15 and 6.63 eV (○, experiment; dot-and-dash lines, calculation) and T_{23}, to levels with energies of 6.63 and 5.86 eV (+, experiment; continuous lines, calculation) of the state $CO_2(^1B_2)$; T_V, vibrational temperature of the CO_2 ground state (◇, experiment; dashed line, calculation); T_V(CO), vibrational temperature of the CO band (∗, experiment). ×, translational temperature of the flow.

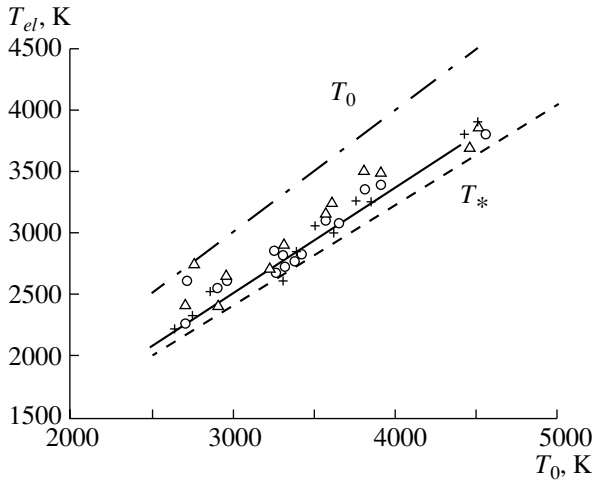

Fig. 2. Measured and calculated electron temperatures for various vibrational levels of the state $^1B_2$ at the flow axis ($x = 8h_*$) vs. slowing-down temperature T_0 (symbols, experiment; line, calculation). Dash-and-dot and dashed lines show T_0 and T_*.

totally defined by gas-dynamic parameters of the jet. The energy distribution in molecules of recombining CO_2 was determined by emission and absorption measurements in the ($^1B_2 \longrightarrow X^1\Sigma_g^+$) band at wavelengths $\lambda_1 = 285 \pm 7$ nm, $\lambda_2 = 353 \pm 3.5$ nm, and $\lambda_3 = 488 \pm 1.5$ nm; in the vibrational bands of CO_2 (2.7 and 4.3 μm); and in the CO band (4.7 μm).

Tentative estimations of the excitation temperatures T_{ij}^* for various vibrational transitions of the excited electron state $^1B_2$ were made under the assumption that the vibrational energy within a term is distributed smoothly. Then, we can make use of the formal relationship

$$I_i/I_j = I_{0i}/I_{0j}\exp((E_i - E_j)/kT_{ij}^*). \quad (1)$$

Here, I_i, I_j and I_{0i}, $I_{0j}$are the measured and equilibrium (at $T_{\text{ref}} = 1600$ K) emission intensities at wavelengths of λ_i and λ_j; E_i and E_j are the respective excitation energies found from special tests that were carried out under thermally equilibrium conditions ($E_1 = 7.15$ eV, $E_2 = 6.63$ eV, and $E_3 = 5.86$ eV).

Figure 1 compares the estimated temperatures of various vibrational transitions for the $^1B_2$ term with the measured vibrational temperature for the CO_2 ground state. It is remarkable that the vibrational temperatures for the excited electron states are mush higher than that for the ground state. Moreover, the relative populations of the most excited levels significantly grow with the flow temperature and dissociated particle concentration. This means that a highly nonuniform distribution of the populations of the highly excited states (HES), with $T_{12}^* > T_{23}^* > T_0$, exists in the flow.

Another approach to treating experimental data is to estimate the integral temperature of population (relative to the CO_2 molecules in the ground state) for the $^1B_2$ state. For this purpose, we employ another formal relationship:

$$I_i/I_{0i} = \exp\left(-\frac{E_i}{T_{\text{ei}}} - \frac{E_i}{T_{\text{ref}}}\right), \quad (2)$$

from which $T_{e,1}$, $T_{e,2}$, and $T_{e,3}$ were found (Fig. 2). The temperatures $T_{e,i}$ markedly exceed the vibrational temperatures of the ground state and are close to each other. In addition, a change in $T_{e,i}$ is linearly related to that in the thermodynamic flow temperatures and the values of $T_{e,i}$ lie between the slowing-down temperature T_0 and the critical flow temperature T_*.

For quantitative characterization of the data obtained and comprehensive description of nonequilibrium processes in supersonic flows of a recombining gas, we elaborated a kinetic model for relaxation and chemical processes in an expanding gas flow.

KINETIC MODEL OF RECOMBINATION IN A DISSOCIATED CO_2 JET

A supersonic flow involving dissociated carbon dioxide obeys two, gas-dynamic and kinetic, sets of equations. The former are the energy and momentum equations (in the Euler form) supplemented by the gas equation. For a steady-state isoentropic flow of a perfect reactive gas out of a cylindrical source, this set (in

the quasi-one-dimensional approximation) looks as follows:

$$\rho u S = \rho_* u_* s_*, \tag{3}$$

$$T\rho^{1-\gamma} = T_* \rho_*^{1-\gamma}, \tag{4}$$

$$\bar{u}^2 + 2H = \bar{u}_*^2 + 2H_*, \tag{5}$$

$$P = \rho R T. \tag{6}$$

Here, T is the translational temperature; T_*, ρ_*, s_*, and u_* are, respectively, critical temperature, critical density, critical cross-section area, and critical velocity of the flow; γ is the effective adiabatic exponent; and H is the gas mixture enthalpy with regard for the energy accumulated by internal degrees of freedom of the gas.

Boundary conditions are the following. (1) A gas mixture (working gas CO_2 and inert diluent Ar) is heated to slowing-down temperature T_0 and pressure P_0 in a shock tube; it is assumed that the residence time of the mixture in the tube is sufficient for the equilibrium dissociated state to set in. (2) It is also assumed that the chemical composition of the mixture in the subsonic flow remains frozen and also that the distribution of mixture components (CO_2, CO) over internal degrees of freedom is equilibrium and has the critical temperature T_* in the critical cross section.

In computation, the gas-dynamic equations are solved at each step of integration to obtain local macroscopic flow parameters T and P, which are input parameters for the BKE. The reverse effect of kinetics on gas dynamics is taken into account through the energy equation including the internal energy of the gas.

The equations of chemical kinetics comprehensively describe the HES population in CO_2 molecules of the jet in the ladder approximation [12] with consideration for the CO vibrational temperature. As in [12], the CO_2 spectrum is represented as a set of discrete levels that have a population A_i and some statistical weight. The energy of each level is $E_i = E_{el} + E_v$, where E_{el} is the energy of an electron term and E_v is the vibrational energy reckoned from the lower level of this electron term. Dissociation is considered as a stochastic motion of reacting molecules along the energy scale up to the dissociation threshold E_0 and above, where they spontaneously decompose. Only transitions between adjacent levels are considered. The energy gap between the levels (a step of the energy ladder), $\Delta E = E_i - E_{i-1}$, is defined as the mean portion of the energy transferred in collisions and is a parameter of the model. For such levels, the BKE can be written in the form

$$\frac{dA_i}{dt} = W_+ + W_- + W_{\text{diss}}(i) + W_{\text{bm}}(i) + W_{el}(i) + W_{\text{rec}}(i). \tag{7}$$

Here, $W_+ = k_a(i)MA_{i-1} + k_{\text{da}}(i+1)MA_{i+1}$ and $W_- = k_{\text{da}}(i)MA_i + k_a(i+1)MA_i$ are the respective operators of the rates of collisional activation and deactivation of the ith level (V–T relaxation), where k_a and k_{da} are the respective rate constants; M is the total particle concentration in the system; $W_{\text{diss}}(i) = k_{\text{diss}}(i)A_i$ is the rate of spontaneous decomposition (dissociation) of the given level with the corresponding constant k_{diss}; $W_{\text{bm}}(i)$ is the rate of bimolecular reactions with the participation of the ith level; $W_{el}(i)$ is the rate of transition to other excited terms of a molecule (V–E relaxation); $W_{\text{rec}}(i) = k_{\text{rec}}(i)BC$ is the rate of recombination population of the ith level with the corresponding constant k_{rec} (B and C are the concentrations of recombining particles).

The continuous population distribution function $f(E_i)$,

$$f(E_i) = \rho(E_i)\frac{\exp(-E_i/RT)}{Q}, \tag{8}$$

(Q is the vibrational statistical sum and $\rho(E_i)$ is the Whitten–Rabinovitch density function of energy states [16]), and the population A_i of a discrete level are related as

$$A_i = \frac{A_0\rho(E_i)\exp(-E_i/T)dE}{Q\Sigma_i f(E_i)dE} = \frac{A_0 f(E_i)dE}{\Sigma_i f(E_i)dE}, \tag{9}$$

where A_0 is the zero-level population.

The rates k_a and k_{da} of the direct and reverse processes are related to each other by the detailed-balancing equation through $f(E_i)$. The rate $k_{\text{diss}}(E_i)$ of spontaneous decomposition is given by [17]

$$k_{\text{diss}}(i) = \nu^*\left[\frac{(E_i - E_0 + aE_z)}{(E_i + aE_z)}\right]^{(s-1+r/2)}, \tag{10}$$

here, $E_i > E_0$; ν^* is the mean geometric frequency of molecular vibration; and s and r are the numbers of vibrational and rotational degrees of freedom of a molecule, respectively.

In this model, the thermal dissociation rate constant k_{diss} is the sum of the microscopic rate constants $k_{\text{diss}}(i)$ for spontaneous decomposition of individual levels:

$$k_{\text{diss}} = \frac{\Sigma_i k_{\text{diss}}(i)A_i}{A_0}. \tag{11}$$

The microscopic rate constants of recombination that fills above-threshold levels ($E_i > E_0$) and the corresponding microscopic decomposition rate constants are related to each other through the principle of detailed balancing:

$$k_{\text{rec}}(i) = \frac{1}{K^p(T)}\frac{f(i)}{\Sigma f(i)}k_{\text{diss}}(i), \tag{12}$$

where $K^p(T)$ is the dissociation rate constant.

Let us consider specific energy-exchange processes included in Eq. (7).

(1) Relaxation processes described by the operators W_+ and W_- cover vibrational relaxation within the states $X^1\Sigma$, $^1B_2$, and $^3B_2$:

$$CO_2(i) + M \rightleftharpoons CO_2(i+1) + M. \quad \text{(I)}$$

(2) Processes described by the operator W_{el} are *V–E* relaxation between electron states:

$$CO_2(X^1\Sigma, i) \rightleftharpoons CO_2(^1B_2, i), \quad \text{(II)}$$

$$CO_2(X^1\Sigma, i) \rightleftharpoons CO_2(^3B_2, i), \quad \text{(III)}$$

$$CO_2(^3B_2, i) \rightleftharpoons CO_2(^1B_2, i); \quad \text{(IV)}$$

collisional quenching $CO_2(^1B_2)$:

$$CO_2(^1B_2, i) + M \rightleftharpoons CO_2(X^1\Sigma) + M; \quad \text{(V)}$$

collisionless transitions between electron states:

$$CO_2(^1B_2, i) \rightleftharpoons CO_2(X^1\Sigma, j) + h\nu. \quad \text{(VI)}$$

(3) Processes described by the operators W_{diss} and W_{rec} are decomposition and recombination in CO_2 (two paths):

$$CO_2(X^1\Sigma, i) \rightleftharpoons CO + O(^1D),$$
$$CO_2(^1B_2, i) \rightleftharpoons CO + O(^1D) \quad \text{(VII)}$$

[the dissociation threshold $D(^1B_2) = 7.42$ eV];

$$CO_2(^3B_2) \rightleftharpoons CO + O(^3P) \quad \text{(VIII)}$$

[the dissociation threshold $D(^3B_2) = 5.45$ eV].

(4) Process described by the operator W_{bm} is the exchange reaction

$$CO_2(^1B_2, i) + O(^3P) \longleftrightarrow CO + O_2. \quad \text{(IX)}$$

We also considered the processes for which the rate constants are well known: collisional excitation and quenching of atomic oxygen (O),

$$O(^3P) + M \longleftrightarrow O(^1D) + M, \quad \text{(X)}$$

and dissociation of molecular oxygen (O_2),

$$O_2 + M \longleftrightarrow 2O(^3P) + M. \quad \text{(XI)}$$

Now let us discuss the rate constants at length. For reaction (I), the rate constant for the deactivation of the CO_2 first vibrational level is well known: $k_I(1) = 1.65 \times 10^{-15} T \exp(-29T^{-1/3})$ cm^3/s [18]; for higher vibrational levels, we used the Landau–Teller formula and expressed the constants $k_I(n)$ in the form $k_I(n) = ank_I(1)$, where a is a variable factor defined below. According to [19], $k_V = 5.0 \times 10^{-13}$ cm^3/s if M = Ar.

The values of the rate constants for *E–V* exchange [(II)–(IV)] were the following: $k_{II} = 10^6$ s^{-1} [20] for the allowed transition ($X^1\Sigma \longrightarrow {}^1B_2$) and $k_{IV} = 10^4$ s^{-1} (our estimate) for the forbidden transition ($X^1S \longrightarrow {}^3B_2$). The rate constant k_{IV} for the transition $^1B_2 \longrightarrow {}^3B_2$ will be discussed later. Note that the associated values for SO_2 [11] were close to those given above. Reaction VI is insignificant, because its rate constant is small: $k_{VI} = 10^2$–10^4 s^{-1} [19].

The rate constants $k_{\text{diss}}(i)$ of unimolecular decomposition [reactions (VII) and (VIII)] were taken in accordance with the above reasoning. It was also assumed that recombination activates the kth level with the energy $E_k = E_i + T_v(\text{CO})$, where $T_v(\text{CO})$ is the vibrational temperature of CO. Accordingly, the recombination rate constants $k_{\text{rec}}(k) = k_{\text{rec}}(E_i + T_i(\text{CO}))$ have the form

$$k_{\text{rec}}(k) = \frac{1}{K^p(T)} \frac{f(i)}{\Sigma f(i)} k_{\text{diss}}(i), \quad (13)$$

where $K^p(T)$ is the dissociation–recombination rate constant taken from [19] [cf. Eq. (12)]. In addition, from [20], we took the rate constants for reaction (IX):

$$k_{IX}(i) = 4.5 \times 10^{10} \exp\left(-\frac{(297.2 - \gamma E_i)}{RT}\right) \text{cm}^3/\text{s}, \quad (14)$$

$$k_{-IX}(i) = 8.4 \times 10^{11} \exp\left(-\frac{(264.4 - \gamma E_i)}{RT}\right) \text{cm}^3/\text{s} \quad (15)$$

(energies of activation in kJ/mol). Here, the contribution of vibrational excitation to overcoming the reaction barrier (with a variable efficiency factor $\gamma \approx 0.5$) is taken into account.

RESULTS

Earlier [12], our model was tested on results of shock-tube experiments. Note that macroscopic rate constants of dissociation (11) and recombination (12) thus computed agree with data in [21, 22].

From the solution to the BKE for the populations of electron excited and vibrational excited states in a steady-state supersonic recombining CO_2 jet, we gained additional information about their distribution functions (DFs), mechanisms behind population inversion between various electron states in CO_2, as well as about factors that have an effect on the amount of inversion.

Supersonic flow of partially dissociated CO_2 is attended by a sharp decrease in the collision frequency in the gas. Therefore, the energy of the excited vibrational and electron degrees of freedom of CO_2 becomes partially frozen. On relaxation freezing, the recombination of dissociation products, which leads to the HES occupation, and radiation cooling of individual levels are imposed. Because of this, the equilibrium particle distribution is disturbed and inverse population may arise, showing up in the form of nonequilibrium emission from the dissociated CO_2 jet.

One basic issue addressed in this work was the study of mechanisms underlying inverse population, that is,

the separation of primary elementary events that are responsible for the effect and its amount. A set of energy-exchange and chemical processes that must be included into consideration is rather wide; therefore, the variable parameters of the model were appropriately adjusted to check the model for adequacy to experimental data. The model was tested based on the large body of our data for the HES distribution in the optically active term $CO_2(^1B_2)$.

In Fig. 1, the calculated plots of the temperatures for the states of the optically active term $CO_2(^1B_2)$ against T_0 are compared with the experiment. One can see that the vibrational distribution within the term is mainly due to vibrational relaxation within the term $^1B_2$ and *V–E* exchange with the triplet $^3B_2$, for which recombination is the most effective [reaction (VIII)]. Since the rates of both processes are pressure-dependent, the $T_{ij}(T_0)$ curves are split into bands according to P_0. The calculations were performed for P_0 = 3 and 10 atm (the upper and lower boundaries of the bands, respectively). A rise in the pressure accelerates vibrational relaxation, smoothing out the vibrational DF within the term and decreasing the difference in the temperatures of the transitions.

The analysis of the vibrational distribution within the states $^1B_2$ and $^3B_2$ showed that the experimentally found relation $T_{12}^* > T_{23}^*$ for the temperatures of the transitions may be accounted for under the assumption of fast *V–E* relaxation $CO_2(^3B_2, 0, 0, v_3) \longrightarrow CO_2(^1B_2, v_1, v_2, v_3)$, which fills the vibrational excited states of the $CO_2(^1B_2)$ term. The rate constant for this reaction was estimated at

$$k_{IV} \approx 5 \times 10^8 \text{ s}^{-1}. \quad (16)$$

The calculation of the vibrational temperature T_v for the CO_2 ground state (at P_0 = 3 and 10 atm) allowed us to determine the variable parameters of the model: a ladder step ΔE was set equal to 2000 K = Θ_1 in accordance with [13], where Θ_1 is a vibrational quantum for the symmetric mode of a CO_2 molecule, and the parameter *a* involved in the rate constant for reaction (I) varied between 1.0 for T = 2000 K and 0.5 for T = 4000 K.

Figure 2 compares the measured electron temperature of the state $^1B_2$ with the results of the model. It was found that the temperature values in Fig. 2 are the result of competition between three processes: collisional deactivation, recombination, and spin conversion for the HES of the $^1B_2$ term. The temperature of the excited electron state $^1B_2$ and, hence, that of $^3B_2$, is governed largely by the rate of collisional quenching according to reaction (V) and by the rate of *V–E* relaxation, reactions (II) and (IV).

Thus, our model well describes the actual distribution of recombination emission from a vibrationally nonequilibrium jet of dissociated CO_2. Further, the model was applied to tackle the problem of population inversion for individual states in supersonic expanding flows.

We considered jets that initially contained 20 to 80% of CO_2 in Ar. The flow parameters were T_0 = 2600–4600 K and P_0 = 4–30 atm. Population inversion was shown to take place between the ground state and the state $^3B_2$ (for which, as was noted, recombination is the most effective) in a wide range of the flow parameters. The inversion effect was also observed between the lower vibrational excited levels of the term $^3B_2$ with energies of ≈4.5 eV and the vibrational levels of the ground state with energies ≈1.5 eV; that is, generation in the forbidden band ($^3B_2 \longrightarrow X^1\Sigma$) at λ = 400 nm is a possibility.

Figure 3 shows a surface depicting the transformation of the distributions for the lower excited ($^3B_2$) state of CO_2 flowing through a slotted sound nozzle of height 1 mm at T_0 = 2400 K and P_0 = 10 atm. For each time instant *t*, the distribution is shown as a function $F_p(E, t)$ normalized to the equilibrium (Boltzmann) DF $F_e(E, T_*)$ at a temperature T_*:

$$F_p(E, t) = \frac{F(E, t)}{F_e(E, T_*)}. \quad (17)$$

Thus, the normalized distribution demonstrates a depletion of the DF with the flow coordinate.

From Fig. 3, it is seen that, as the flow expands, there exists a highly nonuniform distribution within the electron excited term $CO_2(^3B_2)$. In the given coordinates, its slope defines the vibrational temperature for a selected energy level at each time instant. Also, in the immediate vicinity of the nozzle, the populations of several levels are above-critical because of recombination population of states that are near the decay threshold. As the flow expands further, the rate of recombination due to triple collisions drops in comparison with the rate of HES deactivation due to binary collisions. Therefore, the space distribution of the populations of the vibrational states in the $CO_2(^3B_2)$ term is dome-

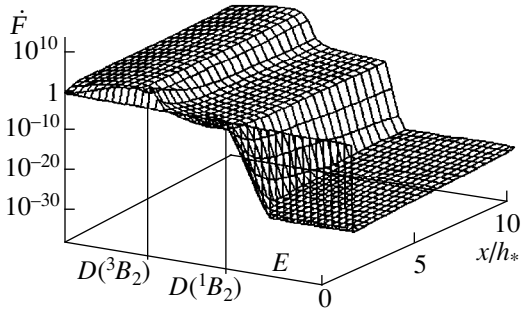

Fig. 3. Transformation of the vibrational distribution of the lower excitation for the $CO_2(^3B_2)$ state at T = 2400 K and P_0 = 10 atm.

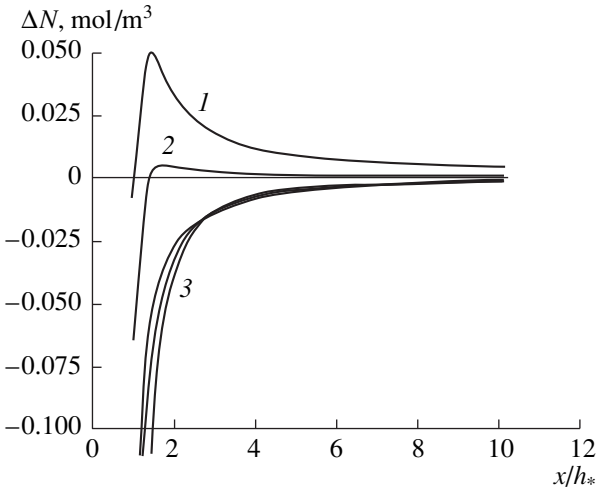

Fig. 4. Population inversion ΔN along the planar slotted nozzle for the initial 20% CO_2 + Ar mixture. P_0 = 10 atm; T_0 = (*1*) 4400, (*2*) 3800, and (*3*) 2700–3400 K.

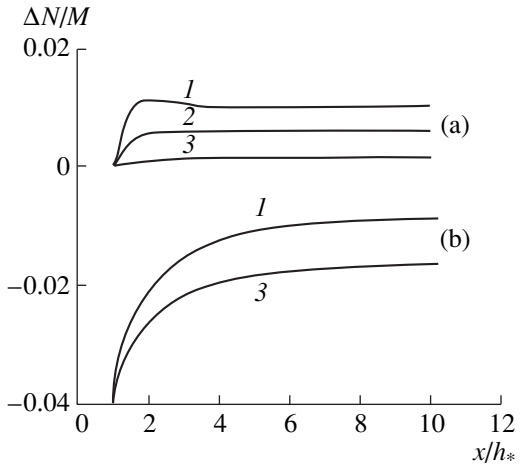

Fig. 5. Population inversion ΔN normalized to the total particle concentration M in the system along the nozzle coordinate: (a) 25% CO + 25% O + Ar and (b) 50% CO_2 + Ar for T_0 = 4400 K. P_0 = (*1*) 10, (*2*) 8, and (*3*) 5 atm.

shaped (Fig. 3). The position of the population peak was shown to depend on the flow parameters and especially on the slowing-down temperature T_0: the higher T_0, the nearer the peak to the nozzle.

Next, our computing technique was applied to analyze the effect of the flow and mixture parameters on the inversion between the states $^3B_2$ and $X^1\Sigma$.

For this transition, the gain $\alpha(0)$ at the center of a Doppler profile is given by [8]

$$\alpha(0) \sim [CO_2(^3B_2)]T^{-2}. \quad (18)$$

It follows that the gain increases when the population of the excited state grows or the translational temperature drops. The existence of the optimum T_0 values is explained by two opposing tendencies. On the one hand, as T_0 increases, the flow temperature rises. On the other hand, the amount of the $CO_2(^3B_2)$ excited states decreases with decreasing T_0.

Quantitative analysis of the gain for the transition $^3B_2 \longrightarrow X^1\Sigma$ is beyond the scope of this article. We will concentrate on the population inversion ΔN for these states. Note only that ΔN and $\alpha(0)$ vary in a similar way. Specifically, an increase in P_0 enhances the recombination rate, causing ΔN to grow. However, at low T_0, a rise in pressure does not lead to inversion because of a low degree of CO_2 dissociation. In Fig. 4, ΔN is plotted against the distance to the slotted nozzle for various T_0 and P_0 = 10 atm in the case of the 20% CO_2 + Ar mixture. At $T_0 < 3400$ K, the effect is absent at any pressure.

From the computations, it directly follows the recombination character of inversion for this transition. In Fig. 5, the inversion ΔN normalized to the total particle concentration in the system is plotted against coordinate along the nozzle axis for various pressures and mixture compositions at T_0 = 4400 K. No inversion is observed (Fig. 5b), because recombination is impossible. This means that relaxation freezing in molecules of an expanding CO_2 jet cannot result in inversion at electron transitions.

The computations also show that there is an optimum composition of the CO + O + CO_2 + Ar mixture at the nozzle inlet that increases the inversion for this transition. A CO + O + Ar mixture would be the most appropriate for an inversion increase. High CO_2 concentrations raise the translational temperature because of an increase in the specific heat of the mixture and the marked effect of exothermic reactions. It is, however, difficult to get rid of CO_2 in practice. The inversion depends on both the recombination rate and the rate of vibrational relaxation. If the latter rate exceeds the rates of other processes, both the populations of all excited levels and the inversion ΔN decrease. Therefore, if the relative fraction of CO and O increases at a given pressure and, accordingly, the rate of vibrational relaxation in CO_2 exceeds that in Ar, ΔN first grows because of an increase in the recombination rate and then drops due to vibrational cooling of the mixture. The optimum composition of the mixture is (20–25)% CO + (20–25)% O + Ar.

It was found by the calculations that recombination, which is responsible for inversion in the UV range, takes places near the nozzle outlet, where the flow is still dense. Therefore, the degree of recombination and, hence, the inversion may readily be controlled by varying the nozzle shape. If the nozzle has a short expanding region where the translational temperature sufficiently drops and then the cross section of the nozzle (and, hence, the density of the recombining flow) remains constant, inversion may occur within a sufficiently large portion of the flow. Figure 6 demonstrates calculated $\Delta N(x/h_*)$ curves for the flow leaving the

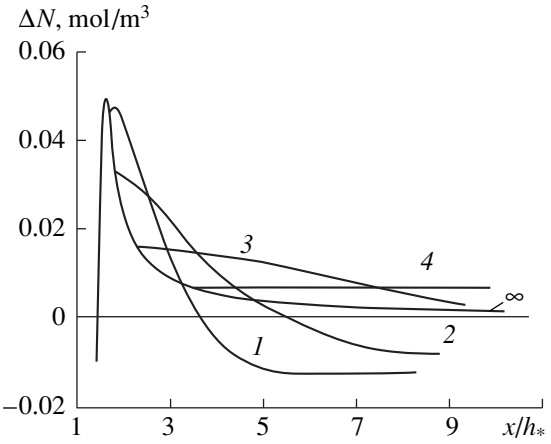

Fig. 6. Calculated ΔN for the flow from the 1-mm-high sonic nozzle at $T_0 = 4400$ K and $P_0 = 10$ atm. The divergent region of the nozzle has the length $L = (1–4)h_*$. $L = \infty$ refers to a flow freely expanding from the planar slotted nozzle. Numbers denote the values of L.

1-mm-high nozzle at $T_0 = 4400$ K and $P_0 = 10$ atm. The length L of the expanding region was taken equal to $(1–4)h_*$ (the case $L = \infty$ for the planar nozzle is also shown for comparison).

Finally, we studied the effect of an inert diluent on the inversion for the $^3B_2 \longrightarrow X^1\Sigma$. It was reported [19] that the rate of collisional quenching of the $^1B_2$ state [reaction (V)] greatly differs for various inert gases [e.g., $k_V(M = \mathrm{He}) \approx 5 \times 10^{-13}$ cm^3/s and $k_V(M = O_2) \approx 3 \times 10^{-10}$ cm^3/s] and the population of this state is strongly related to that of the $^3B_2$ state. Therefore, if a gas that is inefficient in quenching $CO_2(^1B_2)$ is used as a diluent, the inversion is high.

Thus, our model was applied for the description of nonequilibrium DFs of multiatomic molecules in supersonic recombining jets. It is promising in searching for new types of recombination lasers. The optimum conditions for UV generation owing to the $^3B_2 \longrightarrow X^1\Sigma$ transition in a recombining CO_2 jet (for any pressure) are $T_0 \approx 4000$ K and CO : O : Ar = 1 : 1 : 2.

CONCLUSION

The solution (in the ladder approximation) of the BKE for the distribution of the excited state populations in a supersonic recombining jet of CO_2 allowed us to elaborate a detailed model of kinetic processes responsible for the electron and vibrational excited states of CO_2 molecules in a supersonic flow. Inverse population at the transition $^3B_2 \longrightarrow X^1\Sigma$ between $^3B_2$ levels with energies of ≈4.5 eV and those of the ground state with energies ≈1.5 eV is shown to be a possibility. The effect of the mixture and flow parameters on the population inversion at electron vibrational transitions in CO_2 was studied.

ACKNOWLEDGMENTS

This work was supported by the Russian Foundation for Basic Research.

REFERENCES

1. B. F. Gordiets, A. I. Osipov, and L. A. Shelepin, *Kinetic Processes in Gases and Molecular Lasers* (Nauka, Moscow, 1980).
2. S. A. Losev, *Gas-Dynamic Lasers* (Nauka, Moscow, 1977).
3. J. R. Hurle and A. Hertzberg, Phys. Fluids **8** (9), 1601 (1965).
4. A. S. Bashkin and A. N. Oraevskiĭ, Kvantovaya Élektron. (Moscow), No. 5, 1 (1973).
5. L. A. Kernazhitskiĭ, V. E. Nosenko, V. V. Naumov, *et al.*, Khim. Fiz. **4** (8), 1120 (1985).
6. A. S. Biryukov and L. A. Shelepin, Zh. Éksp. Teor. Fiz. **67** (6), 2064 (1974) [Sov. Phys. JETP **40**, 1025 (1974)].
7. A. Yu. Volkov, A. I. Demin, E. M. Kudryavtsev, and N. N. Sobolev, Zh. Éksp. Teor. Fiz. **70** (2), 503 (1976) [Sov. Phys. JETP **43**, 259 (1976)].
8. A. S. Biryukov, E. M. Kudryavtsev, A. N. Logunov, and V. A. Shcheglov, Preprint No. 40, FIAN (Lebedev Institute of Physics, Academy of Sciences of USSR, Moscow, 1989).
9. I. A. Izmaĭlov, V. A. Kochelap, and Yu. A. Kukibnyĭ, Ukr. Fiz. Zh. **21**, 508 (1976).
10. J. Troe, *Fast Reactions in Energetic Systems*, Ed. by C. Capellos and R. F. Walker (Reidel, Dordrecht, 1981), pp. 125–139.
11. L. V. Gaĭduchenya, I. S. Zaslonko, Yu. K. Mukoseev, and A. M. Tereza, Khim. Fiz. **9** (4), 443 (1990).
12. I. S. Zaslonko, A. V. Eremin, and V. V. Shumova, Kinet. Katal. **37** (4), 485 (1996).
13. A. V. Eremin, V. S. Ziborov, and V. V. Shumova, Khim. Fiz. **17** (9), 5 (1997).
14. A. V. Eremin, V. V. Shumova, and V. S. Ziborov, ISSW-22, 1999, Paper No. 3973.
15. A. V. Eremin and V. S. Ziborov, Prikl. Mekh. Tekh. Fiz., No. 4, 31 (1990).
16. G. Z. Whitten and R. S. Rabinovitch, J. Chem. Phys. **38**, 2466 (1963).
17. E. E. Nikitin, *Theory of Elementary Atomic and Molecular Processes in Gases* (Khimiya, Moscow, 1970; Clarendon, Oxford, 1974).
18. A. S. Biryukov, Yu. A. Kulagin, and L. A. Shelepin, Zh. Tekh. Fiz. **47**, 331 (1977) [Sov. Phys. Tech. Phys. **22**, 194 (1977)].
19. A. M. Pravilov, *Photoprocesses in Molecular Gases* (Énergoatomizdat, Moscow, 1992).
20. L. B. Ibragimova, Khim. Fiz. **6** (9), 785 (1990).
21. H. A. Olschewsky, J. Troe, and H. G. Wagner, in *Proceedings of the 11th International Symposium of Combustion, The Combustion Inst., Pittsburgh, 1966*, p. 155.
22. J. Troe, in *Proceedings of the 10th International Symposium on Shock Tubes and Shock Waves, Kyoto, 1975*, p. 29.

Translated by V. Isaakyan

Technical Physics, Vol. 46, No. 4, 2001, pp. 438–441. Translated from Zhurnal Tekhnicheskoĭ Fiziki, Vol. 71, No. 4, 2001, pp. 76–79.

Analysis of the Active Region of Overheating Temperature in Green LEDs Based on Group III Nitrides

G. A. Sukach*, P. S. Smertenko*, P. F. Oleksenko*, and Suji Nakamura**

** Institute of Semiconductor Physics, NASU, Kiev, 03028 Ukraine*

*** Nichia Chemical Industries Ltd., Tokoshima, Japan*

e-mail: sukach@isp.kiev.ua

Received June 19, 2000

Abstract—For the first time, the overheating temperature ΔT_{p-n} of the active region in green light-emitting diodes based on Group III nitrides has been determined as a function of the forward current amplitude I. It has been shown that in contrast to light-emitting diodes, in which the current–voltage characteristics are adequately described by known theories of rectification in p–n junctions and $\Delta T_{p-n} \propto I$, in the structures under study, the dependence $\Delta T_{p-n}(I)$ in the current range of 2×10^{-3}–3×10^{-2} A is quadratic in current. At higher currents, the variation of ΔT_{p-n} with I in the green light-emitting diodes based on Group III nitrides becomes linear, which is the same as in the light-emitting diodes based on known infrared and red III–V structures. © *2001 MAIK "Nauka/Interperiodica".*

INTRODUCTION

Recent advances in the technology of gas epitaxy from metalloorganic compounds (MOCVD) for commercial production of heterostructures based on Group III nitrides made possible the fabrication of highly efficient light-emitting diodes (LED) covering practically the entire range of color emission (including white light). This progress, mainly due to the physical and technological research made at Nichia Chemical Industries [1], opens new prospects for the development of optical devices for recording and displaying information and for the fabrication of light-signaling equipment in which the use of LEDs drastically changed the design technology [2, 3].

At the same time, more stringent requirements have been set to the stability, reliability, and degradation characteristics of the LEDs as the basic elements of this equipment. Therefore, studies have recently been carried out on the injection and thermal degradation mechanisms of LEDs in Group III nitrides encompassing accelerated pulsed [4, 5] and long-term dc [6] tests in a wide range of ambient temperatures T. However, the overheating temperature ΔT_{p-n} of the active LED region under operating conditions, which is a key parameter providing an integrated estimation of these characteristics, and the mechanisms involved were not examined, although it is known that ΔT_{p-n} affects not only the internal generation–recombination processes in a LED but also the stability, reliability, and service life of the device as a whole [7]. For example, a 10 K rise of the p–n-junction temperature reduces its service life by a factor of two [8].

In view of the above, examination of the thermal processes and the mechanisms determining the temperature ΔT_{p-n} and experimental determination of this parameter in LEDs heated by a passing current are of theoretical and practical importance.

EXPERIMENTAL TECHNIQUE AND RESULTS

The green LEDs under study were InGaN/AlGaN/GaN heterostructures with the active layer consisting of the $In_xGa_{1-x}N$ isolated quantum well (x = 0.43, bandgap $E_g \approx 2.5$ eV) with a thickness of 2–4 nm. The epitaxial structures were grown by MOCVD in laboratories of the Nichia Chemical Industries [1, 5].

The overheating temperature of the LED active region was determined by comparing dc and pulsed current–voltage characteristics (IVC) in the current range $I = 10^{-5}$–10^{-1} A, which is approximately the nominal operating regime. To exclude heating of the structures by pulsed current, the on–off time ratio Q and the pulse duration t_i were kept in the ranges $Q > 100$ and $t_i < 10^{-6}$ s, respectively [7].

In Fig. 1, IVCs measured under dc and pulsed conditions are shown. It is seen that, under pulsed conditions, IVCs shift to higher voltages U. With increasing I, the measured voltage difference ΔU_{p-n} rises in both the dc, U_s, and the pulsed, U_p, modes of U. This is evidence of the nonlinearity of the function $\Delta U_{p-n}(I)$ caused, first of all, by the injection-thermal nonlinearity of the band gap E_g and by other factors, the analysis of which is itself interesting. In order to determine the

1063-7842/01/4604-0438$21.00

temperature to which the LED active region $\Delta T_{p-n} = T_{p-n} - T_E$ is heated by the passing current above the ambient temperature T_E, where T_{p-n} is the p–n-junction temperature, the device was precalibrated by determining a temperature-dependent parameter under a stepwise change of T_E. Then, the voltage temperature coefficient γ of the p–n junction was calculated using the expression

$$\gamma = \Delta U_{p-n} \Delta T_E^{-1}. \quad (1)$$

This coefficient was derived from IVCs measured for different T_E values at fixed I in the given ranges of temperature (T = 300–400 K) and current ($I = 10^{-4}$–10^{-1} A). The obtained $\gamma(I)$ plots in Fig. 2 are monotonically increasing functions. It is easily seen that γ increases only slightly in the range $I < 10^{-3}$ A and more significantly in the range $I = 10^{-2}$–10^{-1} A, so that its variation over the range $I > 5 \times 10^{-3}$ A is close to linear.

Using the obtained values of γ and the measured values of the voltage drop across the p–n junction ΔU_{p-n} in the dc and pulsed modes, the overheating temperature of the LED active region was determined:

$$\Delta T_{p-n} = \Delta U_{p-n} \gamma^{-1}. \quad (2)$$

The results are shown in Fig. 3. It is seen that up to $I \sim 2 \times 10^{-3}$ A, within the experimental error, ΔT_{p-n} is equal to zero. With a further increase in I, first superlinear and then approximately linear growth of $\Delta T_{p-n} = f(I)$ is observed.

DISCUSSION

Analysis of the $\Delta T_{p-n}(I)$ dependence will be made using data from [6, 9] in which variations of electrophysical parameters of similar LEDs in the course of prolonged operation were studied. In [10], the ionized impurity distribution profiles in InGaN/AlGaN/GaN structures in fairly wide compensated regions of GaAlN were observed (thickness ~10 nm each), extending to the left and right of the active quantum well layer (Fig. 4a). An estimate in [9] of the electron free path λ = 20–30 nm indicates that for electrons reaching the compensated regions the probability of scattering on the host lattice atoms, i.e., of transferring their energy to phonons without having to overcome the region of varying potential (the total thickness of the two compensated regions and of the quantum well), is greater. This is further evidence that all thermal processes take place in this thin (~30 nm) region of the LED. Consequently, the overheating of the active LED region is mainly due to processes in the electronic subsystem where the kinetic energy of electrons is increased owing to the electric energy supplied to the system. This energy is then transferred to the lattice as the injected (usually hot) electrons interact first with long-wavelength and then with all acoustic phonons [11, 12].

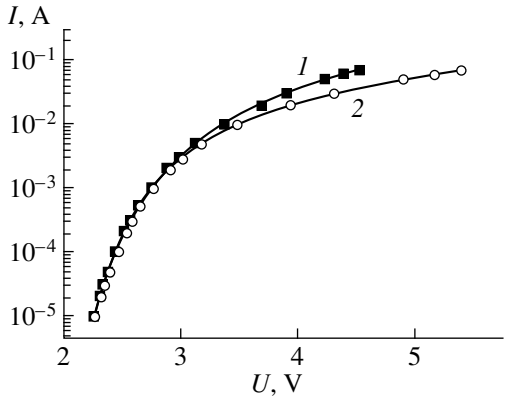

Fig. 1. Forward dc (*1*) and pulsed (*2*) current–voltage characteristics of green LEDs based on Group III nitrides.

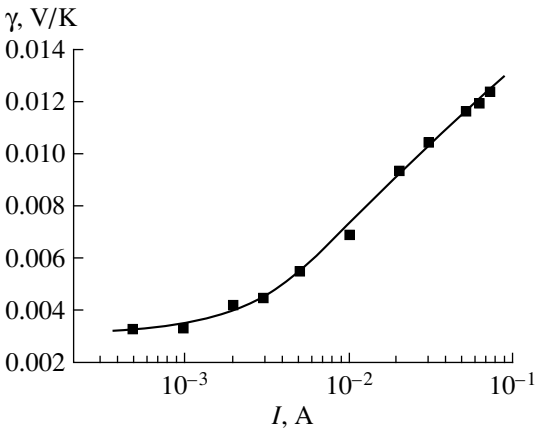

Fig. 2. Dependence of the voltage temperature coefficient of green LEDs on the direct current amplitude.

At $U = 0$, the width of the space-charge layer is comparable to the sum of the thicknesses of the two compensated regions and the quantum well width (Fig. 4b). Also, in the current range $I = 1 \times 10^{-5}$–2×10^{-3} A, the temperature ΔT_{p-n} within the experimental error is close to zero, because the power supplied to the LED is insignificant.

As the voltage applied to the structure becomes close to the built-in potential $\varphi_k \cong E_g/e$, the relative contribution of the potential drop over the compensated layer (in p and n regions) compared with the voltage drop over the quantum well diminishes, so that at $U = \varphi_k \cong E_g/e$ all the voltage applied to the structure will drop across the quantum well (Fig. 4c). In this situation, ΔT_{p-n} tends to increase with I and can be determined experimentally (Fig. 3). In this process, U changes from 2.5 to 3.2 V (in this range, taking into account the voltage drop across two compensated regions, $U \cong E_g/e$).

In the current range $I = 2 \times 10^{-3}$–2×10^{-2} A, where the p–n junction differential resistance, $R = dU/dI$, is essentially constant, the power P supplied to the LED

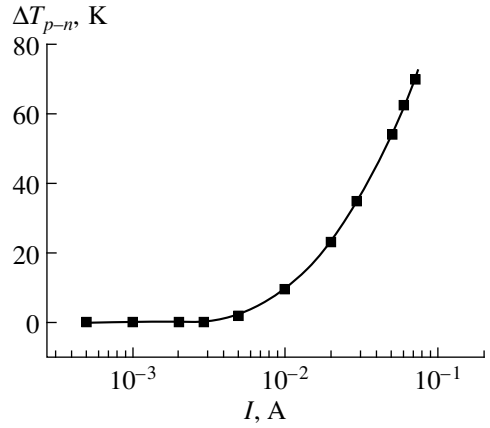

Fig. 3. Dependence of the overheating temperature of the active region (InGaN) in green LEDs on the direct current amplitude.

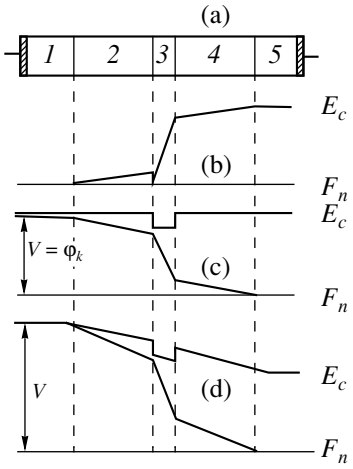

Fig. 4. Schematic of the layer structure of green LED (a) and the energy diagrams (b–d) of *n*-GaAlN/*i*-GaInN/*p*-GaAlN heterostructure with an active region in the form of single quantum well. (b) $U = 0$; (c) $U = \varphi_k$; (d) $U > \varphi_k$; *1*—*n*-GaAlN; *2*, *4*—*i*-GaAlN (compensated regions); *3*—*i*-GaInN (active layer); *5*—*p*-GaAlN.

increases as the square of current $P = I^2R$. In this case, the growth of $\Delta T_{p-n} \sim P$ with I is quadratic. With a further increase in current, the resistance R smoothly decreases, causing gradual straightening of the nonlinear $\Delta T_{p-n} = f(I)$ dependence. This is related to the large nonideality factor of IVCs ($\beta > 6$) in LEDs based on wide bandgap semiconductors, particularly Group III nitrides [9, 13, 14]. This IVC, which does not lend itself to description by known theories, is unusual also in that it is not rectified under reverse bias [13]. Probably, incomplete knowledge of the compensated region, a large impurity ionization energy, short charge carrier lifetimes, and low mobilities preclude application of the existing theories of *p*–*n* junctions to wide bandgap semiconductor heterostructures. Low mobilities drastically reduce the diffusion length L_D, invalidating the condition $L_D > L_e$ (L_e being the Debye screening length), which is the cornerstone of practically all known rectification theories. Therefore, the dependence $\Delta T_{p-n}(I)$ in the LEDs under study substantially differs from similar dependences for red LEDs based on GaAs/GaAlAs structures [15] and infrared LEDs based on GaInAsSb [11], which have IVCs with extensive exponential portions related to diffusion or recombination components of the current through the *p*–*n* junction. At the same time, a qualitative similarity is observed of ΔT_{p-n} curves of the LEDs based on Group III nitrides of this work and blue LEDs [13]. Quantitatively, the heating of green LEDs at maximum currents is lower by a factor of approximately two, which is possibly due to lower electric fields in them.

At $U > E_g/e$, the entire voltage applied to the structure is split into three approximately equal portions between the two compensated regions and the quantum well, because the *n*- and *p*-emitter regions are heavily doped. A third of the applied voltage drops across the quantum well, although its thickness is only a fraction of that of any of the component-compensated regions. The reason for this is that the potential barrier at the quantum well arising from a jump in potential (band discontinuity) at the GaAlN/GaInN interface (Fig. 4d) is not initially reduced. This causes a nearly linear rise of $\Delta T_{p-n} = f(I)$, which is due to R decreasing as I^{-m} with $m \leq 1$.

An essential feature of this portion of the dependence ΔT_{p-n} is the constancy of the voltage drop across the quantum well itself (at $U > E_g/e$). This fact contributes to maintaining $\Delta T_{p-n} = f(I)$ essentially linearly up to the thermal breakdown of the device.

CONCLUSION

In this study, the dependence of the overheating temperature of the active region in green LEDs based on Group III nitrides on dc forward current amplitude has been revealed and described for the first time. It has been shown that, in contrast to those LEDs whose IVCs can be described by the known theories of rectification in *p*–*n* junctions, in the structures studied the dependence $\Delta T_{p-n}(I)$ in the current range 2×10^{-3}–2×10^{-2} A is quadratic in current and gradually changes to linear as in other LEDs with cubic lattices.

ACKNOWLEDGMENTS

The authors are very grateful to A.Yu. Bogoslovskaya for help with experiments.

REFERENCES

1. S. Nakamura, T. Mukai, and M. Senoh, J. Appl. Phys. **76**, 8189 (1994).
2. A. É. Yunovich, Svetotekhnika, Nos. 5–6, 2 (1996).
3. F. A. Ponce and D. P. Bour, Nature **386**, 351 (1997).

4. M. Osinski, P. Perlin, P. G. Eliseev, *et al.*, Mater. Res. Soc. Symp. Proc. **449**, 179 (1997).
5. S. Nakamura, M. Senoh, M. Iwasa, *et al.*, Jpn. J. Appl. Phys., Part 2 **34** (10B), L1332 (1995).
6. A. N. Kovalev, F. I. Manyakhin, V. E. Kudryashov, *et al.*, Fiz. Tekh. Poluprovodn. (St. Petersburg) **33** (2), 224 (1999) [Semiconductors **33**, 192 (1999)].
7. G. A. Sukach, Optoélektron. Poluprovodn. Tekh. **26**, 30.
8. B. Siegel, Electronics **51** (14), 121 (1978).
9. A. N. Kovalev, F. I. Manyakhin, V. E. Kudryashov, *et al.*, Mater. Élektron. Tekh., No. 3, 60 (1998).
10. F. I. Manyakhin, Izmer. Tekh., No. 11, 49 (1996).
11. N. M. Kolchanova, A. A. Popov, G. A. Sukach, and A. B. Bogoslovskaya, Fiz. Tekh. Poluprovodn. (St. Petersburg) **28** (12), 2065 (1994) [Semiconductors **28**, 1137 (1994)].
12. V. S. Vavilov, Usp. Fiz. Nauk **167** (4), 407 (1997) [Phys. Usp. **40**, 387 (1997)].
13. S. V. Svechnikov, P. F. Oleksenko, G. A. Sukach, *et al.*, Ukr. Fiz. Zh. **43** (10), 1290 (1998).
14. V. E. Kudryashov, K. L. Zolin, A. N. Turkin, *et al.*, Fiz. Tekh. Poluprovodn. (St. Petersburg) **31**, 1304 (1997) [Semiconductors **31**, 1123 (1997)].
15. S. V. Svechnikov, G. A. Sukach, N. I. Sypko, and V. V. Nikolaenko, Zh. Tekh. Fiz. **55** (11), 2265 (1985) [Sov. Phys. Tech. Phys. **30**, 1343 (1985)].

Translated by B. Kalinin

Technical Physics, Vol. 46, No. 4, 2001, pp. 442–449. Translated from Zhurnal Tekhnicheskoĭ Fiziki, Vol. 71, No. 4, 2001, pp. 80–88.

OPTICS, QUANTUM ELECTRONICS

Interaction between Multiple Spatial Solitons in the Diffraction Catastrophe Region upon Focusing a High-Power Laser Beam in a Nonlinear Medium

V. Yu. Osipov

Ioffe Physicotechnical Institute, Russian Academy of Sciences,
Politekhnicheskaya ul. 26, St. Petersburg, 194021 Russia
e-mail: osip@vul.ioffe.rssi.ru

Received June 26, 2000

Abstract—When a high-power laser beam is focused in a nonlinear Kerr medium, beam self-diffraction by induced inhomogeneities of the refractive index is observed. A method for calculating the field amplitude and phase in the focal region with regard for self-diffraction by self-induced inhomogeneities is developed. Computer analysis of saturable Kerr media showed that the optical-field region with the least cross section of the focal pattern is followed by that of chaotically radiating "splashes" and long filaments. The latter radiate outward from the region of the caustic waist over long distances. They represent bright spatial solitons, which channel a significant portion of the primary beam energy. No less than 8–12 clear-cut solitons traveling in the positive z direction and moving apart in the transverse (x, y) plane are observed in the cross section. The field amplitude oscillates along each of the solitons. Various parameters of the saturable Kerr medium are taken into account. *© 2001 MAIK "Nauka/Interperiodica".*

INTRODUCTION

Optical spatial solitons propagating in nonlinear media, including Kerr media with saturable nonlinearity, have extensively been studied in the past eight years [1–8]. By a spatial soliton, we usually mean a steady-state self-channeled light beam in which diffraction divergence is compensated for by the effect of self-focusing in a medium where a nonlinear correction to the refractive index saturates. In studies of such objects, emphasis is usually on the properties of the solitons [9] and on interaction between solitons that cross [2, 10–13] or propagate cocurrently [14].

At the same time, of great interest remains the fine structure of electromagnetic field in the focusing region of laser beams with various wave fronts. A vast majority of works in this area have addressed focusing of radiation in linear media [15–22]. Caustic structures that appear in the focal region have thoroughly been studied over the past 35 years for various types of aberration in the converging beam [23, 24]. Most of these studies have calculated the caustics in a scalar approximation; however, a number of recent works have considered the vector fields [20–22]. Note that there are virtually no published data for caustic structures forming in nonlinear media when sharply focused high-power radiation experiences diffraction by induced inhomogeneities of the refractive index in the caustic region. A diffraction catastrophe in the form of an intricate astroid was observed in a nonlinear medium upon the evolution of an elliptic Gaussian beam with a 2 : 1 side ratio and a tapered field distribution over the aperture [25]. However, in this case, the field in the focal region arises directly from the effect of self-focusing rather than from "sharp" focusing, where a converging prefocused beam enters the medium. The filamentary field configuration due to sharp focusing by a conical lens, an axicon, has been calculated in [26]. For beams focused in nonlinear media by other means and having other types of aberration, information is lacking. Therefore, the purpose of this work was to study the caustic field forming in a nonlinear Kerr medium when a converging laser beam is subjected to a complex aberration.

Focusing of a high-power laser beam in a nonlinear medium is accompanied by wave front distortions and self-diffraction of the radiation by Kerr inhomogeneities of the refractive index. These inhomogeneities are determined by the three-dimensional speckle pattern of the caustic field. Wave propagation through a caustic region in a nonlinear medium was first theoretically studied in [27], where a nonlinear correction Δn to the refractive index was unsaturable. In this work, we show that the saturation of Δn leads to a qualitatively new result: multiple spatial solitons appear near the diffraction caustic (or catastrophe).

NUMERICAL TECHNIQUE AND BASIC METHODS OF COMPUTER-AIDED SIMULATION

A method for calculating the wave amplitude and phase in the focal region with regard for self-diffraction by self-induced inhomogeneous is described in [27]. In

computations, we transferred the field from layer to layer using the Fresnel–Kirchhoff integral. The contributions from pure diffraction and from the self-induced inhomogeneities within a small space region Δz between two adjacent layers were calculated separately. This technique, known as the beam propagation method (BPM), is widely used in analysis of wave propagation in inhomogeneous and nonlinear media [28, 29]. However, there exist various modifications of the BPM, as well as other finite-difference methods, for simulating wave propagation in nonlinear media [30–32].

Below, we consider the BPM modification applied. A nonlinear term $\Delta n(x, y, z)$ added to the refractive index $n_0(x, y, z)$ of the medium to allow for the effect of a high field $E(x, y, z_i)$ describes an effective phase screen induced on a Δz-thick thin layer. The complex transmission function of this screen is

$$\exp(i2\pi(n_0(x, y, z_i) - 1 + \Delta n(x, y, z_i))\Delta z/\lambda),$$

where λ is the wavelength. Initially, the medium is assumed to be homogeneous and nonlinear; then, $n_0(x, y, z) = n_0 = \text{const}$. Let the phase screen be placed in the plane $z = z_i$. Then, the complex transmission function of the screen modulates the amplitude and phase distribution of the wave $E(x, y, z_i) = A(x, y, z_i)\exp(i\varphi(x, y, z_i))$ in this plane. As a result, the complex amplitude of the field in the plane $z = z_i + 0$ can be written as

$$E(x, y, z_i + 0) = A(x, y, z_i)\exp(i\varphi(x, y, z_i)) \times \exp(i2\pi(n_0 - 1 + \Delta n(x, y, z_i))\Delta z/\lambda).$$

In the plane $z = z_i + \Delta z$, the field $E(x, y, z_i + 0)$ is then calculated in terms of the Fresnel–Kirchhoff integral:

$$E(x, y, z_i + \Delta z) = \iint_\Omega g(u_x, u_y)\exp(-i\Delta z\sqrt{k^2 - u_x^2 - u_y^2}) \times \exp(-i(u_x x + u_y y))du_x du_y, \quad (1a)$$

where

$$g(u_x, u_y) = \iint_\Sigma E(x, y, z_i + 0) \times \exp(i(u_x x - u_y y))dx dy. \quad (1b)$$

Here, $k = 2\pi/\lambda$ is the wave number; u_x and u_y are the circular spatial frequencies in the x and y directions, respectively; and $g(u_x, u_y)$ is the Fourier spectrum of the complex amplitude $E(x, y, z_i + 0)$. The spatial frequencies u_x and u_y are related to the direction cosines of the partial wave number $\mathbf{k} = k(\cos\alpha, \cos\beta, \cos\gamma)$: $u_x = k\cos\alpha$ and $u_y = k\cos\beta$. The Fresnel–Kirchhoff integral [(1a) and (1b)] here is written in the so-called Rayleigh representation [16, 33], which takes into account the effect of inhomogeneous waves that decay in the z direction and propagate from the layer $z = z_i$ to the layer $z = z_i + \Delta z$ at spatial frequencies $u_x^2 + u_y^2 > k^2$. In the calculations, we, however, took into account the secondary radiation scattered only within an angular range of $\pm 35.5°$ relative to the z axis. Larger angle forward scattering and backscattering were neglected. To simplify the analysis, we used a scalar approximation without considering vector effects, such as rotation of the polarization plane in the radiation scattered by inhomogeneities of the refractive index.

The process of radiation transfer from a layer i to a layer $i + 1$ was iterated in the caustic region over a length of about 9 mm. We set $\Delta z = 6.25$ μm. The saturable Kerr medium was simulated by the following refractive index vs. field amplitude relationship:

$$n = n_0 + \Delta n = n_0 + \frac{n_2|E|^2}{1 + (|E|^2/|E_s|^2)}. \quad (2)$$

Here, $|E|$ is the magnitude of the complex field amplitude at a point x, y, z; $|E_s|$ is the saturating field magnitude; n_2 is a nonlinearity parameter of the medium; and n_0 is the refractive index of the unperturbed medium. Here, $|E|^2$ has the meaning of radiation intensity. Formula (2) for the refractive index is valid not only for purely Kerr fluids but also for gases with local regions of a partially ionized plasma and laser-induced sparks. In particular, formula (2) was used in [26] to characterize a laser-induced spark channel produced in air as a result of focusing with an axicon. Therefore, by a nonlinear Kerr medium, we henceforth will also mean a gas under conditions of laser-induced ionization and breakdown.

The calculations were performed for various parameters of the nonlinear saturable medium. For the sake of simplicity, n_0 was taken equal to 1. The parameter $n_2|E_s|^2$ was 0.003 or 0.006. The high-power radiation entered the nonlinear medium at $z = z_0 = 135.5$ mm, which is the distance between the exit aperture of the focusing system and the medium. It was assumed that the nonlinear medium occupies the half-space $z > z_0$ and the region $0 < z < z_0$ is the free space.

The complex field amplitude distribution in the plane (x_2, y_2) at $z = 0$ over the exit aperture of the focusing element is $E(x_2, y_2, 0) = A_0(x_2, y_2)\exp(i\varphi(x_2, y_2, 0))$. Here, $A_0(x_2, y_2)$ is the distribution of the scalar field amplitude over the aperture at $z = 0$, and $\varphi(x_2, y_2, 0)$ is the phase function of the converging spherical wave distorted by aberrations.

Then, the complex amplitude distribution in the entrance plane of the medium, $z = z_0$, has the form [33]

$$E(x, y, z = z_0) = \frac{i}{\lambda z_0}\exp\left(-\frac{i2\pi z_0}{\lambda}\right) \times \exp\left(-\frac{i\pi(x^2 + y^2)}{\lambda z_0}\right)J(x, y, z_0), \quad (3)$$

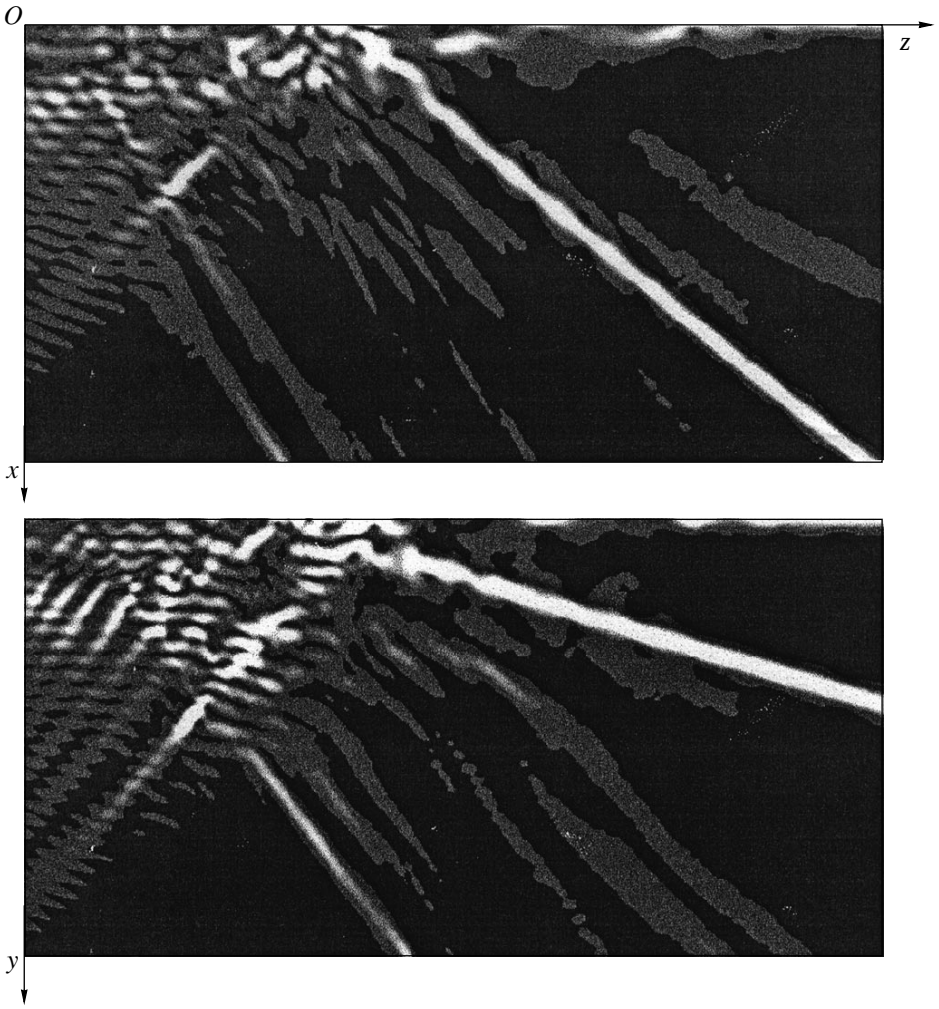

Fig. 1. Intensity distribution of the diffraction catastrophe field in the longitudinal planes *xOz* and *yOz* for field realization 1. Horizontal and vertical dimensions are 9.06 mm and 164 μm, respectively.

where the diffraction integral $J(x, y, z_0)$ is given by

$$J = \iint_S A_0(x_2, y_2)\exp(i\Delta\varphi(x_2, y_2)) \times \exp\left(i2\pi\left(x_2\frac{x}{\lambda z_0} + y_2\frac{y}{\lambda z_0}\right)\right)dx_2dy_2. \quad (4)$$

Here, x and y are the Cartesian coordinates in the entrance plane $z = z_0$ and

$$\Delta\varphi(x_2, y_2) = \frac{2\pi}{\lambda}[z_0 - \sqrt{z_0^2 - x_2^2 - y_2^2}] - \varphi(x_2, y_2, 0)$$

is the phase distortion of the wave front at $z = 0$ relative to the reference sphere whose center lies in the plane $z = z_0$. The integral J is calculated in the plane (x_2, y_2) at $z = 0$ over the exit aperture S of the focusing element.

We consider the situation when $A_0(x_2, y_2) = A_0 = \text{const}$ and the converging wave front is distorted by spherical aberration and astigmatism. In a linear medium, these conditions produce a stable field pattern—diffraction catastrophe—in the focal region [34]. The phase function has the form

$$\varphi(x_2, y_2, 0) = \frac{2\pi}{\lambda}[\tilde{F} - \sqrt{\tilde{F}^2 - x_2^2 - y_2^2} + a(x_2^2 + y_2^2)^2 + c(y_2^2 - x_2^2)]. \quad (5)$$

Here, a is the factor of third-order spherical aberration and c is the effective factor of astigmatism. The first term in brackets in formula (5) describes the reference (ideal) spherical wave front of radius $\tilde{F}$ centered at a point $(0, 0, \tilde{F})$, while the second and third terms describe distortions of the phase front relative to the reference sphere. In order to compare our results with those in [27, 34], we used $a = 1.20 \times 10^{-6}$ mm^{-3}, $c = 9.96 \times 10^6$ mm^{-1}, $\tilde{F} = 141.70$ mm, and $\lambda = 0.6328$ μm. The diameter of the effective beam aperture at the exit from the focusing element was taken to be 20 mm. The

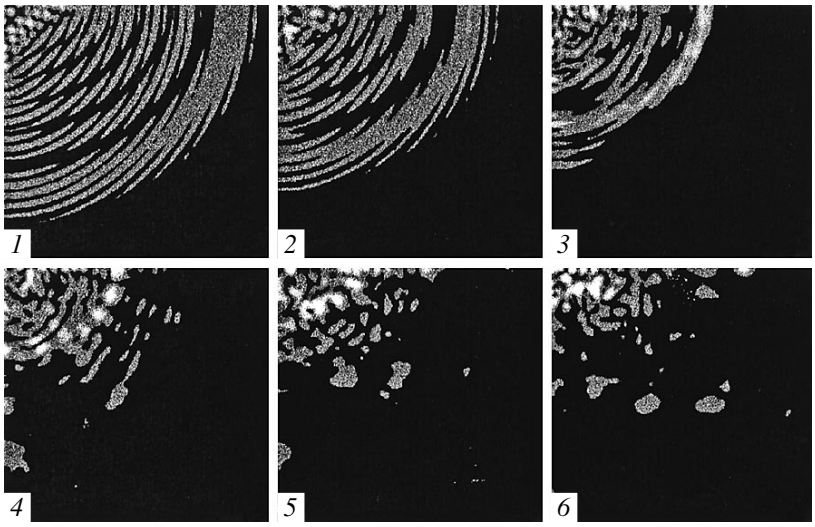

Fig. 2. Distribution of the diffraction catastrophe field intensity over different *xOy* cross sections. The cross sections are taken for $z < 139$ mm before the caustic waist: $z =$ (*1*) 135.5, (*2*) 136.125, (*3*) 136.75, (*4*) 137.375, (*5*) 138.0, and (*6*) 138.625 mm. Field realization 1. The size of the *xOy* quadrant is 164×164 μm. The *Ox* axis is vertical, the *Oy* axis is horizontal, and the origin is at the upper left corner of the quadrant.

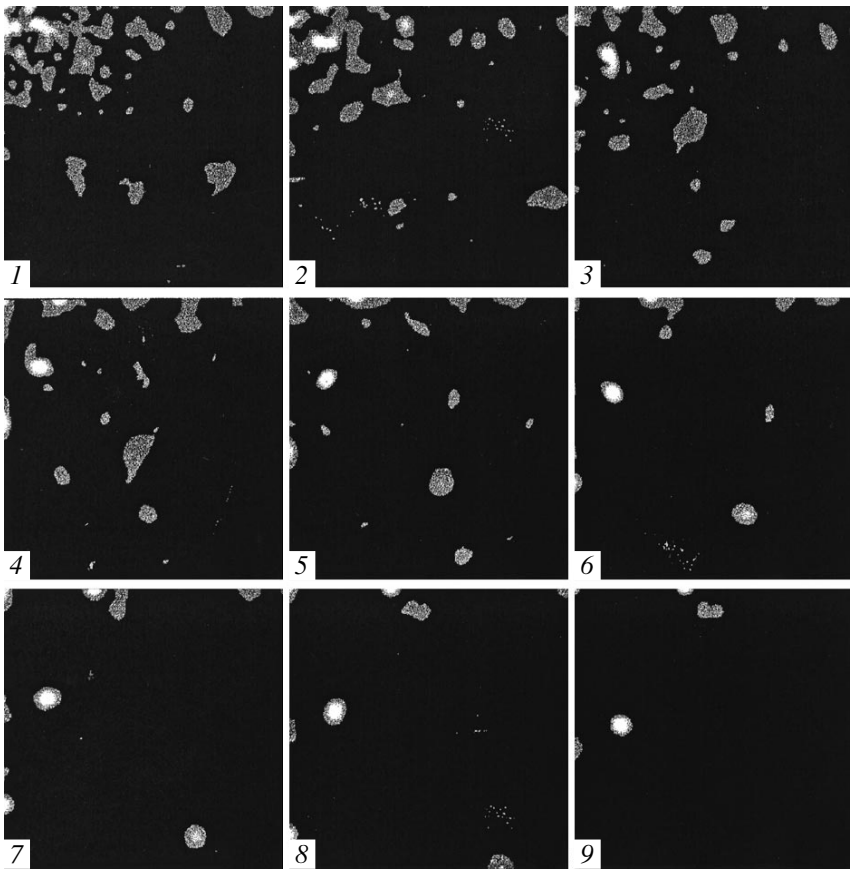

Fig. 3. Same as in Fig. 2, but the cross sections are taken at $z > 139$ mm in the region where multiple solitons appear and exist: $z =$ (*1*) 139.25, (*2*) 139.875, (*3*) 140.5, (*4*) 141.125, (*5*) 141.75, (*6*) 142.375, (*7*) 143.0, (*8*) 143.625, and (*9*) 144.25 mm.

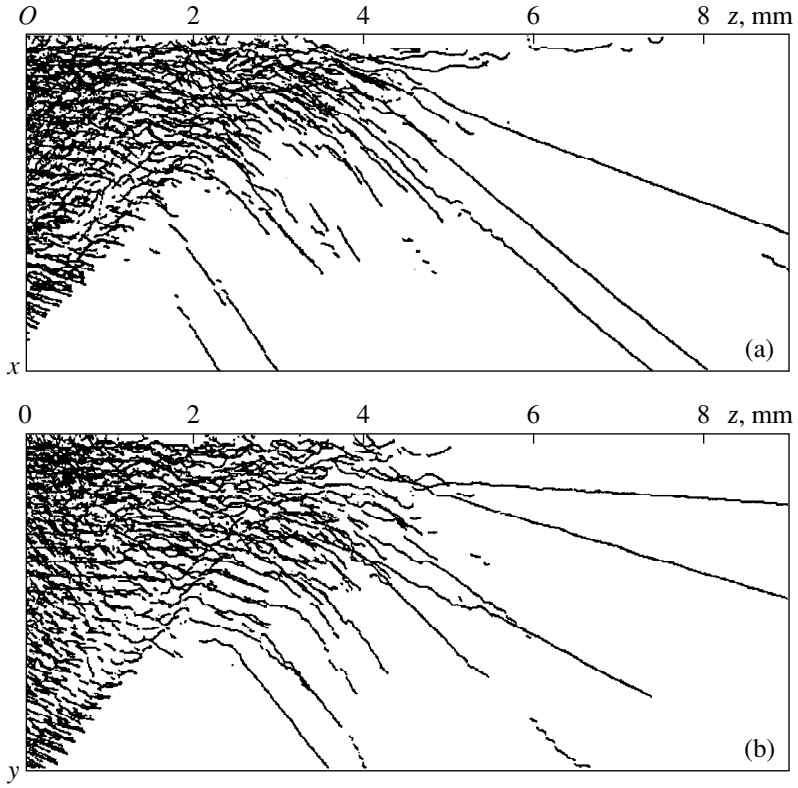

Fig. 4. Projections of the lines traced by the maximums of speckle elements in transverse planes onto the longitudinal planes (a) *xOz* and (b) *yOz*. Field realization 1. The vertical dimension is 139.4 μm.

intensity of the focused radiation was varied: the parameter $n_2A_0^2$ took the values 1×10^{-10} and 2×10^{-10}. At certain points in the entrance plane of the nonlinear medium, the parameter $n_2|E|^2$ was as high as 1×10^{-3}.

RESULTS AND DISCUSSION

The computer-aided simulation of the saturable Kerr media revealed the following. Near the caustic waist of the focused beam, the tubular–cellular field pattern has the form of short curvilinear filaments. These filaments represent spatial solitons, which appear, interact, split, or merge together. Sometimes, they break down after passing through this region. Beyond the region with the minimal cross section of the focal pattern, the optical field has the form of chaotically outgoing splashes and long filaments, as shown in Fig. 1. The filaments, which radiate from the caustic waist over long distances, are bright spatial solitons. They channel a significant part of the primary beam energy. The optical field illustrated in Fig. 1 was obtained at $n_2|E_s|^2 = 0.003$ and $n_2A_0^2 = 2 \times 10^{-10}$.

The field intensity distribution in transverse cross sections $z_i = z_0 + i\Delta z$ of the diffraction catastrophe is shown in Figs. 2 and 3. In each cross section $z = z_i$, we, following [27], found speckle elements whose peak intensity exceeded a certain threshold. The Cartesian coordinates of the intensity peaks of these speckle elements and the field amplitude in them were memorized for subsequent processing. By peak coordinates, we mean the coordinates of the field peaks in the transverse plane. Figures 2 and 3 show that the number of speckle elements strongly depends on coordinate z_i. Indeed, as the caustic waist is approached, the number of closely spaced speckle elements, which, in essence, are the cross sections of microscopic waveguides or short solitons, first increases (fragments *3–5* in Fig. 2), reaches a maximum at the waist (fragment *6* in Fig. 2), and then decreases with increasing z (fragments *1–4* in Fig. 3). Accordingly, the number of spatial solitons first increases, which is associated with their interaction or splitting. Only beyond the narrowest caustic region does the number of solitons drop to a certain level (fragments *6–9* in Fig. 3). Each of the fragments in Figs. 2 and 3 is an *xOy* quadrant (i.e., a quarter) of the cross section. From fragments *4–9* in Fig. 3, it follows that the entire cross section contains eight clear-cut solitons, which do not collapse and do not disappear with increasing z. In other situations ($n_2|E_s|^2 = 0.003$ and $n_2A_0^2 = 1 \times 10^{-10}$), we observed 9–12 distinct solitons in the cross section, which propagated in the positive z direction and also moved apart in the transverse (x, y) plane.

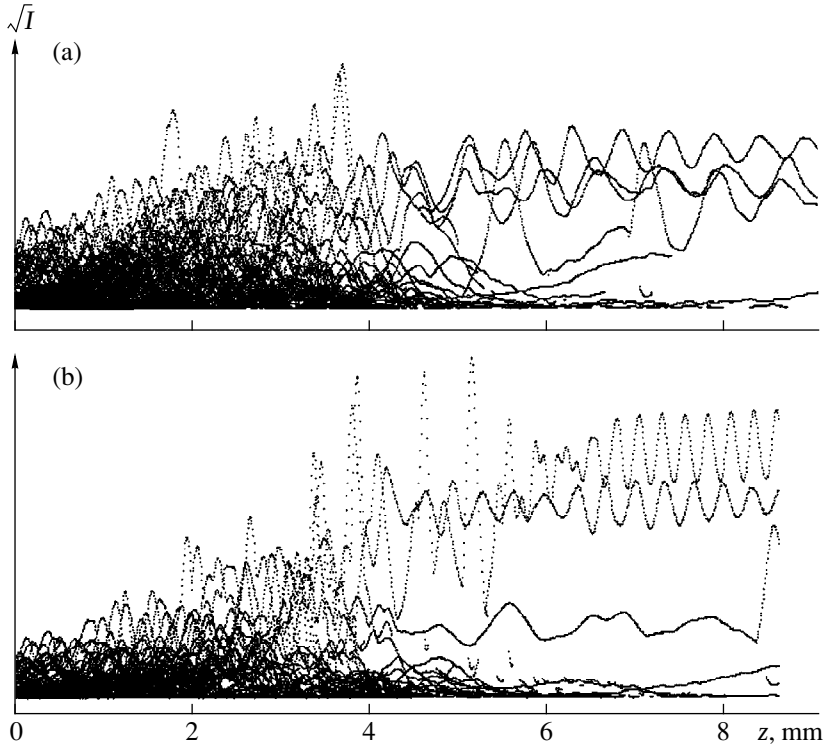

Fig. 5. z dependence of the field amplitudes at the maxima of speckle elements in the transverse planes for field realizations (a) 1 and (b) 2 at $n_2|E_s|^2 = 0.006$ and $n_2 A_0^2 = 1 \times 10^{-10}$.

To characterize the variation of the number of solitons in the region of their interaction, the term "peak of the local field" in place of our "speckle element with the peak intensity above a threshold level" was proposed [13]. In terms of [13], the number of local field peaks in the region of soliton interaction may greatly increase or decrease depending on which process prevails: splitting of single solitons or soliton pairs into two or three solitons, respectively, or merging of soliton pairs into more intense single solitons. The latter process may be accompanied by a decay of single solitons if lossless energy channeling through the soliton waveguide becomes impossible for some reasons. These results are in evident agreement with theoretical findings reported in [13].

The speckle element maxima in the transverse plane trace trajectories in the three-dimensional space, which are curvilinear and piecewise finite in general. Figures 4a and 4b show the projections of these trajectories on the planes yOz and xOz in the form of the loci of x_i, z_i and y_i, z_i, respectively. Here, x_i, y_i, z_i are the Cartesian coordinates of the maxima of all speckle elements in transverse planes (x, y) equally spaced with $z_i = z_0 + i\Delta z$. It is seen that, beyond the waist region, the maxima describe linearly radiating trajectories similar to those of the bright radiating solitons. Extrapolation of these trajectories in the z direction allows one to accurately locate the waist region, which acts as a source of multiple solitons. This region coincides with the one where periodic intensity oscillation in the soliton channels appears.

Figure 5a shows the z dependence of the field amplitude at the maxima of the speckle elements. Beyond the region of the least cross section of the focal pattern for the radiating solitons, the field amplitude oscillates along their major axes. Figure 1 displays oscillation of the soliton cross section. It appears as the solitons extend in the positive z direction and show up as corrugated "soliton tubes." Such effects have repeatedly been observed both directly in soliton channels and in more particular cases. For example, intensity oscillation in soliton channels was calculated in [1, 2]. Cross-size oscillation ("breathing") of a soliton was reported in [1]. Intensity oscillation in the channel that appears as a result of focusing a laser beam with an axicon in a nonlinear medium was studied in [26].

The period and depth of the field amplitude oscillation in the soliton channel vary with the parameters of the Kerr medium (Fig. 5b). Pronounced amplitude oscillation in the soliton channels allows the region of soliton initiation to be clearly located. It is remarkable that the clear-cut multiple solitons arise only after the waist rather than before it.

Among various effects typical of radiating solitons, of interest is a slight rotation of a low-intensity soliton about a more intense bright soliton in the transverse plane (x, y) [11, 35]. Fragments *1–3* (Fig. 6) show that

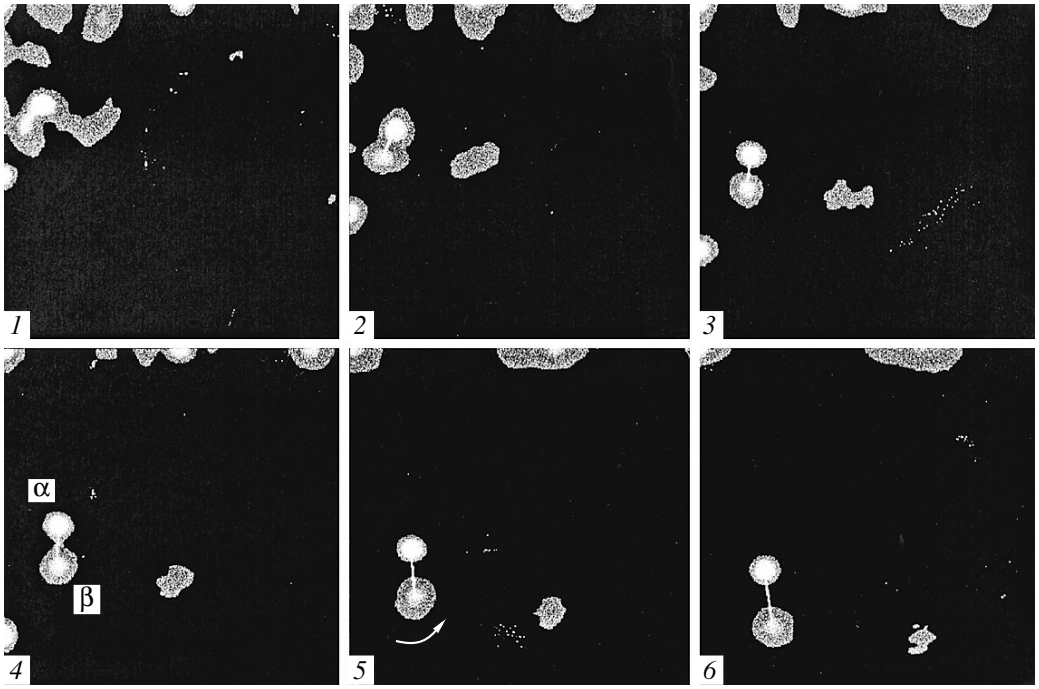

Fig. 6. Rotation of the low-intensity soliton β about the high-intensity soliton α in the transverse plane. The interaction is illustrated for $z > 141$ mm: (*1*) 141.125, (*2*) 141.75, (*3*) 142.375, (*4*) 143.0, (*5*) 143.625, and (*6*) 144.21 mm. Field realization 3 ($n_2|E_s|^2 = 0.003$ and $n_2 A_0^2 = 1 \times 10^{-10}$). The size of the *xOy* quadrant is 164×164 μm. The *Ox* axis is vertical, the *Oy* axis is horizontal, and the origin is at the upper left corner of the quadrant.

the lower intensity soliton–satellite β first partially and then completely separates from the intense soliton α. The soliton β rotates about α until their center distance becomes too long as they travel in the positive *z* direction. In this area of the three-dimensional space, the trajectory of the former (β) is curved, while the latter (α) travels almost rectilinearly.

We have thus shown that multiple bright spatial solitons appear when a high-power laser beam subjected to specific complicated aberrations is focused in the saturable Kerr medium. However, it can be shown that spatial radiating solitons will also form in a nonlinear medium when aberrations are of other types.

REFERENCES

1. V. V. Afanasjev, P. L. Chu, and Yu. S. Kivshar, Opt. Lett. **22**, 1388 (1997).
2. S. Gatz and J. Herrmann, J. Opt. Soc. Am. B **14**, 1795 (1997).
3. A. W. Snyder and Yu. S. Kivshar, J. Opt. Soc. Am. B **14**, 3025 (1997).
4. H. Maillotte, J. Monneret, A. Barthelemy, and C. Froehly, Opt. Commun. **109**, 265 (1994).
5. E. A. Ostrovskaya and Yu. S. Kivshar, J. Opt. B: Quantum Semiclassical Opt., No. 1, 77 (1999).
6. R. de la Fuente, J. Linares, H. Michinel, *et al.*, Pure Appl. Opt. **6**, 31 (1997).
7. A. Ankiewicz, W. Krolikowski, and N. Akhmediev, Phys. Rev. E **59**, 6079 (1999).
8. A. V. Buryak and V. V. Steblina, J. Opt. Soc. Am. B **16**, 245 (1999).
9. E. Granot, S. Sternklar, Y. Isbi, *et al.*, Opt. Commun. **166**, 121 (1999).
10. G. Leo and G. Assanto, J. Opt. Soc. Am. B **14**, 3151 (1997).
11. W. Krolikowski, C. Denz, A. Stepken, *et al.*, J. Opt. B: Quantum Semiclassical Opt., No. 10, 823 (1998).
12. N. V. Vysotina, L. A. Nesterov, N. N. Rozanov, and V. A. Smirnov, Opt. Spektrosk. **85** (2), 239 (1998) [Opt. Spectrosc. **85**, 218 (1998)].
13. N. N. Rozanov, Opt. Spektrosk. **82** (5), 820 (1997) [Opt. Spectrosc. **82**, 761 (1997)].
14. L. Torner and D. V. Petrov, J. Opt. Soc. Am. B **14**, 2017 (1997).
15. E. Wolf and Y. Li, Opt. Commun. **39**, 205 (1981).
16. D. C. Bertilone, Opt. Commun. **85**, 153 (1991).
17. V. Yu. Osipov, Opt. Spektrosk. **75** (1), 155 (1993) [Opt. Spectrosc. **75**, 92 (1993)].
18. B.-Z. Dong, G.-Z. Yang, B.-Y. Gu, and O. K. Ersoy, J. Opt. Soc. Am. A **13**, 97 (1996).
19. D. Y. Jiang and J. J. Stamnes, Pure Appl. Opt. **6**, 85 (1997).
20. W. Hsu and R. Barakat, J. Opt. Soc. Am. A **11**, 623 (1994).
21. P. Torok, P. Varga, and G. R. Booker, J. Opt. Soc. Am. A **12**, 2136 (1995).

22. D. G. Flagello, T. Milster, and A. E. Rosenbluth, J. Opt. Soc. Am. A **13** (1), 53 (1996).
23. M. V. Berry and C. Upstill, in *Progress in Optics*, Ed. by E. Wolf (North-Holland, Amsterdam, 1980), Vol. 18, pp. 257–346.
24. M. Born and E. Wolf, *Principles of Optics: Electromagnetic Theory of Propagation, Interference, and Diffraction of Light* (Pergamon, New York, 1964; Nauka, Moscow, 1973).
25. A. M. Deykoon, M. S. Soskin, and G. A. Swartzlander, Jr., Opt. Lett. **24** (17), 1224 (1999).
26. N. K. Andreev, Yu. A. Aristov, L. Ya. Polonskiĭ, and L. N. Pyatnitskiĭ, Zh. Éksp. Teor. Fiz. **100**, 1756 (1991) [Sov. Phys. JETP **73**, 969 (1991)].
27. V. Yu. Osipov, Zh. Tekh. Fiz. **68** (9), 74 (1998) [Tech. Phys. **43**, 1075 (1998)].
28. M. Scalora and M. E. Crenshaw, Opt. Commun. **108**, 191 (1994).
29. M. D. Feit and J. A. Fleck, Jr., J. Opt. Soc. Am. B **5**, 633 (1988).
30. P. Paakkonen, P. Vahimaa, A. T. Friberg, and J. Turunen, Pure Appl. Opt. **7**, 1033 (1998).
31. D. Li, H. van Brug, and H. J. Frankena, Pure Appl. Opt. **4**, 475 (1995).
32. L. di Menza, J. Opt. B: Quantum Semiclassical Opt., No. 1, 19 (1999).
33. R. J. Collier, C. B. Burckhardt, and L. H. Lin, *Optical Holography* (Academic, New York, 1971; Mir, Moscow, 1973).
34. V. Yu. Osipov, Avtometriya **5**, 48 (1996).
35. L. Poladian, A. W. Snyder, and D. J. Mitchell, Opt. Commun. **85**, 59 (1991).

Translated by A. Khzmalyan

Technical Physics, Vol. 46, No. 4, 2001, pp. 450–455. Translated from Zhurnal Tekhnicheskoĭ Fiziki, Vol. 71, No. 4, 2001, pp. 89–94.

ACOUSTIC, ACOUSTOELECTRONICS

Temperature-Stable Orientations in LGS and LGN Piezoelectric Crystals for Surface Acoustic Waves

M. Yu. Dvoesherstov, S. G. Petrov, V. I. Cherednik, and A. P. Chirimanov

Lobachevskiĭ State University, Nizhni Novgorod, 603600 Russia

Received February 28, 2000; in final form, June 28, 2000

Abstract—The temperature characteristics of surface acoustic waves (SAW) propagating in LGS and LGN crystals are numerically analyzed. The optimal orientations that correspond to the zero value of the first-order temperature coefficient of delay (TCD) for SAW propagating in these crystals are considered. The second-order TCD for SAW is calculated for a wide range of operating temperatures. It is shown that the temperature dependences of the material constants of LGS and LGN crystals are strongly nonlinear. The characteristics of SAW propagating in a structure that consists of an isotropic layer overlying an LGS or LGN piezoelectric crystal are numerically calculated. It is shown that, in the presence of a thin aluminum layer of a certain thickness on the crystal surface, in some cases it is possible to extend the operating temperature range within which the TCD for SAW is equal to zero. *© 2001 MAIK "Nauka/Interperiodica".*

INTRODUCTION

The interest shown lately in studying the properties of surface acoustic waves (SAW) propagating in LGS and LGN crystals is caused by the fact that these crystals possess some orientations characterized by higher values of the coefficient of electromechanical coupling (K^2) of SAW, as compared to the case of the much studied quartz crystals. At the same time, the LGS and LGN crystals are known to exhibit some temperature-stable properties [1, 2]. Certain cuts of these crystals and some directions in them [1] are characterized by a zero value of the first-order temperature coefficient of delay ($TCD^{(1)}$) for SAW at room temperature ($t_0 = 25°C$).

One of the main characteristics in the SAW technique is the sensitivity of the temperature-stable direction in the crystal to changes in the environment temperature. As a rule, the absolute value of the temperature coefficient of delay for SAW widely varies when the operating temperature t departs from the room temperature t_0. It is of interest to study the behavior of $TCD^{(1)}$ for SAW propagating in LGS and LGN crystals in a wide temperature range. For the temperature-stable directions of these crystals, it is also necessary to analyze the behavior of the second-order temperature coefficient of delay ($TCD^{(2)}$).

When a piezoelectric crystal is coated with a thin metal film of a finite thickness h, the general properties of SAW change. The velocity V of SAW and their TCD can either decrease or increase, depending on the properties of the substrate material and the film material. In some cases, a metal film deposited on the substrate surface can improve the thermal stability of the SAW propagation in such a structure [3, 4].

In this paper, we study the cuts of LGS and LGN crystals and the directions in them that are characterized by a zero first-order temperature coefficient of delay, $TCD^{(1)}$, for SAW. We analyze the second-order temperature coefficient of delay, $TCD^{(2)}$, for SAW in these cuts with allowance for the second-order temperature coefficients of the elastic, piezoelectric, and dielectric constants ($TC_{ij}^{(2)}$, $Te_{ij}^{(2)}$, and $T\varepsilon_{ij}^{(2)}$) and the second-order temperature expansion coefficient ($\alpha_{ij}^{(2)}$) at room temperature. We consider the changes that occur in $TCD^{(1)}$ and $TCD^{(2)}$ when the operating temperature varies from –100 to +120°C.

We analyze the variation of the relative delay time $\Delta\tau/\tau_0 = (\tau - \tau_0)/\tau_0$ (where τ and τ_0 are the delay times of SAW) in a wide range of operating temperatures t. We show that the temperature dependences of the material constants of LGS and LGN crystals are strongly nonlinear, and, therefore, even in calculating the $TCD^{(1)}$ for SAW in a wide temperature range, it is necessary to take into account the second-order temperature coefficients of the material constants of these crystals.

We also demonstrate the effect of a thin metal coating of a finite thickness on the characteristics of SAW (the SAW velocity and the TCD).

TEMPERATURE COEFFICIENT OF DELAY FOR SAW

The dependence of all components of the crystal material constants on the operating temperature near room temperature can be represented in the form [5]

$$C_{ij}(t) = C_{ij}(t_0)(1 + TC_{ij}^{(1)}(t - t_0) + TC_{ij}^{(2)}(t - t_0)^2 + \ldots),$$

$$e_{ij}(t) = e_{ij}(t_0)(1 + Te_{ij}^{(1)}(t - t_0) + Te_{ij}^{(2)}(t - t_0)^2 + \ldots),$$

1063-7842/01/4604-0450$21.00 © 2001 MAIK "Nauka/Interperiodica"

$$\varepsilon_{ij}(t) = \varepsilon_{ij}(t_0)(1 + T\varepsilon_{ij}^{(1)}(t-t_0) + T\varepsilon_{ij}^{(2)}(t-t_0)^2 + \ldots), \quad (1)$$

$$\rho(t) = \rho(t_0)(1 + T\rho^{(1)}(t-t_0) + T\rho^{(2)}(t-t_0)^2 + \ldots),$$

$$L(t) = L(t_0)(1 + \alpha_L^{(1)}(t-t_0) + \alpha_L^{(2)}(t-t_0)^2 + \ldots).$$

Here, $TC_{ij}^{(1)}$, $Te_{ij}^{(1)}$, $T\varepsilon_{ij}^{(1)}$, $TC_{ij}^{(2)}$, $Te_{ij}^{(2)}$, $T\varepsilon_{ij}^{(2)}$, $T\rho^{(1)}$, $T\rho^{(2)}$, $\alpha^{(1)}$, and $\alpha^{(2)}$ are the first- and second-order temperature coefficients of the elastic, piezoelectric, and dielectric constants; the first- and second-order temperature coefficients of density; and the first- and second-order thermal expansion coefficients, respectively; i, j = 1–6; L is the length of the sample; t_0 = 25°C is the room temperature; and t is the operating temperature. In calculating the temperature coefficients of delay, $TCD^{(1)}$ and $TCD^{(2)}$, for SAW, it is necessary to take into account the temperature dependences of the material constants C_{ij}, e_{ij}, and ε_{ij} of the piezoelectric crystal and the temperature dependence of its density ρ. In addition, the length L of the working part of the crystal also varies when the operating temperature is varied.

To calculate the first-order coefficient $TCD^{(1)}$ for SAW near room temperature, one usually takes into account the values of the first-order temperature coefficients of the elastic, piezoelectric, and dielectric constants and density and the first-order coefficients of thermal expansion [5]. However, as one can see from Eqs. (1), when the operating temperature widely differs from room temperature, the factor $(t - t_0)$ can take relatively large values. In addition, the second-order temperature coefficients of the material constants can also be large. In this case, in calculating $TCD^{(1)}$ for SAW in a wide temperature range, it is necessary to take into account the values of the second-order (and higher order) temperature coefficients of the material constants.

The temperature coefficient of the crystal density $T\rho^{(1)}$ can be calculated by the formula [6]

$$T\rho^{(1)} = -(\alpha_{11}^{(1)} + \alpha_{22}^{(1)} + \alpha_{33}^{(1)}), \quad (2)$$

where $\alpha_{11}^{(1)}$, $\alpha_{22}^{(1)}$, and $\alpha_{33}^{(1)}$ are the linear thermal expansion coefficients of the crystal in the X_1, X_2, and X_3 directions of the working coordinate system, respectively [2].

To calculate the dependence of the delay time τ of SAW on the temperature t, one can use the Taylor expansion near room temperature:

$$\tau = \tau_0(t_0) + \left.\frac{d\tau}{dt}\right|_{t_0}(t-t_0) + \frac{1}{2}\left.\frac{d^2\tau}{dt^2}\right|_{t_0}(t-t_0)^2 \quad (3)$$

$$= \tau_0[1 + TCD^{(1)}(t-t_0) + TCD^{(2)}(t-t_0)^2 + \ldots],$$

where

$$TCD^{(1)} = \left.\frac{1}{\tau_0}\frac{d\tau}{dt}\right|_{t_0}$$

is the first-order temperature coefficient of delay;

$$TCD^{(2)} = \left.\frac{1}{2}\frac{1}{\tau_0}\frac{d^2\tau}{dt^2}\right|_{t_0} = \left.\frac{1}{2}\frac{dTCD^{(1)}}{dt}\right|_{t_0}$$

is the second-order temperature coefficient of delay; and τ and τ_0 are the SAW delay times at the operating and room temperatures, respectively.

According to [7], the coefficient $TCD^{(1)}$ for SAW can be calculated by the formula

$$TCD^{(1)} = \left.\frac{1}{\tau}\frac{d\tau}{dt}\right|_{t_0} = \alpha_{11}^{(1)} - TCV^{(1)}, \quad (4)$$

where $TCV^{(1)}$ is the first-order temperature coefficient of velocity for SAW. This coefficient is determined by the expression [5]

$$TCV^{(1)} = \frac{1}{V(t_0)}\frac{\partial V}{\partial t}, \quad (5)$$

where $V(t_0)$ is the SAW velocity at the room temperature t_0 and V is the SAW velocity at the operating temperature t.

When the higher orders in Eq. (3) are neglected, the relative variation of the SAW delay time, $\Delta\tau/\tau_0 = (\tau - \tau_0)/\tau_0$, can be represented in the form

$$\frac{\tau - \tau_0}{\tau_0} = TCD^{(1)}(t-t_0) + TCD^{(2)}(t-t_0)^2. \quad (6)$$

In the general case, we can use the general equation for calculating the dependence of the relative delay time of SAW on the temperature t:

$$\frac{\tau - \tau_0}{\tau_0} = \int_{t_0}^{t}\alpha_\tau dt, \quad (7)$$

where

$$\alpha_\tau = \frac{1}{\tau}\frac{d\tau}{dt}$$

is the general TCD of SAW at any temperature t.

We note [7] that the relative variation of the SAW frequency f is expressed as

$$\Delta f/f_0 = (f - f_0)/f_0 = -\Delta\tau/\tau_0. \quad (8)$$

Thus, using Eqs. (1)–(8), one can calculate all temperature characteristics of SAW: $TCD^{(1)}$, $TCD^{(2)}$, $\Delta\tau/\tau_0$, and $\Delta f/f_0$. To do this, it is necessary first to calculate the velocity V of SAW (by numerical computer calculation [2]) for different operating temperatures and for a given crystal cut and a given direction of the SAW propagation (the crystal cut and the propagation direction in the

crystal can be defined by three Euler angles, ϕ, Θ, and ψ [5]).

ANALYSIS OF THE TEMPERATURE-STABLE ORIENTATIONS IN LGS AND LGN CRYSTALS

A number of recent publications [8–10] report on the numerical calculations of the temperature characteristics of SAW for the promising orientations of LGS and LGN crystals. However, the calculated values of $TCD^{(1)}$ and $TCD^{(2)}$ of SAW noticeably differ from the experimental data [10]. This discrepancy is caused by the fact that different sources provide different values of the first- and second-order temperature coefficients of the material constants. In one of the cited papers [9], a numerical analysis of the main properties of SAW in an LGS crystal is performed for three different variants of the material constants. Another paper [10] presents the refined values of the first- and second-order temperature coefficients of material constants and describes the theoretical calculations and the experimental measurements of the quantity $\Delta f/f_0$ for an LGS crystal with the (0, 140°, 24°) orientation in a wide temperature range, from –20 to +80°C (Fig. 1). One can see that the dependences $\Delta f/f_0(t)$ calculated with the use of the LGS material constants taken from [8] (curve *1*) and [10] (curve *2*) are different. However, the experimental values (indicated by crosses on curve *2*) coincide with the theoretical ones obtained by using the refined values of the material constants of LGS.

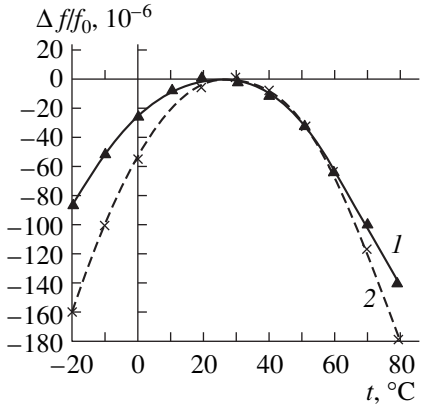

Fig. 1. Theoretical and experimental dependences of $\Delta f/f_0$ on temperature for the (0, 140°, 24°) LGS crystal: (×) experiment and (- - -) calculation.

This result offers the following conclusion: using the material constants for an LGS crystal from [10], one can perform a preliminary numerical calculation of the temperature characteristics ($TCD^{(1)}$ and $TCD^{(2)}$) of SAW for any orientation of the crystal in a wide temperature range, and this calculation will coincide with the experimental data with fair accuracy.

As an example, in Fig. 2a we present the calculated temperature dependences of $TCD^{(1)}$ that were obtained with allowance for the first-order temperature coefficients of material constants only (curve *1*) and with allowance for the first- and second-order temperature coefficients of material constants (curve *2*) for an LGS crystal with the (0, 140°, 22.5°) orientation. One can see that the inclusion of the second-order temperature coefficients of material constants noticeably changes the form of the temperature dependence of $TCD^{(1)}$. For example, using only the first-order temperature coefficients of material constants in our calculations (curve *1*), we obtain that the value of $TCD^{(1)}$ is practically temperature independent and is close to zero. In the second case (curve *2*), in the temperature interval from –100 to +120°C, the value of $TCD^{(1)}$ varies from -20×10^{-6} 1/°C to $+10 \times 10^{-6}$ 1/°C and becomes zero at $t \approx 35$°C.

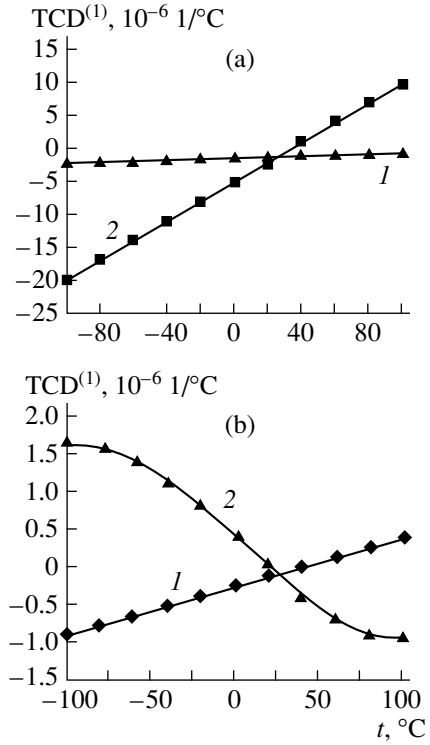

Fig. 2. Temperature dependences of $TCD^{(1)}$ calculated with allowance for the (*1*) first-order and (*2*) second-order temperature coefficients of material constants for (a) the (0, 140°, 22.5°) LGS crystal and (b) the (0, 138.5°, 23°) LGN crystal.

We note that, for a widely used ST, *X*-cut quartz [9], the inclusion of the second-order temperature coefficients of material constants in the calculation of the temperature characteristics of SAW hardly affects the behavior of the temperature dependences of $TCD^{(1)}$ and $\Delta\tau/\tau_0$. When the temperature varies from –100 to +120°C, the value of $TCD^{(1)}$ varies from -8×10^{-6} to 6×10^{-6} 1/°C. The value of $\Delta\tau/\tau_0$ in the given temperature range is about 0.0005, and the temperature dependence of $\Delta\tau/\tau_0$ has the form of a parabola. The corresponding value of $TCD^{(2)}$ is $\approx 31.9 \times 10^{-9}$ 1/°C^2. By con-

trast, in an LGS crystal, the temperature dependences of the material constants are strongly nonlinear.

The experimental temperature dependences of the bulk wave velocity in an LGN crystal, as well as the material constants and the first- and second-order temperature coefficients of the material constants, are taken from [11]. Figure 2b shows the temperature dependences of the coefficient $TCD^{(1)}$ of SAW for an LGN crystal with the (0, 138.5°, 23°) orientation. One can see that the temperature dependence of $TCD^{(1)}$ is linear when the second-order temperature coefficients of material constants are neglected (curve *1*), and it is nonlinear when these coefficients are taken into account. Moreover, in the first case, as the temperature varies from –100 to +120°C, $TCD^{(1)}$ varies from -1×10^{-6} to $+0.4 \times 10^{-6}$ 1/°C, whereas, in the second case, $TCD^{(1)}$ varies from $+1.5 \times 10^{-6}$ to -1×10^{-6} 1/°C. The main characteristics of SAW for the given orientation at room temperature are as follows: the SAW velocity V = 2.6407 km/s, the coefficient of electromechanical coupling [5] K^2 = 0.414%, $TCD^{(1)} = -0.09 \times 10^{-6}$ 1/°C, $TCD^{(2)} = -9.5 \times 10^{-9}$ 1/°C^2, the angle between the phase and group velocities [2] PFA = 4.8°, and the anisotropy coefficient [5] $\gamma = -2.47$.

Thus, we can conclude that the temperature dependences of the material constants of LGS and LGN crystals are strongly nonlinear, and, therefore, in calculating $TCD^{(1)}$ for SAW in a relatively wide range of operating temperatures, it is necessary to take into account the second-order terms in Eqs. (1), unlike the case of piezoelectric quartz.

EFFECT OF A THIN METAL FILM OF A FINITE THICKNESS ON THE TEMPERATURE COEFFICIENT OF DELAY FOR SAW

When the surface of a piezoelectric crystal is covered with a thin isotropic metal film of a finite thickness, it is appropriate to consider the problem of the SAW propagation in a layered structure consisting of an isotropic layer and a piezoelectric substrate. In this case, we have a system of two wave equations of motion [5] one of which relates to the film material and the other relates to the substrate material. In addition, ten boundary conditions must be satisfied for two linear combinations of partial waves, one of these combinations relating to the substrate and the other to the upper layer. These boundary conditions are as follows [5]: the continuity of the stresses T_{31}, T_{32}, and T_{33} at the layer–substrate interface and the zero values of these stresses at the surface of the upper layer $X_3 = h$; the continuity of the displacements u_1, u_2, and u_3 at the interface; and the zero value of the potential φ at the film–substrate boundary in the case of a metallized isotropic film.

In calculating the temperature dependences of the velocity V_s and the coefficient TCD_s for SAW propagating in a layered structure, it is necessary to take into account the following facts: (a) the dependence of the material constants C_{ij}, e_{ij}, and ε_{ij} of the anisotropic substrate on temperature (Eqs. (1)); (b) the thermal expansion of the crystal (see Eqs. (1)); (c) the dependences of the crystal density ρ (Eq. (2)) and the layer density ρ_s on temperature; (d) the dependence of the Lame elastic constants of the isotropic layer on temperature [7]; (e) the thermal expansion of the film [7]; (f) the changes in the film thickness h with varying temperature [7]; and (g) the presence of the initial thermal internal stresses in the layered structure due to the difference in the coefficients of thermal expansion of the film and substrate materials [12].

The temperature coefficient of delay for SAW in a layered structure can be calculated by the formula [7]

$$TCD_s^{(1)} = \frac{1}{\tau_0}\frac{d\tau_s}{dt}\bigg|_{t_0} = \alpha_{11}^{(1)} - TCV_s^{(1)}, \qquad (9)$$

where τ_s and τ_0 are the delay times of SAW in the layered structure at the operating and room temperatures, respectively; $TCV_s^{(1)}$ is the temperature coefficient of velocity for SAW in the layered structure; and $\alpha_{11}^{(1)}$ is the coefficient of thermal expansion of the crystal in the propagation direction.

If the film thickness h is much less than the substrate thickness H, one can assume that, as the operating temperature varies, the substrate length varies in one or another direction and the film length varies simultaneously. However, we note that the film thickness h will also vary in this case [7]. Moreover, if the thermal expansion coefficients of the film and substrate materials are widely different, a change in the operating temperature will cause thermal internal stresses in the structure [12], and these stresses will also contribute to the characteristics of SAW. We do not consider such a case in this paper.

In the presence of a film of finite thickness, the velocity V of SAW and the coefficient $TCD^{(1)}$ will vary in one or another direction, depending on the film thickness and the properties of the layer and substrate materials. According to [13], for certain combinations of the substrate and film materials and for certain values of the film thickness, one can obtain a zero $TCD^{(1)}$ for the SAW propagation along some direction in the crystal and a simultaneous increase in the coefficient of electromechanical coupling of SAW (K^2) in this direction. Alternatively, it is possible to use the film in order to increase the operating temperature range within which the TCD of SAW will remain almost invariable.

Figure 3 shows the dependences of the velocity V and the coefficient $TCD^{(1)}$ of SAW on the ratio h/λ (λ is the wavelength of SAW) in the presence of an aluminum thin film on the surface of an LGS crystal with the (0, 140°, 22.5°) orientation. One can see that both the velocity and the coefficient $TCD^{(1)}$ linearly increase

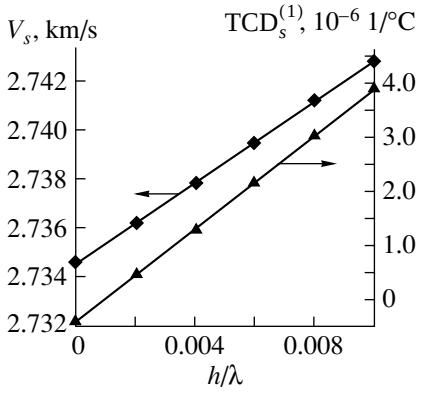

Fig. 3. Dependences of the velocity V_s and the coefficient $TCD_s^{(1)}$ on the ratio h/λ in the Al + (0, 140°, 22.5°) LGN layered structure at room temperature.

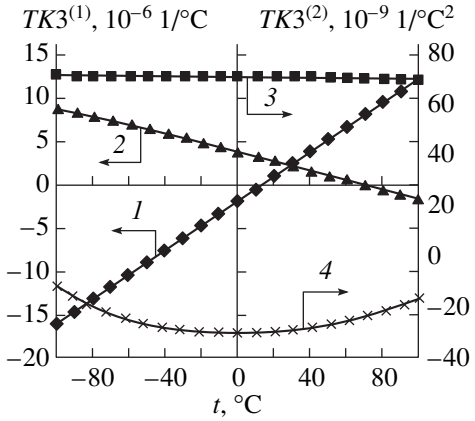

Fig. 4. Temperature dependences of (*1*, *2*) $TCD^{(1)}$ and (*3*, *4*) $TCD^{(2)}$ for two layered structures: Al (h/λ = 0.005) + (0, 140°, 22.5°) LGS and Al (h/λ = 0.005) + (0, 138.5°, 23°) LGN.

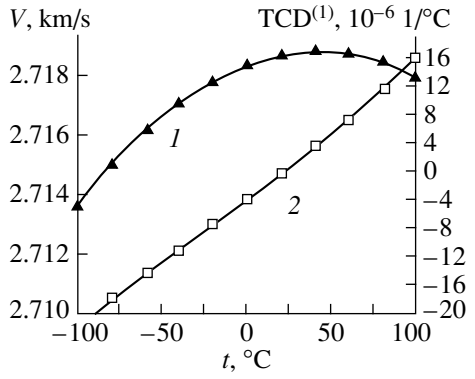

Fig. 5. Temperature dependences of (*1*) the velocity V and (*2*) the coefficient $TCD^{(1)}$ for SAW propagating in the Al (h/λ = 0.003) + (10°, 150°, 37°) LGN layered structure.

with increasing film thickness. For $h/\lambda = 0.01$, we have $TCD^{(1)} = 4 \times 10^{-6}$ 1/°C.

Figure 4 presents the temperature dependences of $TCD^{(1)}$ and $TCD^{(2)}$ for SAW in the following layered structures: an aluminum layer (h/λ = 0.005) and an LGS crystal with the (0, 140°, 22.5°) orientation (curves *1*, *3*); an aluminum layer (h/λ = 0.005) and an LGN crystal with the (0, 138.5°, 23°) orientation (curves *2*, *4*). One can see that, as the operating temperature varies from –100 to +100°C, the value of $TCD^{(1)}$ for the LGS crystal (curve *1*) varies from -15×10^{-6} to $+13 \times 10^{-6}$ 1/°C and becomes zero at a temperature of 10°C. In this case, the presence of the aluminum film on the crystal surface leads to a decrease in the temperature at which $TCD^{(1)}$ becomes zero. At the same time, the value of $TCD^{(2)}$ (curve *3*) varies insignificantly and is about $+70 \times 10^{-9}$ 1/°C^2. For an LGN crystal, the value of $TCD^{(1)}$ (curve *2*) varies from $+8 \times 10^{-6}$ to -2×10^{-6} 1/°C and becomes zero at a temperature of 50°C. The corresponding value of $TCD^{(2)}$ (curve *4*) varies from -30×10^{-9} to -10×10^{-9} 1/°C^2.

Figure 5 shows the temperature dependences of the velocity V and the coefficient $TCD^{(1)}$ for SAW in the presence of a thin aluminum film (h/λ = 0.003) on the surface of an LGN crystal with the (10°, 150°, 37°) orientation. The dependence of the SAW velocity (curve *1*) on temperature has the form of a parabola. The dependence of $TCD^{(1)}$ (curve *2*) on temperature is linear. We note that, for the given orientation of the LGN crystal without an aluminum film on its surface, the main characteristics of SAW at t_0 = 25°C are as follows: the SAW velocity V = 2.721 km/s, the coefficient of electromechanical coupling K^2 = 0.418%, $TCD^{(1)} = -2.4 \times 10^{-6}$ 1/°C, $TCD^{(2)} = 123 \times 10^{-9}$ 1/°C^2, the angle between the phase and group velocities PFA = –6.9°, and the anisotropy coefficient γ = –0.9. From Fig. 5, one can see that, at room temperature, in the presence of the aluminum film (h/λ = 0.003), the temperature coefficient of delay for SAW becomes lower: $TCD_s^{(1)} = -0.4 \times 10^{-6}$ 1/°C. In addition, the numerical calculation shows that the second-order temperature coefficient of delay for SAW propagating in the layered structure is also lower: $TCD_s^{(2)} \approx 11 \times 10^{-9}$ 1/°C^2. Thus, the presence of a thin aluminum film of a given thickness (h/λ = 0.003) on the surface of an LGN crystal with the (10°, 150°, 37°) orientation provides a temperature stabilization of this crystal cut.

CONCLUSION

As a result of the numerical analysis of the temperature characteristics of SAW propagating in LGS and LGN crystals, we have shown that the temperature dependences of the material constants of these crystals are strongly nonlinear, unlike the case of a quartz crystal. For some orientations of LGS and LGN crystals, we

calculated the values of the first- and second-order temperature coefficients of delay ($TCD^{(1)}$ and $TCD^{(2)}$) for SAW in a wide temperature range.

For a layered structure formed by a metal film and an underlying piezoelectric crystal, we demonstrated the changes that occur in the velocity of SAW and in the temperature coefficient of delay with varying thickness of the metal film and with varying operating temperature. It was shown that, in the presence of a thin aluminum layer of certain thickness on the surface of an LGN crystal, it is possible to achieve a better thermal stability of SAW in some propagation directions.

REFERENCES

1. I. B. Yakovkin, R. M. Taziev, and A. S. Kozlov, in *Proceedings of the IEEE Ultrasonics Symposium, 1995*, p. 389.
2. M. Yu. Dvoesherstov, in *Proceedings of the IV IEEE International Symposium on Ultrasonics, Ferroelectrics, and Frequency Control, St. Petersburg, 1998*, p. 149.
3. A. I. Morozov, V. V. Proklov, and B. A. Stankovskiĭ, *Piezoelectric Transducers for Electronic Devices* (Radio i Svyaz', Moscow, 1981).
4. Y. Shimizu, A. Tarazaki, and T. Sakaue, in *Proceedings of the IEEE Ultrasonics Symposium, 1976*, p. 519.
5. *Acoustic Surface Waves*, Ed. by A. A. Oliner (Springer, New York, 1978; Mir, Moscow, 1981).
6. A. J. Slobodnik, Jr., IEEE Trans. Sonics Ultrason. **SU-20** (4), 315 (1973).
7. D. F. Wiliams and F. Y. Cho, in *Proceedings of the IEEE Ultrasonics Symposium, 1979*, p. 627.
8. S. Sarharov, P. Senushencov, A. Medvedev, and Yu. Pisarevsky, in *Proceedings of the IEEE Frequency Control Symposium, 1995*, p. 647.
9. K. Inoue and K. Sato, Jpn. J. Appl. Phys., Part 1 **37** (5B), 2909 (1998) Part 1.
10. A. Bungo, C. Jian, K. Yamaguchi, *et al.*, in *Proceedings of the IEEE Ultrasonics Symposium*, 1999, p. 1.
11. Yu. Pisarevsky, P. Senushencov, P. Popov, and B. Mill, in *Proceedings of the IEEE Frequency Control Symposium, 1995*, p. 653.
12. I. Ya. Ashbel', M. Yu. Dvoesherstov, and S. G. Petrov, Akust. Zh. **36**, 360 (1990) [Sov. Phys. Acoust. **36**, 196 (1990)].
13. T. E. Parker, J. Appl. Phys. **50** (3), 1360 (1979).

Translated by E. Golyamina

Technical Physics, Vol. 46, No. 4, 2001, pp. 456–459. Translated from Zhurnal Tekhnicheskoĭ Fiziki, Vol. 71, No. 4, 2001, pp. 95–98.

RADIOPHYSICS

Slow Electromagnetic Waves in Tangentially Magnetized Ferromagnetic Films

S. V. Grishin and Yu. P. Sharaevskiĭ

Chernyshevsky State University, Saratov, 410026 Russia

e-mail: sharaevskyyp@info.sgu.ru

Received March 13, 2000

Abstract—Dispersion and energy characteristics of slow volume electromagnetic waves in tangentially magnetized ferromagnetic films are computed in a rigorous manner. For a wave that experiences anomalous dispersion and propagates with the external magnetostatic field, distinguishing features of the energy-flux velocity and the ratio of the electric to the magnetic energy density as functions of the wave number are noted. A marked contrast between these results and those obtained within the magnetostatic approximation is revealed for a wide range of wave numbers. © *2001 MAIK "Nauka/Interperiodica".*

It is common practice to rely on the magnetostatic approximation (MSA) when evaluating the main properties (such as dispersion and group velocity) of slow electromagnetic propagation in thin ferromagnetic films. The slow waves that can be treated within the MSA are called magnetostatic waves [1, 2].

The MSA provides a useful framework for computing the dispersion diagrams of slow waves in a single layer and even in thin-film ferrite/dielectric multilayers for different directions of the external magnetic field, as evidenced by experiments (see, e.g., [3]). Also, attempts are being made to apply this approach to energy-related properties: energy density, power-flux density, and energy-flow velocity [4–7]. However, the results may be in contradiction to rigorous electromagnetic theory in some real cases. For example, a rigorous analysis of normally magnetized metal/ferrite/dielectric structures indicates that the energy-flux density of a slow wave is aligned with the wave vector [8], whereas the MSA implies that the energy-flux densities in the ferrite and the dielectric have opposite directions [7].

This paper presents a theoretical investigation into the dispersion and energy characteristics of slow electromagnetic waves in tangentially magnetized ferromagnetic films. The results are contrasted with the MSA data. We address the simplest case: the structure under study is a ferromagnetic layer bounded by two metallic films and exposed to a uniform external magnetostatic field. In this context, the complete system of Maxwell's equations yields a dispersion relation written in an analytic form for different alignments of the magnetostatic field, and validity conditions can be formulated for the MSA [9].

The structure is sketched in Fig. 1. The thickness of the ferromagnetic layer is denoted by d. The external magnetostatic field $\mathbf{H}_0$ is aligned with the Z-axis, and the ferromagnetic layer is magnetized to saturation. The plane electromagnetic waves propagate in the Z direction.

Under the stated conditions, the volume electromagnetic waves obey the dispersion relation [9, 10]

$$\begin{aligned} -k_y^2[\mu k_y^2 + (1+\mu)k^2 - (\mu^2 + \mu - \mu_a^2)k_0^2\varepsilon] \\ = k^4 - 2\mu k^2 k_0^2 \varepsilon + (\mu^2 - \mu_a^2)k_0^4\varepsilon^2, \end{aligned} \quad (1)$$

where k is the wave number; $k_0 = \omega/c$, with $\omega = 2\pi f$ being the angular frequency and c being the speed of light in free space; ε is the relative permittivity of the medium; $k_y = n\pi/d$, with n being the mode number; and μ and μ_a are the variables that determine the rf permeability tensor. Furthermore, $\mu = [\omega_H(\omega_H + \omega_M) - \omega^2]/(\omega_H^2 - \omega^2)$ and $\mu_a = \omega_M\omega/(\omega_H^2 - \omega^2)$, where $\omega_H = \gamma H_0$ and $\omega_M = 4\pi\gamma M_0$, with M_0 and γ being the saturation magnetization and the magnetomechanical ratio, respectively [2].

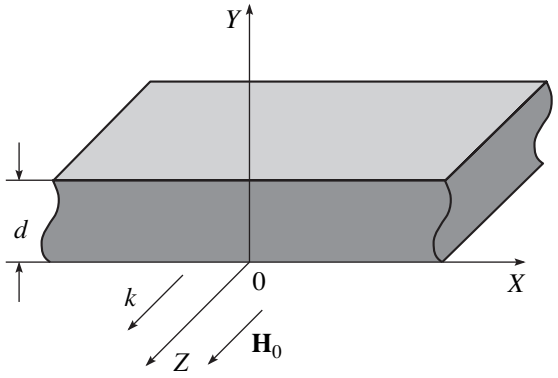

Fig. 1. Schematic diagram of the structure under study.

1063-7842/01/4604-0456$21.00

Dispersion relation (1) is built around a polynomial in f of the sixth degree. The solution to the relation consists of three branches. Two of them represent fast electromagnetic waves (with $k \sim k_0$), whereas the third one corresponds to a slow wave, which is a magnetostatic wave if $k \gg k_0$ [1, 2].

Relation (1) allows us to determine the group velocity $\mathbf{V}_g$ of the wave. In the general case, group velocity is expressed as

$$\mathbf{V}_g = \nabla_k \omega(k) \tag{2}$$

and is regarded as the velocity of a wave packet (i.e., a group of waves) [11, 12]. Equation (2) applies to isotropic dispersive media with gentle dispersion curves for both normal and anomalous dispersion [13] provided that the spectrum of the wave packet is not too wide. If the media "are free from absorption and such phenomena as the rotation of the plane of polarization [12]," the group velocity can be compared to the energy-flux velocity $\mathbf{V}_E$, i.e., $\mathbf{V}_g = \mathbf{V}_E$. In particular, this equality is true of arbitrary profile guiding structures filled with a low-loss isotropic dielectric, as demonstrated in [14]. The two velocities may differ for anisotropic gyromagnetic dispersive media that exhibit rotation of the polarization plane if the external magnetostatic field is applied in certain directions [12].

Figure 2 refers to a slow volume electromagnetic wave with $n = 1$. It shows dispersion curves and the dependences of the component of V_g on the normalized wave number $K = k/k_0\sqrt{\varepsilon}$, with K evaluating the extent to which the wave is slowed down. The computation was based on relation (1) for yttrium–iron garnet ($4\pi\gamma M_0 = 1780$ G) with $H_0 = 890$ Oe and $\varepsilon = 16$. Figure 2a indicates that the wave is affected by anomalous dispersion. For this reason, it is called a magnetostatic backward volume wave. We found that, over the entire range of K, both the dispersion curves and the group-velocity diagrams in Fig. 2 behave in exactly the same fashion as those obtained within the MSA for the values of d in hand.

The complete system of Maxwell's equations written for anisotropic gyromagnetic media yields the field amplitudes of waves in the structure:

$$e_{0x} = \frac{1}{kk_y\mu_a}\{[\mu(k_y^2 + k^2) - (\mu^2 - \mu_a^2)k_0^2\varepsilon]A\cos k_y y + [\mu k^2 - (\mu^2 - \mu_a^2)k_0^2\varepsilon]G\},$$

$$e_{0z} = A\sin k_y y,$$

$$h_{0z} = i\frac{\mu(k_y^2 + k^2) - (\mu^2 - \mu_a^2)k_0^2\varepsilon}{kk_0\mu_a}A\sin k_y y, \tag{3}$$

$$e_{0y} = -i\frac{k}{k_y}(A\cos k_y y + G), \quad h_{0x} = i\frac{k_0\varepsilon}{k_y}(A\cos k_y y + G),$$

$$h_{0y} = \frac{1}{\mu_a k_y k_0}[(k_y^2 + k^2 - \mu k_0^2\varepsilon)A\cos k_y y + (k^2 - \mu k_0^2\varepsilon)G],$$

where

$$G = H\frac{\mu(k_y^2 + k^2) - (\mu^2 - \mu_a^2)k_0^2\varepsilon}{\mu k^2 - (\mu^2 - \mu_a^2)k_0^2\varepsilon}A,$$

$$H = \begin{cases} -1 & \text{at} \quad y = 0 \\ -(-1)^n & \text{at} \quad y = d, \end{cases}$$

and A is an arbitrary constant.

The time and the space averages of the energy-flux density $\mathbf{P}$ and the electromagnetic energy density W are

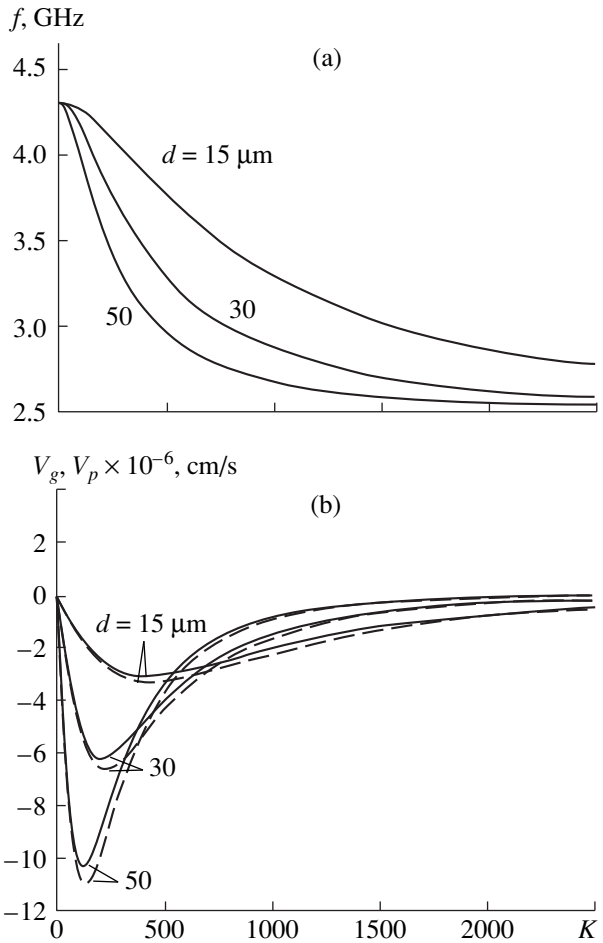

Fig. 2. (a) Dispersion curves and (b) velocity characteristics of a backward slow volume electromagnetic wave. In Fig. 2b, the solid curves refer to the group velocity computed with the rigorous and the MSA approach (they yield the same results) and the dashed curves represent the energy-flux velocity computed within the MSA.

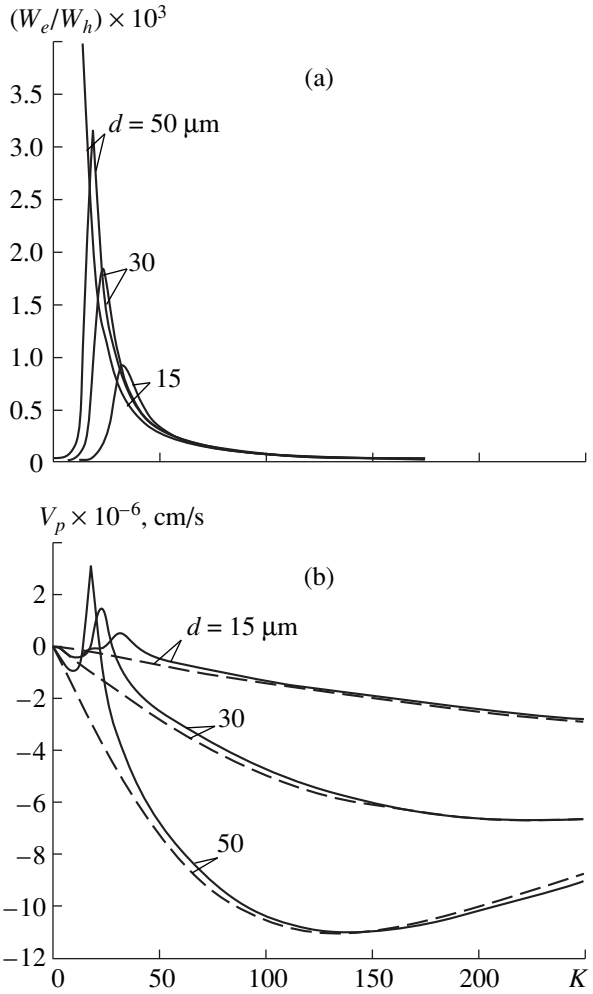

Fig. 3. Energy characteristics of a backward slow volume electromagnetic wave: (a) the energy-density ratio W_e/W_h and (b) the energy-flux velocity as functions of the normalized wave number. The solid curves refer to the rigorous approach, whereas the dashed ones are computed within the MSA.

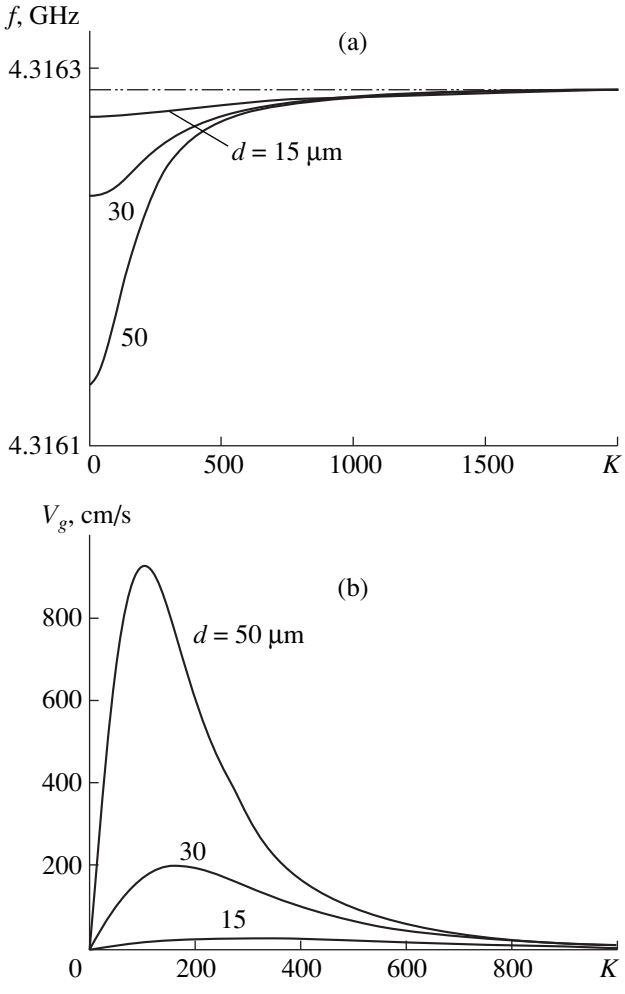

Fig. 4. (a) Dispersion curves and (b) group velocity characteristics of a forward slow volume electromagnetic wave.

computed from the formulas

$$\mathbf{P} = \frac{c}{8\pi V}\int_V \mathrm{Re}[\mathbf{eh}^*]dV, \qquad (4)$$

$$W = \frac{1}{16\pi V}\int_V \mathrm{Re}\left\{\mathbf{e}\frac{\partial(\omega\overleftrightarrow{\varepsilon}^*)}{\partial\omega}\mathbf{e}^* + \mathbf{h}\frac{\partial(\omega\overleftrightarrow{\mu}^*)}{\partial\omega}\mathbf{h}^*\right\}dV, \qquad (5)$$

where $\overleftrightarrow{\varepsilon}^*$ is the permittivity tensor (it is a scalar quantity in this context), V is the volume-to-area ratio of the ferromagnetic structure, and * denotes complex conjugation [15]. Formulas (4) and (5) apply to lossless anisotropic dispersive media.

Using (3) and (4), one can show that **P** has a unique nonzero component, namely, P_z.

Figures 3a and 3b, respectively, depict computed values of W_e/W_h and those of the z-component of $\mathbf{V}_E = \mathbf{P}/W$ as functions of K for backward slow volume electromagnetic waves, where W_e and W_h are the average energy densities for the electric and magnetic fields respectively. The solid curves refer to the rigorous approach based on formulas (1) and (3)–(5), whereas the dashed curves are obtained within the MSA. We see that the rigorous density curves have a pronounced peak (Fig. 3a), which shifts toward larger K ($K > 30$) as d decreases ($d < 50$ μm). In contrast, all of the MSA density curves go to infinity for small K at any d. With a given d, the two types of density curves are the same only if K is large enough ($K > 100$). Qualitative agreement between them is reached at a certain threshold K value, which lies where the rigorous curve reaches its maximum.

The rigorous velocity curves (Fig. 3b) also have pronounced peaks. With a given d, the peaking region is the same as that for the density curve (Fig. 3a). The

presence of a peak in the velocity curves implies that $\mathbf{V}_E$ switches to the opposite direction, although the dispersion remains anomalous. This fact is important, because the analysis of magnetostatic backward volume waves in various ferromagnetic structures yields that $\mathbf{V}_E$ is always opposite in direction to the phase velocity (see dashed curves in Fig. 3b) [2, 4]. Note that the peculiarities of the rigorous velocity curves stem from the features of the W_e–K and W_h–K characteristics only: the behavior of the dispersion curves (Fig. 2a) has no effect on the velocity curves.

Now, let us revert to Fig. 2. As expected, the respective MSA curves for V_g and V_E coincide within the frequency ranges where the dispersion curve levels out (at $K < 100$ or $K > 2000$). If $100 < K < 2000$, then V_g and V_E differ due to significant dispersion. In contrast, the rigorous approach yields that the difference exists even for $K < 100$, as evidenced by the pronounced peak in the behavior of the energy-flux velocity (compare the solid curves in Fig. 2b with those in Fig. 3b). The discrepancy between the two types of velocity characteristic for longitudinal magnetization can be explained by the fact that the slow electromagnetic wave experiences a rotation of the polarization plane as it propagates in a ferromagnetic medium [10]. This factor was highlighted, e.g., in [12].

Finally, we consider the case where the wave travels normally to $\mathbf{H}_0$ (transverse magnetization). Figure 4a demonstrates that the slow volume electromagnetic wave possesses weak normal dispersion, with which the group and phase velocities have the same direction [2] (see also Fig. 4b). There is no rotation of the polarization plane under this type of magnetization [10]. Figure 4b suggests that $V_g = V_E$ for any K, with the group velocity being computed from formula (2). Also notice that the MSA dispersion curve is a straight line for any d (see the dashed line in Fig. 4a). For this curve, $V_g = V_E = 0$.

In summary, the MSA is inapplicable to the energy characteristics of backward slow volume electromagnetic waves in longitudinally magnetized ferromagnetic films, since the results directly contradict the rigorous approach. If $K < 100$, a deviation arises in the behavior of both the energy-density ratio and the energy-flux velocity. For the latter quantity, the MSA yields incorrect values even with $K > 100$, in complete contrast to what is commonly anticipated [2].

The findings presented here may be useful for both unraveling wave phenomena in anisotropic multilayers and computing the characteristics of microwave devices utilizing spin waves.

ACKNOWLEDGMENTS

This study was conducted as part of the program "Universities of Russia: Basic-Research Projects" (grant no. 283).

REFERENCES

1. R. W. Damon and J. P. Eshbach, Phys. Chem. Solids **19** (3/4), 308 (1961).
2. A. V. Vashkovskiĭ, V. S. Stal'makhov, and Yu. P. Sharaevskiĭ, *Magnetostatic Waves in Ultrahigh Frequencies Electronics* (Saratovs. Gos. Univ., Saratov, 1993).
3. A. N. Slavin and Yu. K. Fetisov, Zh. Tekh. Fiz. **58**, 2210 (1988) [Sov. Phys. Tech. Phys. **33**, 1343 (1988)].
4. K. V. Grechushkin, A. V. Stal'makhov, and V. A. Tyulyukin, Radiotekh. Élektron. (Moscow) **21** (8), 1487 (1986).
5. A. V. Vashkovskiĭ, A. B. Valyavskiĭ, A. V. Stal'makhov, and V. A. Tyulyukin, Radiotekh. Élektron. (Moscow) **32** (11), 2450 (1987).
6. Yu. K. Fetisov and V. L. Preobrazhenskiĭ, Zh. Tekh. Fiz. **57** (3), 564 (1987) [Sov. Phys. Tech. Phys. **32**, 341 (1987)].
7. S. S. Gapta, IEEE Trans. Magn. **MAG-18** (6), 1639 (1982).
8. Ya. D. Golovko, I. V. Zavislyak, V. I. Kostenko, and M. A. Sigal, Fiz. Tverd. Tela (Leningrad) **29**, 3492 (1987) [Sov. Phys. Solid State **29**, 2004 (1987)].
9. Yu. P. Sharaevskiĭ and S. V. Grishin, *Problems of Applied Physic. Interuniversity Scientific Collection* (Saratovs. Gos. Univ., Saratov, 1998), No. 4, pp. 85–88.
10. A. L. Mikaélyan, *Theory and Application of Ferrites at Ultrahigh Frequencies* (Gosénergoizdat, Moscow, 1963).
11. L. Brillouin, *Wave Propagation in Periodic Structures* (Dover, New York, 1953; Inostrannaya Literatura, Moscow, 1959).
12. L. M. Mandel'shtam, *Full Collection of Works* (Akad. Nauk SSSR, Moscow, 1950), Vol. 5.
13. M. A. Biot, Phys. Rev. **105** (4), 1129 (1957).
14. L. de Broglie, *Problémes de propagations guidées des ondes électromagnétiques* (Gauthier-Villars, Paris, 1941; Inostrannaya Literatura, Moscow, 1948).
15. L. D. Landau and E. M. Lifshitz, *Course of Theoretical Physics*, Vol. 8: *Electrodynamics of Continuous Media* (Nauka, Moscow, 1982; Pergamon, New York, 1984).

Translated by A. Sharshakov

Technical Physics, Vol. 46, No. 4, 2001, pp. 460–462. Translated from Zhurnal Tekhnicheskoĭ Fiziki, Vol. 71, No. 4, 2001, pp. 99–101.

RADIOPHYSICS

Microwave Pulse Compression in a Chain of Ring-Type Resonators

Yu. Yu. Danilov* and M. L. Taĭ**

** Institute of Applied Physics, Russian Academy of Sciences, Nizhni Novgorod, 603600 Russia*

*** Nizhni Novgorod State University, Nizhni Novgorod, 603600 Russia*

e-mail: danilov@appl.sci-nnov.ru

Received May 22, 2000

Abstract—Compression of a rectangular chirp-pulse waveform by a chain of nondissipative ring-type resonators is studied theoretically. A three-resonator chain is shown to be capable of compressing a microwave pulse by a factor of 8 with an almost 80% efficiency. *© 2001 MAIK "Nauka/Interperiodica".*

INTRODUCTION

Efficiency of single-resonator microwave pulse compressors diminishes with increasing compression ratio [1–3]. For example, at a compression ratio of 5, the efficiency is 80%. To increase the compression, it was proposed to use a system of resonators [4]. In this paper, we study pulse compressors in the form of a chain of ring-type resonators, one possible design of which is illustrated in Fig. 1.

EQUATION OF THE COMPRESSOR AND ITS CHARACTERISTICS

Transformation of a microwave pulse

$$E = \mathrm{Re}\{E_n(t)\exp(i\omega_g t)\}$$

by a chain of N nondissipative resonators is described by the system of equations

$$\frac{dE_n}{dt} - i\Omega_n E_n = \frac{dE_{n-1}}{dt} - i\Omega_n^* E_{n-1} \quad (1 \le n \le N), \quad (1)$$

where $\Omega_n = \omega_n'(1 + i/2Q_n) - \omega_g$ is the mismatch between the complex eigenfrequency of the nth resonator and the carrier frequency of the input pulse, ω_g; Q_n is the radiation Q factor of the nth resonator; E_n is the complex amplitude of the pulse at the output of the nth resonator; and E_0 and E_N are the complex amplitudes of the pulse at the input and output of the pulse compressor, respectively.

In our calculations, we consider a pulse with a rectangular envelope of duration T with the phase modulation specified by the three-parameter function

$$E_0(t) = \exp\left\{i\left[\frac{\mu t^2}{2} + \Delta\varphi H(t - t_p)\right]\right\},$$

where H is the Heaviside function, μ is the pulse frequency-versus-delay slope, and t_p and $\Delta\varphi$ are the instant and magnitude of the phase step.

Since the compressor is intended to operate with linear particle accelerators, we will characterize its performance by the pulse compression ratio

$$s = \frac{T}{\tau}, \quad (2)$$

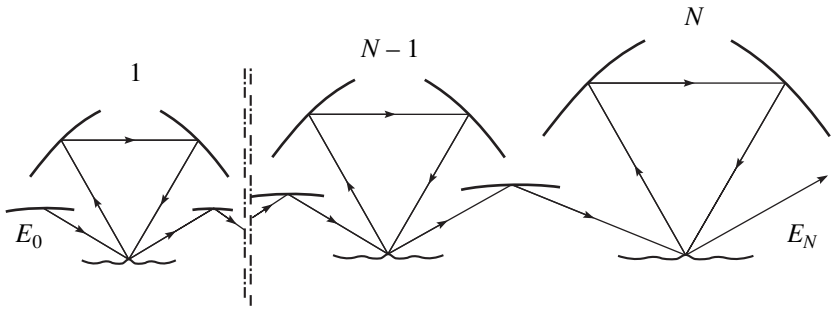

Fig. 1. Microwave pulse compressor in the form of a chain of ring-type resonators.

1063-7842/01/4604-0460$21.00 © 2001 MAIK "Nauka/Interperiodica"

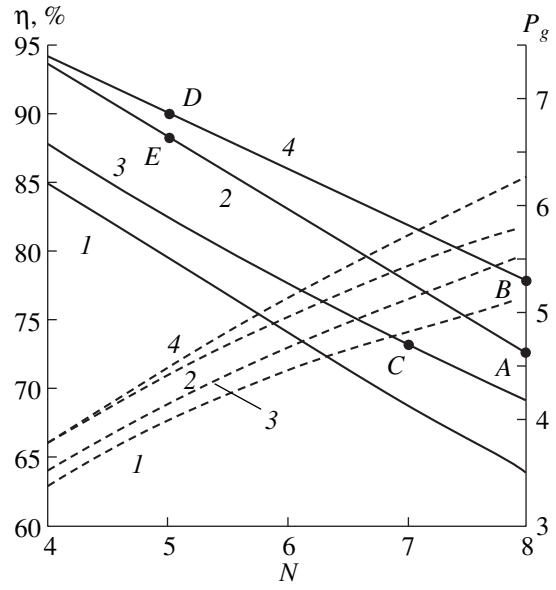

Fig. 2. Characteristics of optimized pulse compressors. Efficiency η (solid lines) and power gain (dashed lines) P_g versus compression ratio *s*.

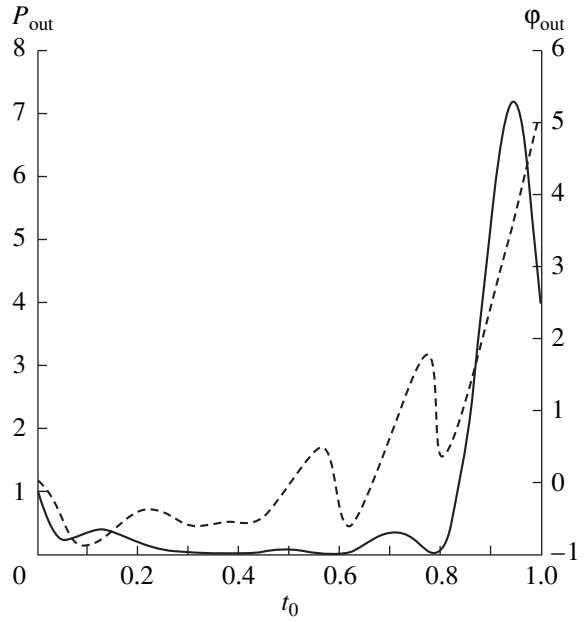

Fig. 3. Power (solid lines) and phase (dashed lines) of the output pulse versus dimensionless time for version *A* in Fig. 2.

efficiency

$$\eta = \frac{\int_{T-\tau}^{T} |E_N|^2 dt}{\int_0^T |E_0|^2 dt}, \qquad (3)$$

and power gain

$$P_g = s\eta,$$

where $\tau = L/v_{gr}$, L is the length of the accelerating structure, and v_{gr} is the group velocity of the wave in the structure.

In the framework of the problem stated above, the efficiency is a function $\eta(\alpha, \delta, \Delta\varphi, \beta_n, \gamma_n)$ of dimensionless parameters

$$\alpha = \frac{\mu T^2}{2}, \quad \delta = \frac{t_p}{T},$$

$$\beta_n = (\omega_n' - \omega_g)T, \quad \gamma_n = \frac{\omega_n' T}{2Q_n} \quad (1 \le n \le N).$$

METHOD OF NUMERICAL ANALYSIS

Equations (1) were solved by Runge–Kutta integration. The maximum of efficiency (3) at a given compression ratio (2) was searched for by the modified Hooke–Jeeves method [5], which performed well in simulations of various microwave devices [6, 7].

For pulse compressors considered in this work, the optimization time on a Pentium-166 MHz computer did not exceed 1.5 min, which corresponded to calculating the goal function 15000 times. The major difficulty stemmed from multiextremal behavior of efficiency (3), which may also be significant in the practical implementation of the pulse compressor.

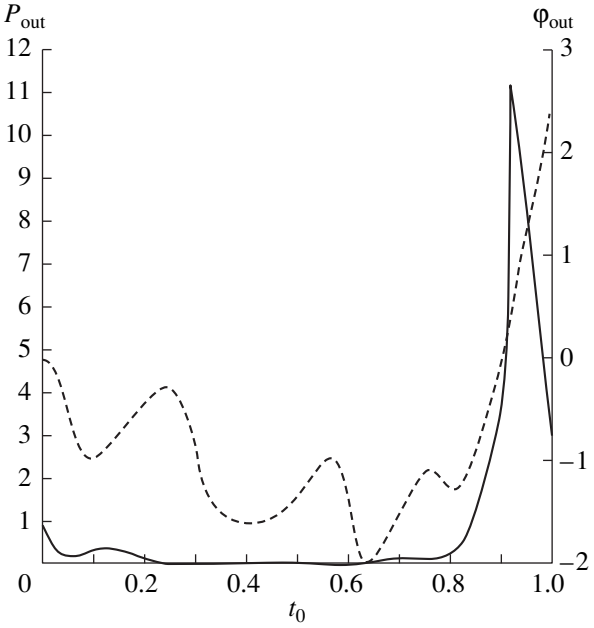

Fig. 4. Same as in Fig. 3 for version *B* in Fig. 2.

Table 1. Parameters of optimized pulse compressors for versions *A*, *B*, *C*, *D*, and *E* in Fig. 2

Version	α	δ	$\Delta\varphi$	β_1	γ_1	β_2	γ_2	β_3	γ_3
A	24.2	–	–	8.65	1.86	16.0	2.67	27.0	4.15
B	20.3	0.909	1.46	5.51	1.54	13.1	2.27	24.3	5.11
C	9.15	0.858	1.89	0.63	1.24	8.71	2.86	–	–
D	17.1	0.921	1.02	1.35	1.82	8.69	2.98	16.8	5.67
E	18.2	–	–	1.26	1.93	8.37	2.88	16.6	4.24

Table 2. Regions of robustness of optimized pulse-compressor parameters for versions *A*, *B*, *C*, *D*, and *E* in Fig. 2

Version	α, %	δ, %	$\Delta\varphi$, %	β_1, %	γ_1, %	β_2, %	γ_2, %	β_3, %	γ_3, %
A	+2	–	–	+7	+38	+4	+24	+3	+19
	–2	–	–	–7	–29	–4	–21	–3	–17
B	+2	+3	+25	+11	+38	+4	+24	+4	+19
	–2	–3	–24	–11	–31	–4	–21	–4	–16
C	+4	+2	+15	+85	+36	+7	+19	–	–
	–4	–(<1)	–15	–84	–30	–7	–17	–	–
D	+3	+4	+39	+50	+42	+7	+22	+6	+17
	–3	–4	–40	–55	–31	–7	–19	–6	–15
E	+3	–	–	+58	+45	+8	+23	+5	+17
	–3	–	–	–60	–33	–8	–20	–5	–15

RESULTS OF SIMULATIONS

Figure 2 plots the efficiency and power gain versus compression ratio for the following optimized systems: (*1*) single-resonator compressor with a phase-reversal pulse; (*2*) three-resonator compressor with a chirp (linearly swept) pulse; (*3*) two-resonator compressor with a chirp phase-reversal pulse; and (*4*) three-resonator compressor with a chirp phase-reversal pulse.

Figures 3 and 4 show the power P_{out} and phase φ_{out} of the output pulse versus dimensionless time for versions *A* and *B* in Fig. 2.

Table 1 lists parameters of the input pulse and resonators for five versions *A*, *B*, *C*, *D*, and *E* illustrated in Fig. 2. Table 2 summarizes ranges of parameters within which the efficiency falls by no greater than 1%. The most critical parameters are the frequency-versus-delay slope and the instant of the phase reversal in the input pulse.

CONCLUSION

Robustness of the optimum parameters of resonators in the pulse compressor diminishes with increasing number of resonators. Therefore, when implementing the compressor in practice, one should presumably restrict the design to two or three resonators. It is likely that the efficiency can be increased by applying a more complicated phase modulation rule to the input pulse.

ACKNOWLEDGMENTS

The authors are grateful to M.I. Petelin for his constant interest in the work and stimulating discussions. We thank A.M. Sterlin for providing us with an optimization program and acknowledge I.S. Gel'fer and D.A. Donskikh for their help and consultation in programming.

This work was supported by the International Science Foundation (grant nos. NOT 000 and NOT 300) and the Russian Foundation for Basic Research (project no. 99-02-17781).

REFERENCES

1. P. B. Wilson, *Application of High-Power Microwaves*, Ed. by A. V. Gaponov-Grekhov and V. Granatstein (Artech House, Boston, 1994), pp. 229–317.
2. Z. D. Farcas, H. A. Hogg, G. A. Loew, and P. B. Wilson, in *Proceedings of the 9th Conference on High Energy Accelerator, SLAC, Stanford, 1974*, p. 576.
3. V. E. Balakin and I. V. Syrachev, in *Proceedings of the III European Particle Accelerator Conference, Berlin, 1992*, p. 1173.
4. M. I. Petelin and M. L. Tai, AIP Conf. Proc. **337**, 303 (1995).
5. B. D. Bunday, *Basic Optimisation Methods* (Edward Arnold, London, 1984; Radio i Svyaz', Moscow, 1988).
6. K. C. Gupta, R. Garg, and R. Chadha, *Computer-Aided Design of Microwave Circuits* (Artech, Dedham, 1981; Radio i Svyaz', Moscow, 1987).
7. M. B. Manuilov, Radiotekh. Élektron. (Moscow) **45** (1), 55 (2000).

Translated by A. Khzmalyan

Technical Physics, Vol. 46, No. 4, 2001, pp. 463–465. Translated from Zhurnal Tekhnicheskoĭ Fiziki, Vol. 71, No. 4, 2001, pp. 102–104.

Exchange Self-Polarization of an Electron Beam

E. V. Orlenko and B. G. Matisov

St. Petersburg State Technical University, Politekhnicheskaya ul. 29, St. Petersburg, 195251 Russia

e-mail: quark@citadel.stu.neva.ru

Received January 26, 2000

Abstract—Self-organization of a beam of free electrons injected by an optical cathode is discussed. It is shown that exchange interaction may cause beam self-polarization in a vacuum and sustain beam polarization in the material. © *2001 MAIK "Nauka/Interperiodica".*

(1) The effect of optical orientation of electron spins in semiconductors is widely used in atomic and molecular physics, condensed-matter physics [1], nuclear physics, and elementary-particle physics [2]. Generation of spin-oriented carriers by absorption of circularly polarized light was first suggested in [3, 4]. The optical orientation phenomenon has been studied in detail [5]; yet, there is no consensus on mechanisms behind high polarization of the beam [6, 7].

The basic mechanism of generation of polarized electrons is photoemission in GaAs thin strained epitaxial layers. Under biaxial strain, the $p_{3/2}$ multiplet in the valence band is split into two pairs of sublevels in such a way that the state of one pair turns out to be below the Fermi energy (light holes), while that of the other pair lies above the Fermi energy (heavy holes). This results in changes in the occupancy of these sublevels. A circularly polarized photon causes the transition to the *s* state of the conduction band with a preferential orientation of the spin projection onto the selected axis of symmetry. Thus, the illumination of cubic GaAs crystals by light with clockwise circular polarization generates a high density of polarized electrons. The use of special surface-activating Cs + O (or Cs + F) films, together with band bending, may increase the fraction of polarized photoelectrons to 83–90%.

Theoretically, this phenomenon is studied by simulating classical electron outdiffusion. Quantum transport [6, 7] and collective quantum events are usually rejected, but spin relaxation mechanisms are taken into account. These mechanisms merit detailed consideration just because spin polarization is a possibility. With regard for such a high degree of electron beam polarization observed in experiments, there obviously should be a mechanism (or mechanisms) that is responsible for spin coorientation. In this case, the coupling constant must far exceed the constants of interactions that cause spin breakdown. For example, any possible self-polarization mechanism must stand up to severe competition with the Bir–Aronov–Pikus mechanism of spin relaxation [8], which has the interaction constant proportional to the exchange splitting of the exciton state energy, about 50 μeV. In this case, the spin relaxation time is about a hundredth of the spin breakdown time in spin–orbital interaction by the Elliott–Jassett mechanism [9], which is much shorter than the electron lifetime. Therefore, the Bir–Aronov–Pikus mechanism effectively destroys the spin. Another breakdown mechanism, which is related to spin splitting of the conduction band, is the D'yakonov–Perel' mechanism [10]. This splitting is akin to the case when the effective magnetic field whose direction depends on the momentum direction acts on the spin. For spin–orbital interaction, the characteristic energy of band splitting is $\hbar\Omega = (32/21)^{1/2}\alpha(T^3/E_g)^{1/2}$. Here, E_g is the energy gap, α is a factor proportional to the orbital quantum number, and T is temperature in terms of energy. This mechanism becomes essential at large electron energies.

In this work, we consider a possible mechanism of spin polarization in an electron beam. This mechanism continues to act when the electrons propagate in a vacuum. Such an interaction, which causes spin ordering, is of Coulomb exchange type, i.e., is similar to electron interaction in the conduction band, and the effect of spin polarization is analogous to free electron ferromagnetism. In this case, the exchange interaction constant greatly exceeds those of any of the relaxation mechanisms mentioned above.

(2) With regard for interaction of the electron beam with all bonded electrons of impurity atoms, the Heisenberg parameter can be calculated within the exchange perturbation theory (EPT) [11], which has specially been developed for analysis of magnetic systems. In terms of the EPT, the first-order correction to the energy is given by [11]

$$E^{(1)} = \langle \Phi(r_1, r_2)|\hat{V}|\Psi(r_1, r_2)\rangle, \qquad (1)$$

where $\hat{V}$ is the operator that describes Coulomb electron–electron interaction, Φ is the ordinary product of the coordinate parts of the single-electron wave functions, and Ψ is the coordinate part of a wave function antisymmetrized with respect to electron permutations.

1063-7842/01/4604-0463$21.00

For beam electrons, the waves are plane; then, the correction to the energy can be rewritten as $E^{(1)} = K \pm A$ or

$$E^{(1)} = K - \frac{A}{2} - 2A\hat{\mathbf{s}}_1 \cdot \hat{\mathbf{s}}_2, \tag{2}$$

where

$$K = \int \frac{e^2}{|\mathbf{r}_1 - \mathbf{r}_2|} d^3r_1 d^3r_2,$$

$$A = \int \frac{\exp(i(\mathbf{k}_1\mathbf{r}_1 + \mathbf{k}_2\mathbf{r}_2 - \mathbf{k}_1\mathbf{r}_2 - \mathbf{k}_2\mathbf{r}_1))}{|\mathbf{r}_1 - \mathbf{r}_2|} d^3r_1 d^3r_2 \frac{e^2}{\Omega^2}.$$

Here, $1/\Omega^2$ is a factor normalizing to the total number of particles in the beam.

The exchange contribution we are interested in (which is responsible for spin correlation in the beam) is

$$A(q) = \frac{e^2 n^{2/3}}{2\pi}\sigma(q),$$

where $q = |\mathbf{k}_1 - \mathbf{k}_2|$, δ is the Dirac delta function, and n is the electron concentration in the beam. It is evident that $q \geq 2\pi\hbar/L$, where L is the film thickness. Only in this sense must the delta function be perceived.

Now, we average the exchange interaction over the energy spread of electrons generated by a radiation the spectral line of which has the Lorentz-type width. Since the frequency interval $\Delta\omega$ related to the spectral line width is proportional to the momentum spread, $\hbar\Delta\omega \simeq \hbar^2 kq/m$, one can write

$$\langle A \rangle = \int A(q) \frac{\alpha}{1 + (\alpha q)^2} dq = \frac{e^2}{2\pi} n^{2/3} \alpha, \tag{3}$$

where $\alpha = \hbar k\tau/m$ and τ^{-1} is the spectral line width. The value of α coincides with the diffusion mean free path by the order of magnitude.

Hence, $\langle A \rangle$ depends on the intensity of incident light causing the valence-to-conduction band electron transition. Let $n \sim \alpha^{-3} \sim n_{\text{dop}} = 3 \times 10^{18}$ cm^{-3}; then,

$$\langle A \rangle = \frac{1}{2\pi} \frac{e^2}{a_B} \left(\frac{a_B}{\alpha}\right) \sim \frac{1}{\pi} E_B \times 10^{-2} \sim 10^{-14} \text{ erg},$$

and the Heisenberg parameter $j = 2A$, where A is taken in view of the averaging. Thus, the constant of interaction responsible for spin coorientation is relatively large, and spin correlation may survive even for a heated cathode.

(3) Let the unit vector $\mathbf{m}$ indicate the spontaneous moment direction. The energy of the particles depends on spin orientation about $\mathbf{m}$ and, therefore, can be expressed as [12]

$$\varepsilon(p, \mathbf{s}) = \varepsilon_0(p) - b(p)\hat{\mathbf{s}} \cdot \mathbf{m}. \tag{4}$$

According to this formula, the energy of an electron with the spin projection parallel to $\mathbf{m}$ is $\varepsilon_0 - b$; accordingly, the equilibrium distribution function is $n(\varepsilon_0 - b) = n_\uparrow$. For the opposite spin projection, we have $\varepsilon_0 + b$ and $n(\varepsilon_0 + b) = n_\downarrow$, respectively. At appropriate spin orientations, the eigenvalues $n_\uparrow$ and $n_\downarrow$ are those of the operator

$$\hat{n}_0(\mathbf{p}, \hat{\mathbf{s}}) = \frac{1}{2}(n_\uparrow + n_\downarrow) + (n_\uparrow - n_\downarrow)\hat{\mathbf{s}} \cdot \mathbf{m}, \tag{5}$$

which is the equilibrium density matrix. The spontaneous spin coorientation of degree $\bar{\sigma} \sim b/\varepsilon_F$ for degenerate gas and $\bar{\sigma} \sim b/T$ for nondegenerate gas is provided by the Boltzmann factor due to a shift of the light and heavy hole states relative to the Fermi level. For the three-dimensional case, the Fermi level is given by

$$\varepsilon_{F\pm} = \varepsilon_F(1 \pm \bar{\sigma})^{2/3}. \tag{6}$$

Replacing ± 1 by the operator

$$\hat{p} = \frac{1}{2}(1 + 4\hat{\mathbf{s}} \cdot \hat{\mathbf{s}}'),$$

whose eigenvalues are ± 1 at the appropriate spin coorientation, we obtain

$$\varepsilon_{F\pm} = \varepsilon_F\left(1 + \frac{\bar{\sigma}}{2} + 2\bar{\sigma}\hat{\mathbf{s}} \cdot \hat{\mathbf{s}}'\right)^{2/3}. \tag{7}$$

Exchange interaction also makes a contribution to the effective energy per particle; the corresponding operator has the form

$$\hat{\varepsilon}_{\text{exc}} = -j\hat{\mathbf{s}} \cdot \hat{\mathbf{s}}'.$$

Thus, the Fermi distribution function can be written in the form of the density matrix for the spin variable:

$$\hat{n}_F = \frac{1}{\exp[(\varepsilon - j\hat{\mathbf{s}} \cdot \hat{\mathbf{s}}' - \varepsilon_{F\pm})/T] + 1}. \tag{8}$$

Since $\bar{\sigma} < 1$, (7) can be expanded as

$$\varepsilon_{F\pm} = \varepsilon_F\left(1 + \frac{\bar{\sigma}}{3} + \frac{4}{3}\bar{\sigma}\hat{\mathbf{s}} \cdot \hat{\mathbf{s}}'\right).$$

Then, operator (8) can be expressed as

$$\hat{n}_F = n_F^0 = \hat{f}\frac{\partial n_F^0}{\partial \varepsilon}, \tag{9}$$

where n_F^0 is the Fermi distribution function without corrections to the kinetic energy and the Fermi energy and $\hat{f}$ is an analog of the Landau function [9]:

$$\hat{f} = \frac{1}{Sp\int \hat{n}_0(\mathbf{p}, \hat{\mathbf{s}}) d^3p}\left[\frac{\Delta}{2} + (2\Delta + j)\hat{\mathbf{s}} \cdot \hat{\mathbf{s}}'\right]. \tag{10}$$

In GaAs, the conduction band lies above the Fermi energy; hence, the distribution function for the elec-

trons is the Boltzmann function:

$$n_\uparrow - n_\downarrow = n_0\exp(-b/T) - n_0\exp(b/T), \tag{11}$$

where $n_0 = e^{\frac{\mu-\varepsilon}{T}}$ and μ is the chemical potential of classical perfect gas.

In this case,

$$\begin{aligned} &Sp\int \hat{n}_0(\mathbf{p}, \hat{\mathbf{s}})d^3p \\ &= n_0\exp(-b/T) + n_0\exp(b/T) = 2\cosh\frac{b}{T}. \end{aligned} \tag{12}$$

Due to exchange effects, there is a certain relationship between (4) and (10). It can be established if we consider [9] how the electron energy changes when the vector $\mathbf{m}$ rotates through an angle $\delta\theta$. We have $\delta\mathbf{m} = [\delta\boldsymbol{\theta} \times \mathbf{m}]$ and, according to (4),

$$\delta\varepsilon = -b[\mathbf{m} \times \hat{\mathbf{s}}]\delta\boldsymbol{\theta}, \tag{13}$$

where brackets mean vector product.

However, a change in $\mathbf{m}$ causes a change in the distribution function (5),

$$\delta\hat{n}_0(\mathbf{p}, \hat{\mathbf{s}}) = \frac{1}{2}(n_\uparrow - n_\downarrow)[\mathbf{m} \times \hat{\mathbf{s}}]\delta\boldsymbol{\theta}, \tag{14}$$

and in the energy,

$$\begin{aligned} \delta\varepsilon &= Tr_{s'}\int \hat{f}\delta\hat{n}_0(\mathbf{p}', \hat{\mathbf{s}}')d^3p' \\ &= Tr_{s'}\int\frac{1}{2}\hat{f}(n_\uparrow - n_\downarrow)[\mathbf{m} \times \hat{\mathbf{s}}']\delta\boldsymbol{\theta}d^3p'. \end{aligned} \tag{15}$$

Equating (13) and (15) at an arbitrary $\delta\theta$, we come to the expression for conduction-band electrons:

$$-b[\mathbf{m} \times \hat{\mathbf{s}}] = \frac{Tr_{s'}\int\frac{1}{2}\left(\frac{\Delta}{2} + (2D + j)\hat{\mathbf{s}}\hat{\mathbf{s}}'\right)(n_\uparrow - n_\downarrow)[\mathbf{m} \times \hat{\mathbf{s}}']d^3p}{Sp\int \hat{n}_0(\mathbf{p}, \hat{\mathbf{s}})d^3p}.$$

Substituting (11) and (12) into this expression and taking the trace yields

$$-b[\mathbf{m} \times \hat{\mathbf{s}}] = -\frac{\sinh(b/T)}{\cosh(b/T)}\frac{1}{2}(2\Delta + j) \tag{16}$$

or

$$\begin{aligned} &b = \tanh(b/T)\frac{2\Delta + j}{2}, \quad \frac{2b}{2\Delta + j} = \tanh\frac{b}{T}, \\ &\frac{b}{T}\frac{T}{\Delta + j/2} = \tanh\frac{b}{T}, \quad \bar{\sigma}\frac{T}{\Delta + j/2} = \tanh\bar{\sigma}. \end{aligned} \tag{17}$$

Eventually, we arrive at transcendental equation (17), which has a nonzero solution ($b \neq 0$) if the coefficient $T/(\Delta + j/2)$ is less than unity. Thus, both deformation splitting Δ and exchange interaction j favor spontaneous spin coorientation; at $(\Delta + j/2) > T$, the second-order transition takes place in the system that sets polarization with $\sigma \longrightarrow 1$. The values of Δ and j are of the same order of magnitude: $\Delta_1 = 50$ meV $= 8 \times 10^{-13}$ erg (for GaAs) and $\Delta_2 = 25$ meV $= 4 \times 10^{-13}$ erg (for GaAsP) [13]. For both materials, $j = (10–25) \times 10^{-14}$ erg. One can conclude that the exchange interaction is a significant factor in inducing spontaneous polarization in the electron beam. Such an effect might be interpreted as ferromagnetic enhancement of the spin polarization in the beam. The mechanisms responsible for spin polarization breakdown that were mentioned above cannot have a severe impact on a self-polarized system, because their interaction constants are two orders of magnitude lower than the constants of spin structure ordering. Such is an explanation of most available experimental data for spin-polarized beams.

ACKNOWLEDGMENTS

We thank B. Oskotskiĭ for submission of experimental findings.

This work was supported by the Russian Foundation for Basic Research (grant no. 99-02-17076).

REFERENCES

1. C. Siegmann, J. Phys: Condens. Matter **4** (44), 8395 (1992).
2. C. Y. Prescott, W. B. Atwood, and R. L. A. Gottrell, Phys. Lett. B **77B** (3), 347 (1978); C. Y. Prescott, W. B. Atwood, and R. L. A. Gottrell, Phys. Lett. B **84B** (4), 524 (1979).
3. E. Garwin, T. Pierce, and H. C. Siegmann, Helv. Phys. Acta **74**, 393 (1974).
4. G. Lampel and C. Weibush, Solid State Commun. **16** (7), 877 (1975).
5. *Optical Orientation*, Ed. by F. Meier and B. P. Zakharchenya (North-Holland, Amsterdam, 1984; Nauka, Leningrad, 1989).
6. L. G. Gerchikov, B. D. Oskotskii, and A. V. Subashiev, Phys. Rev. B **50** (20), 15416 (1994).
7. A. V. Subashiev, Yu. A. Mamaev, Yu. P. Yashin, and J. E. Clenderin, Phys. Low-Dimens. Struct. **1** (1), 1 (1999).
8. G. L. Bir, A. G. Aronov, and G. E. Pikus, Zh. Éksp. Teor. Fiz. **69** (4), 1382 (1975) [Sov. Phys. JETP **42**, 705 (1975)].
9. R. J. Elliott, Phys. Rev. **96** (1), 266 (1954); J. R. Jassett, Solid State Phys. **14** (1), 1 (1963).
10. M. I. D'yakonov and V. I. Perel', Fiz. Tverd. Tela (Leningrad) **13** (12), 3581 (1971) [Sov. Phys. Solid State **13**, 3023 (1972)].
11. E. V. Orlenko and A. A. Rumyantsev, Zh. Éksp. Teor. Fiz. **97** (2), 439 (1990) [Sov. Phys. JETP **70**, 244 (1990)]; E. V. Orlenko and T. Yu. Latyshevskaya, Zh. Éksp. Teor. Fiz. **113** (6), 2129 (1998) [JETP **86**, 1167 (1998)].
12. A. A. Abrikosov, *Fundamentals of the Theory of Metals* (Nauka, Moscow, 1987; North-Holland, Amsterdam, 1988).
13. R. Mair, SLAC-Report No. 488 (1996).

Translated by V. Isaakyan

Technical Physics, Vol. 46, No. 4, 2001, pp. 466–471. Translated from Zhurnal Tekhnicheskoĭ Fiziki, Vol. 71, No. 4, 2001, pp. 105–110.

ELECTRON AND ION BEAMS, ACCELERATORS

Computation of the Third-Order Matrizant for a Sectorial Electrostatic Field

S. N. Mordik and A. G. Ponomarev

Institute of Applied Physics, National Academy of Sciences of Ukraine, Sumy, 244030 Ukraine

Received May 12, 2000

Abstract—It is suggested to study the ion–optical properties of sectorial electrostatic charged-particle analyzers with the matrizant technique. The matrizants can effectively be used in investigating beam dynamics in sectorial electrostatic fields with consideration for edge effects within rectangular and smooth field models. © *2001 MAIK "Nauka/Interperiodica".*

Many modern techniques for investigating solids and plasmas are based on the examination of the mass and energy spectra of charged particles. Electrostatic and magnetic analyzers are common investigation facilities in this field. In studying the ion–optical properties of charged particle analyzers, matrix techniques for solving equations of beam motion in electric and magnetic fields of various configurations have found wide acceptance. For example, a matrix technique is used in the well-known TRANSPORT numerical code [1]. Its refined version makes it possible to analyze beam transport in accelerating static and magnetic arrangements with starting equations of motion approximated up to the third order. This code lacks an element like an electrostatic toroidal sectorial capacitor and, hence, cannot be applied to designing double-focusing mass analyzers, where this element is present.

In this work, we derived an analytical expression for the third-order matrizant of the sectorial electrostatic field of a toroidal capacitor with consideration for edge effects using the method of matrizants [2, 3]. The specific case of this matrizant is the transfer matrix in ray optics. The resulting matrix $P^{(3)}$ can be used for both numerical (using the shuttle-sum method [4]) and analytical (using the method of matrizants within a rectangular field model) determination of third-order aberration coefficients for phase variables. Information on these aberration coefficients is contained in the upper four rows of the matrizant derived by analytically or numerically solving a set of differential equations of motion for charged particles. The use of conservative methods for matrizant computation (at each step of computation, the phase volume remains unchanged) would refine conditions for charged particle transport through ion–optical systems.

Let us introduce a natural coordinate system x, y, s related to an arbitrary plane curve that is uniquely defined by the radius of curvature ρ. Such a system completely coincides with Brown's system [5]. A Cartesian system $\tilde{x}$, $\tilde{y}$, $\tilde{z}$ with the origin at the starting point of an axial particle and the natural coordinate system with the origin at the center of curvature of the reference-particle path are related as

$$\tilde{x} = (x + \rho)\cos(s/\rho) - \rho, \quad \tilde{y} = y,$$
$$\tilde{z} = (x + \rho)\sin(s/\rho).$$

Consider nonrelativistic motion of the particles. Since the Lame coefficients for our coordinate system are $h_1 = 1$, $h_2 = 1$, and $h_3 = 1 + x/\rho$, trajectory equations can be written as [6]

$$x'' + \frac{GT'}{\vartheta}x' - \frac{h_3}{\rho} = \frac{q(T')^2}{m\vartheta^2}E_x,$$
$$y'' + \frac{GT'}{\vartheta}y' = \frac{q(T')^2}{m\vartheta^2}E_y, \tag{1}$$
$$G = \frac{d}{ds}\left(\frac{\vartheta}{T'}\right) = \frac{q}{mh_3}\frac{T'E_s}{\vartheta} + -\frac{2\vartheta x'}{T'h_3\rho};$$
$$T' = \sqrt{h_3^2 + x'^2 + y'^2};$$

where a prime means differentiation with respect to s; T is the absolute value of the increment of the trajectory length when all the coordinates increase simultaneously; and ϑ, m, and q are the velocity, mass, and charge of a particle, respectively.

Let us define ϑ^2 as a function of the potential increment at any point relative to the potential at points of the central path:

$$\vartheta^2 = \frac{p_0^2}{m_0^2}\left((1 + \mu^2) - \frac{\Delta U_x}{U_0}\right), \tag{2}$$

where ϑ is the velocity of a particle of mass $m = m_0$ that has a momentum spread $\mu = \Delta p/p_0$; ΔU_x is the potential difference between a point $M(x, y, s)$ of the ion trajectory and points on the axis $x = 0$, $y = 0$; and U_0 is the accelerating voltage of an ion source.

With regard for the symmetry condition, third-order expansions in series for the potential $V(x, y, s)$ and strength $\mathbf{E}(x, y, z)$ of the electric field near the axial path are given by

$$V(x, y, z) = V_{10}(s)x + \frac{1}{2}V_{20}(s)x^2 + \frac{1}{6}V_{30}(s)x^3 + \frac{1}{24}V_{40}(s)x^4 + \frac{1}{2}V_{02}(s)y^2 + \frac{1}{2}V_{12}(s)xy^2 + \frac{1}{4}V_{22}(s)x^2y^2,$$

$$E_x(s) = V_{10}(s) + V_{20}(s)x + \frac{1}{2}V_{30}(s)x^2 + \frac{1}{6}V_{40}(s)x^3 + \frac{1}{2}V_{12}(s)y^2 + \frac{1}{2}V_{22}(s)xy^2, \quad (3)$$

$$E_y(s) = V_{02}(s)y + V_{12}(s)xy + \frac{1}{2}V_{22}(s)x^2y,$$

$$E_s(s) = \frac{1}{h_3^3}\left(V'_{10}(s)x + \frac{1}{2}V'_{20}(s)x^2 + \frac{1}{3!}V'_{30}(s)x^3 + \frac{1}{2}V'_{02}(s)y^2 + \frac{1}{2}V'_{12}(s)xy^2\right).$$

Taking into account that the electric potential V must meet the Laplace equation $\Delta V = 0$ and that the relationship

$$E_x(x, 0, s) = E_0(s)\frac{\rho}{\rho + xa_e + x}\frac{a_e}{} \text{ [7]}$$

must be satisfied for a toroidal capacitor, we come to expressions for the potential components near the axial path up to the third order:

$$V_{10}(s) = E_0(s), \quad V_{20}(s) = E_0(s)(-g - h),$$
$$V_{30}(s) = E_0(s)(g^2 + hg + h^2),$$
$$V_{40}(s) = 6E_0(s)(-g^3 - hg^2 - h^2g - h^3), \quad (4)$$
$$V_{02}(s) = E_0(s)g, \quad V_{12}(s) = E_0(s)(-2g^2 - hg) - E'_0(s),$$
$$V_{22}(s) = E_0(s)(6g^3 + 4hg^2 + 2h^2g) + E'_0(s)(g + 5h),$$

where $h = 1/\rho$, $g = 1/a_e$, and a_e is the radius of curvature of the toroidal capacitor electrodes.

We did not consider the case of small electrode deformations, which may affect the toroidal capacitor potential [8]. The electrostatic field strength can be expressed as

$$E_0(\tau) = \breve{E}_0\Theta(\tau). \quad (5)$$

For the rectangular field model,

$$\Theta(\tau) = u_+(\tau - s_0) - u_+(s - \tau), \quad (6)$$

where $u_+(t)$ is the step function [9] that satisfies the conditions

$$\frac{d}{dt}u_+(t) = \delta_+(t),$$

$$\int_{a+0}^{b} \varphi(\tau)\delta_+(\tau - t)d\tau = \begin{cases} 0 & t < a, \quad t \geq b \\ \varphi(t + 0) & a \leq t < b, \end{cases}$$

$$\int_{a+0}^{b} \varphi(\tau)\delta_+^{(r)}(\tau - t)d\tau = \begin{cases} 0 & t < a, \quad t \geq b \\ (-1)^r\varphi^{(r)}(t + 0) & a \leq t < b. \end{cases}$$

For the smooth field model,

$$\Theta(\tau) = \begin{cases} 1 & s_1 \leq \tau < s_2 \\ 0 & \tau < s_0, \ \tau > s \\ \dfrac{1}{1 + eC_0 + C_1\tau + C_2\tau^2 + C_3\tau^3} & s_0 \leq \tau < s_1 \\ 1 - \dfrac{1}{1 + eC_4 + C_5\tau + C_6\tau^2 + C_7\tau^3} & s_0 \leq \tau \leq s. \end{cases} \quad (7)$$

The points s_1 and s_2 specify the boundaries of scattered fields. The smooth model is a fairly good approximation of the actual longitudinal field distribution. In particular, it includes the effect of scattered fields on beam dynamics in a specific ion–optical system.

To solve the trajectory equations, we apply the method of embedding in the phase moment space [2]. Let the third-order phase moments be defined as $\hat{Q}^{(3)} = \{x, x', y, y', x^2, xx', x'^2, y^2, yy', y'^2, xy, x'y, xy', x'y', x^3, x^2x', xx'^2, x'^3, xy^2, xyy', xy'^2, x'y^2, x'yy', xy'^2, y^3, y^2y', yy'^2, y'^3, yx^2, yxx', yx'^2, y'x^2, y'xx', y'x'^2\}$.

In matrix form, trajectory equations (1) can be written as

$$\frac{d}{ds}(\tilde{\hat{Q}}^{(3)}) = P^{(3)}(s)\tilde{\hat{Q}}^{(3)}. \quad (8)$$

On rearrangement, we obtain the matrix $P^{(3)}$:

$$P^{(3)} = \begin{Bmatrix} P^{1.1} & 0 & P^{1.3} & P^{1.4} & 0 & P^{1.6} & P^{1.7} & 0 & 0 \\ 0 & P^{2.2} & 0 & 0 & P^{2.5} & 0 & 0 & P^{2.8} & P^{2.9} \\ 0 & 0 & P^{3.3} & 0 & 0 & P^{3.6} & P^{3.7} & 0 & 0 \\ 0 & 0 & 0 & P^{4.4} & 0 & 0 & P^{4.7} & 0 & 0 \\ 0 & 0 & 0 & 0 & P^{5.5} & 0 & 0 & P^{5.8} & P^{5.9} \\ 0 & 0 & 0 & 0 & 0 & P^{6.6} & 0 & 0 & 0 \\ 0 & 0 & 0 & 0 & 0 & 0 & P^{7.7} & 0 & 0 \\ 0 & 0 & 0 & 0 & 0 & 0 & 0 & P^{8.8} & 0 \\ 0 & 0 & 0 & 0 & 0 & 0 & 0 & 0 & P^{9.9} \end{Bmatrix},$$

$$P^{1.1} = \begin{Bmatrix} 0 & 1 \\ -k & 0 \end{Bmatrix}, \quad P^{1.3} = \begin{Bmatrix} 0 & 0 & 0 \\ -h^3n^2 - h^3 & he_1 & h \end{Bmatrix},$$

$$P^{1.4} = \left\{ \begin{array}{cc} 0 & 0\ 0 \\ \frac{h}{2}e_2 + h^3\left(n^2 - \frac{7}{2}n + 3\right) & 0\ -h \end{array} \right\},$$

$$P^{1.6} = \left\{ \begin{array}{cccc} 0 & 0 & 0 & 0 \\ h^4\left(-n^3 + \frac{4}{3}n^2 - \frac{8}{3}n + \frac{1}{3}\right) & \frac{1}{2}e_2h^2(n-3) & -h^2(n+1) & 0 \end{array} \right\},$$

$$P^{1.7} = \left\{ \begin{array}{ccccc} 0 & 0 & 0 & 0 & 0\ 0 \\ \frac{h^2}{2}e_2(n-1) + h^4(3n^3 - 13n^2 + 19n + 3) & 0 & h^2(1-n) & e_2h^2\left(1 - \frac{1}{2}n\right) & 0\ 0 \end{array} \right\},$$

$$P^{2.2} = \left\{ \begin{array}{cc} 0 & 1 \\ -f & 0 \end{array} \right\}, \quad P^{2.5} = \left\{ \begin{array}{cccc} 0 & 0 & 0 & 0 \\ e_2h + h^3(2n^2 - 5n + 2) & e_1h & 0 & 2h \end{array} \right\},$$

$$P^{2.8} = \left\{ \begin{array}{cccc} 0 & 0 & 0 & 0 \\ h^4(-n^2 + 4n - 4) & \frac{1}{2}e_2h^2(2-n) & h^2(n-2) & 0 \end{array} \right\},$$

$$P^{2.9} = \left\{ \begin{array}{ccccc} 0 & 0 & 0 & 0 & 0\ 0 \\ \frac{h^2}{2}e_2(n+1) + h^4(3n^3 - 11n^2 + 13n - 6) & 0 & h^2(n-2) & \frac{h^2}{2}e_2(n-3) & -2h^2\ 0 \end{array} \right\},$$

$$P^{3.3} = \left\{ \begin{array}{ccc} 0 & 2 & 0 \\ -k & 0 & 1 \\ 0 & -2k & 0 \end{array} \right\}, \quad P^{3.6} = \left\{ \begin{array}{cccc} 0 & 0 & 0 & 0 \\ -h^3(n^2+1) + 1 & e_1h & h & 0 \\ 0 & -2h^3(n^2+1) & 2e_1h & 2h \end{array} \right\},$$

$$P^{3.7} = \left\{ \begin{array}{ccccc} 0 & 0\ 0 & 0 & 0\ 0 \\ \frac{h}{2}e_2 + h^3\left(n^2 - \frac{7}{2}n + 3\right) & 0\ -h & 0 & 0\ 0 \\ 0 & 0\ 0 & he_2 + h^3(2n^2 - 7n + 6) & 0\ -2h \end{array} \right\},$$

$$P^{4.4} = \left\{ \begin{array}{ccc} 0 & 2 & 0 \\ -f & 0 & 1 \\ 0 & -2f & 0 \end{array} \right\}, \quad P^{5.5} = \left\{ \begin{array}{cccc} 0 & 1 & 1 & 0 \\ -f & 0 & 0 & 1 \\ -k & 0 & 0 & 1 \\ 0 & -k & -f & 0 \end{array} \right\},$$

$$P^{4.7} = \left\{ \begin{array}{ccccccc} 0 & 0 & 0 & 0 & 0 & 0 \\ he_2 + h^3(2n^2 - 5n + 2) & 0 & 0 & 0 & 2h & 0 \\ 0 & 2he_2 + h^3(4n^2 - 10n + 4) & 2he_1 & 0 & 0 & 4h \end{array} \right\},$$

$$P^{5.8} = \left\{ \begin{array}{cccc} 0 & 0 & 0 & 0 \\ 0 & 0 & 0 & 0 \\ \frac{h}{2}e_2 + h^3\left(n^2 - \frac{7}{2}n + 3\right) & 0 & -h & 0 \\ 0 & \frac{h}{2}e_2 + h^3\left(n^2 - \frac{7}{2}n + 3\right) & 0 & -h \end{array} \right\},$$

$$P^{5.9} = \left\{ \begin{array}{cccccc} 0 & 0 & 0 & 0 & 0 & 0 \\ he_2 + h^3(2n^2 - 5n + 2) & 0 & 0 & he_1 & 2h & 0 \\ -h^3(n^2 + 1) & he_1 & h & 0 & 0 & 0 \\ 0 & he_2 + h^3(2n^2 - 5n + 2) & 0 & -h^3(n^2 + 1) & 2he_1 & 3h \end{array} \right\},$$

$$P^{6.6} = \left\{ \begin{array}{cccc} 0 & 3 & 0 & 0 \\ -k & 0 & 2 & 0 \\ 0 & -2k & 0 & 1 \\ 0 & 0 & -3k & 0 \end{array} \right\},$$

$$P^{7.7} = \left\{ \begin{array}{cccccc} 0 & 2 & 0 & 1 & 0 & 0 \\ -f & 0 & 1 & 0 & 1 & 0 \\ 0 & -2f & 0 & 0 & 0 & 1 \\ -k & 0 & 0 & 0 & 2 & 0 \\ 0 & -k & 0 & -f & 0 & 1 \\ 0 & 0 & -k & 0 & -2f & 0 \end{array} \right\},$$

$$P^{8.8} = \left\{ \begin{array}{cccc} 0 & 3 & 0 & 0 \\ -f & 0 & 2 & 0 \\ 0 & -2f & 0 & 1 \\ 0 & 0 & -3f & 0 \end{array} \right\},$$

$$P^{9.9} = \left\{ \begin{array}{cccccc} 0 & 2 & 0 & 1 & 0 & 0 \\ -k & 0 & 1 & 0 & 1 & 0 \\ 0 & -2k & 0 & 0 & 0 & 1 \\ -f & 0 & 0 & 0 & 2 & 0 \\ 0 & -f & 0 & -k & 0 & 1 \\ 0 & 0 & -f & 0 & -2k & 0 \end{array} \right\}. \quad (9)$$

Here, $k = nh^2$, $n = 2 - \frac{g}{h}$, $f = \frac{g}{h}$, $e_1 = \frac{E_0'(s)}{\tilde{E}_0}$, and $e_2 = \frac{E_2''(s)}{\tilde{E}_0}$.

The solution to Eq. (8) is represented through the matrizant in the form

$$\tilde{\tilde{Q}} = X(P^{(3)}, s/s_0)\tilde{\tilde{Q}}_0. \quad (10)$$

The matrizant $X(P^{(3)}, s/s_0)$, as the matrix $P^{(3)}$ of coefficients, has a block–triangular structure,

$$X(P^{(3)}, s/s_0)$$

$$= \left\{ \begin{array}{ccccccccc} X^{1.1} & 0 & X^{1.3} & X^{1.4} & 0 & X^{1.6} & X^{1.7} & 0 & 0 \\ 0 & X^{2.2} & 0 & 0 & X^{2.5} & 0 & 0 & X^{2.8} & X^{2.9} \\ 0 & 0 & X^{3.3} & 0 & 0 & X^{3.6} & X^{3.7} & 0 & 0 \\ 0 & 0 & 0 & X^{4.4} & 0 & 0 & X^{4.7} & 0 & 0 \\ 0 & 0 & 0 & 0 & X^{5.5} & 0 & 0 & X^{5.8} & X^{5.9} \\ 0 & 0 & 0 & 0 & 0 & X^{6.6} & 0 & 0 & 0 \\ 0 & 0 & 0 & 0 & 0 & 0 & X^{7.7} & 0 & 0 \\ 0 & 0 & 0 & 0 & 0 & 0 & 0 & X^{8.8} & 0 \\ 0 & 0 & 0 & 0 & 0 & 0 & 0 & 0 & X^{9.9} \end{array} \right\},$$

and satisfies the differential equation

$$X'(P^{(3)}, s/s_0) = P^{(3)}X(P^{(3)}, s/s_0), \quad X(P^{(3)}, s_0/s_0) = I, \tag{11}$$

where I is the unit matrix.

Let $r_{i,j}$ be elements of the block matrix $X^{1.1}$ and $q_{i,j}$ be elements of the block matrix $X^{2.2}$; $i, j = 1, 2$. Then, for diagonal matrix blocks $X^{k,k}$ ($k = 2, 4, 5, \ldots, 9$), analytical solutions to Eq. (11) within the rectangular model are easy to obtain by straightforward algebraic manipulation. For example, for the x^2 row of the matrix block $X^{3.3}$,

$$x^2 = (r_{11}x_0 + r_{12}x_0')^2 = r_{11}^2x_0^2 + 2r_{11}r_{12}x_0x_0' + r_{12}^2x_0'^2, \tag{12}$$

we get $X_{1.1}^{3.3} = r_{11}^2$, $X_{1.2}^{3.3} = 2r_{11}r_{12}$, and $X_{1.3}^{3.3} = r_{12}^2$. For the off-diagonal blocks $X^{i,k}$ ($k > j$), the general formula [7]

$$X^{i,k}(s/s_0) = \sum_{j=1+i}^{k} \int_{s_0}^{s} X^{i,j}(s/\tau)P^{i,j}(\tau)X^{j,k}(\tau/s_0)d\tau \tag{13}$$

is valid.

For the rectangular model, the integrals in (13) can be taken by quadratures; hence, elements of the matrizant $X(P^{(3)}, s/s_0)$ will have an analytical form. For matrix (6), solutions to the equations

$$\frac{dX^{1.1}(s/s_0)}{ds} = P^{1.1}(s)X^{1.1}(s/s_0), \quad X^{1.1}(s_0/s_0) = I, \tag{14}$$

$$\frac{dX^{2.2}(s/s_0)}{ds} = P^{2.2}(s)X^{2.2}(s/s_0), \quad X^{2.2}(s_0/s_0) = I \tag{15}$$

can be written as

$$X^{1.1} = \begin{Vmatrix} r_{11} & r_{12} \\ r_{21} & r_{22} \end{Vmatrix} = \begin{Vmatrix} \cos(\sqrt{k}(s-s_0)) & \frac{1}{\sqrt{k}}\sin(\sqrt{k}(s-s_0)) \\ -\sqrt{k}\sin(\sqrt{k}(s-s_0)) & \cos(\sqrt{k}(s-s_0)) \end{Vmatrix}, \tag{16}$$

$$X^{2.2} = \begin{Vmatrix} q_{11} & q_{12} \\ q_{21} & q_{22} \end{Vmatrix} = \begin{Vmatrix} \cos(\sqrt{f}(s-s_0)) & \frac{1}{\sqrt{f}}\sin(\sqrt{f}(s-s_0)) \\ -\sqrt{f}\sin(\sqrt{f}(s-s_0)) & \cos(\sqrt{f}(s-s_0)) \end{Vmatrix}. \tag{17}$$

Then, for a cylindrical capacitor,

$$X^{2.2} = \begin{Vmatrix} q_{11} & q_{12} \\ q_{21} & q_{22} \end{Vmatrix} = \begin{Vmatrix} 1 & (s-s_0) \\ 0 & 1 \end{Vmatrix}. \tag{18}$$

Now we will obtain the second-order aberration coefficients $\hat{Q}_{x,x'}^{(2)} = \{x, x', x^2, xx', x'^2\}$ with respect to phase variables. To do this, it is first necessary to find elements of the matrix block $X^{1.3}(s/s_0) = \int_{s_0}^{s} X^{1.1}(s/\tau)P^{1.3}(\tau)X^{3.3}(\tau/s_0)d\tau$, where $X^{1.1}(s/\tau)$, $P^{1.3}(\tau)$, and $X^{3.3}(\tau/s_0)$ are determined from (16), (9), and (12), respectively.

The second-order transfer matrix for the phase variables $\hat{Q}_{x,x'}^{(2)}$ can be written as

$$M_{\hat{Q}_{x,x'}^{(2)}}(s/s_0) = \begin{Vmatrix} X^{1.1}(s/s_0) & X^{1.3}(s/s_0) \\ 0 & X^{3.3}(s/s_0) \end{Vmatrix}.$$

The second-order transfer matrix for the phase variables $\hat{Q}_{x,a}^{(2)}$ in the Cartesian system can be written as

$$R^{(2)}(s/s_0) = M_{\hat{Q}_{x,a}^{(2)}}(s/s_0) = A_{(x,y,s)\to(\tilde{x},\tilde{y},\tilde{z})}^{(2)} \times M_{\hat{Q}_{x,x'}^{(2)}}(s/s_0)A_{(\tilde{x},\tilde{y},\tilde{z})\to(x,y,s)}^{(2)}, \tag{19}$$

where

$$A_{(x,y,s)\to(\tilde{x},\tilde{y},\tilde{z})}^{(2)} = \begin{Vmatrix} 1 & 0 & 0 & 0 & 0 \\ 0 & 1 & 0 & -h & 0 \\ 0 & 0 & 1 & 0 & 0 \\ 0 & 0 & 0 & 1 & 0 \\ 0 & 0 & 0 & 0 & 1 \end{Vmatrix},$$

$$A_{(\tilde{x},\tilde{y},\tilde{z})\to(x,y,s)}^{(2)} = \begin{Vmatrix} 1 & 0 & 0 & 0 & 0 \\ 0 & 1 & 0 & h & 0 \\ 0 & 0 & 1 & 0 & 0 \\ 0 & 0 & 0 & 1 & 0 \\ 0 & 0 & 0 & 0 & 1 \end{Vmatrix}$$

are coordinate-transforming matrices, which are easily found from the boundary conditions

$$a = \frac{d\tilde{x}}{d\tilde{z}} = \frac{x'}{1+hx}, \quad b = \frac{d\tilde{y}}{d\tilde{z}} = \frac{y'}{1+hx}.$$

Thus, the second-order aberration coefficients for the rectangular field model have the form

$$\langle\tilde{x}|\tilde{x}^2\rangle = R_{1.5}^{(2)} = \frac{h}{3n}((-2+n-2n^2) + (1-2n+n^2)C + (1+n+n^2)C^2),$$

$$\langle\tilde{x}|\tilde{x}a\rangle = R_{1.6}^{(2)} = \frac{1}{3n^{3/2}}(2(1+n+n^2)SC + (-2+n-2n^2)S) + \zeta\left(\frac{1}{\sqrt{n}}S\right),$$

$$\langle\tilde{x}|a^2\rangle = R_{1.7}^{(2)} = -\frac{1}{3hn^2}((1-2n+n^2) + (-2+n-2n^2)C + (1+n+n^2)C^2),$$

$$\langle a|\tilde{x}^2\rangle = R_{2.5}^{(2)} = \frac{h^3}{3-\sqrt{n}}((-2+n-2n^2)SC + (-1+2n-n^2)S) + \zeta(h^2\sqrt{n}SC),$$

$$\langle a|\tilde{x}a\rangle = R_{2.6}^{(2)} = \frac{h}{3n}((-2+n-2n^2) + (-2+n-2n^2)C + (-2+4n+4n^2)C^2) + \zeta(h(C+S^2-C^2)),$$

$$\langle a|a^2\rangle = R_{2.7}^{(2)} = \frac{1}{3n^{3/2}}((2-n+2n^2)SC + (-2+n-2n^2)S) + \zeta\left(-\frac{h}{\sqrt{n}}SC\right),$$

where $S = \sin(\sqrt{k}(s-s_0))$, $C = \cos(\sqrt{k}(s-s_0))$, and $\zeta = 1$ if Eq. (6) is true. If ζ is set equal to zero [i.e., $E'(s) = 0$ and $E''(s) = 0$], we arrive at the equations [7, 9] that are widely used in designing ion–optical systems when the actual field is replaced by an idealized one equivalent in rotation to take into account scattered fields.

To derive the third-order transfer matrix for the phase variables $\hat{Q}^{(3)}_{x,x',y,y',\delta}$, we use the Cauchy formula

$$\hat{Q} = X(P, s/s_0)\hat{Q}_0 + \int_{s_0}^{s} X(P, s/\tau)\Psi(\tau)d\tau. \qquad (20)$$

In Cartesian coordinates, the third-order transfer matrix for the phase variables $\hat{Q}^{(3)}_{\tilde{x},a,\tilde{y},b,\delta}$ will have the form

$$R^{(3)}(s/s_0) = A^{(3)}_{(x,y,s)\to(\tilde{x},\tilde{y},\tilde{z})} \times M_{\hat{Q}^{(3)}_{x,x',y,y',\delta}}(s/s_0)A^{(3)}_{(\tilde{x},\tilde{y},\tilde{z})\to(x,y,s)}, \qquad (21)$$

where

$$M_{\hat{Q}^{(3)}_{x,x',y,y',\delta}}(s/s_0) = \left\{X(P^{(3)}, s/s_0), \int_{s_0}^{s} X(P^{(3)}, s/\tau)\Psi^{(3)}(\tau)d\tau\right\}$$

is the extended transfer matrix in the $\hat{Q}^{(3)}_{x,x',y,y',\delta}$ space.

The matrix block Ψ is determined by the method of embedding in the space of phase moments $\hat{Q}^{(3)} = \{\delta, x\delta, x'\delta, \delta^2, \ldots, \delta^3\}$.

Within the rectangular field model, the third-order aberration coefficients are given by

$$\langle\tilde{x}|\hat{Q}^{(3)}_{\tilde{x},a,\tilde{y},b,\delta}\rangle = R^{(3)}_{1,i}, \quad \langle a|\hat{Q}^{(3)}_{\tilde{x},a,\tilde{y},b,\delta}\rangle = R^{(3)}_{2,i}, \quad \langle\tilde{y}|\hat{Q}^{(3)}_{\tilde{x},a,\tilde{y},b,\delta}\rangle = R^{(3)}_{3,i}, \quad \langle b|\hat{Q}^{(3)}_{\tilde{x},a,\tilde{y},b,\delta}\rangle = R^{(3)}_{4,i}, \qquad (22)$$

where i is the serial number of a phase variable.

Thus, for the rectangular longitudinal distribution of the field of a toroidal sectorial capacitor, we derived analytical expressions for all matrizant elements and, hence, all third-order aberration coefficients. The expressions were obtained with consideration for edge effects. For a smooth longitudinal field distribution, the matrix $P^{(3)}$ of coefficients was found to compute the matrizant with the numerical shuttle-sum method with consideration for the edge effects.

REFERENCES

1. D. C. Carey, K. L. Brown, and F. Rothacher, Third-Order TRANSPORT with MAD Input. A. Computer Program for Designing Charged Particle Beam Transport Systems. SLAC-R-530. Fermilab-Pub-98-310 (1998).
2. A. D. Dymnikov and R. Hellbord, Nucl. Instrum. Methods Phys. Res. A **330**, 323 (1993).
3. A. D. Dymnikov *et al.*, Nucl. Instrum. Methods Phys. Res. A **403**, 195 (1998).
4. A. D. Dymnikov, Nucl. Instrum. Methods Phys. Res. A **363**, 435 (1995).
5. K. L. Brown *et al.*, Rev. Sci. Instrum. **35**, 481 (1964).
6. M. Szilagyi, *Electron and Ion Optics* (Plenum, New York, 1988; Mir, Moscow, 1990).
7. A. A. Sysoev and G. A. Samsonov, *Theory and Computation of Static Field Mass-Spectrometer*, Preprint MIFI (Moscow, 1972), Vols. 1, 2.
8. M. I. Yavor, Nucl. Instrum. Methods Phys. Res. A **298** (1–3), 223 (1998).
9. H. Hinterberger and L. A. Kenig, *Advances in Mass Spectrometry*, Ed. by J. D. Waldron (Pergamon, London, 1959; Inostrannaya Literatura, Moscow, 1963).

Translated by V. Isaakyan

Technical Physics, Vol. 46, No. 4, 2001, pp. 472–483. Translated from Zhurnal Tekhnicheskoĭ Fiziki, Vol. 71, No. 4, 2001, pp. 111–121.

ELECTRON AND ION BEAMS, ACCELERATORS

Dynamics of Electron Beams in Plasmas

A. S. Mustafaev

St. Petersburg State Mining Institute (Technical University), Vtoraya liniya 21, St. Petersburg, 199026 Russia

Received May 16, 2000

Abstract—The characteristic features of the relaxation of the energy and momentum distribution functions of the electrons in a plasma produced by a low-voltage beam discharge in helium are investigated. It is established that, contrary to widely held opinion, the energy of an intense electron beam may relax due to the wave excitation. The critical currents corresponding to a jumplike transition from one relaxation mechanism to another are measured. The density of metastable helium atoms is determined from the comparative analysis of theoretical and experimental results on the structure of the energy spectrum of the electrons of an intense beam. An intense electron beam is found to become more isotropic in the course of its interaction with Langmuir waves in a collisionless plasma. The cross section for quasi-elastic collisions between the electrons and Langmuir plasmons is estimated. The wave nature of the beam–plasma mechanism for the relaxation of the anisotropic electron energy distribution function is demonstrated, and the mechanism itself is shown to come into play when the discharge current exceeds a certain critical level. The experimental threshold criterion for the energy relaxation of an intense monoenergetic beam is obtained for the first time. It is shown that the relaxation occurs in two stages: the isotropization stage, in which the beam energy decreases insignificantly, is followed by the stage in which the beam relaxes to a state with a plateau-like energy distribution function. The threshold criterion for the relaxation of the anisotropic electron energy distribution function is universal in character regardless of the cause of anisotropy. © *2001 MAIK "Nauka/Interperiodica".*

1. INTRODUCTION

This paper is aimed at studying the dynamics of an electron beam in a plasma produced by a low-voltage beam discharge (LVBD) in helium. By the LVBD, we mean a discharge in which the electrons obey a nonequilibrium distribution function and are usually represented by two different groups: a group of slow (thermal) plasma electrons and a group of fast (nonequilibrium) beam electrons.

Low-voltage discharges in alkali-metal vapors have been investigated in great detail [1]. The physical properties of such discharges are shown to be governed by the relaxation of low-density electron beams in discharge plasmas [2–6]. There are two mechanisms for the relaxation of the electron distribution function (EDF): a collisional mechanism and a beam–plasma mechanism. The first mechanism was investigated for discharge plasmas in which the neutral gas pressure is sufficiently high, $l_{ea} \ll d$, where $l_{ea} = 1/N_a\sigma_{ea}^t$ is the mean free path of the beam electrons, d is the length of the discharge gap, N_a is the atom density, and σ_{ea}^t is the corresponding transport cross section. Under these conditions, the distribution function $f(z, \vartheta)$ of fast electrons is almost spherically symmetric (here, z is the distance from the cathode). Traditionally, the beam in such a plasma is assumed to relax due to binary collisions, while the relaxation of the beam by the waves that it itself excites in a discharge plasma is neglected.

The beam–plasma relaxation mechanism was studied under the conditions prevailing in Knudsen discharges, for which $l_{ea} > d$ and the distribution function $f(z, \vartheta)$ is anisotropic. The beam relaxes because it excites Langmuir waves [2–4, 7]. In this case, a substantial amount of the beam energy is converted into wave energy and the thermal plasma electrons are heated via the collisional damping of the excited waves.

LVBDs in noble gases have been less studied. These discharges differ markedly from beam discharges in alkali-metal vapors [8, 9]. Thus, in noble gases, in which the excitation and ionization potentials are both high, low-voltage discharges are characterized by the presence of an intense monoenergetic electron beam. In such discharges, the gas is ionized and the plasma current is transported by fast electrons rather than by thermal electrons, as is the case with discharges in alkali-metal vapors. Another distinctive feature of noble gases is that the transport cross section σ_{ea}^t for the scattering of thermal plasma electrons by the gas particles is very small; as a result, the collisional damping rate of Langmuir waves is slow. These circumstances govern the formation and relaxation of the anisotropic electron distribution functions over momenta and energies in the plasma of beam discharges in noble gases.

Knowledge of the regular features of the dynamics of electron beams in plasmas is important for developing a new class of devices in plasma electronics, specifically controlled general-purpose stabilizers [10, 11],

1063-7842/01/4604-0472$21.00

high-power sources of electromagnetic radiation, controlled key cell elements [1, 5, 12, 13], plasmochemical reactors [9, 14], and new types of energy sources capable of operating under extreme conditions (in a surrounding medium with high radiation levels and temperatures above 1000 K) [15].

A comprehensive study of the anisotropic EDF in the plasma of LVBDs in noble gases has shown that the model of an LVBD plasma can be used as a universal model of a low-temperature electrode plasma [6, 16].

2. EXPERIMENTAL DEVICE AND MEASUREMENT TECHNIQUE

The experiments were carried out in a device with flat circular electrodes [17]. A 0.15-cm-thick porous tungsten plate impregnated with barium–calcium aluminate served as a cathode, whose temperature was measured by W–Re microthermocouples and was controlled by a stabilizing unit to lie in the range 1000–1800 K (to ±10 K accuracy). The interelectrode gap was designed so as to ensure the symmetry of the discharge plasma about the device axis. The plasma column was such that its side boundary was a 1.1-cm-diameter conducting cylindrical surface held at the cathode potential. The distance between the electrodes varied from 0.1 to 2 cm. After the heat and vacuum treatment of the device, a residual working pressure of 10^{-9} torr was ensured. The pressure of chemically pure helium was controlled by a needle inlet valve in the range 10^{-1}–10^{1} torr.

In order to measure the EDF, a 30-μm-thick single-sided flat probe made of tantalum foil in the form of a disk 0.05 cm in diameter was introduced into the plasma through the side boundary. A 0.02-cm-diameter tantalum wire was welded to the probe. All of the conducting elements (including the conducting surface of the probe) were protected by an insulating Alundum coating. The probe installed at a three-coordinate micrometer system was moved at steps of ±0.1 mm along the discharge axis inside the interelectrode gap. The probe was oriented at angles from 0 to 180° to the device axis to within an error of ±1°. The error in the initial orientation of the probe did not exceed ±30′. The coordinates of the probe and its orientation were controlled by an eyepiece micrometer.

The single-sided flat probe method [18, 19] was used to measure the Legendre coefficients f_j and to reconstruct the total EDF. The method implies that the second derivative I_U'' of the probe current is reconstructed from the potential measured in the plasma by the probe oriented at different angles to the device axis. The EDF $f(eU, \alpha)$ is related to the quantity I_U'' by

$$I_U''(eU, \cos\Theta_m) = \frac{2\pi e^3 S}{m^2}\left[f(eU, \alpha) - \frac{1}{2\pi}\int_0^{2\pi} d\varphi \int_{eU}^{\infty} \frac{\partial f(\varepsilon, \Theta_m)}{\partial(eU)} d\varepsilon \right], \quad (1)$$

where

$$\cos\Theta_m = \sqrt{\frac{eU}{\varepsilon}}\cos\alpha + \sqrt{1 - \frac{eU}{\varepsilon}}\cos\varphi\sin\alpha;$$

Θ is the angle between the electron velocity vector and the polar axis z directed from the cathode to the anode along the symmetry axis of the discharge; ε, e, and m are the energy, charge, and mass of an electron, respectively; α is the angle between the normal to the nonconducting probe surface and the discharge axis; U is the retarding potential of the probe with respect to the plasma; and S is the area of the conducting surface of the probe.

The isotropization of the momentum distribution function of the beam electrons and the relaxation of their energy were studied separately by constructing polar diagrams of the directed motion of electrons with different energies and by analyzing the spatial relaxation of the quantity I_U''.

The second derivative I_U'' of the probe current was recorded by modulating the probe potential by a double-frequency differentiating signal of the form

$$U = U_0(1 + \cos\omega_1 t)\cos\omega_2 t. \quad (2)$$

The influence of plasma oscillations and instrumental distortions were taken into account by the method of [18], which was also used to choose the optimum amplitude U_0: $U_0 = 0.1$ V. The frequencies were set to $\omega_1 = 10^3$ Hz and $\omega_2 = 10^5$ Hz. The plasma potential was determined by the zero of the second derivative of the probe current. The anisotropic part $f_0(\vartheta)$ of the EDF and the electron density n were calculated from the formulas

$$f_0(eU) = \frac{m^2}{4\pi e^3 S}\int_{-1}^{1} I_U''(eU, \cos\Theta) d\cos\Theta,$$
$$n = 4\pi\int_0^{\infty} \vartheta^2 f_0(\vartheta) d\vartheta, \quad (3)$$

where $\vartheta = (2eU/m)^{1/2}$. The inaccuracy of the measurements of I_U'' was thoroughly analyzed in [19] and was found to stem primarily from unstable discharge conditions. A special technological treatment of the experimental device and the method for optimizing the discharges modes ensured that the signal-to-noise ratio

was about 200 and the degree to which the discharge parameters were stable was ±5%.

3. COLLISIONAL MECHANISM FOR THE RELAXATION OF THE EDF (SUBCRITICAL CURRENT)

We begin by considering the results of investigations of the electron distribution in a collision-dominated ($l_{ea} \ll d$) LVBD plasma at low discharge currents for which the wave processes are unimportant and the electron beam relaxes primarily due to the binary collisions.

3.1. The Structure and the Main Parameters of the LVBD Plasma

First, note that the gas-discharge gap between the electrodes can be divided into three regions: the space-charge anode and cathode regions and an extended quasineutral plasma region between them. The current j flowing through the electrode region gives rise to a so-called Langmuir sheath, whose length L_0 satisfies the relationship

$$L_0 \approx L_D\left(\frac{e\varphi_0}{T_e}\right)^{3/4}, \qquad (4)$$

where

$$L_D = \left(\frac{T_e}{4\pi n e^2}\right)^{1/2}$$

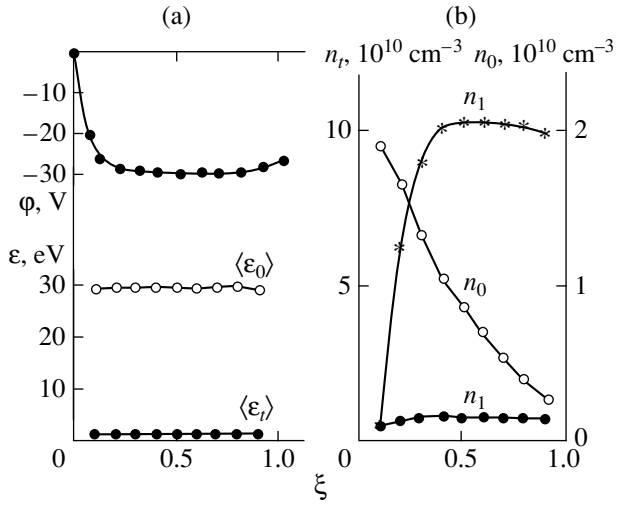

Fig. 1. Axial profiles of the parameters of the plasma of an LVBD in helium at a pressure of $p_{He} = 2$ torr for $d = 1.2$ cm, $T_c = 0.1$ eV, and j_s = (●) 0.14 and (×) 0.84 A cm^{-2}: (a) the potential φ and the mean energies $\langle\varepsilon_t\rangle$ and $\langle\varepsilon_0\rangle$ of the slow and fast electrons and (b) the densities n_t and n_0 of the slow and fast electrons.

is the Debye length, T_e is the plasma electron temperature, n is the electron density, and φ_0 is the voltage drop across the Langmuir sheath.

Across the quasineutral region, the plasma potential changes insignificantly ($\Delta\varphi \approx T_e/e \ll \varphi_0$), in which case the potential has a slightly pronounced minimum between the potential barriers φ_c and φ_a near the cathode and anode, respectively. For the range of plasma parameters under investigation, with helium at the pressure $p_{He} \approx 10^{-1}$–5 torr, an interelectrode distance of $d \approx 1$ cm, and a cathode temperature of $T_c \approx 0.1$ eV, the potential drop near the cathode and anode is equal to $\varphi_c \approx 25$–30 V and $\varphi_a \approx 1$–2 V, respectively.

Figure 1a shows representative profiles of the potential in the plasma of an LVBD in helium. Over a broad parameter range, the situation is seen to be typical of a weakly ionized plasma: charged particles collide only in a quasineutral plasma region of length $L_0 \ll l_{ea}$. The shape of the profiles of the measured quantity I_U'' shows [20] that there are two different electron groups in the plasma: slow electrons with energies $\langle\varepsilon_t\rangle \approx 1$–2 eV and fast electrons with energies $\langle\varepsilon_0\rangle \approx 30$ eV. The beam is formed as a result of electron acceleration at the potential barrier near the cathode. Since the initial electron energy spread is small, $\Delta\varepsilon_0 \ll \varepsilon_0$, the beam can be assumed to be monoenergetic. Because of elastic scattering by helium atoms, the momentum distribution function of fast electrons relaxes (becomes isotropic) at a distance $z \approx l_{ea}$ from the cathode. A distinguishing feature of LVBDs in noble gases is that, due to the binary collisions of the beam electrons with thermal plasma electrons and helium atoms, the beam energy relaxes only slightly. Thus, in the discharge modes under investigation, the corresponding energy relaxation lengths were found to be $L_\varepsilon^{ea} \gg d$ and $L_\varepsilon^{ee} \gg d$ [20]. We can conclude that, over most of the interelectrode gap, the discharge plasma properties are governed by the beam. The current density j_0 of fast electrons is determined by their diffusion toward the anode: $j_0(z) = -eD_0(dn_0/dz)$, where n_0 is the density of the fast electrons. Since the anode potential drop φ_a is considerably less than the beam electron energy, $((e\varphi_a)/\varepsilon_0 \ll 1, \varepsilon_0 = e\varphi_c)$, the beam electrons freely reach the anode surface.

The group of thermal electrons results from inelastic processes of the excitation and ionization of helium atoms. Since the excitation and ionization energies of helium atoms are fairly high (the ionization energy is $E_{ion} \approx 24.6$ eV, and the excitation energy of the lowest metastable state He(2^3S_1) is $E_m \approx 19.8$ eV), these inelastic processes are governed exclusively by the group of fast electrons, which also carry the bulk of the discharge current. The total electron current density is equal to the density of the currents carried by the fast (j_0) and thermal (j_t) electrons. Since the potential barrier at the anode acts to reduce the flow of thermal electrons

toward the anode, we have $j_t(d) + j_0(d) = j_s$, where j_s is the emission current from the cathode [1]

$$j_t(d) = 0.25en_t(d)\left(\frac{8T_e}{\pi m}\right)^{1/2} \times \exp\left(-\frac{2\varphi_a}{T_e}\right)\left[1-\psi_0\left(\frac{e\varphi_a}{T_e}\right)\right]^{-1},$$

$$\psi_0(y) = 0.5[(1+y)^{-y} - \sqrt{\pi}y^{3/2}(1-\mathrm{erf}\sqrt{y})].$$

The characteristic spatial profiles of the densities n_0 and n_t of the fast and slow electrons are displayed in Fig. 1b. We can see that, for the current density $j_s \approx 0.8$ A cm^{-2}, the plasma density is markedly nonuniform: the onset of the density gradient dn_t/dz in the cathode sheath is associated with the ambipolar diffusion of the produced ions toward the cathode. The rate at which the ions are produced is approximately proportional to the beam current. Consequently, plasma density variations are no longer important for low current densities ($j_s \approx 0.1$ A cm^{-2}).

The above characteristic features of LVBDs in noble gases are associated with the presence of an intense monoenergetic electron beam; thus, we will focus most of our attention on the group of fast electrons. Note that, near the cathode, the structure of the spectrum of the fast electrons almost always reflects inelastic processes in the plasma. Detailed measurements of the EDF of the beam in the cathode sheath made it possible to investigate the effect of inelastic processes on the formation of the EDF and to determine the density of the excited helium atoms in the 2^3S_1 metastable state.

In the next section, the generation of fast electrons in the plasma of an LVBD in helium will be considered in more detail.

3.2. Elementary Processes Involving Metastable Helium Atoms

In the kinetics of a low-temperature plasma of an LVBD in helium, an important role is played by reactions involving helium atoms in the 2^3S_1 metastable state [21]. The rates of these reactions were calculated for the EDF measured in a discharge mode with $p_{He} = 1$ torr and $j_s \approx 0.3$ A cm^{-2}. The calculations were carried out for the following processes of the population and quenching of the metastable helium atoms.

The population reactions include excitation by direct electron impact [22]

$$\mathrm{He} + e \longrightarrow \mathrm{He}(2^3S_1) + e, \quad (5)$$

collisional–radiative recombination [23]

$$\mathrm{He}^+ + 2e \longrightarrow \mathrm{He}(2^3S_1) + e, \quad (6)$$

dissociative recombination [23]

$$\mathrm{He}_2^+ + e \longrightarrow \mathrm{He}(2^3S_1) + \mathrm{He}, \quad (7)$$

and the Phelps reaction [24]

$$\mathrm{He}(2^1S_0) + e \longrightarrow \mathrm{He}(2^3S_1) + e. \quad (8)$$

The quenching reactions include the processes of Penning ionization and associative ionization [25]

$$\mathrm{He}(2^3S_1) + \mathrm{He}(2^3S_1) \begin{cases} \nearrow \mathrm{He}^+ + \mathrm{He} + \mathbf{e} \\ \searrow \mathrm{He}_2^+ + \mathbf{e}, \end{cases} \quad (9)$$

step ionization by electron impact [26]

$$\mathrm{He}(2^3S_1) + e \longrightarrow \mathrm{He}^+ + 2\mathbf{e}, \quad (10)$$

superelastic collisions [26]

$$\mathrm{He}(2^3S_1) + e \longrightarrow \mathrm{He} + \mathbf{e}, \quad (11)$$

triplet–singlet transitions [24]

$$\mathrm{He}(2^3S_1) + e \longrightarrow \mathrm{He}(2^1S_0) + e, \quad (12)$$

and diffusion toward the walls [17].

The calculated rates of the population and quenching processes are listed in Table 1. One can see that, in the discharge mode at hand, $\mathrm{He}(2^3S_1)$ metastable atoms are produced primarily through excitation from the ground state by direct electron impact and are quenched predominantly through step ionization and binary interactions, which are accompanied by the generation of fast electrons. An analysis of the time-independent diffusion equation under the assumption that the spatial distribution of metastable helium atoms in a discharge plasma follows the distribution of the density of fast electrons revealed that the dominant role in the quenching of metastable atoms is played by diffusion processes. The density of $\mathrm{He}(2^3S_1)$ metastable atoms at the discharge axis is estimated as $N_m \approx 7 \times 10^{12}$ cm^{-3}. In a collision-dominated plasma of an LVBD in helium at a subcritical current, the contribution of step ionization reactions to the total ionization rate is about 40% [17].

Hence, in the discharge mode under investigation, $\mathrm{He}(2^3S_1)$ metastable atoms play an important role in both plasma kinetics and the ion content of the LVBD plasma, in which case the elementary reactions (9)–(11) should cause the appearance of the following elec-

Table 1. Rates of different reactions changing the density of metastable helium atoms

Reactions	$\Gamma \times 10^{17}$, cm^{-3} s^{-1}
(5)	6
(6)	0.01
(7)	0.001
(8)	$0.5 \times 10^{-14} N_m$
(9)	$1.8 \times 10^{-25} N_m^2$
(10)	$0.8 \times 10^{-13} N_m$
(11)	$0.02 \times 10^{-13} N_m$
(12)	$0.8 \times 10^{-13} N_m$

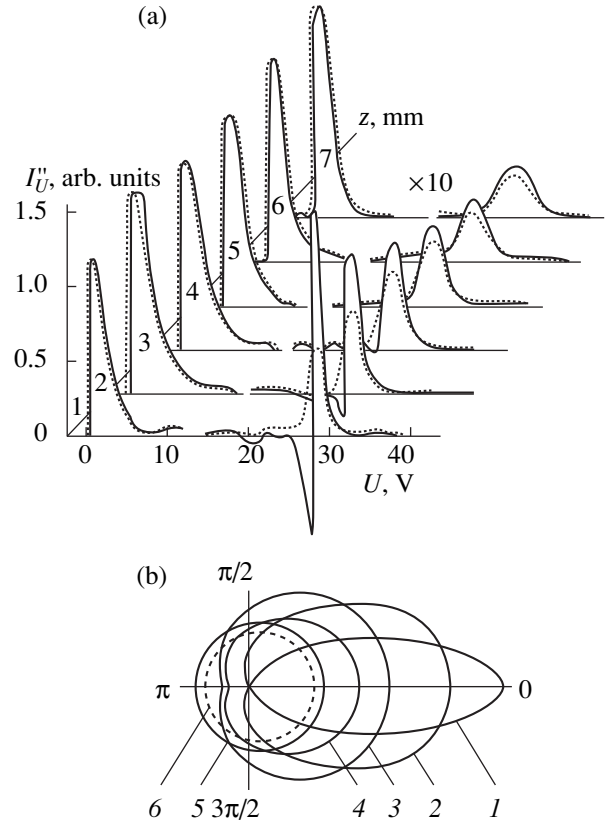

Fig. 2. (a) Evolution of the I''_U profile and (b) polar diagrams of the directed motion of beam electrons in a collision-dominated LVBD plasma at a subcritical current for p_{He} = 2 torr, l_0 = 0.25 cm, d = 1.2 cm, T_c = 0.1 eV, j_s = 0.14 A cm^{-2}, and U_a = 29 V at the distances z = (*1*) 0.5, (*2*) 1, (*3*) 1.5, (*4*) 2, (*5*) 3, and (*6*) 6 mm from the cathode.

tron groups in the energy spectrum: reactions (9) produce electrons with energies of $\varepsilon \approx 14$–17 eV, reaction (10) produces electrons with energies of $\varepsilon_1 \approx \varepsilon_0 - \Delta\varepsilon$ (where $\Delta\varepsilon = E_{ion} - E_m \approx 4.8$ eV), and reaction (11) produces electrons with energies of $\varepsilon_2 \approx 20$–21 eV.

3.3. Spatial Relaxation of an Electron Beam

Let us consider in more detail the results of both an experimental investigation of the EDF in a collision-dominated LVBD plasma and an analysis of the mechanisms for beam relaxation in a discharge plasma at a low discharge current density.

Figure 2a illustrates the spatial relaxation of the quantity I''_U for two orientations of the planar probe: the solid curves refer to a probe whose absorbing surface faces the cathode, and the dashed curves refer to a probe whose absorbing surface faces the anode. For thermal electrons, the values of I''_U are lowered by a factor of ten. The results presented in Fig. 2a are characteristic of low discharge currents such that the beam energy relaxes only due to the binary collisions of the beam electrons with thermal plasma electrons and helium atoms. We can see that, at a distance $z < 3$ mm from the cathode, the quantity I''_U gradually becomes positive and, at a distance $z > 3$ mm farther from the cathode, the profiles calculated for different orientations of the probe essentially coincide. The polar diagrams of the directed motion of beam electrons at different distances z from the cathode (Fig. 2b) provide strong evidence for the isotropization of the EDF. After the isotropization stage, a weakly anisotropic beam travels throughout the entire interelectrode gap, keeping its energy almost unchanged. The beam loses fast electrons as a result of inelastic collisions, and the electron–electron and electron–atom elastic collisions act to increase the energy spread of the beam and to slightly lower the mean beam energy. Figure 3 illustrates the character of the spatial relaxation of the isotropic part $F_0(\varepsilon, z)$ of the distribution function of an electron beam emitted by the cathode, the energy spread $\Delta\varepsilon_0$ of the beam, and the mean beam energy $\langle\varepsilon_0\rangle$. For comparison, the results obtained using the collisional relaxation theory [27] are also shown. The spread $\Delta\varepsilon_0$ of the initial beam energy is seen to increase as the beam electrons diffuse toward the anode (the half-widths of the corresponding profiles become larger). This effect is described by the collisional relaxation theory. The mean beam energy $\langle\varepsilon_0\rangle$ decreases fairly gradually. The energy $\Delta\langle\varepsilon_0\rangle$ lost by the beam when it traverses the interelectrode gap is fairly low specifically; it is on the order of $\Delta\langle\varepsilon_0\rangle \approx 0.3$ eV.

Inelastic collisions markedly reduce the density of the beam propagating along the interelectrode gap. The ionization of He(2^3S_1) metastable atoms by the beam electrons and the quenching of metastables in collisions with thermal plasma electrons give rise to electron groups with energies of $\varepsilon_1 \approx 24.4$ eV and $\varepsilon_2 \approx 20$–21 eV, respectively. Figure 4 depicts the EDF measured experimentally in the cathode sheath (at the distance $z = 0.15d$ from the cathode) and clearly shows that the energy spectrum of fast electrons actually contains the related electron groups F_1 and F_2. The spatial relaxation of the electron groups F_1 and F_2 in the experimentally measured EDF is illustrated in Figs. 5a and 5b. We can see that, along the discharge axis, the profiles of the distribution functions F_1 and F_2 of the electron groups change more gradually than the profile of the isotropic part F_0 of the initial electron beam (cf. Fig. 3). The electron energy spread for each of these groups ($\Delta\langle\varepsilon_1\rangle$ and $\Delta\langle\varepsilon_2\rangle$) is substantially larger than $\Delta\langle\varepsilon_0\rangle$. Presumably, this is explained by the fact that the energies ε_1 and ε_2 are lower than ε_0 and accordingly the cross sections for the excitation of helium atoms by the electrons from these groups are also lower. Consequently, the diffusion lengths $L_{hy}^{(1)}$ and $L_{hy}^{(2)}$ are longer than $L_{hy}^{(0)}$. As a result,

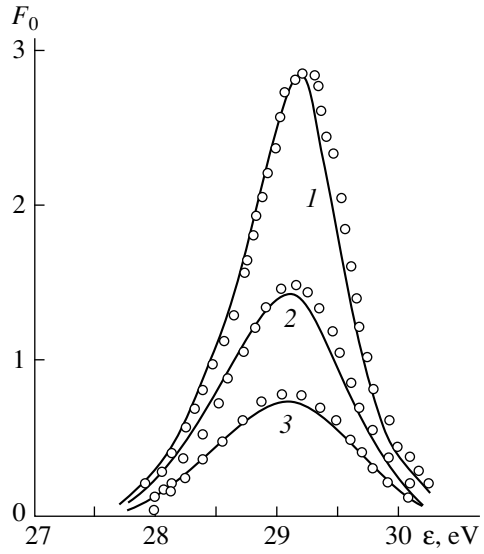

Fig. 3. Isotropic part F_0 of the EDF at different points on the symmetry axis of the discharge: $\xi = z/d$ = (*1*) 0.25, (*2*) 0.5, and (*3*) = 0.75. The profiles are calculated for a discharge mode with the parameters p_{He} = 2 torr, d = 1.2 cm, ε_0 = 29 eV, T_e = 1.5 eV, $T_a = T_c$ = 0.1 eV, $n_t/N_a = 5 \times 10^{-5}$, N_m = 10^{13} cm^{-3}, and j_s = 0.32 A cm^{-2}. The solid curves are for theoretical results, and the experimental data are illustrated by open circles.

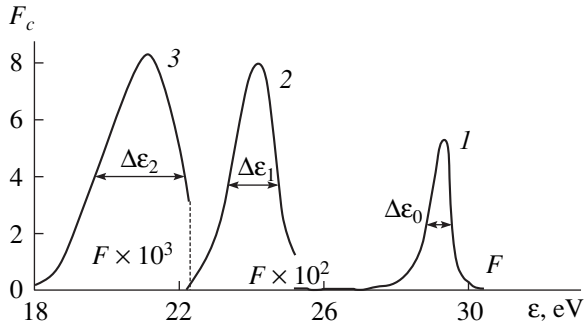

Fig. 4. Profiles of the distribution functions (*1*) F_0, (*2*) F_1, and (*3*) F_2 of different electron groups in the EDF measured experimentally in the cathode sheath of an LVBD with the parameters p_{He} = 2 torr, d = 1.2 cm, ε_0 = 29 eV, T_e = 1.5 eV, and j_s = 0.1 A cm^{-2}.

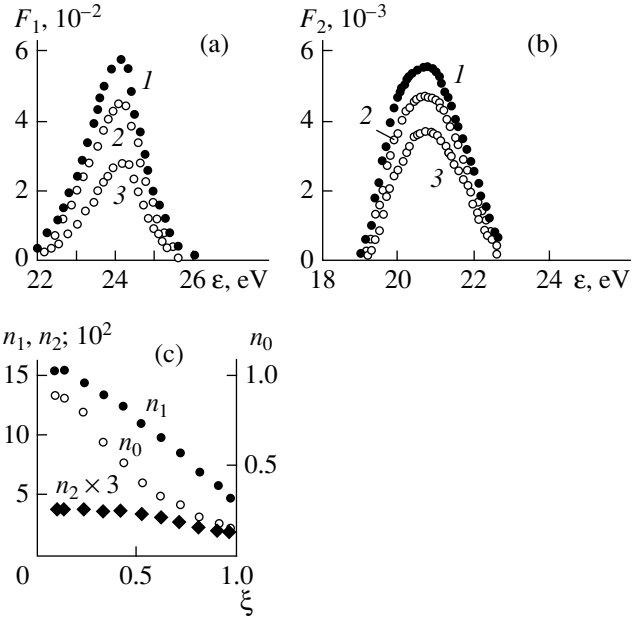

Fig. 5. Experimentally obtained distribution functions F_c and densities n_c of different groups of fast electrons for the same discharge parameters as in Fig. 3. Shown are the axial profiles of (a) the distribution function of the group of electrons produced by the ionization of He(2^3S_1) metastable atoms, (b) the distribution function of the group of electrons produced by superelastic collisions, and (c) the densities n_c of different groups of fast electrons.

the lifetime of the electrons of the initial beam is shorter than the lifetimes of the electrons from the remaining groups in the EDF. This analysis explains why the energy spread $\Delta\langle\varepsilon_0\rangle$ is small in comparison with $\Delta\langle\varepsilon_1\rangle$ and $\Delta\langle\varepsilon_2\rangle$.

In this paper, it is proposed to determine the density N_m of metastable helium atoms by comparing the calculated energy spectrum of fast electrons [27] with the experimental spectrum. In fact, the functions F_1 and F_2 are proportional to N_m. Consequently, the most reliable value of the density N_m in an LVBD plasma is such that the calculated total EDF $F = F_0 + F_1 + F_2$ is close to the EDF obtained by probe measurements. Figure 6 compares the experimental and theoretical EDFs near the energy ε_0. When the density of metastable helium atoms is equal to $N_m = 10^{13}$ cm^{-3}, the theoretical profile is seen to agree well with the experimental one, so that this density value is what is desired.

The densities of fast electrons from different groups, n_0, n_1, and n_2, were determined from relationships (3) by integrating the experimental EDF over the energies. The axial profiles of the densities of fast electrons are displayed in Fig. 5c. We can see that the density n_0 decreases almost exponentially: $n_0(z) \approx \exp(-z/L^0_{hy})$. As for the remaining groups, the inelastic collisions of fast electrons with helium atoms do not lead to such a sharp decrease in the corresponding electron densities. Consequently, we can assume that $n_1(z)$, $n_2(z)$, $F_1(z, \varepsilon)$, and $F_2(z, \varepsilon)$ are approximately proportional to N_m. By this assumption, the proposed method of comparing the related experimental and theoretical electron energy distribution functions yields more reliable estimates for the density N_m. Note that, for the discharge modes under investigation, the ratio of the densities of the secondary electrons from two different groups is essentially independent of N_m and is approximately equal to $n_1/n_2 \approx 10$.

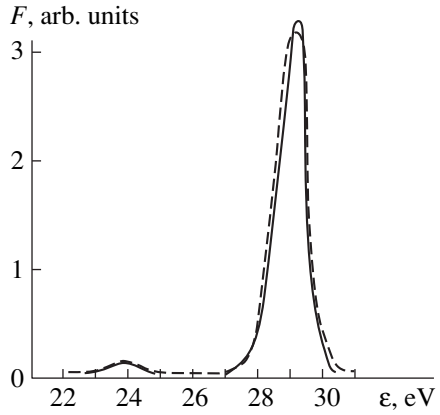

Fig. 6. Total EDF over the range of beam energies under consideration, $F = F_0 + F_1 + F_2$, at the distance $z = 0.25d$ from the cathode for the same discharge parameters as in Fig. 3. The solid curve gives the theoretical results obtained for $N_m = 10^{13}$ cm^{-3}, and the experimental data are illustrated by the dashed curve.

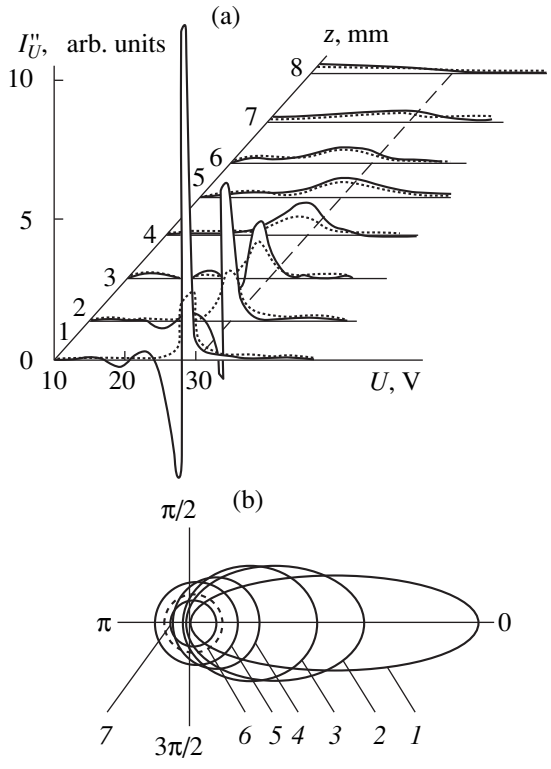

Fig. 7. (a) Evolution of the I''_U profile along the discharge axis and (b) polar diagrams of the directed motion of beam electrons in a collision-dominated LVBD plasma at a critical discharge current for $p_{He} = 2$ torr, $d = 1.2$ cm, $l_0 = 0.25$ cm, $T_c = 0.1$ eV, $j_s = 0.8$ A cm^{-2}, and $U_a = 29$ V at the distances $z =$ (*1*) 1, (*2*) 2, (*3*) 3, (*4*) 4, (*5*) 5, (*6*) 6, and (*7*) 8 mm from the cathode.

Hence, we can conclude that, in a collision-dominated plasma of an LVBD in helium, the ionization of metastable atoms by the beam electrons emitted by the cathode has a much greater effect on the formation of the electron energy spectrum than superelastic collisions.

4. BEAM–PLASMA MECHANISM FOR THE RELAXATION OF THE EDF

4.1. Collision-Dominated Plasma (Supercritical Current)

In a collision-dominated plasma of an LVBD, the initial EDF is weakly anisotropic at distances of $z > l_0$ from the cathode. For this reason, the relaxation of electron beams in such discharge plasmas was investigated theoretically without allowance for the processes of wave excitation. However, based on the results of the above experiments, we will show that, even if the beam anisotropy is comparatively weak, the beam energy in discharges with supercritical currents relaxes primarily by the beam–plasma mechanism, which is more efficient than the collisional mechanism.

The dynamics of the spatial relaxation of an electron beam depends substantially on the discharge current density [28]. Figure 7 presents the axial profiles of I''_U and the polar diagrams of the directed motion of beam electrons for a current density of $j_s^* \approx 0.8$ A/cm^2. As before, the isotropization of the EDF occurs at a distance $z \approx 3$ mm from the cathode. However, at larger distances, the beam relaxation differs radically from that by the collisional mechanism (Fig. 2). After the isotropization stage, the beam does not reach the anode. At the distance $z \approx 4$ mm, the energy spread $\Delta\varepsilon$ of the beam begins to increase sharply. Then, the beam rapidly loses its energy, and the EDF is essentially symmetric (Fig. 7b) and relaxes toward a state with a plateau-like distribution function. Figure 8 illustrates the dependence of the energy spread $\Delta\varepsilon$ calculated as a function of the discharge current density j_s from the isotropic part $f_0(z, \varepsilon)$ of the EDF at a distance $z = 0.75d$ from the cathode. The figure provides clear evidence for the existence of the critical discharge current density $j_s^* = 0.8$ A/cm^2: when the discharge current increases above the critical level, the energy spread of the beam begins to increase abruptly and the beam itself is decelerated. The critical current density calculated theoretically in [27] for the density $n_t \approx 10^{12}$ cm^{-3} of thermal plasma electrons and for $p_{He} = 2$ torr, $\varepsilon_0 = 30$ eV, and $T_e = 1$ eV is equal to $j_0^* \approx 0.79$ A cm^{-2}. Such a close agreement between the theoretical and experimental critical current densities implies that it is because of the quasineutral relaxation of the beam by the beam-driven Langmuir waves that the beam–plasma mechanism begins to play a more important role than the collisional mechanism.

For $j_0 > j_0^*$, a more efficient mechanism for the beam energy relaxation—the beam–plasma mechanism—comes into play in a jumplike manner. Presum-

ably, this is explained by the fact that, when the discharge current increases above the critical level, the intensity of the beam-driven Langmuir waves begins to increase sharply. This is accompanied by the efficient energy relaxation of the distribution function of fast electrons, because the beam energy is converted into wave energy.

An analysis of the mechanisms responsible for the heating of thermal plasma electrons in the collisional mode of an LVBD [29] showed that, even when the critical current is reached, the heating of thermal electrons by binary Coulomb collisions still dominates over the heating due to collisional wave damping.

4.2. Collisionless Plasma

In a collisionless discharge plasma, both momentum and energy distribution functions of the electron beam do not relax due to binary collisions. Under such conditions, the EDF is highly anisotropic and the beam is unstable against Langmuir waves [30–32] and the instability is threshold in character: Langmuir waves grow only when the discharge current exceeds the critical level. Up until now, the growth rates, the critical currents, and the relaxation dynamics of the EDF have been studied theoretically only for low-density ($n_0 \ll n_t$) beams with a velocity spread satisfying the condition [33, 34]

$$(\Delta\vartheta_0/\vartheta) \geq (n_0/n_t)^{1/3}. \quad (13)$$

In a collisionless plasma of an LVBD in helium, the density of fast electrons is, as a rule, on the order of the density of slow electrons, $n_0 \leq n_t$, whereas the velocity spread of the beam satisfies the condition $(\Delta\vartheta_0/\vartheta_0) \ll (n_0/n_t)^{1/3}$, which is opposite to condition (13). This indicates the validity of the approximation of an intense monoenergetic beam [32], which cannot be described by quasilinear theory [33, 34]. Presumably, this circumstance may explain why there are only a few theoretical papers on this topic and the main results on the anisotropic EDFs in collisionless plasmas were obtained experimentally [8, 20, 35–38].

From relationship (1), we can readily see that, for an isotropic EDF, the quantity I_U'' should be independent of the orientation of the planar probe in a plasma. For an anisotropic EDF, the quantity I_U'' takes on not only positive but also negative values. Figure 9 illustrates how the anisotropy of the model EDF influences both the axial profiles of I_U'' ($\alpha = 0$) calculated from formula (1) and the polar diagrams of the directed electron motion.

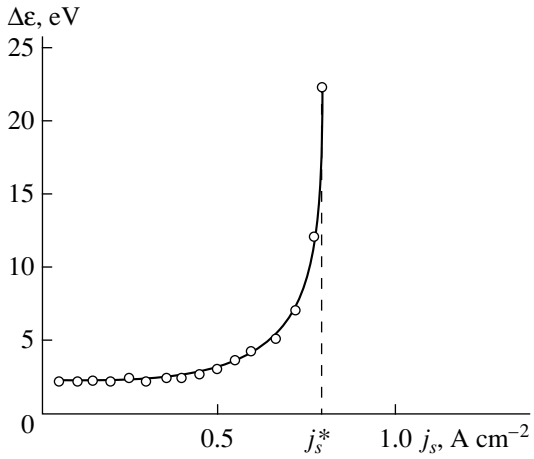

Fig. 8. Energy spread Δε of the beam electrons vs. the discharge current density j_s at the point $z = 0.75d$ for the same discharge parameters as in Fig. 7.

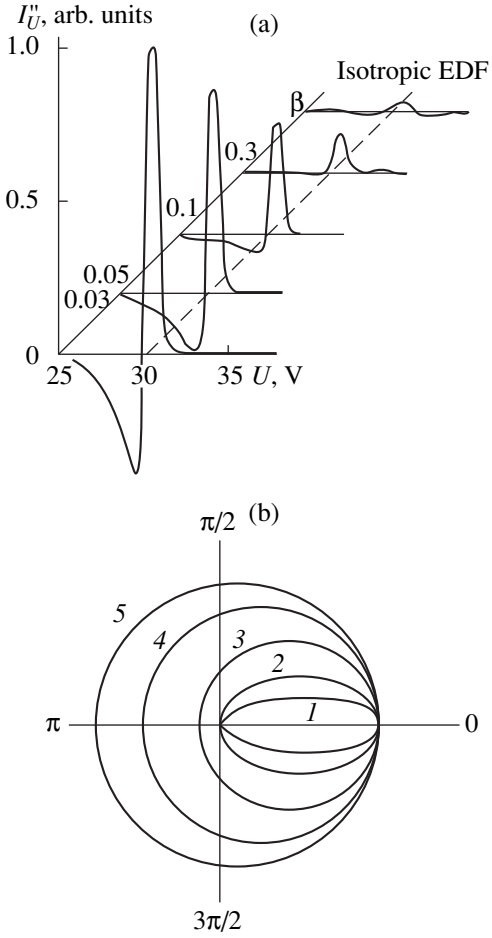

Fig. 9. (a) Evolution of the I_U'' profile along the discharge axis and (b) polar diagrams of the directed electron motion for different degrees of anisotropy β of the model EDF: β = (*1*) 0.1, (*2*) 0.3, (*3*) 1, (*4*) 3, and (*5*) 10.

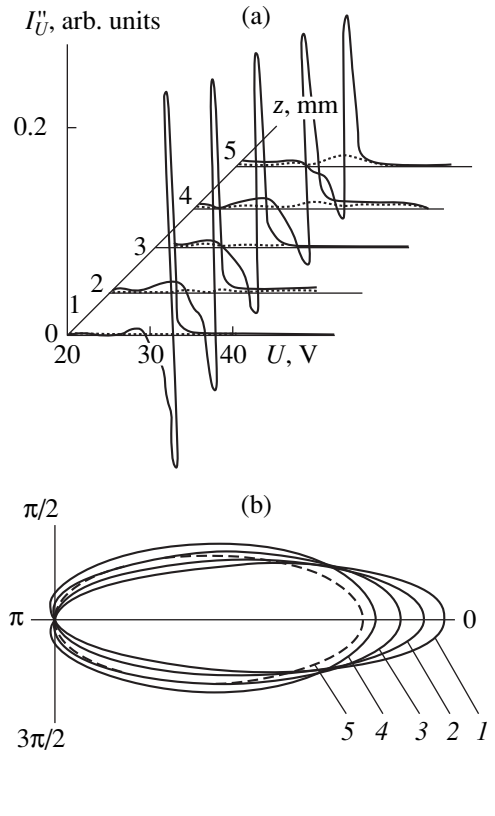

Fig. 10. (a) Evolution of the I''_U profile along the discharge axis and (b) polar diagrams of the directed motion of beam electrons in a collisionless LVBD plasma at a subcritical discharge current for p_{He} = 0.5 torr, l_0 = 1 cm, d = 0.6 cm, j_s = 0.1 A cm^{-2}, $n_t = 6.7 \times 10^{10}$ cm^{-3}, and $n_0 = 9 \times 10^9$ cm^{-3} at distances of z = (*1*) 1, (*2*) 2, (*3*) 3, (*4*) 4, and (*5*) 5 mm from the cathode.

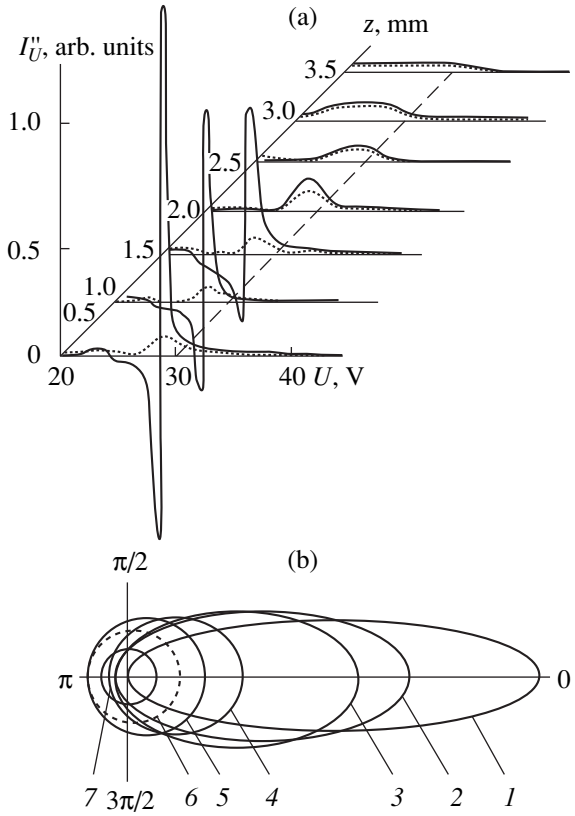

Fig. 11. (a) Evolution of the I''_U profile along the discharge axis and (b) polar diagrams of the directed motion of beam electrons in a collisionless LVBD plasma at a supercritical discharge current for p_{He} = 0.5 torr, l_0 = 1 cm, d = 0.6 cm, j_s = 0.5 A cm^{-2}, $n_t = 2.8 \times 10^{11}$ cm^{-3}, and $n_0 = 6 \times 10^{10}$ cm^{-3} at distances of z = (*1*) 0.5, (*2*) 1, (*3*) 1.5, (*4*) 2, (*5*) 2.5, (*6*) 3, and (*7*) 3.5 mm from the cathode.

Here, the model EDF is taken to be a function describing a beam of fast electrons in a Maxwellian plasma:

$$f(\varepsilon, \Theta) = n_t\left(\frac{m}{2\pi T}\right)^{3/2}\left[\exp\left(-\frac{\varepsilon}{T}\right) + \gamma_1 \times \exp\left\{-\left(\frac{\varepsilon - \varepsilon_0}{\gamma_2}\right)^2 + \frac{\cos\Theta - 1}{\beta}\right\}\right], \quad (14)$$

where the degree of anisotropy β, the mean energy ε_0, the characteristic half-width γ_2 of the EDF in energy space, and the electron density γ_1 are all determined by the parameters of the fast electron beam.

A comparative analysis of the I''_U profiles and the polar diagrams shows that, in the isotropization stage, the regions in which the function I''_U is negative disappear and the function itself becomes less peaked, while the mean beam energy remains unchanged.

The experimental results obtained for a collisionless discharge plasma at a subcritical current are illustrated in Fig. 10, which displays the axial profiles of I''_U and the polar diagrams of the directed electron motion. The solid curves ($\alpha = 0$) correspond to a planar probe whose absorbing surface faces the cathode, and dashed curves ($\alpha = \pi$) refer to the probe whose absorbing surface faces the anode. One can see that, for $\alpha = 0$, the function I''_U takes on rather large negative values across the entire interelectrode gap. The shape of the polar diagrams indicates that the EDF is highly anisotropic and the beam relaxation in the discharge plasma is insignificant. With increasing discharge current, the quantity I'' reaches a certain critical value above which the mechanisms for beam relaxation are switched on in a jumplike fashion. The corresponding discharge mode with I'' = 0.5 A is illustrated in Figs. 11a and 11b. We can see that, at distances $0 < z < 2$ mm from the cathode, the maximum negative magnitudes of $I''_U(\alpha = 0)$ decrease (in absolute value) to zero, while the mean energy of the beam electrons and their energy spread change insignificantly. A comparison between the polar diagrams in Fig. 11b allows us to describe the propagation

of an intense electron beam in a collisionless plasma as follows. First, the momentum distribution function of the beam electrons becomes more isotropic. At distances farther from the cathode, the beam with a weakly anisotropic EDF rapidly loses its energy and does not reach the anode. The axial profiles of I_U'' are practically independent of the orientation of the probe and acquire a plateau-like shape. A simultaneous analysis of the shapes of the axial profiles of I_U'' and the polar diagrams shows that, even in the absence of binary collisions in a discharge plasma with $I > I''$, the isotropization of the beam electrons at distances $z < 2$ mm from the cathode is accompanied by insignificant energy losses ($\varepsilon < 2$ eV). The EDF of a weakly anisotropic beam relaxes at larger distances from the cathode ($2 < z < 3$ mm). Note that, in a collisionless plasma, the distance l_i over which an intense electron beam becomes almost isotropic is longer than the distance l_ε over which the beam spreads out. Since the isotropization and relaxation processes occur on spatial scales shorter than the electron mean free path l_0, they can be explained only in terms of the interaction between the beam electrons and Langmuir waves.

Let us estimate first the volume energy density of Langmuir waves W required for a monoenergetic electron beam to become anisotropic at the indicated distance in a collisionless plasma and second the effective cross section σ_{e-pl} for the interaction between the beam electrons and Langmuir waves. To do this, we assume that the electron–wave interactions are analogous to quasi-elastic collisions between particles and that the Langmuir plasmons have the same energy $\hbar\omega_0$. We also use the following relationship between the effective collision frequency $\nu_{\text{eff}} = \vartheta_0/l_i$ and the energy density W of isotropic Langmuir waves [30]:

$$\nu_{\text{eff}} = \frac{\pi}{4}\omega_0\frac{\vartheta_{\text{ph}}}{\vartheta_0}\frac{W}{n_t m\vartheta_0^2}, \qquad (15)$$

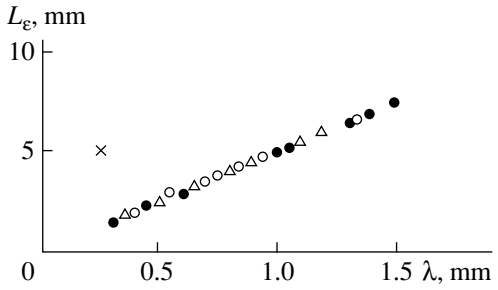

Fig. 12. Total energy relaxation length $L_\varepsilon = l_i + l_\varepsilon$ of the EDF vs. the wavelength λ of Langmuir oscillations in an LVBD plasma for p_{He} = (●) 0.25, (○) 0.5, (△) 1, and (×) 2.5 torr. In the discharge mode marked by the cross, the beam relaxation by Langmuir waves is followed by the relaxation by binary collisions, so that the relaxation length L_ε sharply increases.

where $\omega_0 = \sqrt{(4\pi n_t e^2)/m}$, $\vartheta_0 = \sqrt{2\varepsilon_0/m}$, and ϑ_{ph} is the wave phase velocity.

The values of $\vartheta_{\text{ph}} \approx \vartheta_0$ and W calculated for $\sigma_{e-pl} = \hbar\omega_0/Wl_i$ are listed in Table 2. We can see that, for $p_{\text{He}} = 0.5$ torr, the wave energy density is equal to $W \approx 1.2$ erg cm^{-3} (cf. $n_t\varepsilon_t \approx 0.5$ erg cm^{-3} and $n_0\varepsilon_0 \approx 2.4$ erg cm^{-3}) and the effective cross section for the electron–plasmon interaction is equal to $\sigma_{e-pl} \approx 10^{-16}$ cm^{-2}.

Table 2 compares the threshold current I_{hd} for the onset of a hydrodynamic instability [30] and the experimentally measured critical current I^*. Table 2 also presents the isotropization length l_i (the isotropization stage is analogous to the hydrodynamic stage [32]) and the length l_ε over which the beam relaxes to a state with a plateau-like EDF (the relaxation stage is analogous to the kinetic stage). In addition, Table 2 gives the energy densities $n_t\varepsilon_t$ and $n_0\varepsilon_0$ of the thermal and fast electrons, respectively. The results listed in Table 2 were calculated for different discharge modes. We can see that, at a constant pressure of helium gas, an increase in the discharge current leads to an increase in the density n_t

Table 2

P_{He}, torr	n_t, cm^{-3}	n_0, cm^{-3}	I_s, A	I^*, A	I_{hd}, A	l_0, cm	l_i, cm	l_ε, cm	$n_t\varepsilon_t$, erg cm^{-3}	$n_0\varepsilon_0$, erg cm^{-3}	W, erg cm^{-3}	σ_{e-pl}, cm^{-2}	l_0/λ
0.9	6.6×10^{10}	5.8×10^{9}	0.16		0.059		*	–	0.11	0.23	–	–	4.4
	9.2×10^{10}	7.3×10^{9}	0.2	0.18	0.076	0.56	0.4	0.2	0.15	0.3	0.12	4×10^{-16}	5.1
	1.7×10^{11}	1.0×10^{10}	0.3		0.12		0.3	0.1	0.27	0.4	0.34	2×10^{-16}	7
0.6	4.6×10^{10}	3.4×10^{9}	0.08		0.037		–	–	0.074	0.16	–	–	4.6
	5.3×10^{10}	5.0×10^{9}	0.1	0.09	0.049	0.83	0.6	0.1	0.085	0.24	0.057	4×10^{-16}	5.5
	2.8×10^{11}	4.0×10^{10}	0.8		0.35		0.27	0.03	0.44	1.9	0.71	2×10^{-16}	12
0.5	6.7×10^{10}	9×10^{9}	0.1		0.015		–	–	0.074	0.43	–	–	4.9
	3×10^{11}	6×10^{10}	0.5	0.25	0.57	1.0	0.2	0.1	0.48	2.4	1.2	1×10^{-16}	15.1

* No relaxation by waves.

of the thermal plasma electrons, a decrease in the wavelength $\lambda = \frac{2\pi\vartheta_0}{\omega_0}$ of Langmuir waves, and an increase in the parameter l_0/λ. A comparative analysis of the experimental data shows that the critical regime of the beam–plasma relaxation of the EDF occurs only when the electron mean free path is longer than five wavelengths of Langmuir oscillations. Consequently, the condition $l_0/\lambda \geq 5$ can serve as a threshold criterion for the energy relaxation of an electron beam in a collisionless plasma.

Figure 12 shows the dependence of the total energy relaxation length $L_\varepsilon = l_i + l_\varepsilon$ of the beam on the wavelength λ of Langmuir oscillations. We can see that, over a broad parameter range, the quantity L_ε is well approximated by the linear dependence $L_\varepsilon \approx 5\lambda$. When the distance between the electrodes is $d < L_\varepsilon \approx 5\lambda$, the beam experiences no energy relaxation.

This result was overwhelmingly confirmed by investigations of plasma objects in which the anisotropy of the EDF was induced by different causes. In particular, in the study of the kinetic instability of a low-temperature decaying plasma [39], the threshold criterion for the relaxation of the EDF was obtained in the form $n_t \geq 1.7 \times 10^8 \varepsilon_0 \sigma_{ea}^t N_A^2$. Hence, the experimentally established criterion for the energy relaxation of an anisotropic EDF is independent of the cause of anisotropy and thus is universal in character.

5. CONCLUSION

The relaxation dynamics of the energy and momentum distribution functions of electrons has been studied by probe measurements.

It has been shown for the first time that, in a collision-dominated plasma, the energy of an intense electron beam may relax due to the excitation of waves. The critical currents corresponding to a jumplike transition from one relaxation mechanism to another have been measured. The role of metastable helium atoms in the formation of the distribution function of fast electrons has been investigated, and the density of metastables has been determined.

The phenomenon of the isotropization of an electron beam in the course of its interaction with Langmuir waves in a collisionless plasma has been revealed, and the cross section for quasi-elastic collisions of the beam electrons with Langmuir plasmons has been estimated. The wave nature of the mechanisms for the relaxation of an intense electron beam has been demonstrated. It is shown that the mechanisms themselves come into play when the critical discharge current is reached. It is established that the beam energy relaxes over the distance $L_\varepsilon \approx 5\lambda$ and that the relaxation process occurs in two stages. First, as the beam travels the distance l_i from the cathode, the electron momentum distribution function becomes essentially isotropic, in which case the beam energy decreases only slightly (the isotropization stage). Second, over the distance l_ε farther from the cathode, the beam relaxes to a state with a plateau-like EDF (the energy relaxation stage).

The experimentally established criterion for the energy relaxation of an anisotropic EDF is independent of the cause of anisotropy and thus is universal in character. Although the experiments have been conducted in a plasma of an LVBD in helium, all of the results obtained are not exclusively valid for helium and can be used for a comparative analysis of the role of collisional and collective interactions in anisotropic plasmas of discharges in other noble gases.

ACKNOWLEDGMENTS

I am grateful to V.S. Litvinenko and G.A. Dyuzhev for support and for their constant interest in this work. This work was supported by the Ministry of Education of the Russian Federation (under the program Basic Research on Beam Plasma in the Efforts at Environmental Protection, 2000).

REFERENCES

1. F. G. Baksht, G. A. Djuzhev, *et al.*, *Thermionic Converters and Low-Temperature Plasma* (Department of Energy, Washington, 1978).
2. G. A. Djuzhev *et al.*, in *Proceedings of the 3rd International Conference on Themionic Electrical Power Generation, Julich, 1972*, Vol. 3, p. 1700.
3. G. A. Dyuzhev *et al.*, Zh. Tekh. Fiz. **41**, 2393 (1971) [Sov. Phys. Tech. Phys. **16**, 1900 (1972)].
4. G. A. Dyuzhev *et al.*, Zh. Tekh. Fiz. **41**, 2406 (1971) [Sov. Phys. Tech. Phys. **16**, 1910 (1972)].
5. F. G. Baksht, B. I. Kolosov, *et al.*, *Mathematical Modeling of Processes in Low-Voltage Beam–Plasma Discharges* (Énergoatomizdat, Moscow, 1990).
6. F. G. Baksht and V. F. Lapshin, Zh. Tekh. Fiz. **57**, 841 (1987) [Sov. Phys. Tech. Phys. **32**, 513 (1987)].
7. Yu. K. Gus'kov, A. I. Kiryushchenko, *et al.*, Zh. Tekh. Fiz. **43**, 327 (1973) [Sov. Phys. Tech. Phys. **18**, 213 (1973)].
8. A. S. Mustafaev and A. P. Mezentsev, J. Phys. D **19**, L69 (1986).
9. V. F. Lapshin, A. P. Mezentsev, and A. S. Mustafaev, J. Phys. D **22**, 857 (1989).
10. A. S. Mustafaev, A. P. Mezentsev, *et al.*, USSR Inventor's Certificate No. 1185429, Byull. Izobret., No. 38 (1985).
11. A. S. Mustafaev, A. P. Mezentsev, *et al.*, USSR Inventor's Certificate No. 1542316, Byull. Izobret., No. 5 (1990).
12. V. B. Kaplan, A. S. Mustafaev, A. Ya. Énder, *et al.*, Zh. Tekh. Fiz. **47**, 2068 (1977) [Sov. Phys. Tech. Phys. **22**, 1202 (1977)].
13. A. S. Mustafaev, A. M. Martsinovskiĭ, A. Ya. Énder, *et al.*, USSR Inventor's Certificate No. 693472, Byull. Izobret., No. 39 (1979).

14. A. A. Ivanov and T. K. Soboleva, *Nonequilibrium Plasmochemistry* (Atomizdat, Moscow, 1978).
15. V. I. Babanin, A. S. Mustafaev, A. Ya. Ender, *et al.*, in *Proceedings of the International Thermionic Convertion Specialists Meeting, Eindhoven, 1975*, Contributed Papers, paper no. 10.6.
16. A. S. Mustafaev, A. P. Mezentsev, *et al.*, in *Low-Voltage Beam–Plasma Discharge: Model of the Electrode Sheath in a Low-Temperature Plasma* (Leningr. Gos. Iniv., Leningrad, 1984), VNTITs. No. 02850038192.
17. V. I. Demidov, A. S. Mustafaev, *et al.*, Zh. Tekh. Fiz. **59** (4), 55 (1989) [Sov. Phys. Tech. Phys. **34**, 414 (1989)].
18. A. S. Mustafaev, A. P. Mezentsev, *et al.*, Zh. Tekh. Fiz. **54**, 2153 (1984) [Sov. Phys. Tech. Phys. **29**, 1263 (1984)].
19. V. F. Lapshin and A. S. Mustafaev, Zh. Tekh. Fiz. **59** (2), 35 (1989) [Sov. Phys. Tech. Phys. **34**, 150 (1989)].
20. A. S. Mustafaev, V. F. Lapshin, and A. P. Mezentsev, *Ionization Processes Involving Excited Atoms*, Ed. by N. P. Penkin and A. N. Klyucharev (Leningr. Gos. Univ., Leningrad, 1989).
21. L. M. Biberman and V. S. Vorob'ev, *Kinetics of Nonequilibrium Low-Temperature Plasmas* (Nauka, Moscow, 1982; Consultants Bureau, New York, 1987).
22. E. W. McDaniel, *Collision Phenomena in Ionized Gases* (Wiley, New York, 1964; Mir, Moscow, 1967).
23. R. Deloche, P. Monchicourt, M. Chert, *et al.*, Phys. Rev. A **13** (3), 1140 (1976).
24. G. N. Gerasimov and G. P. Startsev, Opt. Spektrosk., No. 5, 834 (1974).
25. A. Z. Devdariani, V. I. Demidov, *et al.*, Zh. Éksp. Teor. Fiz. **84**, 1646 (1983) [Sov. Phys. JETP **57**, 960 (1983)].
26. L. A. Vaĭnshteĭn, I. I. Sobel'man, *et al.*, *Atom and Ion Excitation Cross Section by Electrons* (Nauka, Moscow, 1973).
27. F. G. Baksht, V. F. Lapshin, and A. S. Mustafaev, J. Phys. D **28**, 694 (1995).
28. F. G. Baksht, V. F. Lapshin, and A. S. Mustafaev, J. Phys. D **28**, 689 (1995).
29. F. G. Baksht, V. F. Lapshin, A. P. Mezentsev, and A. S. Mustafaev, Fiz. Plazmy **17**, 119 (1991) [Sov. J. Plasma Phys. **17**, 217 (1991)].
30. V. N. Tsytovich, *Nonlinear Effects in Plasmas* (Nauka, Moscow, 1967; Plenum, New York, 1970).
31. A. A. Ivanov, *Physics of Strongly Nonequilibrium Plasma* (Atomizdat, Moscow, 1977).
32. M. V. Nezlin, *Beam Dynamics in Plasma* (Énergoatomizdat, Moscow, 1982).
33. A. A. Vedenov, E. P. Velikhov, and R. Z. Sagdeev, Nucl. Fusion **2**, 465 (1962).
34. R. S. Churaev and A. V. Agapov, Fiz. Plazmy **6**, 422 (1980) [Sov. J. Plasma Phys. **6**, 232 (1980)].
35. V. F. Lapshin, A. P. Mezentsev, and A. S. Mustafaev, in *Proceedings of the XIX International Conference on Phenomena in Ionized Gases, ICPIG, Belgrade, 1989*, Vol. 4, p. 910.
36. V. F. Lapshin, A. P. Mezentsev, and A. S. Mustafaev, in *Proceedings of the XIX International Conference on Phenomena in Ionized Gases, ICPIG, Belgrade, 1989*, Vol. 2, p. 360.
37. V. F. Lapshin, A. P. Mezentsev, and A. S. Mustafaev, Pis'ma Zh. Tekh. Fiz. **15** (6), 54 (1989) [Sov. Tech. Phys. Lett. **15**, 229 (1989)].
38. A. S. Mustafaev, A. P. Mezentsev, and V. L. Fedorov, NATO ASI Ser., Ser. B **367**, 531 (1998).
39. V. I. Demidov, A. S. Mustafaev, *et al.*, Teplofiz. Vys. Temp. **27**, 818 (1989).

Translated by O. Khadin

Technical Physics, Vol. 46, No. 4, 2001, pp. 484–489. Translated from Zhurnal Tekhnicheskoĭ Fiziki, Vol. 71, No. 4, 2001, pp. 122–127.

EXPERIMENTAL INSTRUMENTS AND TECHNIQUES

Molding Loose Metal Particles into Briquettes with the Use of Short Pulses of High Density Current

K. B. Abramova*, Yu. N. Bocharov, S. D. Samuĭlov*, and I. P. Shcherbakov***

** Ioffe Physicotechnical Institute, Russian Academy of Sciences, Politekhnicheskaya ul. 26, St. Petersburg, 194021 Russia*

e-mail: abramova.mhd @pop.ioffe.rssi.ru

*** St. Petersburg State Technical University, Politekhnicheskaya ul. 29, St. Petersburg, 195251 Russia*

e-mail: elmf-dean@phtf.stu.neva.ru

Received March 13, 2000

Abstract—Theoretical estimates and experimental investigations were carried out on the process of molding a mixture of metal particles and a dielectric (air) into briquettes with the use of short pulses of high density current. Four groups of specimens were studied consisting of metal fragments and the dielectric in various proportions. In the experiments and the current and voltage oscillograms, the electrical resistance and the temperature of the specimens before and after passing the current were measured and their ultimate strength was determined. It has been found that the processes affecting the distribution of the current over the specimen cross section and the specimen inductance during the current pulse play an important role in molding briquettes of sufficient strength for transportation and processing. © *2001 MAIK "Nauka/Interperiodica".*

Composite materials, in particular, those comprising metals and dielectrics, find ever-growing use in technology. A number of fabrication processes have been proposed in which the required result is achieved by passing a high density electric current through a mixture of metal particles and a dielectric (the electric pulse strengthening of consumable extruded electrodes, the fabrication of porous articles from granules and powders, and the electric-arc melting of coke-ore mixtures at the initial stage [1–3]). However, while the phenomena and processes occurring in solid conductors through which an electric current of such a density and duration is passed cause irreversible changes in the conductor and have been studied in detail [4, 5], studies are only beginning of the more general case, in which a high density current is passed through a medium composed of a mixture of a conductor and a dielectric [1, 6, 7].

A high-density electric current passing through a solid conductor can either strengthen it by healing pores and microcracks and reducing the grain size, or bring about its destruction as a result of defect accumulation, disintegration, and dispersion. In a mixture of conducting and dielectric particles, a new effect is possible: the linking of separate conducting fragments and, as a result, strengthening of the material and increasing its conductivity. Still higher current densities can destroy the thin links between the fragments and reduce the conductor strength and conductivity, produce cracks, and even disperse the initial fragments.

In the present investigation, we study the processes taking place when a pulsed current of high density is passed through a conducting mixture consisting of loose metal particles with air filling the space between them when such processes lead to the molding of briquettes possessing sufficient strength for transportation and processing.

The electrical conduction in the mixture is spatially nonuniform, and its electrical resistance is mainly that of the links between the metal particles. Therefore, using short electric current pulses, the energy can be delivered mainly to the links between the metal particles. If this energy is sufficient, the links will be welded, resulting in the formation of a strong briquette. The accompanying heating of the material bulk may be insignificant. Such a process, on the one hand, saves energy and, on the other hand, makes the briquetting of materials that oxidize on heating (for example, titanium alloys) possible.

The material studied was metal cuttings compacted in a dielectric mold. This material was chosen for a number of reasons: it is simple to produce, it is cheap, and its starting parameters can easily be varied over a wide range for studies of the electric pulse briquetting process.

The cuttings are first compacted and then, maintaining the pressure, a pulse of electric current of high density is passed through them, thus binding the cuttings into a briquette. Compacting even with pressures of up 3–4 t/cm^2 does not give mechanical strength to the cuttings, which disintegrate into the initial fragments after the pressure is released. Strong specimens are formed only as a result of passing an electric current through a material preliminarily compacted to a certain density

1063-7842/01/4604-0484$21.00

[8–11]. This process can be useful, in particular, in metallurgy [12, 13] where cuttings are the basic source of secondary raw material, and its utilization using conventional technologies meets considerable difficulties. In addition, this process can serve as a basis for producing new materials for filters and getters, for noise absorption and attenuation of radio waves, and so on. Thus, the present study is of interest for both electrophysics and technology.

To calculate the dependence of the specimen strength on the magnitude and duration of the electrical current passed through the specimen, a simplified model similar to that in [6] will be used. Let us represent the heterogeneous composite material as a three-dimensional grid of resistors (with the links between the conducting fragments as the resistors and the fragments themselves as connecting wires) immersed in a continuous medium of density γ_c and specific electrical resistance ρ_c. The grid of resistors consists of $N = (H/h)(\gamma_c/\gamma_m)^{1/3}$ layers connected in series, each having $M = (S/s)(\gamma_c/\gamma_m)^{2/3}$ parallel connections (H is the specimen length; h, the mean thickness of the conductor fragments; S, the cross sectional area of the specimen; s, the mean area of the conductor fragments per link; and γ_m, the metal density). Let us assume that the link resistance is the resistance of a current constriction region $r = \rho_m/a$, where a is the diameter of the metal links [14] and ρ_m is the metal resistivity. Then, the average link size a_0 can be calculated using measured specific resistances of the compacted cuttings ρ_c and of the metal ρ_m. We assume, for simplicity, that the link sizes are uniformly distributed from 0 to $2a_0$.

To exclude heating of the specimen due to heat conduction, the current pulse must be short. Short current pulses give rise to the skin effect; the shorter the current pulse, the smaller the skin layer thickness. When the skin layer thickness becomes comparable with the size of metal particles, the model becomes inapplicable. Thus, the current pulse duration τ is defined by the inequality

$$\frac{30\mu\mu_0 h^2}{\rho_c}\left(\frac{\gamma_m}{\gamma_c}\right)^{2/3} < \tau < \frac{a_0^2 c\gamma_m}{10k}, \qquad (1)$$

where μ is the magnetic permeability of the specimen, c is the specific heat of the metal, and k is the thermal conductivity of the metal.

The link will weld when its temperature exceeds half that of the metal melting point (at released energy density e_1), because of higher ductility of the metal under applied pressure and the electrostatic attraction of the material developing in the link area with additional pressure arising due to thermal expansion of the metal. If the energy released in the link is sufficient for melting the metal (at released energy density e_2), the link will be destroyed as a result of magnetohydrodynamic instability.

The energy density released in a link drops with link size; therefore, if the considered model is valid, then the passing current will melt and destroy small-size links ($a < a_2$); larger links ($a_2 < a < a_1$) will become ductile, then weld, and give strength to the specimen; and still larger links ($a > a_1$) will remain essentially unchanged. The sizes $a_{1,2}$ can be calculated if the energy released in a link as a result of passing the current is equated to the energy necessary for adequate heating or melting of the link. After transformations, we have

$$a_{1,2} = \left(\frac{h^2}{e_{1,2}H^2\gamma_m^{1/3}\gamma_c^{2/3}}\int_0^\tau \frac{U^2(t)}{\rho_m(t)}dt\right)^{1/2},$$

where $U(t)$ is the voltage applied to the specimen and H is the specimen length.

The strength Q of an obtained specimen (that is, the maximum breaking load) depends on two factors: compaction and the electrical welding of the links. As a result of the latter, the specimen acquires strength defined by the force Q_i of the resistance to breaking. As an estimate of this force, one can use the total strength of all welded links in the conductor cross section, which is obtained by multiplying the number of links (M) by their area (a^2), and by the ultimate strength q of the link (the considered link is similar to that obtained in spot or projection welding, whose strength may achieve 90% of the metal strength. In the calculations, we assumed $q \sim 0.5$ of the ultimate strength of the metal). Taking into account the scatter in the link sizes [$f(a)$ is the distribution function of the link sizes; $f(a) = 1/2a_0$ at $a < 2a_0$ and $f(a) = 0$ outside this range], we obtain

$$Q_i = \int_{a_2}^{a_1} mqSa^2 f(a)da = \frac{qS\gamma_c^{2/3}(a_M^3 - a_2^3)}{6sa_0\gamma_m^{2/3}}.$$

The summation of the strength values is performed over all welded links from the smallest a_2 to the largest a_M. As for a_M, it is either the largest link a_1 that can be welded (if $a_1 < 2a_0$) or the largest link $2a_0$ that exists in the specimen (if $a_1 > 2a_0$).

As is known [12, 15], at high compaction pressures (300–900 MN/m^2, depending on the kind of material and properties of the cuttings) yielding densities of $\gamma_c > 0.5\gamma_m$, strong briquettes can be molded. In this case, the electrical current treatment can additionally increase the briquette strength. In specimens welded under lower compaction pressures, residual elastic stresses will exist due to the elasticity of the cuttings, which reduce the conductor strength. Hence, the force arising in the specimen as a result of compaction can be expressed roughly as $Q_c \sim 0.5PS(\gamma_c/\gamma_m - 0.5)$, where P

is the compaction force and S is the specimen cross sectional area. Thus,

$$Q = Q_c + Q_i. \quad (2)$$

According to this model, it should be expected that, at a small amplitude of the current pulse, strong specimens cannot be molded. As the current is increased, the size and strength of the welded links increase as well; when their total strength exceeds the residual elastic stress, formation of a briquette starts. With further growth of the current, the briquette strength rises as long as the condition $a_1 < 2a_0$ is met; subsequently, the briquette becomes less strong, because the size of the welded links do not grow any longer, although larger links will be destroyed.

The calculations performed on the basis of the model developed allowed us to estimate the necessary parameters of the experimental facility. The experimental setup consisted of a hand-operated press providing a compaction force of up to 2 t, a porcelain mold, and a pulsed electric current source (a capacitor bank of C = 15 mF, U_{max} = 5 kV, and E_{max} = 200 kJ) that supplied current pulses with a duration of 250 μs and an amplitude up to 500 kA at a low-ohmic load (~0.001 Ω).

The first experiments [8, 9] confirmed the possibility of molding strong specimens, namely, briquettes of cuttings of various metals and of alloys of different sort and quality, as well as the possibility of applying this process in metallurgy.

In the present study, four groups of specimens consisting of titanium cuttings were investigated. The cuttings of a 3M titanium alloy consisted of strips of various sizes with the following average parameters: $l \sim$ 30 mm, $b \sim 5$ mm, and $h \sim 1$ mm. The groups differed in density to which the initial material was compacted. Specimens in group 12 had a density of 0.5 g/cm^3 (12% Ti and the rest air), which was close to the bulk density of the cuttings. Specimens in the other groups had the following densities: group 16, 0.75 g/cm^3 (16% Ti); group 18, 0.8 g/cm^3 (18% Ti); and group 25, 1.1 g/cm^3 (25% Ti). The specimens were 50 mm in diameter and 100–140 mm in length. The magnitude of the current passed through the specimens was controlled by the capacitor bank voltage U_b. The experiments were carried out at the capacitor bank voltages of 250, 300, 500, 1000, 1500, …, 4000 V. In each of the experiments, we recorded oscillograms of the voltage across the specimens and the current passed through them; the electrical resistance of the specimens was measured before and after the passage of current, and the specimen temperature was measured in the latter case. The specimens underwent breaking tests to measure the maximum breaking load.

Breaking tests of the specimens were carried out under static axial loads using an RD-0.5 tensile-testing machine. Specially designed clamps were used to prevent the crushing of the briquettes when mounting them into the grips of the tensile-testing machine. The machine grips could be used in breaking tests at loads up to 500 N. Stronger specimens slipped out of the grips. Breaking of the specimen occurred outside the grips, although no centralizers were used. The results of the experiments are tabulated.

In the first subdivisions of the table, columns referring to different specimen groups with calculated values of the breaking loads are given. The calculations were made using a specially developed estimation model. Given in the next columns are the breaking load data from the tensile-testing machine and the ultimate strength values. It is seen from the table that there is a threshold in the process of mechanical strengthening of the specimens by the electric current. If the capacitor bank is charged at a low voltage (and, consequently, the currents are low), molding of the briquettes does not occur; at higher voltages, the briquettes acquire some strength; at still higher voltage, the strength of briquettes rises sharply and then grows slowly over a wide current range. A reduction of strength, according to the calculations, must take place at current values (the capacitor bank voltages) that are larger than those used in the experiment. In the experiment, this reduction was not observed except for a run at 4000 V with a specimen from group 12, for which both the calculation and the experiment indicated the reduction of strength.

The strength tests of the specimens show that the pulsed electric current treatment can yield strong briquettes of various densities. The calculation gives correct results for the initial strengthening stage; however, the calculated strength values are overestimated, apparently due to the fact that they are obtained by summation over all welded points, whereas, in the tests, these points are not loaded simultaneously.

The energy needed for molding strong briquettes is larger for composite mixtures of higher density.

The electric resistance of the specimens after the current treatment drops considerably (to half the initial value) both in strong briquettes and in specimens that disintegrated after release of the pressure. No dependence of the final resistance on the capacitor bank voltage and the current pulse amplitude is observed.

Results of the measurements of the volume-averaged temperature of the specimens are presented in Fig. 1. The temperature was measured by a thermocouple 2 min after termination of the current pulse; then, its value two minutes back in time was retraced. From the graphs, it is seen that, in the experiments described, the specimens of low density are heated only by 400°C, and denser specimens, by no more than 200°C. This is in good agreement with the amount of energy supplied to the load as deduced from the current oscillograms, as well as with the outward appearance of the specimens. These data also agree with the results of studies in which chemical analysis of the briquette metal was carried out [7, 8]. The results obtained conform to the process model proposed.

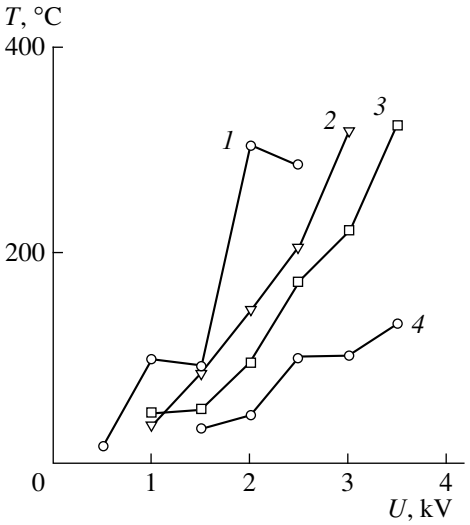

Fig. 1. Dependence of the specimen temperature T on the capacitor bank voltage U_b for different groups of specimens. The specimen density: (*1*) 0.5 (12% of the metal), (*2*) 0.75 (16% of the metal), (*3*) 0.8 (18% of the metal), and (*4*) 1.1 g/cm^3 (25% of the metal).

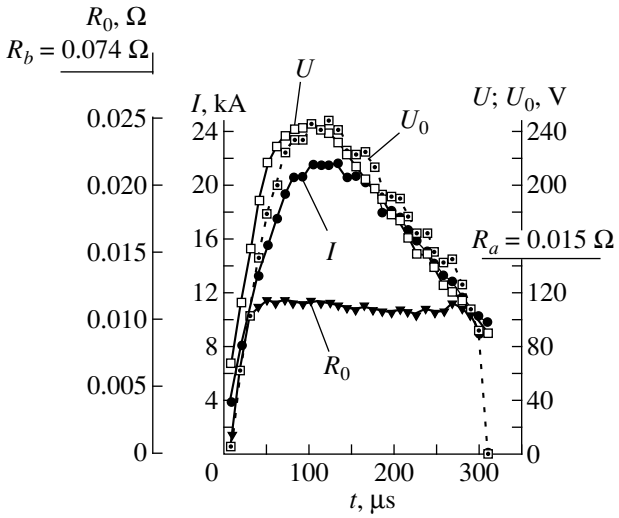

Fig. 2. Typical current and voltage oscillograms and variations of R_0 and U_0 with time for a group-12 specimen. U_b = 500 V; the specimen has zero strength and disintegrates when out of mold.

Figures 2–4 illustrate typical oscillograms of the current I and the voltage U for a specimen from group 12. Shown in the same figures are the values of $R_0 = U_0/I$ and the voltage U_0, which reflects processes occurring inside the specimen and is defined as $U_0 = U - L_{out}dI/dt$, where L_{out} is the fraction of the specimen inductance related to generation of the magnetic field outside the specimen (L_{out} was calculated by the specimen dimensions and the oscillograms of the current and voltage recorded for a metal tube of the same dimensions). The resistances of the compacted specimens before and after passing the current, R_b and R_a, respectively, are also given.

The form of the current oscillograms depends on the complex impedance of the discharge circuit. The volt-

Results of breaking tests of specimens under static axial load

U_b, V	E, kJ	Sample 12 (γ_c = 0.5 g/cm^3, W = 170 g, P = 700 kN/m^2)			Sample 16 (γ_c = 0.75 g/cm^3, W = 200 g, P = 1400 kN/m^2)			Sample 18 (γ_c = 0.8 g/cm^3, W = 250 g, P = 1800 kN/m^2)			Sample 25 (γ_c = 1.1 g/cm^3, W = 250 g, P = 6000 kN/m^2)		
		strength of specimens			strength of specimens			strength of specimens			strength of specimens		
		calculation, N	experiment		calculation, N	experiment		calculation, N	experiment		calculation, N	experiment	
			N	kN/m^2		N	kN/m^2		N	kN/m^2		N	kN/m^2
250	0.48	–140	*										
300	0.68	–5	**										
500	1.9	110	35	16	–88	*		–1260	*				
1000	7.5	400	30	14	1290	170	77	–750	15	7	–170	**	
1500	17		190	86	1480	350	160	550	420	190	–134	5	2
2000	30	410	180	82	2010	450	200	2030	540	240	5200	360	160
2500	47	1500	310	140				3890	>1140	>510	8100	940	430
3000	68	1250	110	50	1520	>450	>200						
3500	92	1370	>260	>120									
4000	120	6	**										

* Strong specimen is not formed (cuttings can be removed).

** Specimen formed partially, not the entire volume (separate fragments and cuttings can be removed).

W is the briquette weight.

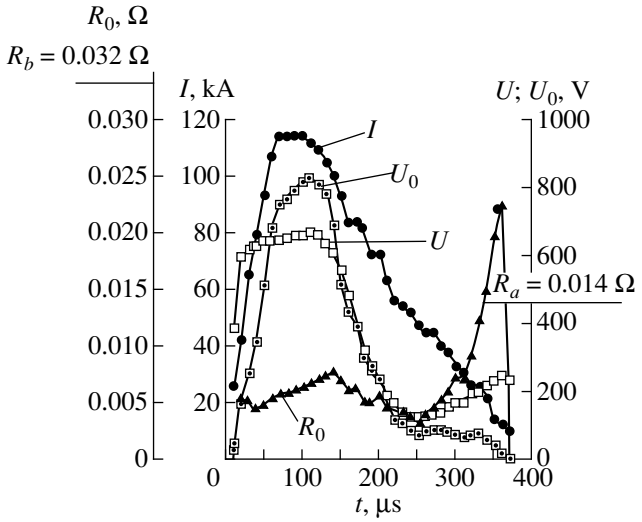

Fig. 3. Same as in Fig. 2. U_b = 1500 V; the breaking load is 190 N.

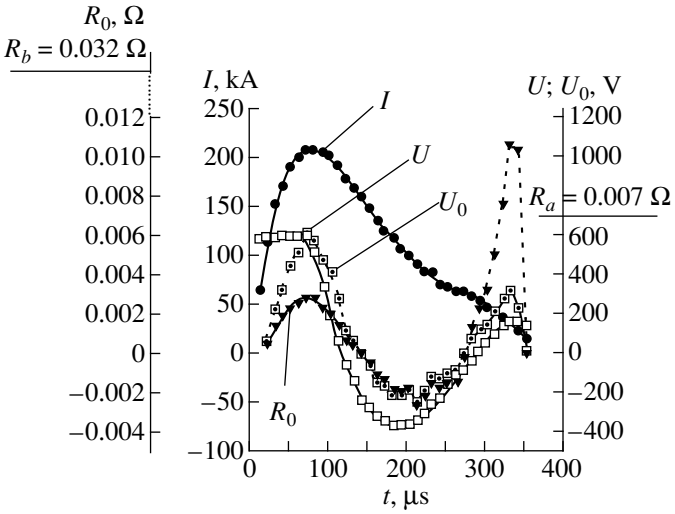

Fig. 4. Same as in Fig. 2. U_b = 2500 V; the breaking load is 310 N.

age oscillograms are of greater interest as they are more sensitive to the processes occurring in the specimen.

With the capacitor bank charged to a low voltage of 250–500 V (see Fig. 2), the voltage oscillograms are identical to the current oscillograms, and the specimen resistance R_0 is practically constant over the current pulse duration.

As the capacitor bank voltage is increased (to 1000–1500 V), the character of oscillograms of the voltage across the specimen changes (Fig. 3). After a steep rise to 500–600 V, the voltage ceases to increase, although the current continues to grow; that is, the voltage curve forms a plateau followed by a steep voltage drop. At higher capacitor bank voltages (1000–4000 V), the height and extent of the voltage plateau are practically unchanged, but the amplitude of the voltage backswing drastically increases (Fig. 4). The specimen resistance R_0 does not stay constant, remaining appreciably less than the initial resistance R_b while the current is passed, and at the end of the first half-period of the current pulse, it becomes close to the final specimen resistance R_a measured after passing the current.

The oscillograms for the material compacted to a higher density have approximately the same form. The only difference is that the voltage backswing amplitude decreases with increasing specimen density.

The character of the oscillograms changes at the same value of the capacitor bank voltage at which the specimens begin to acquire mechanical strength. Thus, the experimental results confirm the initial assumption concerning processes giving mechanical strength to the specimens and allow us to develop them still further.

A short time (hardly a few microseconds) after applying the voltage to a specimen, the breakdown of thin oxide films occurs both at the periphery of the existing *a*-spots and probably beyond. As a result, the specimen resistance drops. The entire observed process then develops in a conducting system.

If the voltage applied to a specimen is low, the energy released in the links is sufficient for destroying only a limited number of small-size links and for softening and strengthening of a small number of larger links. This does not result in an appreciable change of the specimen resistance or noticeable strengthening of the specimen. After the current is terminated, the oxide film is partially restored, eliminating some of the links, and the specimen resistance rises ($R_b > R_a > R_0$).

If the voltage across a layer of metal and the current through each link (the linking *a*-spot) exceed certain values, then the destruction of some of the link, followed by an increase in the current through other links, causes an avalanche-like destruction of the small links. As a result, the current passing through the conductor is redistributed among the large links, and their conductivity becomes higher as they soften and spread over larger area. Now, the current no longer passes through a continuous medium, but a considerable part of it flows through separate channels. At this point, the specimen inductance rises appreciably and the growing inductance of the current channel being formed limits the rate of the current redistribution process.

To conclude, in forming briquettes from a mixture of loose metal particles and a dielectric by compaction with the application of high-density short current pulses, the current redistribution processes are important.

The study was supported by the Russian Foundation for Technological Development (contract no. 149/97 of April 12, 1998) and the Federal Grant-in-Aid Program (project KO854).

REFERENCES

1. A. V. Pakhomov, B. P. Peregud, A. K. Sarychev, and A. P. Vinogradov, Mater. Res. Soc. Symp. Proc. **195**, 217 (1990).
2. Ya. E. Geguzin, *Physics of Agglomeration* (Nauka, Moscow, 1984).
3. *Thermal Electric Equipment: Handbook*, Ed. by A. P. Al'tgauzen (Énergiya, Moscow, 1980).
4. K. B. Abramova, N. A. Zlatin, and B. P. Peregud, Zh. Éksp. Teor. Fiz. **69** (6), 2007 (1975) [Sov. Phys. JETP **42**, 1019 (1975)].
5. V. A. Burtsev, N. V. Kalinin, and A. V. Luchinskiĭ, *Electrical Explosion of Semiconductors and Its Application in Electrophysical Plants* (Énergoizdat, Moscow, 1990).
6. T. N. Dul'nev, Inzh.-Fiz. Zh. **41** (1), 172 (1981).
7. S. A. Baranov, Zh. Tekh. Fiz. **69** (7), 128 (1999) [Tech. Phys. **44**, 853 (1999)].
8. K. B. Abramova, S. D. Samuĭlov, and Yu. A. Filin, RF Patent No. 2 063 304, 1994, Byull. Izobret., No. 19 (1996).
9. K. B. Abramova, S. D. Samuĭlov, and Yu. A. Filin, Tsvetn. Met. (Moscow), No. 12, 70 (1998).
10. K. B. Abramova, S. D. Samujlov, and Yu. A. Filin, in *Abstracts of the 9th World Conference on Titanium, St. Petersburg, 1999*, p. 8.
11. K. B. Abramova, S. D. Samuĭlov, V. V. Antipov, *et al.*, in *Proceedings of the IV All-Russia Scientific and Practical Conference with International Participation "Novel in Ecology and Security of Vital Functions," St. Petersburg, 1999*, Ed. by N. I. Ivanov, Vol. 2, p. 57.
12. V. P. Tamurov, S. M. Yaroshevskiĭ, M. I. Levin, and S. G. Rudevskiĭ, *Processing Equipment of Secondary Metals* (Metallurgiya, Moscow, 1976).
13. V. V. Sergeev, A. B. Bezukladnikov, and V. M. Mal'shin, *Metallurgy of Titanium* (Metallurgiya, Moscow, 1979).
14. R. Holm and E. Holm, *Electric Contacts Handbook* (Springer-Verlag, Berlin, 1958; Inostrannaya Literatura, Moscow, 1961).
15. Yu. N. Skvortsov, E. I. Morozov, and V. N. Usov, Tekhnol. Legk. Splavov, No. 5, 112 (1971).

Translated by N. Mende

Technical Physics, Vol. 46, No. 4, 2001, pp. 490–491. Translated from Zhurnal Tekhnicheskoĭ Fiziki, Vol. 71, No. 4, 2001, pp. 128–129.

BRIEF COMMUNICATIONS

Anomalous Behavior of Arsenic Ions Implanted into Silicon at 850°C

K. D. Demakov and V. A. Starostin

Russian Research Centre Kurchatov Institute, pl. Kurchatova 1, Moscow, 123182 Russia

e-mail: vastarostin@mail.ru

Received May 3, 2000; in final form, September 26, 2000

Abstract—The concentration profile of arsenic in silicon was found to have two peaks at large depths. An implantation model is suggested. A comparison with results for other species is made. It is shown that mechanisms behind low- and high-temperature migrations of defect–vacancy pairs are similar to each other (D_{dv} is about 10^{-12} cm^2/s). © *2001 MAIK "Nauka/Interperiodica".*

INTRODUCTION

The behavior of implanted ions in semiconductor materials according to ion current density and ion energy, temperature of the material, and chemical properties of interacting substances is of great theoretical and applied importance. In this work, we studied arsenic implantation (40 keV, 40 μA/cm^2) into a silicon target at a high temperature (850°C).

EXPERIMENT

Irradiation was carried out in an ILU-3 ion-beam accelerator [1]. During irradiation, the target (single-crystal silicon) was heated with a special high-temperature ion collector. The implantation dose was 2×10^{17} ion/cm^2. The ion distribution in the target was studied by X-ray diffraction analysis combined with layer-by-layer etching. The profile measured is depicted in the figure. It differs from the conventional profiles by the presence of two "deep-seating" maxima.

THEORETICAL MODEL

To explain impurity drift to a depth that is much greater than the ion range at implantation, we invoked the modified Beloshitsky model [2, 3]. In this model, it is assumed that diffusion transfer is accompanied by impurity capture by vacancies. Note that, in the presence of a source, the purely diffusion equation does not yield a peak beyond the ion range. Importantly, the model is nonequilibrium: diffusion proceeds in parallel with defect generation and annihilation. These processes are described by the set of coupled equations

$$\partial n_a/\partial t = D_a \partial^2 n_a/\partial x^2 - n_a n_v k_{\text{cap}} + n_c n_d k_{\text{act}} + j_0 \exp(-(R_p - x + x_0)^2/2\Delta R_p^2)/\sqrt{2\pi}\Delta R_p, \quad (1)$$

$$\partial n_c/\partial t = n_a n_v k_{\text{cap}} - n_c n_d k_{\text{act}}, \quad (2)$$

$$\begin{aligned} \partial n_d/\partial t &= D_{dv}\partial^2 n_d/\partial x^2 - n_c n_d k_{act} - n_v n_d k_{\text{ann}} + j_0 N \sigma_d \Theta(R_p - x + x_0), \\ \partial n_v/\partial t &= D_{dv}\partial^2 n_v/\partial x^2 - n_a n_v k_{\text{cap}} - n_v n_d k_{\text{ann}} + j_0 N \sigma_d \Theta(R_p - x + x_0), \end{aligned} \quad (3)$$

$$x_0 = -v_b t, \quad N = 5.04 \times 10^{22}\ \text{cm}^{-3}, \quad \sigma_d = 3.52 \times 10^{-16}\ \text{cm}^2. \quad (4)$$

Here, $\Theta(x)$ is a unit step; N is the density of silicon

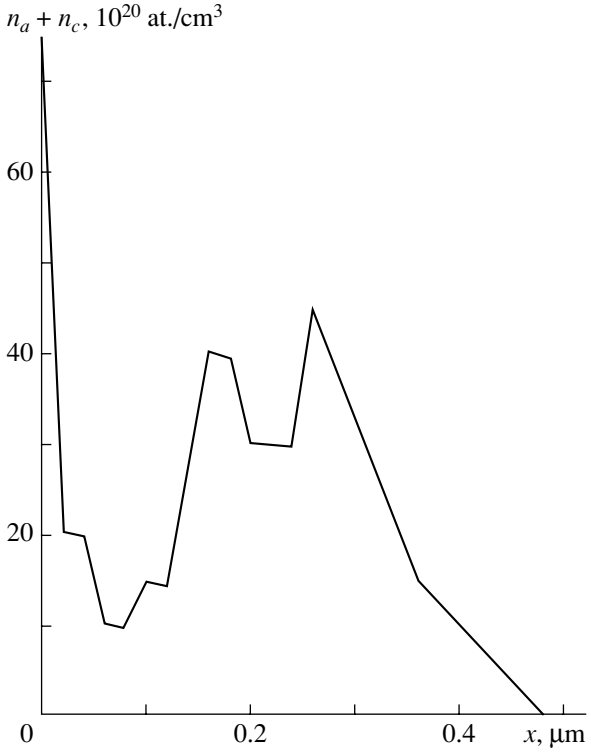

Figure.

1063-7842/01/4604-0490$21.00

Table 1

D_a, $cm^2/s \times 10^{-11}$	D_{dv}, $cm^2/s \times 10^{-11}$
0.199	0.1070
53.630	0.1037

Table 2

k_{cap}, $cm^3/s \times 10^{-23}$	k_{act}, $cm^3/s \times 10^{-23}$	k_{ann}, $cm^3/s \times 10^{-23}$
3.005	13.315	3.852
19.582	6.743	1.872

nuclei; σ_d is the tentative cross section of defect formation; R_p and ΔR_p is the projected ion range and ion struggling, respectively; and D_a, D_{dv}, k_{cap}, k_{act}, and k_{ann} are free model parameters that have the obvious meaning of diffusion coefficients of impurity and defects and rate constants for impurity capture by vacancies, impurity activation by interstitials, and vacancy–interstitial annihilation.

The boundary condition for the impurity concentration was set equal to zero; in other words, the impurity was believed to evaporate from the surface, following the experimental observation. It was assumed that the flux of interstitials causes the material boundary to shift with a rate v_b (Stefan-type problem). For interstitials and vacancies, the initial conditions and those at the opposite boundary were also zero. It should be noted that, within our model, an experimental profile can be described by only two sets of free parameters. System (1)–(4) with the above initial and boundary conditions was numerically solved by the finite difference method. The free parameters were adjusted by the least squares technique so as to provide the best fit to experimental profiles. The associated data are summarized in Tables 1 and 2.

CONCLUSION

Comparison with Results for Other Species

In [4], concentration profiles of molecular and atomic hydrogen implanted (600 eV, 2.5 μA/cm^2) at 40 K were studied using the $^1H(^{15}N, \alpha\gamma)^{15}C$ resonance reaction. We obtained similar diffusion coefficients for Frenkel pairs (0.107×10^{-11} cm^2/s). Noteworthy, however, is the much higher quasi-chemical activity of molecular hydrogen (compared with atomic hydrogen) in reactions of impurity capture, Frenkel pair annihilation, and impurity activation (by a factor of 76.21, 83387.1, and 12.194, respectively). We also determined the diffusion coefficients for molecular and free hydrogen in Si (2.522×10^{-11} and 1.512×10^{-11} cm^2/s, respectively). The low- and high-temperature diffusion coefficients for Frenkel pairs in Si nearly coincide (Table 1, column 2). These values are close to 0.101×10^{-11} cm^2/s, which was obtained by us from data [5] for deuterium implantation (27 keV, 400 μA/cm^2) into diamond-like carbon films at room temperature. The diffusion coefficients of deuterium in C (2.612×10^{-11} cm^2/s) and molecular hydrogen in Si are also close to each other. The similarity of C and Si properties was reported in [2].

ACKNOWLEDGMENTS

The authors thank O.L. Golovin for taking the concentration profile.

REFERENCES

1. V. M. Gusev, N. P. Busharov, S. M. Naftulin, and A. M. Pronichev, Prib. Tekh. Éksp., No. 4, 19 (1969).
2. V. A. Starostin, Fiz. Khim. Obrab. Mater., No. 5, 104 (1999).
3. P. A. Aleksandrov, E. K. Baranova, V. V. Beloshitsky, *et al.*, Radiat. Eff. **88**, 249 (1986).
4. S. Fabian, S. Kalbitzer, Ch. Klatt, *et al.*, Phys. Rev. B **58** (24), 16144 (1998).
5. T. Ahlgren, E. Vainonen, J. Likonen, and J. Keinonen, Phys. Rev. B **57** (16), 9723 (1998).

Translated by V. Isaakyan

Technical Physics, Vol. 46, No. 4, 2001, pp. 492–494. Translated from Zhurnal Tekhnicheskoĭ Fiziki, Vol. 71, No. 4, 2001, pp. 130–132.

BRIEF COMMUNICATIONS

The Ion-Optical Scheme of a Portable Mass Spectrometer

V. T. Kogan, G. Yu. Gladkov, and O. S. Viktorova

Ioffe Physicotechnical Institute, Russian Academy of Sciences, Politekhnicheskaya ul. 26, St. Petersburg, 194021, Russia

Received May 12, 2000; in final form, June 5, 2000

Abstract—An ion-optical scheme for a portable magnetic double-focusing mass spectrometer that makes it possible to analyze several components simultaneously over a wide mass range (the mass-spectrograph operating mode) is proposed. This scheme effectively solves the research and technological problems involving the analysis of rapidly varying compositions. *© 2001 MAIK "Nauka/Interperiodica".*

INTRODUCTION

The level of mass-spectrometric investigations using portable instruments equally depends both on the main characteristics of analyzers (sensitivity and resolving power) and on their weight, dimensions, power consumption, the rate of operation, and their reliability under the field operation conditions. These instruments can be most effectively used in ecological monitoring of the environment and in the production process monitoring in industry. A design of the instrument must provide for the full automation of the measurement process and for real-time analysis. Static mass spectrometers to a large extent meet the requirements to a portable design [1–4]. First of all, these are mass spectrometers with homogeneous prismatic or sector fields created by permanent magnets. With a small-size magnet, the former type provides for a rather high resolution due to a high dispersing power of the mass analyzer [5], while the latter type ensures a good resolution due to obeying the conditions of angle and energy focusing in the mutually perpendicular (as a rule) magnetic and electric fields. The Mattauch–Herzog scheme [6], which is among the most popular ones, allows for the simultaneous analysis of substances over a wide mass range in the mass-spectrograph operating mode. This mode has many advantages over the regime used in sector-type mass spectrometers and makes it possible to improve the sensitivity of analyzer and/or its operation speed.

DECIDING ON A MASS-SPECTROMETER SCHEME

This paper is concerned with realizing a mass spectrometer scheme that, on the one hand, should possess all advantages of the devices described previously [3, 4] meeting the portability requirements and, on the other hand, make it possible to simultaneously analyze substances over a wide mass range (as in the case of the instruments implementing the Mattauch–Herzog scheme), being superior to the latter by possessing a markedly smaller angle of the sector magnet. The combination of these features in one instrument does not impair its resolving power and allows a wide range of components to be measured.

The scheme discussed in [4] is presented in Fig. 1. It comprises source *1*, cylindrical capacitor *2*, and sector magnet *3*, where the field boundary facing the capacitor is selected at right angles to the principal optical axis of the instrument for the sake of the ease of computation and design. The properties of the scheme were investigated by numerically calculating its parameters over a wide range of their values. This allowed us to choose an appropriate shape of the exit boundary for the magnetic system: its shape offers the simultaneous ion focusing on a detector over the whole range of mass numbers at a low weight and low dimensions of the mass analyzer.

The optimum values of the angle β_{opt} for the magnet exit boundary vs. the magnet sector angle γ are presented in Fig. 2a. For any angle γ chosen, the maximum resolving power is obtained when a certain relationship among γ and $\beta(\gamma)_{opt}$ is obeyed. This relationship depends on the ratio r_0/r_m, where r_0 and r_m are the radii of particle trajectories in the electric and magnetic fields, respectively. For $r_0/r_m = 0.4$, the values of β_{opt} fall on boundary *1*, and for $r_0/r_m = 1.5$, they fall on boundary *2*. (The chosen values of r_0/r_m are boundary ones within the region under consideration, being

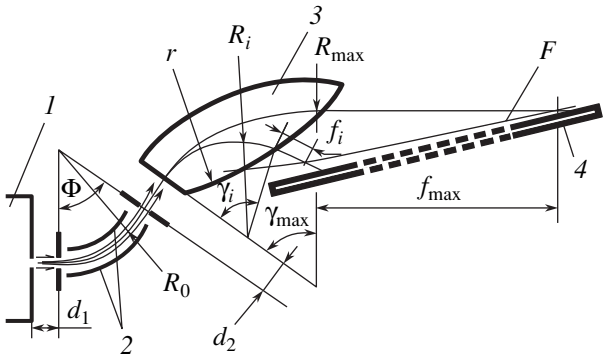

Fig. 1. Mass spectrometer scheme presented in [4].

1063-7842/01/4604-0492$21.00 © 2001 MAIK "Nauka/Interperiodica"

defined by the relationship among the values of the magnet dispersing power and the aberration of the electrostatic analyzer that provides a required resolving power of the instrument within these boundaries at its small size and light weight.) For r_0/r_m ranging between 0.4 and 1.5, β_{opt} varies through the range of values between these boundaries.

The maximum resolving power $(M/\Delta M)_{max}$ of the scheme expressed in terms of the relative units of its maximum value $\{(M/\Delta M)_{max}\}_{max}$ vs. the magnet sector angle γ for the magnet exit boundaries at various values of the inclination angle β = (*1*) β_{opt}, (*2*) 0, and (*3*) $(\pi - \gamma)/2$ are presented in Fig. 2b. (All the points in the curves are provided by double angle and energy focusing of the first order with an allowance for the finite width of a source exit slit.)

As is seen from Fig. 3, when the magnet straight-line exit boundary chosen passes through the intersection point of the principal optical axis and a magnet exit window (0–0'), the value of angle β shown in Fig 2a, curve *3*, meets the condition $\beta = (\pi - \gamma)/2$ and, at $r_0/r_m = 1.5$, the scheme resolving power (see Fig 2b, curve *3*) peaks at the values of γ at which the angle β is close to β_{opt}. As is also seen from Fig 2b, at normal incidence of an ion beam on the magnet entrance boundary, the Mattauch–Herzog scheme ($\gamma = \pi/2$, $\beta = \pi/4$) ranks below the ones with a markedly smaller value of γ (where the focusing properties of the magnet exit boundary are used) in the value of the resolving power.

However, at such a magnet exit boundary, we are forced to significantly cut down the range of mass numbers being measured within the most attractive region with low values of γ, because we need to form a uniform field at the magnet entrance and, at the same time, to position the lines of scheme focuses beyond the magnetic field limits. This is due to the need for decreasing the size of the magnet exit windows (0–0') shown in Fig. 3. To keep a wide range of mass numbers being measured, the magnet exit boundary has been positioned in the actual device as shown in Fig. 3. Then, for particles of different mass numbers m_i, the values of β_i and γ_i (depending on the mass number) meet the condition $\beta_i \le (\pi - \gamma_i)/2$.

A comparison between $\beta(\gamma_i)$ and $\beta_{opt}(\gamma_i)$ shown in Fig. 2a reveals that, for the chosen configuration of the fields with the united linear exit boundary of a magnetic system, the maximum resolving power of the mass spectrometer can be provided only for $\gamma < 75°$ when the condition given by $\beta(\gamma_i) = \beta_{opt}(\gamma_i)$ is met. This condition cannot be met over the whole range of mass numbers being measured, and the requirements on the resolving power of the portable instrument are conventionally defined by the requirements for the analysis of ions of the maximum mass number being measured; therefore, we will restrict ourselves to the condition given by $\beta(\gamma_{max}) = \beta_{opt}(\gamma_{max})$. However, in this case, for the design having a small sector angle γ, choosing a curved magnet exit boundary allows us to obtain a higher resolving power for ions with the maximum mass number and to keep the resolving power of particles with lower mass numbers at a level necessary for their resolution. The overall scheme configuration of the proposed mass spectrometer is presented in Fig. 4, where R_{max} is the radius of an ion trajectory for ions with the maximum mass number being measured; R_0 and Φ are the mean radius and the sector angle of a cylindrical capacitor, respectively; r is the radius of curvature for a magnet exit boundary; d_1 is the distance from the ion source to the electrostatic capacitor; and d_2 is the distance from the capacitor to the magnet. The values of R_0 and R_{max} are chosen based on the requirements to the range of mass numbers measured and to the resolving power of

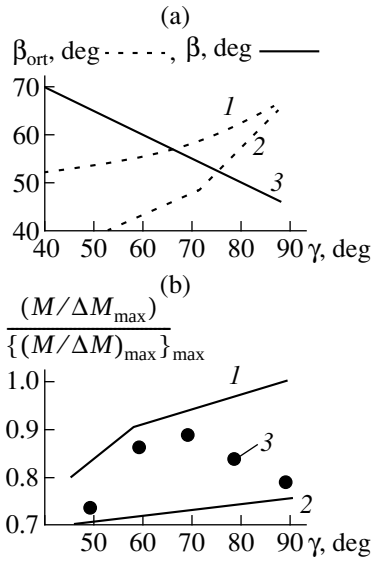

Fig. 2. Characteristics of the scheme presented in [4]: (a) the optimum angles β_{opt} of the magnet exit boundary providing the maximum resolving power of the scheme (*1*, *2*) and the angles β (*3*) of the exit boundary (coinciding with the chord of an ion trajectory in the magnet) vs. magnet sector angle γ (the angles are expressed in degrees); (b) the relative resolving power vs. magnet sector angle γ at various values of magnet-exit-boundary angle β = (*1*) β_{opt}, (*2*) 0, and (*3*) $(\pi - \gamma)/2$.

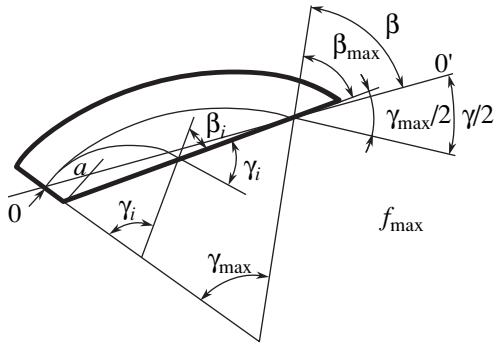

Fig. 3. Sector magnet with a straight-line exit boundary.

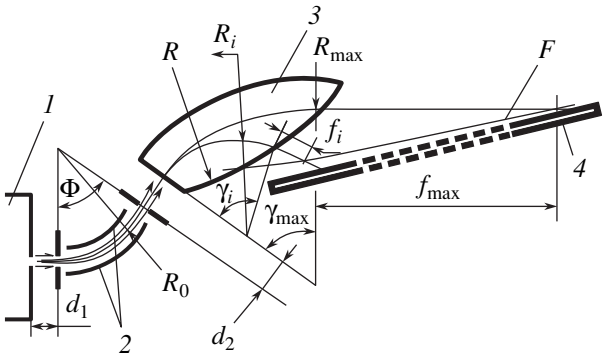

Fig. 4. The proposed ion-optical scheme: (*1*) ion source, (*2*) cylindrical capacitor, (*3*) magnet pole tips, and (*4*) detector; *F* is the focal line.

the instrument; γ_{max} is taken so as to meet the requirements to the resolving power, instrument dimensions, and its weight; and r is determined by the optimum resolving power for small and large mass numbers. The limits of the ranges of the values of d_1 and d_2 are chosen with consideration for the requirements on the portable instrument size, and the value of Φ is taken with consideration for the optimum relationship between it and γ_m. The values of d_1, d_2, and Φ are determined from a numerical calculation of the ion-optical scheme providing the maximum resolving power. The parameters of the scheme under consideration are taken from the ranges defined by

$$\begin{gathered}\pi/3 \geq \gamma_{max} \geq \pi/4,\\ (R_{max}^2/R_0)\tan(3\gamma_{max}/2) \geq r \geq R_{max},\\ R_{max}/3 \geq d_1 \geq 0, \quad R_{max}/2 \geq d_2 \geq 0,\\ \gamma_{max}/2 + \pi/8 \geq \Phi \geq \gamma_{max}/2 + \pi/8 - \pi/18.\end{gathered} \tag{1}$$

CALCULATION OF THE PARAMETERS

The parameters of the mass spectrometer are calculated successively in several steps. First of all, the mass spectrometer is numerically calculated within the approximation of the scheme with a straight-line exit window of a magnet at $\beta = 0$ for ions of the maximum mass numbers in the range being measured. On the one hand, the individual requirements to the instrument dimensions and weight for gaining the resolving power needed are considered in the computation; on the other hand, the special features of the emittance (that is, spatial, angular, and energy distributions of beam particles) for an ion source used in the instrument are taken into account. In the process of the calculation with the use of the procedure presented in [3, 4], the values of parameters can be taken in the wide ranges given by $\gamma_{max} = \pi/4$–$\pi/3$, $d_1/R_{max} = 0.0$–1.0, $d_2/R_{max} = 0.0$–1.0, $\Phi = \pi/6$–$\pi/3$, and $R_0/R_{max} = 0.3$–2.0. The calculation gives us a set of the values of d_1, R_{max}, d_2, Φ, R_0, and γ_{max} that offer the maximum resolving power for the prescribed conditions of the instrument scheme. Next, the shape of the window exit boundary for an actual magnet is selected in accord with relationships (1) on retention of the parameters chosen in the numerical calculation. The given computing procedure for the portable mass-spectrometer parameters provides for the simultaneous analysis of several components in complicated mixtures.

EXPERIMENTAL

Using the computing procedure described above and the well-known output characteristics of an electron-impact ionization source (at a 0.1-mm-wide exit slit, the angular spread is ±2° and the energy spread is ±2%), we obtained the values of the ion-optical parameters ($d_1 = 18$ mm, $R_0 = 125$ mm, $\Phi = 42°$, $d_2 = 21$ mm, $\gamma_{max} = 52°$, $R_{max} = 90$ mm, and $r = 90$ mm) and constructed a prototype mass spectrometer. With the use of this setup, various components in a wide range of masses (from methane to chlorobenzene) were analyzed. The resolving power of this instrument for the maximum mass number of the range measured was 145 on the base level for a numerical calculation and 134 on a 3% level for experiments. For the separation of heavier ions with mass numbers up to 500 and above, the resolving power of the instrument can be improved by restricting the mass analyzer entrance aperture or the ion source emittance [4].

CONCLUSION

A portable mass spectrometer ion-optical scheme offering advantages over the well-known ones is presented. First, the sector angle and, therefore, the mass-analyzer magnet weight are well below those in the Mattauch–Gerzog scheme. Second, in contrast to the devices with small angles of a magnetic analyzer, our scheme makes it possible to perform simultaneous multicomponent chemical analysis without sacrificing the instrument characteristics.

REFERENCES

1. Yu. I. Ermolaev, G. N. Zastenker, V. T. Kogan, *et al.*, Kosm. Issled. **24**, 192 (1986).
2. A. O. Nier, Int. J. Mass Spectrom. Ion Processes **66**, 55 (1985).
3. V. T. Kogan, A. K. Pavlov, Yu. V. Chichagov, *et al.*, Field Anal. Chem. Technol. **1** (6), 331 (1997).
4. V. T. Kogan, A. K. Pavlov, M. I. Savchenko, and O. E. Dobychin, Prib. Tekh. Éksp., No. 4, 141 (1999).
5. V. M. Kel'man, I. V. Rodnikova, and L. M. Sekunova, *Static-Field Mass-Spectrometers* (Nauka, Alma-Ata, 1985).
6. J. Mattauch and R. Herzog, Z. Phys. **89**, 786 (1934).

Translated by B. Malyukov

Technical Physics, Vol. 46, No. 4, 2001, pp. 495–497. Translated from Zhurnal Tekhnicheskoĭ Fiziki, Vol. 71, No. 4, 2001, pp. 133–135.

BRIEF COMMUNICATIONS

Formation of Oriented Cadmium Telluride Films on an Amorphous Substrate under Extremely Nonequilibrium Conditions

A. P. Belyaev, V. P. Rubets, and I. P. Kalinkin

St. Petersburg State Institute of Technology, Zagorodnyĭ pr. 49, St. Petersburg, 198013 Russia
e-mail: belyaev@tu.spb.ru

Received June 20, 2000

Abstract—The results of the first experiments related to oriented CdTe film growth on a nonorienting substrate (glass) cooled to negative Celsius temperatures under extremely nonequilibrium conditions are reported. Technological, electron-diffraction, and X-ray investigation results are presented. A condensation diagram characterized by two regions within which the growth rate of films is anomalously low is obtained. The films grown at these rates are shown to possess a nearly perfect crystalline texture. The formation processes of the oriented films on an amorphous substrate under the above conditions are adequately interpreted in the context of a heteroepitaxy soliton model. *© 2001 MAIK "Nauka/Interperiodica".*

INTRODUCTION

As a rule, oriented films are obtained at elevated temperatures (in order to achieve the required mobility of particles) under conditions that are close to equilibrium. However, recently, exceptions to this rule have been observed. In particular, we unexpectedly obtained highly oriented films during condensation of cadmium telluride on a cooled mica substrate under extremely nonequilibrium conditions [1, 2]. Afterwards, we managed to obtain fairly well oriented films by the same method even on an amorphous substrate. In what follows, the first results of studying this phenomenon are reported.

EXPERIMENTAL TECHNIQUE

The specimens under investigation were prepared in a vacuum chamber (with residual pressure of 10^{-3} Pa) by the quasiclosed volume method on a glass substrate cooled by liquid nitrogen [1]. The reactor-evaporator temperature was equal to 900 K. The substrate temperature was measured with a copper–constantan thermocouple. To control overheating of the substrate surface, we applied the technique from [2]. The deposition rate was evaluated from experimental data on film thickness and growth time.

Thickness measurements were performed using an MII-4 interferometer. To investigate the structure, we used an ÉMR-100 electron-diffraction camera and a DRON-4 X-ray diffractometer using CuK_α radiation at room temperature. Surface morphology investigations were carried out using a PÉM-100 electron microscope.

EXPERIMENTAL RESULTS

We studied the formation of CdTe films under extremely nonequilibrium conditions during CdTe condensation on a glass substrate. The investigations involved technological experiments, surface morphology studies with an electron microscope, and X-ray and electron diffraction studies. The main results are presented in Figs. 1–4.

A typical film surface in the final growth stage is shown in Fig. 1, which demonstrates layer-by-layer and normal formation. One can distinctly see nuclei (disperse particles of a new layer) on the surface of an already formed continuous layer of the film.

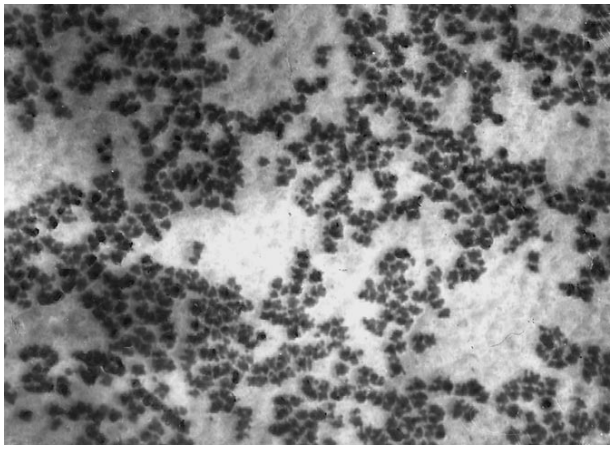

Fig. 1. A fragment of a typical CdTe-film surface in the final growth stage. The substrate temperature T_S = 210 K. Magnification is ×70 000.

1063-7842/01/4604-0495$21.00

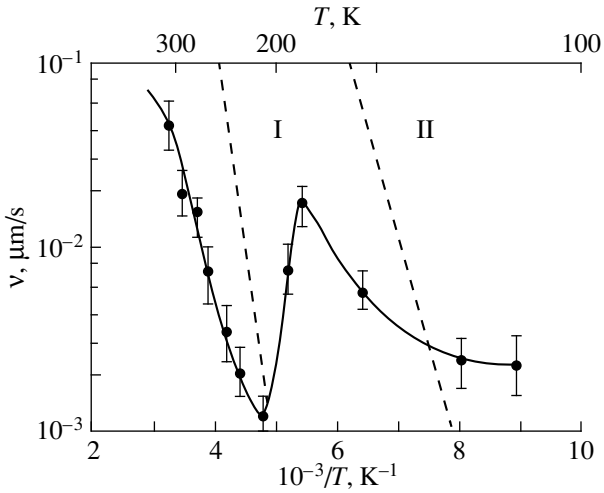

Fig. 2. The condensation diagram of CdTe films on a glass substrate under extremely nonequilibrium conditions.

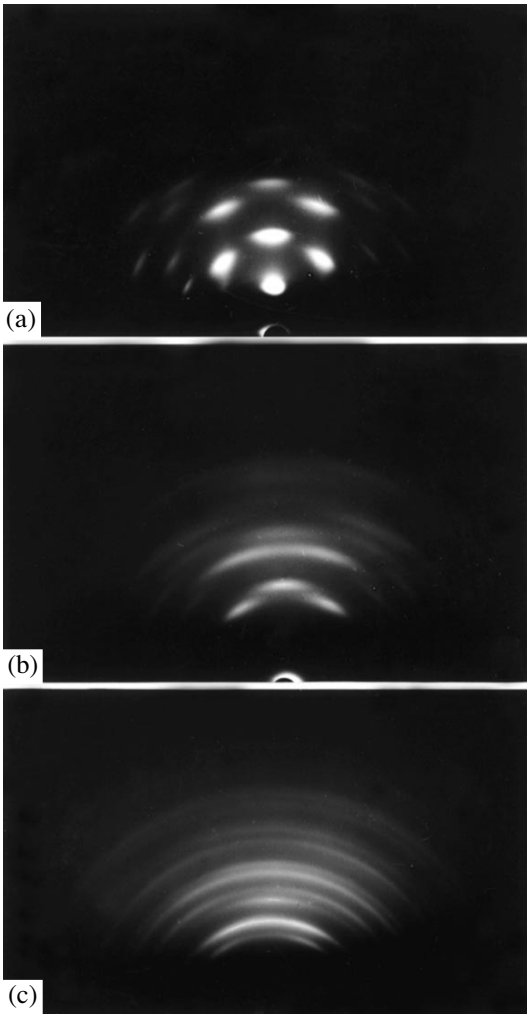

Fig. 3. Electron diffraction patterns of CdTe *h*-thick films grown under extremely nonequilibrium conditions on a glass substrate at the temperatures (a, b) T_s = 210 and (c) 250 K; *h* = (a, c) 0.8 and (b) 0.1 μm.

Figure 2 is a condensation diagram that shows two regions of anomalously low condensation rates. The film growth rate decreased by several orders of magnitude in these regions. The thick films (with a thickness greater than 0.8 μm) grown under these conditions were distinguished by good crystal quality. This can be seen from Fig. 3a, where a typical electron diffraction pattern of a 0.8-μm-thick film is shown. In the earlier growth stage, the same film had lower crystal perfection. In Fig. 3b, this is confirmed by the typical electron-diffraction pattern of a 0.1-μm-thick film. In addition, the earlier stage of film growth was characterized by a very high rate of layer formation. We failed to obtain an island film directly on a glass substrate under all conditions covered by the condensation diagram in Fig. 2.

We note that the films grown outside the modes of anomalous condensation rate had polycrystalline structure even if these films were thick. This is evident from Fig. 3c, in which a typical electron-diffraction pattern of a 0.8-μm-thick film grown at the substrate temperature of T_s = 250 K is shown.

The structural distinction between oriented films grown in different regions of the anomalous condensation rate is illustrated in Fig. 4. The portions of typical X-ray diffraction patterns from the films grown at the substrate temperatures of T_s = 140 and 210 K are shown in Figs. 4a and 4b, respectively. Their comparison indicates that the films have different crystallographic growth directions.

DISCUSSION

Formation of an oriented layer on an orienting substrate under highly nonequilibrium conditions consists of nucleation, condensation, incorporation, coalescence, and merging into a continuous layer. Nucleation and incorporation are the characteristic features of the above process [1, 2]. For such supersaturation levels, the former occurs in a vapor phase, whereas the latter results from the motion of disperse particles of a new phase due to a soliton mechanism of mass transport at low temperatures [3]. The combined effect of these factors leads to the correlated orientation of disperse particles and to a low rate of layer formation.

Emergence of solitons is caused by a certain relation between lattice constants of a disperse particle $a(T_r)$ and a substrate $b(T_s)$. In the case of their closeness, the needed relation between them can be attained by varying the substrate temperature T_s in view of its distinction from the disperse particle temperature T_r.

Theoretically, the necessary condition for the origination of solitons was derived only for a one-dimensional model. The corresponding specific expression

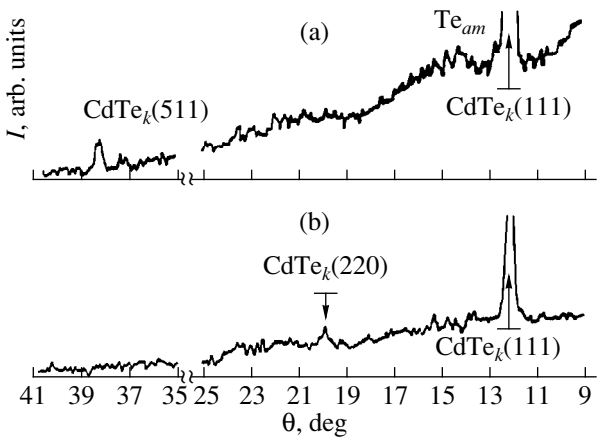

Fig. 4. A portion of an electron diffraction pattern of CdTe 1-μm-thick films grown at the substrate temperatures of T_s = (a) 140 and (b) 210 K.

with allowance for the temperature dependence of the lattice parameters $a(T_r)$ and $b(T_s)$ is written as [2]

$$\frac{a(T_r) - b(T_s)}{b(T_s)} > (2/\pi)^{3/2}\sqrt{f/\lambda a(T_r)}\ldots, \qquad (1)$$

where f and λ are the parameters characterizing the interaction forces between atoms of a disperse particle and a substrate and those between the substrate atoms, respectively. At the onset of film formation on an amorphous substrate, the origination of solitons is impossible due to the absence of a regular crystal lattice on the substrate surface. However, in the case of normal layer-by-layer growth, all film layers (except for the first layer) are already formed on even highly defective crystalline substrates (we recall that, under the above conditions, layers are produced by the condensation of disperse particles rather than individual atoms). Then, at certain substrate temperatures T_s satisfying the conditions (1), the origination of solitons is quite possible. In view of their features [4], solitons enhance the mobility of disperse particles and delay the dissipation of their excess energy for a finite period of time, which results in a smaller accommodation coefficient and in the formation of oriented layers.

In our case, the experimental conditions completely correspond to the aforesaid. The oriented films were grown only at the strictly specified substrate temperatures (when conditions (1) were satisfied). When the oriented layers were formed, the integral growth rate abruptly dropped. In Fig. 2, the soliton energy was slowly dissipated and the temperature of disperse particles remained high for a finite time. It follows that the accommodation coefficient was small. The crystal perfection of a film became better as its thickness increased. In Fig. 3, the film grew layer-by-layer, and the healing of preceding layer defects occurred with each new layer. The initial stage of film growth was characterized by a high rate (when solitons could not yet emerge). In two temperature ranges (I and II) of the oriented growth, our films had two different crystallographic directions of the layer growth: in Figs. 2 and 4, the constants $a(T_r)$ and $b(T_s)$ were different in the contact plane of lattices in diverse temperature ranges.

CONCLUSIONS

(1) Under extremely nonequilibrium conditions of the condensation of films on an amorphous cooled substrate, there are regimes that give rise to the formation of oriented layers.

(2) Formation of oriented films on an amorphous substrate under the above conditions is well described in the framework of a heteroepitaxy soliton model.

ACKNOWLEDGMENTS

This study was supported by the Russian Foundation for Basic Research, project no. 99-03-32676.

REFERENCES

1. A. P. Belyaev, V. P. Rubets, and I. P. Kalinkin, Fiz. Tverd. Tela (St. Petersburg) **39** (2), 383 (1997) [Phys. Solid State **39**, 333 (1997)].
2. A. P. Belyaev, V. P. Rubets, and I. P. Kalinkin, Neorg. Mater. **34** (3), 281 (1998).
3. S. A. Kukushkin and A. V. Osipov, Fiz. Tverd. Tela (St. Petersburg) **36** (5), 1461 (1994) [Phys. Solid State **36**, 799 (1994)].
4. R. K. Dodd, J. C. Eilbeck, J. Gibbon, and H. C. Morris, *Solitons and Nonlinear Wave Equations* (Academic, New York, 1982; Mir, Moscow, 1988).

Translated by Yu. Vishnyakov

Technical Physics, Vol. 46, No. 4, 2001, pp. 498–502. Translated from Zhurnal Tekhnicheskoĭ Fiziki, Vol. 71, No. 4, 2001, pp. 136–140.

BRIEF COMMUNICATIONS

Study of the Effect of Manganese Impurities on Dielectric Characteristics of BSTO Films

S. F. Karmanenko*, A. I. Dedyk*, N. N. Isakov*, A. S. Gordeichuk*, A. A. Semenov*, L. T. Ter-Martirosyan†*, and J. Hagberg**

** St. Petersburg State University of Electrical Engineering, St. Petersburg, 197376 Russia*

*** Microelectronics Laboratory, University of Oulu, Oulu, Finland*

Received June 29, 2000

Abstract—Capacitance voltage and current voltage characteristics of BSTO ferroelectric films containing a manganese dioxide impurity (~ 1.5–2 mol %) are compared to those of impurity-free samples. It is shown that in Mn-doped samples $\tan\delta$ drops to 10^{-3}, and the dependence of $\tan\delta$ on the applied voltage changes as well. IVCs of these samples are strictly ohmic and do not show a nonlinearity at high voltages. A mechanism is proposed of the effect of Mn on the charge state of the defects comprising oxygen vacancies in BSTO films. © *2001 MAIK "Nauka/Interperiodica".*

Studies of the effect of various impurities on RF and microwave dielectric characteristics of $Ba_xSr_{1-x}TiO_3$ (BSTO) films started in the 1970s [1] in a number of institutions in this country [2, 3] and abroad [4, 5]. These studies dealt mainly with such impurities as Zr and Sn [2–5] and Zn, Ca, and Mg [1, 6]. In recent years, physicotechnological studies of ferroelectric films (FEF) for radioelectronic applications were resumed. For example, BSTO ceramics with additions of manganese oxide was experimented on [7], but no noticeable improvement of the dielectric characteristics was achieved. A decrease of less than 0.01 in the dielectric loss tangent ($\tan\delta$) was observed only for considerable additions of manganese oxide powder (up to 50 mol %). In this case, the dielectric permeability decreased considerably and the FEF capacitor became practically untunable.

In [3], single crystals of $SrTiO_3$ (STO) synthesized in a gas plasma with various amounts of manganese dioxide (~0.1 mol %) added to the molten mixture were studied. It was found that the dielectric permeability of the starting undoped $SrTiO_3$ crystals in FEF capacitors after application of an electric field up to ~10^5 V m^{-1} and return to a zero field was lower by a factor of 1.5–2; i.e., a strong hysteresis was observed, $\eta = C_0 - C(0)/C_0$. The hysteresis displayed by capacitance voltage characteristics (CVC) was ascribed to the remanent field due to the space charge resulting from the deficit of oxygen [8, 9].

Alongside deviations of the cation composition and the deformational strain [10], the FEF characteristics are strongly influenced by the state of the oxygen sublattice. Oxygen vacancies in FEF give rise to electrical conduction (leakage currents), accelerate aging, and increase the dielectric losses [11]. It is found that crystals doped with manganese reduce the initial capacitance of planar capacitors [4] and hysteresis in CVC and $\tan\delta$.

The initial capacitance decreases with increasing manganese content, from 5320 pF in undoped samples to 1140 pF in samples containing ~0.1 mol % Mn. With increasing manganese content, the tunability $K = (C(0)/C(500\text{ V}))$ drops appreciably: from 19 for undoped samples to 4.2 for samples containing 0.1 mol % manganese (at $T = 4.2$ K). It should noted that there is practically no hysteresis in the $C(U)$ curves for samples doped with manganese.

In [5], the effect of small additions of manganese oxide or manganese carbonate on characteristics of BSTO films produced by laser sputtering of a ceramic target was studied. For films containing 1% manganese impurity, very good characteristics have been obtained. BSTO/LAO structures measured at $f = 10$ GHz and $T = 300$ K had a tunability of 56% or ~1.5–1.6. The starting dielectric permeability was $\varepsilon = 1800$ and $\tan\delta \approx 0.006$. The underlying physical mechanisms are outside the scope of this report.

Processes causing considerable changes of the dielectric characteristics of piezocapacitors containing manganese impurities are related to the compensation of the positively charged oxygen vacancies. But it remains unclear how this mechanism operates and what the reason is for the substantial difference in manganese concentrations required to produce noticeable changes of the dielectric characteristics in crystals and films.

To study these problems, technological processes of the ion-plasma sputtering of BSTO targets containing

† Deceased.

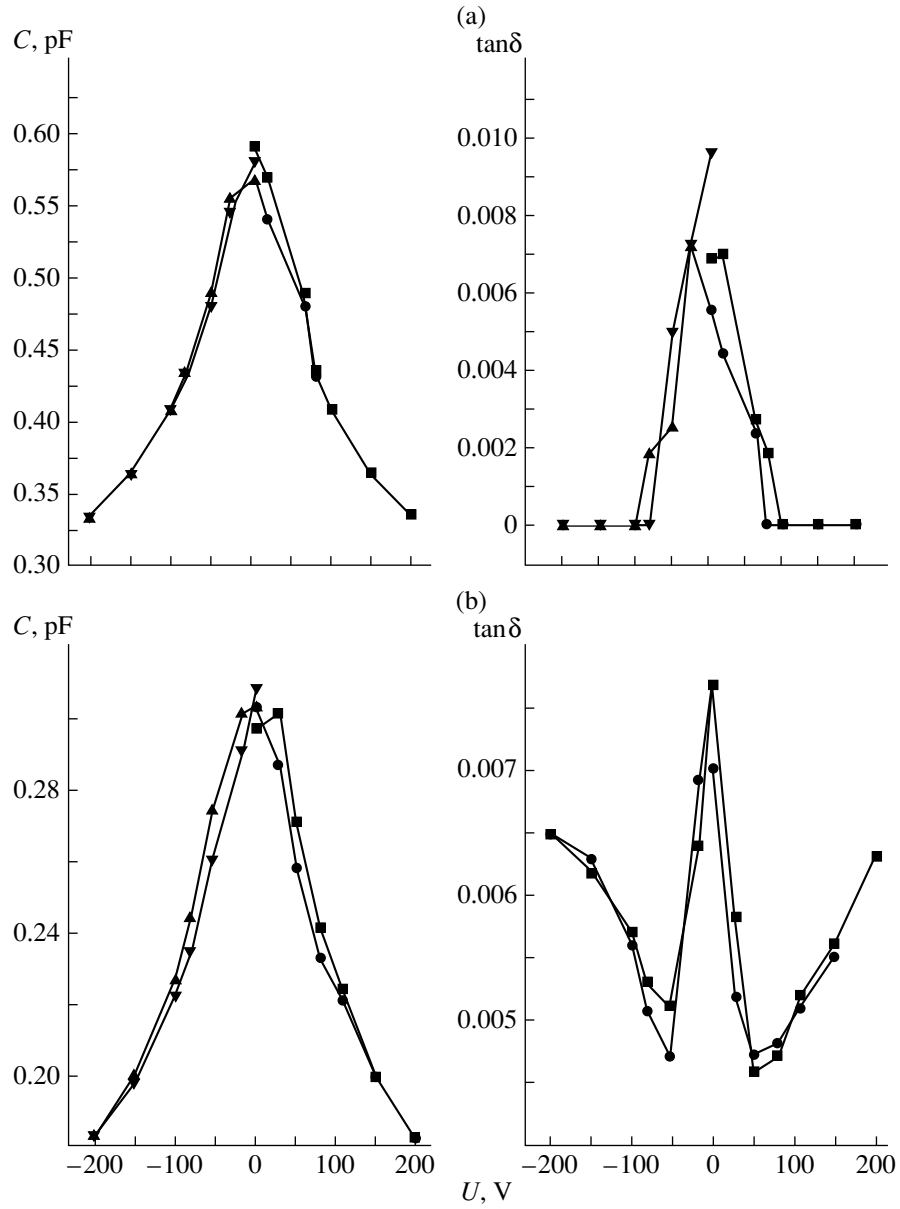

Fig. 1. Capacitance–voltage characteristics and plots of $\tan\delta$ versus applied voltage measured on BSTO/α-Al_2O_3 planar capacitors: (a) without impurities; (b) containing ~2 mol % manganese oxide.

0, 1.0, 1.75, and 2.0 wt % MnO_2 impurity at the ratio Ba/Sr ≈ 1 were carried out and films were grown. The composition and structure were analyzed using X-ray diffraction, medium energy ion backscattering (MEIBS) [10], and Raman scattering. Planar capacitors with copper plates were fabricated using ferroelectric films grown on LAO substrates, sapphire, and polycor (polycrystalline Al_2O_3). Measurements of the dielectric characteristics of the capacitors were carried out at a frequency of 1 MHz. Figure 1 presents a comparison of the dielectric characteristics of the films with and without manganese impurity grown on $[10\bar{1}2]$-α-sapphire. The technological process was carried out in the following manner: the target was $Ba_xSr_{1-x}TiO_3$ of composition $x = 0.55$; the sputtering ambient was oxygen; the substrate temperature was ~650°C; and the film growth rate ~0.1 μm/h. Some films were annealed in oxygen ex situ at 900°C (Fig. 1a). As a result of annealing, $\tan\delta$ dropped significantly by a factor of 2.5–3, but the tunability became less (by 30–50%). At voltages above 100 V, $\tan\delta$ of planar FEF capacitors dropped to ~5×10^{-4}. CVCs of all annealed samples displayed larger hysteresis.

In BSTO films containing manganese impurities (Fig. 1b), hysteresis is more pronounced (reaching ~5%) and the behavior of $\tan\delta$ with bias voltage is sig-

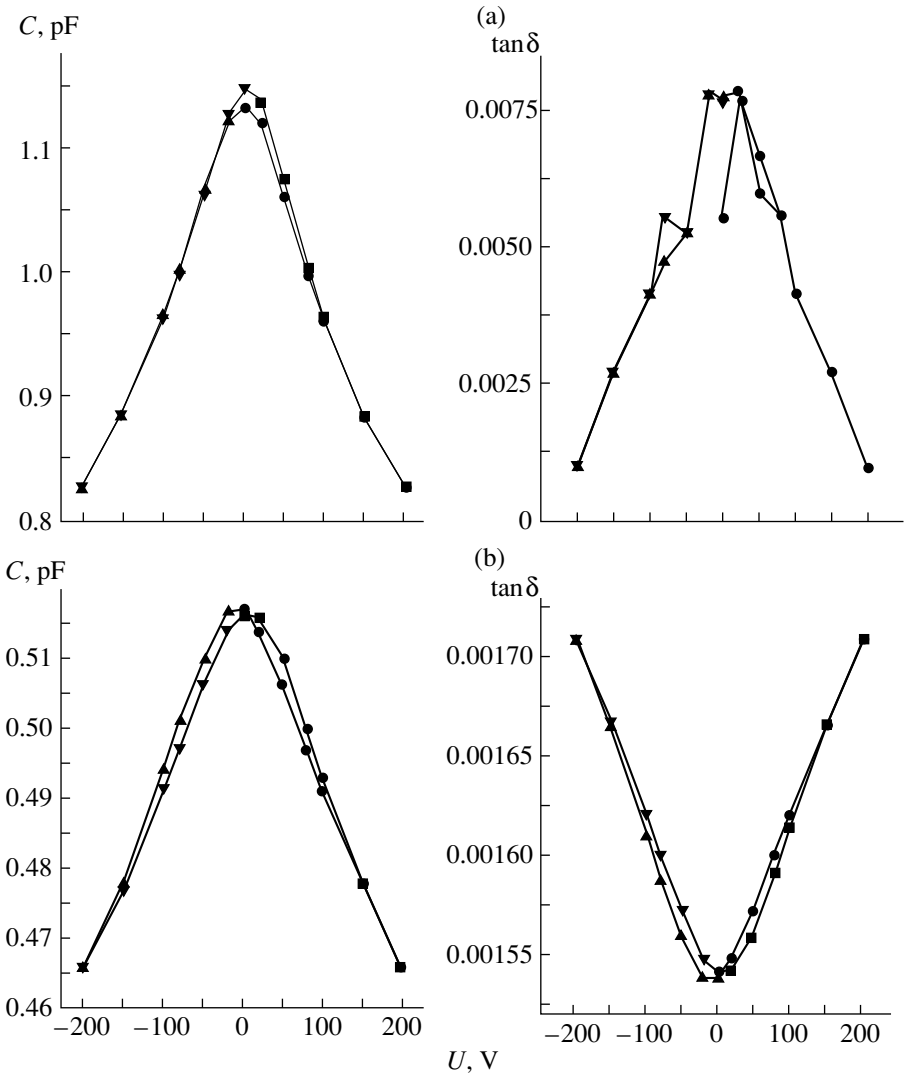

Fig. 2. Capacitance–voltage characteristics and plots of $\tan\delta$ versus applied voltage measured on BSTO/LAO planar capacitors: (a) without impurities; (b) containing ~2 mol % manganese oxide.

nificantly different. In undoped films, there was no lowering of losses in electric fields up to 10^5 V/cm; in some samples, $\tan\delta$ increased considerably at 3×10^4 V/cm after a drastic drop. Most of the films containing 1.5–2.0% manganese had $\tan\delta$ below 5×10^{-4} at radio frequencies.

A different behavior is seen in BSTO films grown on LAO substrates (Fig. 2). Annealing had no noticeable effect on CVCs and the behavior of $\tan\delta(T)$, but the manganese impurity is significantly reduced ε. The dependence $\tan\delta(U)$ undergoes changes. Bias voltage causes an increase in $\tan\delta$, which is probably an indication that the loss mechanism does not involve charged defects [12].

In studies of BSTO : Mn films, the use of various methods for determining Mn content meets considerable difficulties, because of the similarity between Ti ($z = 22$) and Mn ($z = 25$). Use of the characteristic X-ray radiation can only indicate the presence of manganese. RS spectra did not reveal any differences between BSTO films with the same Ba/Sr ratio grown on various substrates and the doped films. X-ray diffraction analysis of FEFs grown on polycor has shown the presence in the samples of the $Ba_{0.5}Sr_{0.5}(Mn_{0.33}, Ti_{0.67})O_{3-2.84}$ phase with a lattice parameter of ~0.395 nm, which is close in structure to the major $BaSrTiO_3$ phase.

Thus, the measurements and analytical studies have shown that manganese ions can partially substitute for titanium in the crystal lattice. It is known that titanium in $BaSrTiO_3$ has a valency of (+4), but can also be found at a valency of (+3) [13]. In barium titanate films, a modified phase of $Ba(Ti^{+3}_{0.48}Ti^{+4}_{0.52})O_3$ can form, which has an imperfect tetragonal structure. The defect phase

can be identified by splitting of the (200) and (002) reflections in X-ray patterns and represents a tetragonal distortion of the perovskite cell. A manganese ion is comparable in size to a titanium ion and has a close value of electronegativity (~1.5) [14]; however, it is an ion that can have different valencies.

If it is assumed that Mn^{+2} occupies the position of Ti^{+4} forming a substitutional defect, then its charge state can be represented by the following model (Fig. 3): $(Ba_xSr_{1-x})^{2+}Ti^{4+}_{1-y}[Mn_{Ti}]^{2-}_y O^{2-}_{3-z}[V_O]^{2+}_z$.

Oxygen vacancies might introduce shallow acceptor levels in the band gap of barium strontium titanate. Ionization of these levels activates the conduction process. Partial substitution of manganese for titanium ions compensates the positive charge of oxygen vacancies, which also affects the sample conductivity. This is confirmed by IVCs of the capacitors. The measurements of IVCs were made at direct current employing registration of the voltage drop across a reference resistor located in the electrometer input unit.

Shown in Fig. 4 are IVCs of three FEF capacitors measured at room temperature. The capacitors were formed on various substrates: polycor, sapphire, and lanthanium aluminate. The dependences for pure and doped samples have important differences related, possibly, to the concentration ratios and sufficiency of the doping level in crystals and films for compensation of the vacancies. A mere 0.01 mol % of manganese impurity produces considerable changes in the dielectric characteristics of a single crystal, whereas as much as 1 mol % of the manganese oxide will be needed to produce the same changes in BSTO films.

It is important whether a Mn atom occupies a lattice site, as shown in Fig. 3, or whether it is in an interstitial position at the block boundary or in the intergranular space. There being no intergranular phase in single crystals, the impurity atoms in the melt from which the crystal is grown have a greater chance of being incorporated in the crystal lattice.

In films with a high degree of structural perfection and homogeneity, the content of the interblock phase is considerably less than in polycrystalline films. An example of such structures is provided by samples grown under identical regimes on LAO and polycor substrates; their CVCs and IVCs are shown in Figs. 2 and 4.

IVCs of undoped samples have distinct nonlinear portions beginning at a voltage of ~80 V. Similar nonlinearity of IVCs has been observed in conductivity studies of STO single crystals not intentionally doped [15] and was explained by the Frenkel–Poole hopping conduction mechanism. Apparently, in undoped BSTO films as well, an activation-type electrical conduction takes place, which involves oxygen vacancies. The presence of linear portions in the IVCs suggests that samples grown on lanthane aluminate have lower conductivity.

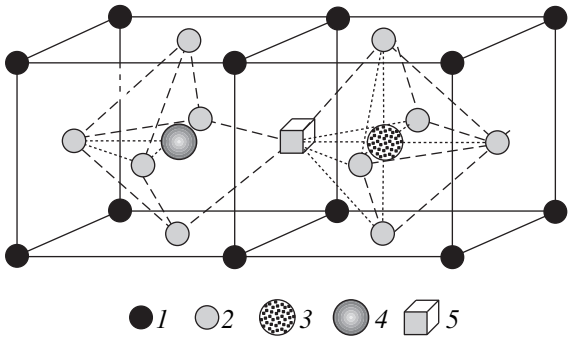

Fig. 3. Model of compensation of the oxygen vacancy $[V_O]^{2+}$ with a substitutional point defect $[Mn_{Ti}]^{2-}$ yielding $(Ba_xSr_{1-x})^{2+}Ti^{4+}_{1-y}[Mn_{Ti}]^{2-}_y O^{2-}_{3-z}[V_O]^{2+}_z$. *1*, Ba(Sr)–*A*; *2*, O *X*; *3*, Ti *B*; *4*, Mn_{Ti}—substitutional defect; *5*, oxygen vacancy.

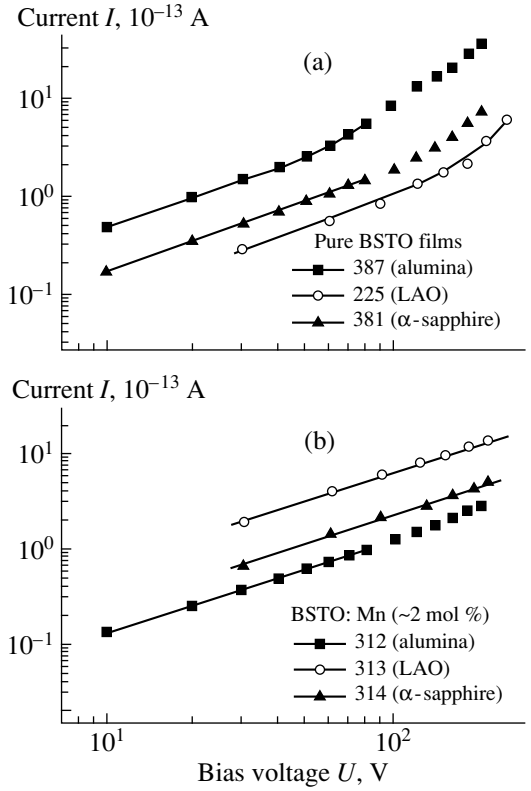

Fig. 4. Current-voltage characteristics of FEF capacitors based on (a) impurity-free BSTO films and (b) BSTO films containing ~2 mol % manganese oxide.

In IVCs of Mn-containing films (~2 mol %) practically no nonlinear portions are observed; so, in this case, it can be assumed that the centers responsible for the activation mechanism of electrical conduction are compensated by the Mn impurity. The lowest conductivity is found in BSTO/polycor structures.

Features of the dependence $\tan\delta(U)$ for BSTO/polycor, BSTO/LAO, and BSTO/α-Al_2O_3 structures indicate different defect formation mechanisms. Lowering of the dielectric loss factor with bias voltage is, possibly, evidence of excess positive space charge in the FEFs. Electron injection occurring as a result of voltage applied to the plates compensates the charge and lowers $\tan\delta$. In doped BSTO/LAO films, in contrast, $\tan\delta$ increases with U. Possibly, the doping level of BSTO/LAO films (~2 mol %) is above the optimum; i.e., the concentration of the donor impurity $N(Mn_{Ti})$ is larger than $N[V_O]$.

In doped BSTO/polycor and BSTO/α-Al_2O_3 structures, the charge due to oxygen vacancies is compensated at low bias voltages. In electric fields of $\sim 3 \times 10^4$ V/cm, the space charge is compensated and, moreover, the injected electrons produce a charge of opposite sign (–), which increases the tangent of dielectric loss angle.

Thus, the analysis of the CVCs and IVCs of planar capacitors made from EFEs of various compositions can be used to study features of defect formation in perovskite films and interfaces. Knowledge of the processes of formation and compensation of the space charge helps to improve the technology of forming tunable device structures based on ferroelectric films.

ACKNOWLEDGMENTS

The study was supported by the Interface project (no. 98055) of the State Program on Superconductivity and by the Program "Higher School Research on Industrial Technologies (Electronics), project no. K0416 of the St. Petersburg State University of Electrical Engineering.

REFERENCES

1. A. V. Borisov, V. I. Molchanov, and Yu. M. Poplavko, *Novel Piezo- and Ferroelectric Materials and Their Application* (Znanie, Moscow, 1972), pp. 87–91.
2. T. N. Verbitskaya, L. M. Aleksandrova, and E. I. Shirobokova, Izv. Akad. Nauk SSSR, Ser. Fiz. **29**, 2104 (1965).
3. V. D. Belyaev, A. Ya. Zaĭonchkovskiĭ, A. S. Ruban, *et al.*, Izv. Leningr. Élektrotekh. Inst. im. V. I. Ul'yanova **236**, 72 (1978).
4. H.-D. Wu and F. S. Barnes, Integr. Ferroelectr. **22**, 291 (1998).
5. L. C. Sengupta and S. Sengupta, Ferroelectr. Newslett., Nos. 1–4, 4 (1996).
6. Y. M. Poplavko and V. Meriakri, Electromagn. Waves Electron. Syst. **2** (6), 35 (1997).
7. J. Synowszynski, L. C. Sengupta, and L. H. Chiu, Integr. Ferroelectr. **22**, 341 (1998).
8. V. Ya. Kunin, A. N. Tsikin, and N. A. Shturbina, in *Proceedings of Conference "Physics of Dielectrics," Leningrad, 1973*, Vol. 2, p. 190.
9. R. Waser and D. N. Smyth, in *Ferroelectric Thin Films: Synthesis and Basic Properties* (Gordon and Breach, Sidney, 1996), p. 150.
10. S. F. Karmanenko, A. I. Dedyk, N. N. Isakov, *et al.*, Pis'ma Zh. Tekh. Fiz. **25** (19), 50 (1999) [Tech. Phys. Lett. **25**, 780 (1999)].
11. J. F. Scott, C. A. Araujio, B. M. Melnick, *et al.*, J. Appl. Phys. **70** (1), 382 (1991).
12. O. G. Vendik and L. T. Ter-Martirosyan, Zh. Tekh. Fiz. **69** (8), 93 (1999) [Tech. Phys. **44**, 954 (1999)].
13. V. P. Dudkevich and E. G. Fesenko, *Physics of Ferroelectric Films* (Rost. Gos. Univ., Rostov-on-Don, 1979).
14. E. M. Sokolovskaya and L. S. Guzeĭ, *Chemistry of Metals* (Mosk. Gos. Univ., Moscow, 1986).
15. A. I. Dedyk, A. M. Prudan, and L. T. Ter-Martirosyan, Fiz. Tverd. Tela (Leningrad) **27** (6), 1615 (1985) [Sov. Phys. Solid State **27**, 973 (1985)].

Translated by B. Kalinin

Technical Physics, Vol. 46, No. 4, 2001, pp. 503–504. Translated from Zhurnal Tekhnicheskoĭ Fiziki, Vol. 71, No. 4, 2001, pp. 141–142.

BRIEF COMMUNICATIONS

Condensation in Pulsed Free Jets of Silane–Argon Mixture: Time Characteristics of the Pulses

A. E. Zarvin, N. G. Korobeĭshchikov, V. Zh. Madirbaev, and R. G. Sharafutdinov

Novosibirsk State University, ul. Pirogova 2, Novosibirsk, 630090 Russia

e-mail: zarvin@phys.nsu.ru

Received August 28, 2000

Abstract—Condensation of a 5% SiH_4 + 95% Ar mixture in pulsed supersonic jets was studied. The sequence of process steps was determined from time characteristics of the jet that were recorded by pulse molecular-beam mass spectrometry. It is shown that pulsed jet condensation of the silane–argon mixture causes selective heating of the components, the heating process being dependent on the density of the mixture in the settling chamber of a nozzle. © *2001 MAIK "Nauka/Interperiodica".*

In this work, we continue discussion about new experimental findings on clustering and developed condensation in pulsed supersonic nonequilibrium jets of pure gases and their mixtures [1, 2]. Free jets of silane and silane-containing mixtures have been shown to be a promising source for the deposition of amorphous and polycrystalline silicon films [3]. Experiments with the LÉMPUS complex of gas-dynamic stations at the Novosibirsk State University, which provides extremely high densities of a jet freely expanding into a vacuum in the pulsed regime, have shed new light on condensation mechanisms.

In the experiments, we recorded the point in time T at which the leading edge of a gas pulse arrives at the detector of a mass spectrometer (Fig. 1) and the half-width D of the pulse (Fig. 2). The stagnation pressure P_0 of a 5% SiH_4 + 95% Ar mixture was varied between 0 and 700 kPa. Experimental conditions and equipment were similar to those used in [1, 2]. We traced variations of T and D with P_0 for monomers of argon (m/e = 40) and silane components (m/e = 31 and 33), for hydrogen (m/e = 1), as well as for di-, tri-, and tetramers of Ar and SiH_4 (m/e = 63, 80, 94, 111, and 160). The data obtained, which are in close agreement with those for the intensities of mass peaks [1], may provide a deeper insight into condensation mechanisms and conditions.

From the dependences of T and D on pressure (Figs. 1, 2), one can separate out several process stages.

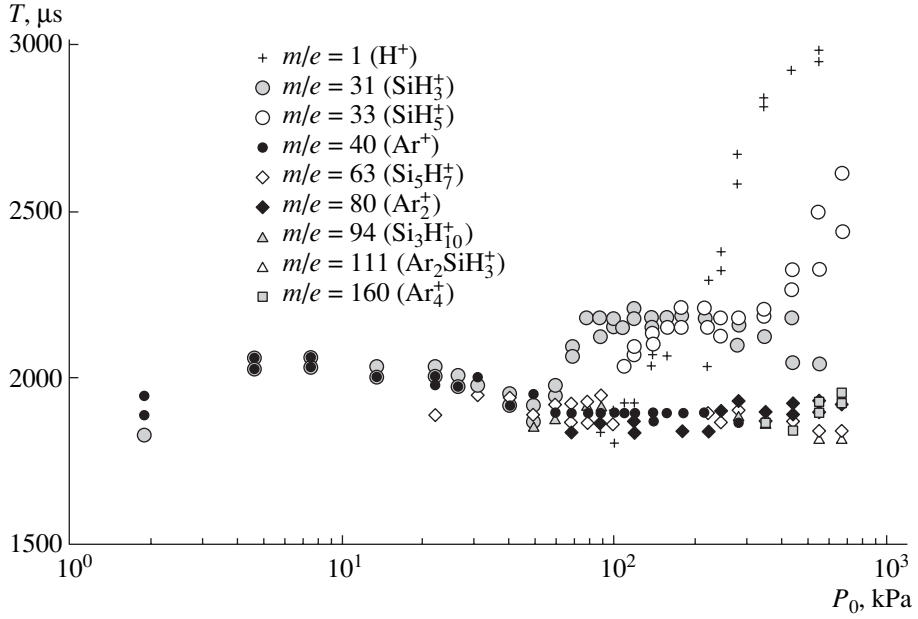

Fig. 1.

1063-7842/01/4604-0503$21.00 © 2001 MAIK "Nauka/Interperiodica"

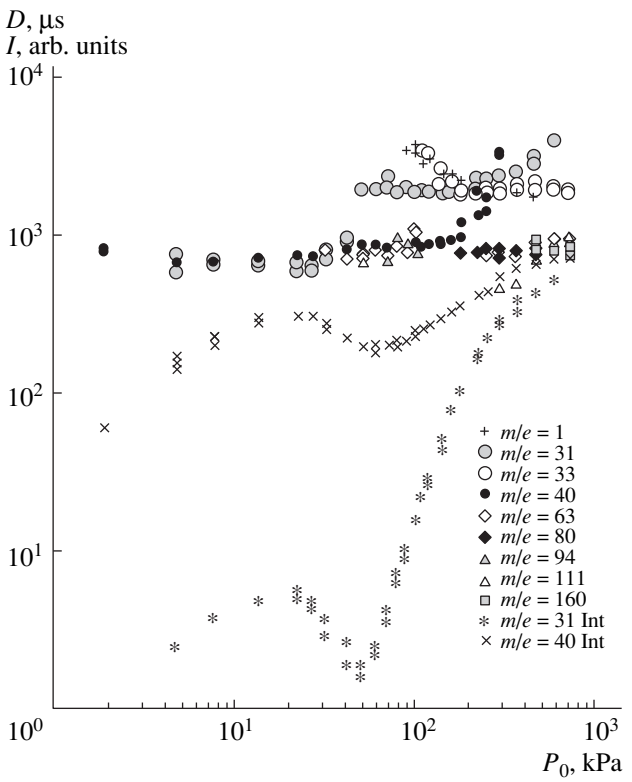

Fig. 2.

At $P_0 < 20$ kPa, the data for SiH_4 and argon monomers ($m/e = 31$ and 40, respectively) coincide; that is, SiH_4, being a minor impurity in argon, expands as a monoatomic carrier gas. In this pressure range, the pulse half-width is nearly constant and the time of pulse arrival gradually decreases. This is explained by an increased number of collisions in the supersonic flow, which results in the formation of the undisturbed flow core and increases the limiting Mach number.

When P_0 increases to 50 kPa, D for the monomers begins to rise. Its increment for the silane components is almost three times greater than for argon. Also, silane dimers ($m/e = 63$ for $Si_2H_7^+$ is shown in the figures) are recorded. Hence, silane condensation starts in this range. The velocities of the Ar and SiH_4 monomers continue to increase, judging from the T vs. P_0 dependence. Therefore, the pulses broaden due to the tail of slowed-down particles.

As P_0 grows to 100 kPa, T for the silane monomers substantially increases; in addition, argon clusters and argon–silane complexes appear in the mass spectra. The time of arrival and the pulse half-width saturate for all the recorded masses (except $m/e = 31$). It appears that, in this pressure range, the growth of silane clusters and also mixed clusters, initiated by silane nuclei, prevails.

Starting from $P_0 \approx 100$ kPa, the pulse half-width for the Ar monomer slowly grows. Then, from $P_0 > 200$ kPa, this growth becomes sharp. For silane ($m/e = 31$), D increases starting from $P_0 \approx 180$ kPa. It can be assumed that large Ar clusters begin to grow at $P_0 > 100$ kPa. At $P_0 > 200$ kPa, skimmer interactions in the condensing gas [2] seem to become significant. This assumption is substantiated by a slower increase in the intensities of masses $m/e = 31$ and $m/e = 40$ (Fig. 2). Hydrogen ions H^+ ($m/e = 1$) and SiH_5^+ ions ($m/e = 33$) also appear at $P_0 > 100$ kPa (their intensities grow by nearly the same amount with increasing P_0). The half-widths of these signals approach the limit that coincides with the saturation level for $m/e = 31$, and the time of arrival T monotonically increases with P_0 but starting from pressures corresponding to small clusters rather than to the monomers. The H^+ and SiH_5^+ ions appear presumably as a result of dissociative ionization of the clusters. First, small silane clusters ionize; then, as P_0 rises, large mixed clusters ionize in the ionizer of the mass spectrometer. In addition, if skimmer interactions are intense, the H^+ and SiH_5^+ peaks may broaden owing to the breakdown of large clusters in the skimmer. A reason for the increase in D for the silane and argon monomers may be electron-impact-induced breakdown of the large clusters in the detector of the mass spectrometer, since these clusters have lower velocities in the jet compared with the monomers because of the slip effect [4]. However, a severalfold decrease in the velocities of the clusters, as well as a great difference in the stability of the silane, argon, and mixed clusters at various process stages, seems to be unrealistic. Most likely, such an increase in D for the monomers, which is different for the argon and silane ones, means that they undergo selective heating due to the release of condensation heat in the pulsed jet of the mixture.

ACKNOWLEDGMENTS

This work was supported by the Russian Foundation for Basic Research (project no. 00-03-33021a) and by the Program of the Ministry of Science and Technical Policy in support of experimental facilities of national significance (project 06-05).

REFERENCES

1. R. G. Sharafutdinov, A. E. Zarvin, N. G. Korobeĭshchikov, *et al.*, Pis'ma Zh. Tekh. Fiz. **25** (21), 48 (1999) [Tech. Phys. Lett. **25**, 865 (1999)].
2. A. E. Zarvin, N. G. Korobeĭshchikov, V. Zh. Madirbaev, and R. G. Sharafutdinov, Pis'ma Zh. Tekh. Fiz. **26** (22), 21 (2000) [Tech. Phys. Lett. **26**, 989 (2000)].
3. R. G. Sharafutdinov, A. V. Skrinnikov, A. V. Parakhnevich, *et al.*, J. Appl. Phys. **79** (9), 7274 (1996).
4. O. F. Hagena, Surf. Sci. **106**, 101 (1981).

Translated by V. Isaakyan